Magnetic Resonance Imaging Techniques for Thermofluid Applications

Vom Fachbereich Maschinenbau
der Technischen Universität Darmstadt
zur Erlangung des Grades eines
Doktors der Ingenieurwissenschaften
(Dr.-Ing.)
genehmigte

Dissertation

von

M.Sc. Florian Wassermann
aus Mainz

Referent:	Prof. Dr.-Ing. Cameron Tropea
Korreferent:	Prof. Dr.-Ing. Sven Grundmann
Korreferent:	Prof. Dr. rer. nat. Andreas Dreizler
Tag der Einreichung:	30.07.2015
Tag der mündlichen Prüfung:	28.09.2015

Darmstadt 2015
D 17

Abstract

In this PhD thesis, Magnetic Resonance Imaging (MRI) techniques were applied to thermofluid applications. Magnetic Resonance Velocimetry (MRV) was utilized to measure the three-dimensional, three-component mean velocity field in forced convection flows. Flow models were investigated that contain complex internal structures (e.g. compact heat exchangers) that would not be measurable with conventional optical velocity measurement techniques. The effects of the internal structures on the fluid flow were analyzed to understand the flow physics and to introduce further improvements in performance. Modern three-dimensional manufacturing processes, such as direct polymer laser sintering, were used to manufacture MR compatible flow models of arbitrary complexity. Measuring velocity fields in such flow models highlighted the unique features of MRV.
Magnetic Resonance Thermometry (MRT), based on the temperature-dependent Proton Resonance Frequency (PRF) shift of the water molecule, is a comparatively novel approach with which the scalar temperature difference field can be measured. Novel experimental setups meeting the requirements given by MRT were developed and applied to MRT and MRV. The chosen flow models were taken from thermofluid sciences and exhibit mixed convection flows, whereby temperature-induced buoyancy forces play an important role. In their velocity and temperature fields three-dimensional structures develop. The three-dimensional temperature and velocity vector fields were measured utilizing optimized adjustments of both techniques. The results show the applicability of MRT and MRV to thermofluid applications and demonstrate these MRI techniques as valuable engineering measurement tools.

Kurzfassung

Die vorgelegte Doktorarbeit befasst sich mit der Anwendung von bildgebenden Magnetresonanzverfahren (MR-Verfahren) für die Vermessung von Thermofluid-Applikationen. Magnetresonanz-Velocimetrie (MRV) wird dabei verwendet, um das zeitlich gemittelte, dreidimensionale Geschwindigkeitsfeld mit drei Komponenten in erzwungenen Konvektionsströmungen zu vermessen. Es wurden Strömungsmodelle mit komplexen inneren Strukturen (beispielsweise wie in kompakten Wärmetauschern) untersucht, die in dieser Art und Weise nicht mit konventionellen optischen Strömungsmesstechniken messbar wären. Die Auswirkungen der Strukturen auf die Strömung wurden analysiert, was ein Zugang zur zugrundeliegenden Strömungsphysik ermöglichte und so Verbesserungsmaßnahmen vorgeschlagen werden konnten. Moderne dreidimensionale Fertigungsverfahren, wie selektives Polymer-Laser-Sintern, wurden verwendet, um MR-geeignete Strömungsmodelle von beliebiger Komplexität herzustellen. Die Vermessung von Strömungsfeldern in solchen Strömungsmodellen zeigte die einzigartigen Fähigkeiten von MRV.
Ein verhältnismäßig neuer Ansatz ist die Magnetresonanz-Thermometrie (MRT) basierend auf der temperaturabhängigen Verschiebung der Protonenresonanzfrequenz (PRF) der Wassermoleküle mit dem es möglich ist, das skalare Temperaturdifferenzenfeld zu vermessen. Es wurden neuartige MR-geeignete experimentelle Aufbauten entwickelt und mit MRT und MRV vermessen. Die verwendeten Strömungsmodelle, die aus den Thermofluidwissenschaften stammen, zählen zu den gemischten Konvektionsströmungen, bei denen temperaturbedingte Auftriebskräfte eine große Rolle spielen. In den Temperatur- und Geschwindigkeitsfeldern entstehen dreidimensionale

Strukturen. Die dreidimensionalen Temperatur- und Geschwindigkeitsvektorfelder wurden gemessen unter der Verwendung von optimierten Einstellungen in beiden Verfahren. Die Ergebnisse zeigen die Anwendbarkeit von MRT und MRV für Thermofluid-Applikationen und bestätigen die Wertigkeit dieser MR-Verfahren als Messtechnik für Ingenieure.

Acknowledgements

I thank the Deutsche Forschungsgemeinschaft (DFG) for funding the research project through GR 3524/3-1 and JU 2687/10-1.

I am thoroughly grateful to my supervisors Prof. Dr.-Ing. Cameron Tropea and Prof. Dr.-Ing. Sven Grundmann, without their frontier spirit this project and my work could not have been conducted. Both persons invested considerable time improving this thesis. I thank Prof. Dr. rer. nat. Andreas Dreizler for being my co-referee.

I would like to express my gratitude to Dr. Markus Piro of CNL (Chalk River, Canada) who introduced a cooperation between CNL and Technische Universität Darmstadt and provided suggestions for improvements to the work. Furthermore, I would like to acknowledge Prof. Dr. Ahmed Naguib of Michigan State University who gave input to many sections of this thesis.

Since the foundation of the MRV group in 2011 at the Center of Smart Interfaces of Technische Universität Darmstadt, numerous people were involved. I thank all colleagues at the Department of Fluid Mechanics and Aerodynamics who supported me during this period. I appreciate the efforts of our workshop, under the leadership of Ilona Kaufhold. Many complex experimental setups shown in this thesis would not have been possible without their precise work.
Most important for the MRV group was the cooperation to the Department of Radiology, Medical Physics of the University Medical Center Freiburg under the leadership of Prof. Jürgen Hennig. People part of this inter-

disciplinary group (all former members of the University Medical Center Freiburg) were Prof. Dr. Michael Markl, Dr. Bernd Jung, Dr. Ramona Lorentz and Dr. Robin Simpson. Each of them provided his/her experience and knowledge improving the final outcome, for which I am very grateful. I thank my colleagues Martin Bruschewski and Daniel Freudenhammer. Both of them supported my work with their knowledge and man power. I am thoroughly grateful to Waltraud B. Buchenberg. She has the greatest share in the project and was a fantastic companion over the last years.
A huge amount of the work presented in this thesis could not have been done without the helping hands and the ideas of many outstanding students. This includes the work of the research assistances Marcel Bonnert, Johannes Feldmann, Sebastian Gößlein, Simon Matthes, Timon Tsoukas and Stafan Wahlig, as well as the students graduated to a B.Sc. or M.Sc. degree: Jan Allendorf, Andreas Bauer, Salima Bourajrouf, Konstantin Dietrich, Daniel Hecker, Julius Siebner and Sebastian Wegt. Additional help was provided by student research project groups. Thank you all, it was a pleasure for me to work with you.

Last but not least, I appreciate the people standing behind me, my family. I am grateful to my parents Heike and Harald and my sister Sina. You always believed in me and helped me to find my way. The most valuable support came from my wife Caroline. You were my source of motivation. Caroline, there are no words that can express my gratitude.

Contents

Chapter 1

Introduction and Motivation

Visualizing and understanding fluid flow physics dates back to the research of pioneers like Ludwig Prandtl. At the beginning of the 20th century, he developed a closed-circuit water tunnel, which was capable of visualizing the water flow by using small particles distributed on the water surface. His result was the qualitative analysis of fluid flow around different bodies, such as the flow separation behind an inclined airfoil. More recently, optical techniques, such as digital particle image techniques, have been developed and enable researchers to investigate higher-dimensional flow and temperature fields quantitatively.

A completely different flow measurement technique has its origins in medical diagnostics. Magnetic Resonance Imaging (MRI) techniques were introduced in 1973 by Lauterbur and Mansfield and are commonly used for clinical analysis of human tissue. It provides three-dimensional information from inside opaque objects without being intrusive. In the field of cardiovascular diagnostics, Magnetic Resonance Velocimetry (MRV) proved its applicability, capable of measuring the three-dimensional flow field inside a human heart. In its current state, MRI is able to capture multiple quantities, such as the flow velocity field, the scalar temperature field and the scalar concentration field, to name only a few. This makes MRI a highly applicable tool for engineering research and a viable competitor to conventional measurement techniques, such as digital particle imaging techniques. Currently, only few research groups are capable of applying MRI techniques to engineering applications. Most experiments involving MRI for engineering purposes have a fluid mechanics background. With each conducted experiment, more facets

of the techniques' possibilities and limitations are understood. Nevertheless, there are still many more lessons to learn for the engineering community by further exploring the technique´s capabilities. This is the purpose of the presented PhD thesis.

Thermofluid applications unite the fundamentals of the scientific disciplines fluid mechanics and thermodynamics. In this thesis, the focus is placed on applications where heat and mass transfer processes are important, like in heat exchangers, fluid mixing systems (e.g. Heating, Ventilation and Air-Conditioning systems - HVAC) or complex three-dimensional natural convection flows, such as those occurring in airplane cabins. Research within this field is associated with the analysis, measurement and modeling of energy transfer processes in a thermofluid system by interaction with its surroundings.
A standard experimental approach for the characterization of such an application is to measure characteristic quantities before, within and after the test section. By variation of the systems´ boundary conditions, a performance map can be constructed showing the integral behavior of the system. Modifications applied to the test section lead to performance alteration and can be evaluated by calculating appropriate dimensionless numbers, such as the Nusselt number. The results are often used to formulate a universal behavior by means of correlations (VDI, 2010). They are frequently considered during the design process of an application.
The overall performance of a thermofluid application can be attributed to thermodynamic and fluid mechanic processes taking place on length scales of the size of the boundary layer and time scales determined by unsteady behavior. Of great interest are the interactions between wall-fluid and fluid-fluid boundaries. On the one hand, models based on the fundamental equations describing the physics of the application can be developed. They are sometimes analytically and in most cases numerically solvable, which is predominantly done with the help of Computational Fluid Dynamics (CFD). On the other hand, spatially resolved information (velocity field, acceleration field, Reynolds stresses, temperature field, pressure field, etc.) inside the test section can be measured by utilizing appropriate experimental techniques. The data field that was either achieved in an analytical way, in a numerical way or in an experimental way can be used to work out the physical mechanisms. Nevertheless, in engineering research all data have to be evaluated. CFD results especially have to be verified in order to provide

reliable data. This is often done experimentally by reducing the application to a measurable model and comparing the CFD data to quantities obtained with extensive experiments. The decision for the utilization of a certain measurement technique is made according to data quality and quantity, as well as applicability. However, increasing computer performance enables to increase the CFD complexity (model complexity, information content,...). The increased complexity also affects the experiments. With increasing experimental effort certain measurement techniques become unreasonable. This underlines the need for considering all existing measurement techniques and to judge their suitability for a specific application.

On the one hand, Magnetic Resonance Velocimetry (MRV) is utilized to analyze forced convection flows, where the temperature field is assumed to be uniform. As the investigated flow models contain a complex internal structure, conventional optical measurement techniques are often applicable only with undue experimental effort. This is the point where MRV has its advantages. No optical access is needed and nevertheless volumetric data is acquired. The heart flow of a living human is an excellent example for the applicability of MRV. This could never be measured with a velocity measurement technique conventionally used in engineering. When the flow model is made of MR appropriate material, then MRV only detects the parts of the flow model where measurement fluid is present. Modern three-dimensional manufacturing processes, such as direct polymer laser sintering, enable the construction of complex structures suitable for MR usage. These setups and the analysis of the velocity fields measured with MRV are one part of this thesis. By analyzing characteristic parts of the flow important features influencing heat transfer processes can be revealed.
A comparatively novel approach is Magnetic Resonance Thermometry (MRT), based on the temperature-dependent Proton Resonance Frequency (PRF) shift of the water molecule with which the scalar temperature difference field can be measured. Compared to MRV, this technique is more sensitive to the experimental setting. In this thesis, the flow models and the experimental setup were improved to meet the requirements demanded by MRT. To demonstrate the applicability of MRT laminar flow through a double pipe heat exchanger setup was measured. The results show that the MR experiments are applicable for a wide range of thermofluid applications.

1.1 Interdisciplinary Project

For the engineering utilization of the MRT technique a joint research project between the Technische Universität Darmstadt and the University Medical Center Freiburg was granted by Deutsche Forschungsgemeinschaft (DFG) through GR 3524/3-1 JU and 2687/10-1. It is desired to utilize and promote the MRT technique with suitable applications coming from the field of engineering sciences. For the sake of completeness, MRT is combined with MRV, to provide full three-dimensional and three-component velocity vector fields. The overall goal is to assess the applicability of the MRT technique as a measurement tool for engineers and physicists. In this joint effort, both partners aim to explore the possibilities and the limitations of MRT and present possible experimental setups, also for future considerations.

Throughout this PhD thesis, the *project partner* is Waltraud B. Buchenberg (University Medical Center Freiburg). She is an MR physics specialist and responsible for the development of the procedures, strategies and data processing needed for MRT. Among many other activities, she evaluates the experimental setup in terms of MR physics and proposes rules for the design and arrangement of an MR appropriate flow model.
Situated at the Technische Universität Darmstadt, the author of the current work is specialized in fluid mechanics. His part of this work is the development of appropriate flow models on the basis of thermofluids and the composition of the fluid mechanical and thermodynamical setup. The results are used to assess the applicability of the measurement technique. For this reason, conventional measurement techniques are applied and compared to the MR data. Results are used for analyzing heat transfer applications.

1.2 Objectives and Outline of the Current Work

This PhD thesis discusses the applicability of MRI techniques as an engineering measurement tool and provides guidelines of how to apply experimental setups of thermofluid background. In combination with the work

conducted within the scope of the interdisciplinary project, the following objectives are:

- Conventional flow velocity and temperature measurement techniques are reviewed and compared to MRV/MRT in order to show advantages and disadvantages of the MRI technique. This is presented as part of the "Introduction".

- The physics of MRI in general and MRV/MRT specifically are reviewed from an engineering perspective. A focus is set on the capabilities and limitations of the measurement technique. This is the topic of chapter "MR Imaging". The basics of convective heat transfer based on fluid mechanics and thermodynamics are reviewed as complementary material in the appendix.

- For the utilization of MRV/MRT, different experimental setups are necessary. They are composed of different parts that were designed and constructed with the goal to meet the requirements of the available MR setting. Components of the flow apparatus utilized and developed in this thesis, the flow model design as well as the construction process are explained in the "Methodology" chapter. Recommendations regarding MRT proposed by the project partner are summarized and translated into engineering language.

- Two thermofluid applications associated with forced convection flow in channels filled with complex internal structures are investigated using data measured with MRV. This includes fluid flow through a tetradecahedral grid and the flow through a CANDU nuclear fuel bundle replica. The focus is set on the assessment of data quality and applicability as well as data analysis. These results are presented and discussed in the "MRV Experiments" chapter.

- A major part of this thesis is the application of MRT. This is also the background of the interdisciplinary project done in close cooperation with the project partner. Different flow models were designed and constructed utilizing the components described in the "Methodology" chapter. Preliminary experiments show the progress and important lessons learned during the project. The MRV/MRT data obtained for the double pipe setup are assessed and analyzed by inspecting the flow and temperature

field and comparing to literature. Additionally, conventional measurement techniques were used for data comparison.

1.3 A Review on Selected Velocity and Temperature Measurement Techniques

In this section, well established velocity and temperature measurement techniques are reviewed. This provides a basis to compare conventional techniques with the MRI techniques. The discussion intends to clearly define the capabilities and limitations of selected velocity and temperature measurement techniques. A detailed description of MRV and MRT is given in Chap. 2.

1.3.1 Measuring Fluid Velocity

A variety of measurement techniques are available that are capable of measuring fluid velocity for compressible and incompressible fluids. The most widely-used techniques are explained in detail by Tropea et al. (2007). These techniques differ mainly in features like the invasiveness, the required optical accessibility, the capability of achieving temporally-resolved and spatially-resolved data and the number of measured velocity components. Established invasive methods measure velocity from pressure measurements (e.g. Pitot tubes) and from the thermal response of a probe (e.g. hot wire anemometry). As MRV is a non-invasive technique, the following discussion concentrates on optical techniques, such as laser Doppler Velocimetry (LDV) or Particle Image Velocimetry (PIV).
The velocity u of an object can be calculated by measuring the distance Δs and the time span Δt it traveled with the following equation:

$$u = \frac{\Delta s}{\Delta t} \tag{1.1}$$

This is also the basic principle of the optical techniques LDV and PIV that are also capable of resolving multi-dimensional velocity fields by applying Eq. 1.1 to multiple directions. Both techniques utilize seeding particles (also termed tracer particles) added to the measurement fluid. Hence, particle-based techniques only measure the flow indirectly via the particle movement. Particles scatter light that can be used to measure Δt and Δs. This also means that a light source is needed. Signal quality is strongly influenced by the particle size. Additionally, particles have to follow the flow properly. They have to be small enough to prevent particle slip such that the particle´s trajectory is a good representation of the surrounding fluid. In the following, the principles of LDV and PIV are introduced as they are most frequently used. The main limitations and advantages are presented in order to compare these technologies to MRV.

1.3.1.1 Laser Doppler Velocimetry

LDV which is often referred to as laser Doppler anemometry (LDA), is capable of acquiring point-wise velocity data (up to three components) with high accuracy. There are different models to explain the basics of LDV. One is the model of interference fringes. An LDV system utilizes the fringe pattern (constructive and destructive interferences) occurring in the intersection of two coherent laser beams. The intersection volume is also termed the measurement volume and the configuration is termed dual-beam. The fringes have a constant spacing of distance Δs. A particle crossing the intersection is illuminated according to the fringe pattern. The scattered light with intensity i is received over some solid angle by a photo detector and yields the transit time Δt which is proportional to the velocity component normal to the fringe pattern. Utilizing Eq. 1.1 yields the velocity component in that direction. The time signal can also be interpreted in the frequency domain. Therefore, the signal frequency f_s can be introduced. Then Eq. 1.1 changes to $u = \Delta s f_s$. The basic LDV principle is depicted in Fig. 1.1. With the above setup, the particle direction through the measurement volume cannot be recognized. By changing the light frequency of one the laser beams relative to the other one by a relatively small amount, the fringe pattern moves with a constant shift velocity. This can be achieved by a Bragg cell, which is a crystal that modulates the light frequency by density changes

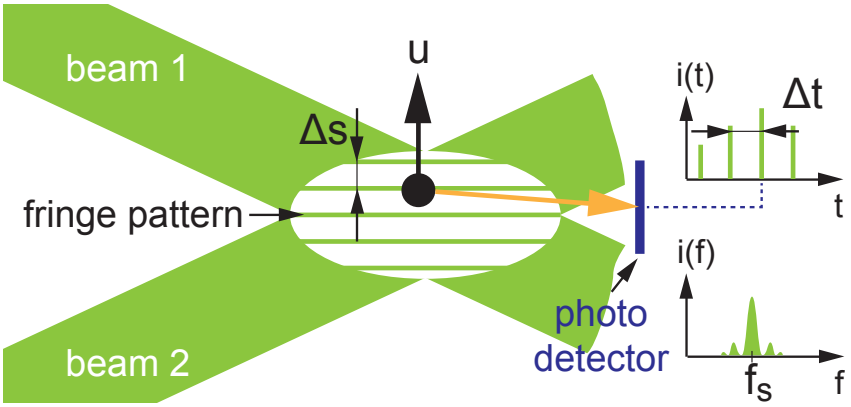

Fig. 1.1: Basic principle of LDV for a dual beam configuration.

evoked by pressure waves compressing the material. A particle moving in the same direction as the moving fringe pattern is detected with a lower frequency and a particle moving against the fringe pattern with a higher frequency. The frequency shift of the laser beam results in a directional sensitivity.

Light scattering of particles is a very complex topic and a central point for LDV. It depends on the particle size, the particle material, the illuminating intensity and many other factors. For spherical particles smaller than the beam diameter and larger than the light wave length, the Lorenz-Mie scattering of light can be applied (Albrecht et al., 2003). In brief, it describes the scattered light intensity distributed over angular positions. This indicates possible locations for the placement of the detector. The receiver can be operated in the forward scatter mode, yielding the best light intensity. It can be operated in the side scatter mode, which still has a good light intensity. Or it can be operated in the backward scatter mode, which has an acceptable light intensity but is also easiest to set up. For each experimental setup, a compromise between signal quality and experimental effort has to be found.

Each particle acquired in the measurement volume provides information about the flow. The signal from one detected particle is called a burst. In order to obtain statistically correct flow information, many bursts have to be detected, depending on the flow velocity, turbulence and particle size. Due to that, LDV is able to provide higher moments of the measured velocity component, as for instance the root-mean-square (RMS) value.

More detailed information can be found in Albrecht et al. (2003) and Tropea et al. (2007).

A conventional one-component dual-beam LDV system comprises a trans-

mitting and a receiving probe as well as a data processor. The transmitting probe consisting of a laser, a beam splitter, a Bragg cell and a focussing lens. The receiving probe contains the receiving lens and the photo detector. A signal processing unit controls the system and processes the acquired measurement signal. This simple setup is depicted in Fig. 1.2. By apply-

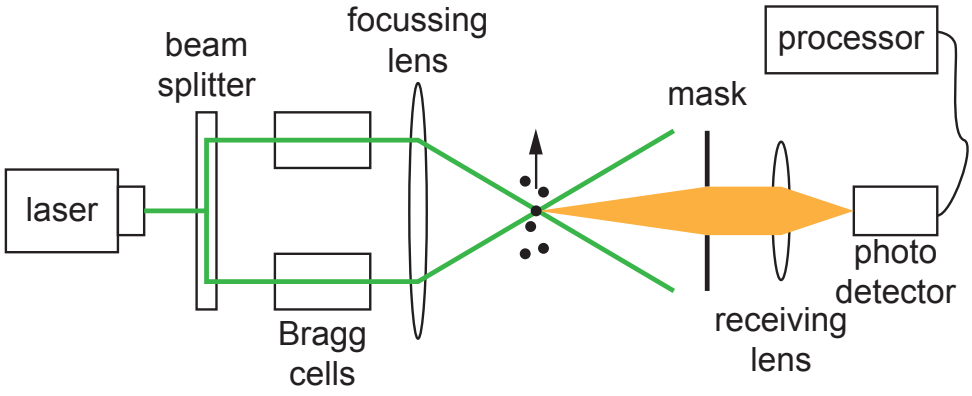

Fig. 1.2: Setup of a dual-beam LDV system in forward scattering mode.

ing multiple dual-beam lasers with different orientations and with different laser wave lengths, up to three velocity components can be measured in one measurement volume with one burst. Three axis traversing systems enable one to subsequently acquire point-wise velocity data and build up a three-dimensional flow data field with high spatial and temporal resolution.
The described features of LDV result in advantages and limitations presented in Tab. 1.1.

Tab. 1.1: Advantages and limitations of LDV.

Advantages	**Limitations**
Non-invasive	Particle seeding needed
No calibration	Optical access needed
High spatial and temporal resolution	Complex equipment
2C simple, 3C more complex	Spatial traversing is time consuming
High accuracy	

1.3.1.2 Particle Image Velocimetry

With the ability to acquire up to three-component velocity vectors over two or three spatial dimensions, PIV can resolve coherent flow structures; thus, is the most common multi-velocity component measurement technique.
Similar to LDV, particle imaging techniques rely on light scattered by seeding particles. In contrast to LDV, the light source is a two-dimensional laser light-sheet prepared by special light sheet optics. All particles flowing through this 2D area with finite thickness are illuminated. Again, Eq. 1.1 is applied for velocity measurement. Therefore, two images at the temporal interval Δt of the illuminated 2D area containing the particles are photographed. By comparing both images, the pixel-wise particle displacement Δs can be calculated. This also implies a major requirement for particle imaging techniques: During Δt the particles have to obtain a sufficient displacement that is detectable by the camera image. As the photograph is two-dimensional, a displacement in the x-direction (Δs_x) and the y-direction (Δs_y) can be determined. Utilizing the resolution of the camera and the interval Δt between two consecutive images, a two-dimensional velocity field can be derived. For PIV, the displacement field can be derived automatically by using smart reconstruction algorithms based on cross-correlations. The basic principle of particle imaging techniques and the required setup is depicted in Fig. 1.3. The foregoing basic principle applies to all parti-

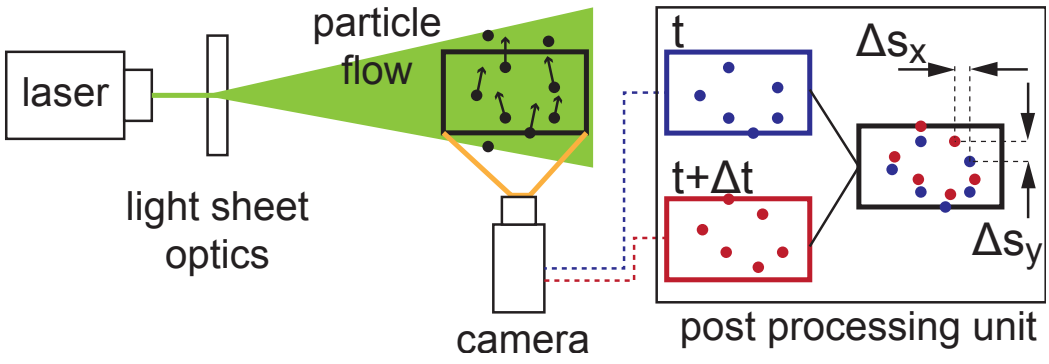

Fig. 1.3: Basic principle and setup for particle imaging techniques.

cle imaging techniques. They are classified according to the concentration of tracer particles. If the particle concentration is low a tracking of single particles is possible (Particle Tracking Velocimetry - PTV). For very high seeding concentrations, individual particles are no longer visible to the cam-

era. They form random speckle patterns that move and transform with the fluid flow. This technique is called Laser Speckle Velocimetry (LSV). When the seeding is held at medium concentration levels, then this is termed PIV. It is also the most commonly used technique. There exist a variety of PIV modes and configurations that are available and that are suitable for different problems. More details about PTV/LSV/PIV are provided by Adrian (1991) and Raffel (2007).
The "classical" PIV setup shown in Fig. 1.3 comprises a laser, light sheet optics, a digital camera and a post-processing unit. The faster the camera can take an image, the shorter Δt becomes. This shows a major advantage of PIV that can resolve unsteady processes by using high speed cameras. Utilizing a second camera adjusted at a different angle, stereoscopic PIV is accomplished. Hereby, the reconstruction of the through-plane velocity component (2D3C) is achievable. Tomographic PIV or volume PIV even utilizes several cameras. With this technique, volumetric data with three velocity components (3D3C) can be acquired. With every modification the system complexity increases. As is obvious from the PIV setup, the camera has to be focussed on the imaging plane. This is done with the help of a calibration target. The calibration procedure has to be done several times (before, after and during the measurements). This indicates the large experimental efforts especially for stereoscopic or tomographic PIV setups. Furthermore, post-processing the data is time-consuming. Advantages and the limitations of the PIV technique are listed in Tab. 1.2.

Tab. 1.2: Advantages and limitations of PIV.

Advantages	**Limitations**
Non-invasive	Particle seeding needed
High temporal resolution	Optical access needed
Quasi-instantaneous	Elaborate calibration
Very high spatial resolution	Complex setup for 3D3C
2D2C simple, 3D3C possible	Time-consuming post processing
	Illumination, light intensity

1.3.1.3 Refractive Index Matching

In order to measure the flow in complex geometries with solid/fluid interfaces (e.g. undercuts, inside grid space,...) with optical measurement techniques, transparent materials (such as Lucite or quartz) are utilized as windows. A problem for both LDV and PIV is the presence of solid/fluid interfaces and/or curved walls. The laser beams of an LDV system are retracted when measuring through curved surfaces. This leads to a beam misalignment and signal loss. In a PIV setup, the laser sheet can bend or be reflected at solid/fluid interfaces. Parts of the measurement field would suffer from insufficient illumination.
The effects of solid/fluid interfaces or curved walls can be avoided by using the refractive index matching method (RIM) (Albrecht et al., 2003; Budwig, 1994). Hereby, the refractive index of the measurement fluid is adjusted that it is equal to the refractive index of the flow model and the surrounding channel walls. The flow model requires a high optical quality that has to be realized during the manufacturing process or with an appropriate after-treatment. In some cases it may not be practical (or even possible) to manufacture flow models in Lucite or quartz. An example combining RIM and LDV is presented by Liu et al. (1990) and the combination of RIM and PIV is presented by Scholz et al. (2012).

1.3.1.4 Comparison to MRV

It is difficult to benchmark and rank LDV, PIV and MRV. Every technique has advantages and disadvantages that make each technique uniquely applicable to specific problems. LDV and PIV are mature techniques in fluid mechanic research. As MRV is still a not well established measurement technique for engineers, it has to find its niche in future research.
For a quantitative comparison between LDV, PIV and MRV, dedicated experiments were taken from literature. All have in common that they utilize water as measurement fluid and that they acquired spatial data sets. According to that Tab. 1.3 summarizes the main experimental parameter (flow conditions, FOV size, spatial resolution) of the chosen experiments. Most important for a quantitative comparison is the amount of collected data

(FOV size) during a certain time interval (acquisition time).
The data presented for the tomographic PIV experiment show a very high spatial resolution and are time-resolved. As there are no values for the measurement time and the calibration time, the processing time is listed with 4 h. With 26 hours the longest total acquisition time was accomplished with the LDV experiment. Nevertheless, the geometric complexity of the flow model is remarkably as well as the obtained data quality. Measuring the flow inside a stochastic foam replica the flow model in the MRV experiment was the most complex one. The spatial resolution is very good and the measurement time (1.5 hours) relatively short. The MRC and MRT experiments even showed shorter acquisition times, whereas the model complexity and the FOV size is reduced. They have been listed for the sake of completeness.
In summary, by comparing the listed experiments (that have been chosen for demonstration purposes) the advantages of MRV and its related techniques (MRC, MRT) compared to LDV and PIV can be worked out. Especially in terms of three-dimensionality, model complexity and accessability as well as acquisition time the MR-based techniques are superior. A major drawback is the availability of the expensive MR device which is typically situated at a radiology department and, hence, not available during the week. MRV as utilized for the presented experiment measures time-averaged velocity fields. LDV and PIV have access to higher order moments. Measuring flow turbulence or time-resolved flow with MRI are still a big issue in research.

Tab. 1.3: Comparison of experiments conducted with PIV, LDV and MRV/MRC/MRT.

Lit.	**Meas. tech.**	**Exp. setup**	**Flow cond.**	**FOV [voxels]**	**Res. [mm/voxel]**	**Acquisition time**
Michaelis et al. (2006)	Tomo PIV, 3D3C, time-resolved, glass spheres (30 μm)	water flow in cylinder wake	0.015 - 0.21 m/s	1730 x 1089 x 377	0.0424 iso	calibration after each measurement, 4 h processing time per volume
Xiong et al. (2014)	LDV 3C+RMS, 3D traversing, polyamide particles (5 μm)	water flow through fuel rod bundle with spacer grids	Re = 6,600 to 70,000	18 x 35 x 3	1 x 1 every 170mm	50 s per data point = 26 h total
Onstad et al. (2011)	MRV (3 T), 3D3C	water flow through stochastic foam replica	0.07 m/s (44.6 L/min)	124 x 512 x 512	0.6 x 0.47 x 0.47	6 x 15.2 min = 1.5 h total

Benson et al. (2010)	MRC (1.5 T), 3D	mixing layer of parallel water flow	0.4 m/s (4 L/min); 0.14 m/s (0.6 L/min)	256 x 512 x 32	1.17 x 0.59 x 0.69	several calibration and experimental scans, 36 s per 3D scan
Small et al. (2009)	MRT (9.4 T), 3C + Temperature, 2D multi slice	water flow through a heated shape memory polymer foam	13 mm/s (3.8 ml/min)	128 x 128 x 2	0.078 x 0.078 x 2	2 min

1.3.2 Measuring Fluid Temperature

The following review provides the background of selected fluid temperature measurement techniques. On the one hand, invasive techniques are presented that are easy-to-use and applicable in the MR environment. They can be used for temperature validation or temperature monitoring during MRT measurements. On the other hand, non-invasive measurement techniques are explained that are capable of measuring multi-dimensional temperature fields. All techniques are then compared in a table by extending the work of Childs et al. (2000). Due to the large number of temperature measurement techniques, only a selection is explained. Due to the fact that the PRF method (in the current state) is only applicable in liquids, the review concentrates on measurement techniques which are applicable to water flows. A detailed review of the most important techniques is provided by Camci (2010), Childs et al. (2000), and Tropea et al. (2007).

1.3.2.1 Invasive Techniques

The point-wise measurement of the fluid temperature using invasive probes is, compared to most other techniques, inexpensive and easy-to-use.

Very often applied is a thermo-electric device termed thermocouple. It is based on the Seebeck effect. Two conductors of different material in an electrical circuit experience an electromotive force (emf), when exposed to a temperature gradient. Due to thermal diffusion processes between the two conductors, an electrical field develops that can be measured as a voltage. Each conductor material has a thermoelectric coefficient (k-value), measured relatively to the one of platinum. For a desired application a suitable thermocouple material pair can be chosen, depending on the temperature range, accuracy, chemical resistance.
Most common is the thermocouple of type K. It is composed of a nickel chromium - nickel (NiCr-Ni) pair. Another important one is the type T thermocouple comprising a copper - copper nickel alloy (constantan) pair. This type is especially applicable in a temperature range of -250 to 300 °C and applicable in oxidizing environments. Thermocouples can be made of

non-metal material (e.g. carbon) for the application at very high absolute temperatures. Such devices are not commercially available. It is expected that these devices are suitable for the usage in MR environment. Type T thermocouples with a sheath diameter of 0.2 mm have been successfully implemented in a 0.2 T electromagnet scanner by Grimault et al. (2004). Thermocouples are cheap, robust and available in many different versions. An advantage is their sheath size that can be 0.1 mm or even smaller. Thermocouples can be easily embedded into surfaces.

Another class of invasive probes are electric resistance devices. The principle is simple and most often applied. Each electrical conductor has a temperature-dependent resistance. This is based on the movement of the free electrons and the behavior of the atomic lattice at different temperatures. In an electrical circuit the temperature-dependent voltage at the conductor can be measured when a constant current is applied. A Wheatstone balancing-bridge circuit is used and the differential voltage is measured. The conductor material can be a metal, a ceramic or a semiconductor.
Platinum Resistance Thermometers (RTDs) are most accurate with a very stable resistance-temperature characteristic. They are most often applied an known as pt100 probe. For industrial use, the platinum wire conductor is embedded into a ceramic compound and protected by an additional metal coating. Hence, RTDs are much thicker and have a decreased response time compared to thermocouples. However, they are more accurate than thermocouples.

Invasive temperature probes can utilize optical effects to measure the temperature. Different principles are available for temperature measurement. The most important ones are based on optical reflection, fluorescence, absorption and radiation. Optical fibers can be used to transport this information. As they typically consist of glass or crystals, the probes can be used in chemical aggressive or high temperature environments. One of the commercially available systems utilizes a semiconductor crystal (e.g. gallium-arsenide crystal) fixed at the tip of the optical fiber. The band edge position of the crystal is temperature-dependent. White light sent to the crystal is scattered with a different spectrum according to the band edge position. A change in temperature also changes the scattered light spectrum. The scattered light transported through the optical fiber can be analyzed in a spectrometer. This principle is very precise (0.1 $^{\circ}C$) in a temperature

range of -200 to +300 $°C$ and not affected by fiber strain in comparison to most other fiber-optical principles.
Another advantage of optical systems is that the probe can be exposed to strong magnetic and electromagnetic fields. It has to be calibrated when used inside an MRI device (Buchenberg et al., 2014). A fiber-optical system is more expensive compared to a thermocouple or an RTD system. As a consequence, less probes are available for the instrumentation of a setup. The fibers are very sensitive to strain and can easily break. Single point probes have a head diameter of about 1 mm. In terms of accuracy they are better than thermocouples but less accurate than RTDs.

Due to the intrusion into the flow the point-wise probes can significantly alter the velocity profile. Some point-wise probes have the problem that they suffer from errors due to thermal conduction along the sensor body (Minn Khine et al., 2013). The positioning of the sensor in the flow is often difficult and can lead to significant positioning errors. The probe head should be adjusted opposing the main flow direction. Hence, the static temperature is measured correctly (Nitsche and Brunn, 2006). This has to be considered when friction leads to an increase in the fluid temperature.
In order to obtain spatially resolved temperature data, multiple probes have to be arranged in an array or a rake. If the velocity and temperature fields are stationary, a single probe can be traversed within the flow field. However, point-wise intrusive temperature measurement techniques are mainly used at fixed positions. Multiple probes can be integrated into the surface of the flow model with which a two-dimensional surface temperature distribution can be measured.

1.3.2.2 Non-invasive Techniques

Likewise the velocity measurement, optical techniques are the solution for more-dimensional temperature acquisition.

By seeding the flow with temperature-sensitive particles and utilizing a similar setup as explained for the particle imaging techniques, a two-

dimensional temperature map within fluid flow can be achieved. Thus, the technique was termed Particle Image Thermometry (PIT). The temperature-dependent features of Thermochromic Liquid Crystals (TLCs) are utilized (Gennes and Prost, 2007). They are substances that have both liquid and crystal properties. TLCs consist of either Cholesteric-based Liquid Crystals (CLCs) or Chiral-Nematic-based Liquid Crystals (CNLCs) (Dabiri, 2009; Oswald and Pieranski, 2005). They are composed of different layers comprising rod-like molecules. They form an anisotropic arrangement that only reflects a band of certain light frequencies. This frequency band is temperature-dependent. By illuminating the TLCs with white light, the TLCs scatter the light in different colors according to the temperature of the surrounding fluid. CLCs and CNLCs have a different colorimetry. TLCs are typically microencapsulated in a polymer or gelatine in order to prevent them from degrading. The TLCs have to be suspended in the measurement fluid. They are neutrally buoyant when applied in water. UV light can damage the TLCs. Profound information about PIT and successfully applied experimental setups utilizing PIT are shown in Dabiri (2009).
Additionally to the advantages and limitations discussed for the particle imaging techniques used for velocity measurements, PIT also has a high spatial and a good temporal resolution (according to the performance of the camera). The temperature resolution depends on the TLC substance, the illumination and the color camera calibration. The latter one is a major experimental task. Additionally, PIT can be combined with PIV in the same setup. Thus, temperature and velocity fields are accessible.

By utilizing Temperature-Sensitive Paint (TSP) applied on a surface the quantitative measurement of the surface temperature distribution is possible. TSP consists of luminophore molecules embedded into a binder matrix. Therefore, phosphors (e.g. certain lanthanide-complexes) show a temperature-dependent (and/or pressure dependent, → pressure sensitive paint - PSP) luminescence. Incident light is absorbed by the luminophore and, in turn, emitted at a color according to the temperature. In some cases the luminescent material has also a temperature-dependent decay time. This can be utilized for temperature evaluation (Liu and Sullivan, 2005).
A typical setup comprises the paint as a compound of the luminophore material embedded into a a polymeric matrix which is then applied on a surface and exposed to a convective flow. For illumination typically a narrow-band white light source is used. The emitted light is recorded with a camera.

1. Introduction and Motivation

Temperature evaluation can be done with different techniques according to Tropea et al. (2007).
An advantage of TSP in comparison to TLC is, that the emitted color is independent of the viewing angle, the pressure and the UV light intensity (Tropea et al., 2007). TSP has a good temporal response according to the used luminophore and technique. Limitations are that TSP can only resolve temperatures on a surface and, hence, is more likely used as heat flux measurement technique.
In a feasibility study, Fey et al. (2013) develop a water-specialized TSP they termed "waterTSP" technique. They applied it on a heated/cooled cylinder wall that provided a surface temperature range of $0.5 < \Delta T < 1.5°C$. The flow rate was maintained at different Reynolds numbers $3500 < Re_d < 14500$. The chosen luminophore had a high sensitivity. Hence, unsteady temperature fluctuations and thermal signatures of the wall shear stress could be qualitatively analyzed.

An additional temperature measurement technique based on the temperature dependency of the refractive index of fluids in incompressible flow, are the Schlieren or the shadowgraphy methods (Tropea et al., 2007). They are optical, non-invasive and the results are two-dimensional whereas the measurement quantity is an integrated value over third dimension of the measurement volume. They are typically used to measure free convection flows. Quantitative results can be obtained by using the Background-Oriented Schlieren (BOS) technique. The setup is rather simple. A background target with a random dot pattern is used as a reference and a camera is focussed on the background plane. In between, a measurement object/fluid is placed that, for instance, can be a wind tunnel or a water reservoir containing a heatable cylinder. If the object is heated it evokes density changes in the fluid. They can be detected by the camera as displacement of the dot pattern. By correlating the image taken without heating and with heating applied, a displacement field can be derived yielding a refraction index map. This can be transferred into a temperature difference field.
For BOS, equal post-processing methods as used for particle imaging techniques can be utilized. BOS can be combined with PIV and applied simultaneously. Therefore, additional seeding, a PIV camera and optical filters are required.
The combination of BOS and PIV was successfully applied by Tokgoz et al. (2012) to a thin water layer that was fed by a hot and a cold jet. Tem-

perature differences of less than 1 K could be measured and temperature fluctuations resolved.

1.3.2.3 Comparison to MRT

For qualitative comparison of the different temperature measurement techniques, Tab. 1.4 summarizes the main features. It is based on the work of Childs et al. (2000) and additionally adds water-specialized temperature measurement techniques, such as MRT, waterTSP and BOS in water.
In general, the measurement of temperatures is more complicated than the measurement of velocities, since the techniques are more sensitive to environmental influences. Nevertheless, there is a variety of measurement techniques available. In MR environment, only the liquid-in-glass thermometer, fiber-optical techniques or optical techniques and in some cases thermocouples would be applicable.
For comparison to MRT, a focus is set on techniques which are non-invasive and applicable in the medium water. PIT, TSP and BOS have advantages in terms of spatial and the possibility to measure unsteady processes. They are typically two-dimensional, whereas in combination with PIT also a quasi 3D field can be obtained, by traversing the light sheet and camera. The temperature range is comparable for all techniques. BOS shows the best temperature resolution within the mK-range.

PIT and BOS can be combined with PIV in one setup and applied simultaneously (with additional experimental efforts). Hence, these techniques can be used for the investigation of thermofluid applications. As the discussed non-invasive methods need optical access, the model complexity is limited or elaborate RIM techniques have to be applied. This is also the point where temperature and velocity measurements using MRI are superior. If a thermofluid experiment is especially designed for MR application, then flow models of arbitrary complexity can be investigated. Results can be resolved spatially. The measurement can be conducted in an appropriate measurement time typically within minutes. However, MRI techniques have to prove their reliability and applicability for thermofluid sciences. This is one goal of the present PhD thesis.

Tab. 1.4: Comparison of MRT to different temperature measurement techniques presented in Wassermann et al. (2014a) and Tsoukas (2014) based on Childs et al., 2000. The table shows the method name, the physical effect (if not defined by method name), the temperature range, the accuracy (Accu.), the response (Resp.), the measurement dimension (Meas. Dim.), the MR suitability (MR suit.), the costs and the commercial availability (Comm. avail.).

Method	**Physical Effect / Principle**	**Temp. range [°C]**	**Accu.**	**Resp.**	**Meas. dim.**	**MR suit.**	**Costs**	**Comm. avail.**
Liquid-in-glass thermometers	temperature-dependent liquid-volume	-200 to 600	0.01 °C	slow	point	partly	low	yes
Thermocouple	metal	-270 to 3000	0.5 - 2 °C	fast	point	partly	low	yes
	non-metal (carbon, boron, carbide, etc.)	-	1 °C	-	point	good	-	no
Electrical resistance thermometer		-260 to 1064	0.1 °C	fast	point/ area	no	low	yes
Fiber optical temperature sensors	thermographic phosphors	-200 to 330	0.2 $°C$	fast	point	very good	mid	yes
	Gallium Arsenide crystals: temperature-dependent band edge location	-200 to 300	0.2 °C	fast	point	good	mid	yes
	continuous measurement along fiber	-50 to 300	0.2 °C	fast	line	good	high	yes

discrete measurement points along fiber (Bragg grating)	-	-	fast	line	good	high	yes
Infrared thermometer	-40 to 2000	2 °C	very fast	area	partly	high	yes
Laser-induced fluorescence	0 to 2700	10%	very fast	area	no	high	yes
Thermographic phosphors	-250 to 2000	0.1% to 5%	very fast	area	partly	high	yes
Thermochromic liquid crystals	-40 to 283	1 °C	med	area	partly	mid	yes
Specialized temperature measurement techniques for the medium water							
Water temperature sensitive paint	10 to 40	5-10%	up to 1 kHz	area	partly	mid	no
Background oriented Schlieren in water	-	10 mK	high	area	partly	low	yes
MR Thermometry	H_2O PRF shift	-15 to 100	0.5 °C	slow	volume	-	500€/h	no

Chapter 2

MR Imaging

MRI is an umbrella term standing for a variety of diagnostic tools for qualitative and quantitative analysis of quantities measured utilizing the principles of Nuclear Magnetic Resonance (NMR). By enhancing the research of Bloch (1946) and other forerunners in MRI, Lauterbur and Mansfield in 1973 manipulated the Proton Resonance Frequency (PRF) in space by applying spatially varying magnetic gradients. With their research, first spatially resolved images of tissue could be produced, enabling the medical analysis of regions in the body which was not possible with conventional X-ray diagnostics. This invention paved the way for many applications and, nowadays, is one of the most advanced diagnostic tools in medicine.
Contrary to MRI, but with similar physical principle, Magnetic Resonance Spectroscopy (MRS) uses NMR to extract the physical properties of certain atomic nuclei in a small sample of matter. The idea behind this technique is to receive information about single molecules and their atomic structure.

This chapter is written from an engineering perspective and starts with a summary of the physical principles of MRI in order to provide a knowledge base. Following are details about the advanced MR techniques for the measurement of velocity and temperature. The chapter is closing with a discussion about measurement error.

2.1 MR Basics

2.1.1 Nuclear Magnetic Resonance

The interaction of the atomic nuclear spin with an external magnetic field $\vec{B}_0$ is a basic physical principle. A nucleus has a quantum mechanical spin $\vec{I}$, only when the atomic number[1] is odd and/or the atomic weight[2] is odd. With only one proton in the nucleus of the hydrogen isotope and a spin quantum number of $I = \frac{1}{2}$, ^{1}H is the basis for most MR techniques (Brown et al., 2003).
Being a quantum mechanical property the spin of elementary particles is not part of our everyday experience. However, the motion of the proton spin in a magnetic field can be compared with a gyroscope. A rotating current can interact with magnetic fields and, hence, produce its own magnetic field, which is termed magnetic dipole moment vector $\vec{\mu}$. The dipole moment is the product of the gyromagnetic constant γ, which is approximately $2.67 * 10^8$rad/s/T (42.57MHz/T) for pure water, and the angular momentum (spin) $\vec{J}$:

$$\vec{\mu} = \gamma \vec{J} \tag{2.1}$$

The vector $\vec{\mu}$ will not completely align along the field lines of the magnetic field $\vec{B}_0$. Due to the interaction between $\vec{B}_0$ and $\vec{\mu}$ an angular momentum $\vec{J}$ is generated leading to a precessional motion of the rotational axis of the spinning proton around the magnetic field lines. Fig. 2.1 illustrates the spin precession. The precession frequency for this motion can be calculated with the torque $\vec{N}$:

$$\vec{N} = \frac{d\vec{J}}{dt} = \vec{\mu} \times \vec{B}_0 \tag{2.2}$$

With the use of Eq. 2.1 the magnitude of torque $|\vec{N}|$ results in:

$$|\vec{N}| = \gamma J B_0 \sin\alpha = J \sin\alpha \frac{d\phi}{dt} \tag{2.3}$$

[1] The atomic number is the number of protons.

[2] The atomic weight is the sum of protons and neutrons.

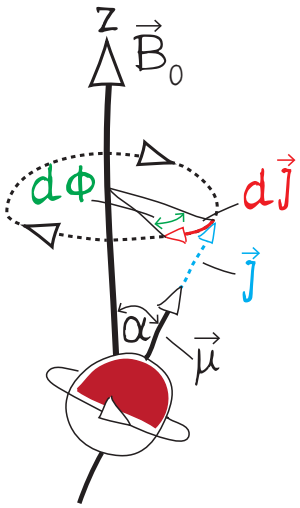

Fig. 2.1: Illustration of the spin precession. $\vec{B}_0$ is the magnetic field along the z-axis, $\vec{\mu}$ is magnetic dipole momentum of the proton, $\vec{J}$ is angular momentum leading to the spin precession.

The term $\frac{d\phi}{dt}$ is the PRF or Larmor frequency ω_0. By solving Eq. 2.3 for ω_0 the important expression can be given (Haacke et al., 1999; McRobbie et al., 2002; Weishaupt et al., 2009):

$$\omega_0 = \gamma B_0 \tag{2.4}$$

As explained above the spins in the magnetic field align along the magnetic field lines. In quantum physics, a hydrogen proton in an external magnetic field has two energetic states: The spin can align parallel (up-spins) or anti-parallel (down-spins) to the magnetic field lines. (Zeeman interaction see Liboff (2003)). Both states are stable. The transition energy, which would be required to switch between these two states is directly connected to the Larmor frequency:

$$\Delta E = \hbar\omega_0 \tag{2.5}$$

In Eq. 2.5 $\hbar$ is the Planck´s constant. This quantum is also referred to as spin energy. Fig. 2.2 shows the Zeeman diagram for the hydrogen isotope with the two possible spin states.
In thermal equilibrium the ratio of both states is Boltzmann-distributed, with an excess in the energetic lower state (up-spins). By comparing the magnetic field interaction to the absolute thermal energy kT of the system, an expression for the 'spin excess' is achieved:

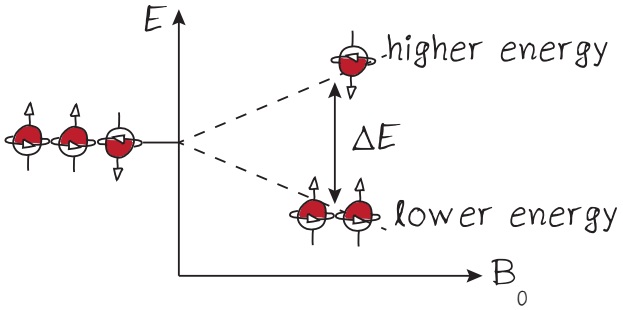

Fig. 2.2: Zeeman diagram for hydrogen isotope. Spins are oriented in either up-spin state or down-spin state, due to the presence of a magnetic field B_0.

$$\text{spin excess} \simeq N \frac{\hbar \omega_0}{4\pi k T} \tag{2.6}$$

Hereby, N is the total number of spins in the sample, k is the Boltzmann constant and T the absolute temperature. The spin excess is comparatively small[3]. Eq. 2.6 implies, that a stronger main magnetic field results in increased spin excess. Fig. 2.3 illustrates the orientation of spins in space and in a strong magnetic field, as well as the resulting spin excess.

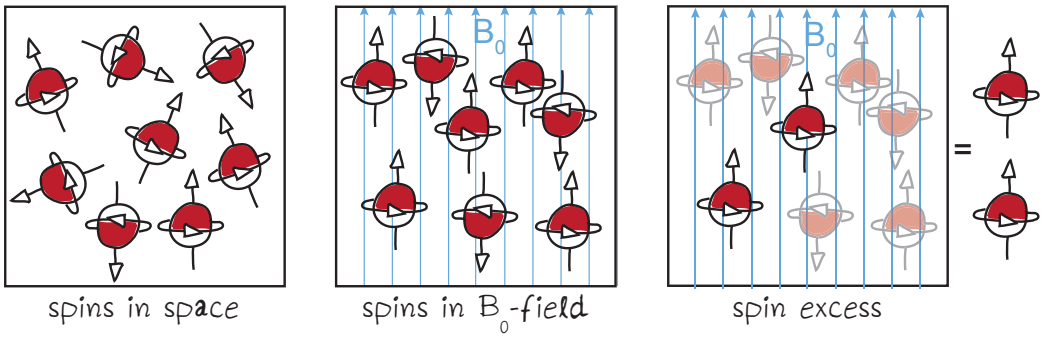

Fig. 2.3: Orientation of spins in space and inside a magnetic field. Resulting spins excess after pairwise canceling of up-spins and down-spins.

[3] one in a million spins for 0.3 Tesla (Haacke et al., 1999)

2.1.2 Equilibrium Magnetization

Although the spin excess is rather small, the huge amount of protons (Avogadro number) in a macroscopic sample of matter (e.g. a drop of water) results in the existence of an equilibrium magnetization or net magnetization M_0 of the protons, which can be calculated by Curie's law (Bloch, 1946):

$$M_0 = C\frac{B_0}{T} = \chi B_0 \tag{2.7}$$

The constant C is the Curie constant and T is the absolute sample temperature. The term $\frac{C}{T}$ is also known as the magnetic susceptibility χ, describing the magnetization potential of matter. Fig. 2.4 illustrates the two different perspectives in NMR: Viewed from a microscopic point-of-view the focus lies on one single proton spin interacting with the B_0-field. From a macroscopic point-of-view many proton spins (and their magnetic dipole moments) in a sample of matter unite to a spin ensemble with volume V, which, in turn, has a resulting magnetization $\vec{M} = \frac{1}{V}\sum \vec{\mu}_{\text{protons}}$ (Haacke et al., 1999). In the depicted spin ensemble, the phase of the spins is statistically distributed (phase incoherence).

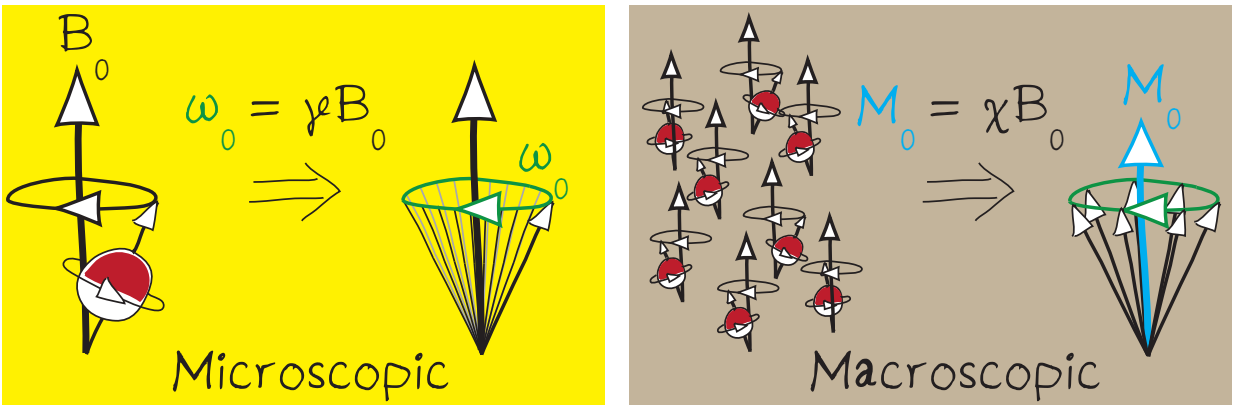

Fig. 2.4: Microscopic perspective: development of Larmor frequency ω_0 of single spin in magnetic field. Macroscopic perspective (spin ensemble): resulting net magnetization M_0 of many spins in a sample of matter. Spins have different phase angle, which leads to phase incoherence.

The net magnetization M_0 is only of the order of a few μT. In comparison to the main magnetic field, which is of order 1 T, the net magnetization is not

measurable. Although all spins are rotating with equal Larmor frequency, the phase incoherence of the proton spins in the spin ensemble impedes the measurement of the proton spin magnetization.

2.1.3 Radiofrequency Excitation

The spins can be stimulated with a short radio frequency pulse (RF pulse or RF excitation). The RF pulse, provided by a transmitter coil, produces a linear polarized magnetic field rotating at Larmor frequency ($\vec{B_1}$-field) (McRobbie et al., 2002).
In the microscopic perspective the RF pulse (which is in resonance with the spin precession frequency) emits energy, which is then absorbed by the protons (resonance absorption). As a consequence, up-spins switch to the higher energetic state (down-spins) and run synchronized with the $\vec{B_1}$-field. Phase coherence is the result. As more and more up-spins convert to down-spins the spin excess decreases, which leads to a decrease of the longitudinal magnetization M_z.
In the macroscopic perspective a spin ensemble reacts on the RF pulse with a tilting of the magnetization vector $\vec{M} \equiv M_0 \vec{e_z}$ (which was initially longitudinal) into the x-y-plane. $\vec{M}$ develops a transverse magnetization component $\vec{M_{xy}}$. The magnetic reaction of matter on an arbitrary external magnetic field $\vec{B}$ is described by Bloch´s equation:

$$\frac{d\vec{M}}{dt} = \gamma(\vec{M} \times \vec{B}) \tag{2.8}$$

Hereby, it is helpful to introduce a rotating frame of reference[4], denoted with the axis system x' and y' rotating at $\vec{\omega_0}$. Eq. 2.8 in the rotating frame changes to:

$$\left(\frac{d\vec{M}}{dt}\right)_{rot} = \gamma(\vec{M} \times \vec{B}) - \vec{\omega} \times \vec{M} = \gamma\vec{M} \times (\vec{B} + \frac{\vec{\omega}}{\gamma}) \tag{2.9}$$

[4] The rotating frame of reference is a coordinate transformation, by which the x-y-plane rotates around the z-axis at the Larmor frequency.

The additional term $\frac{\vec{\omega}}{\gamma}$ represents a fictitious magnetic field, developing from the rotation. Situated in the rotating frame of reference, the RF pulse only adds a static magnetic field $\vec{B_1}$ perpendicular to the $\vec{B_0}$-field (x'-axis taken here to coincide with the x-axis). Inserting $\vec{\omega} \hat{=} -\vec{\omega_0}$ and $\vec{B} = \vec{B_0} + \vec{B_1}$ into Eq. 2.9 gives:

$$\left(\frac{d\vec{M}}{dt}\right)_{rot} = \gamma\vec{M} \times (\vec{B_0} + \frac{\vec{\omega_0}}{\gamma} + \vec{B_1}) = \gamma\vec{M} \times \vec{B_1} \tag{2.10}$$

The cross product in Eq. 2.10 defines the geometric operation on $\vec{M}$. It is tilted around the B_1-axis. The flip angle at which $\vec{M}$ is rotated is denoted by α, where (Haacke et al., 1999):

$$\alpha = \gamma B_1 \tau \tag{2.11}$$

The longer the RF pulse duration τ is (when the RF transmitter is turned on) or the stronger the B_1-field is, the more protons absorb the pulse's energy and the flip angle increases. A complete 360° rotation takes about tens to hundreds of microseconds (Bushberg et al., 2002). The resulting magnetization vector $\vec{M}$ is a composition of the two components transversal magnetization $|\vec{M}_{xy}|$ and longitudinal magnetization $|\vec{M}_z|$. All parameters of the RF excitation process are illustrated in Fig. 2.5. The maximum flip angle is α =180°. In this case the net magnetization changes to the opposite direction and $|\vec{M}_z| = -|\vec{M}_0|$. By applying a 90° flip angle, the magnetization vector completely tilts into the transverse plane and $|\vec{M}_{xy}| = |\vec{M}_0|$. Fig. 2.6 illustrates the flip angle α, the 90° pulse and the 180° pulse. When the RF transmitter is turned off again, the spins have reached a certain amount of phase coherence, and the magnetization vector has gained a certain amount of transverse magnetization $|\vec{M}_{xy}|$. This is the basis for measuring a MR signal.

2.1.4 MR Signal

As the spins are in an excited state, they have to lose the energy on their way to the initial equilibrium state. In a receiver coil, perpendicularly oriented

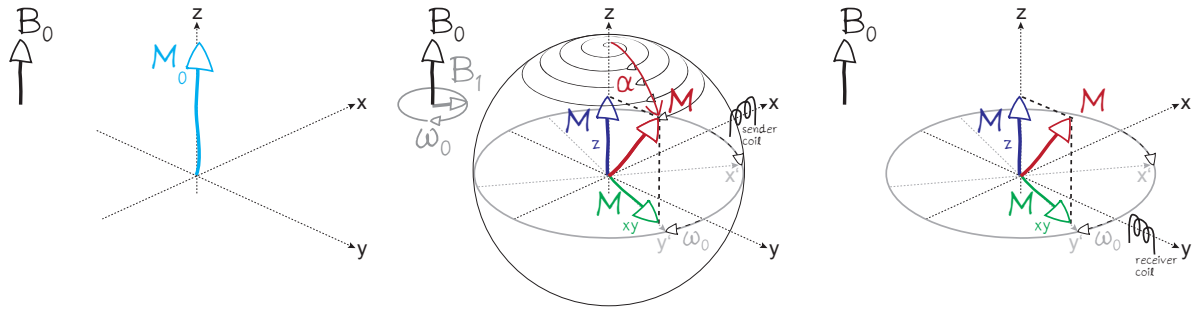

(a) (b) (c)

Fig. 2.5: RF excitation process. (a) Equilibrium magnetization M_0 aligned along B_0-field. (b) Excitation of RF pulse as a magnetic field B_1 rotating at Larmor frequency ω_0. Magnetization vector M spirales into x-y-plane. This leads to a development of the transversal magnetization component $|\vec{M}_{xy}|$. The longitudinal magnetization M_z decreases. The flip angle is denoted with α. The x'-y'-plane is rotating with the Larmor frequency (rotating frame of reference). (c) After the RF pulse is shut off again a receiver coil can detect the rotating transversal magnetization.

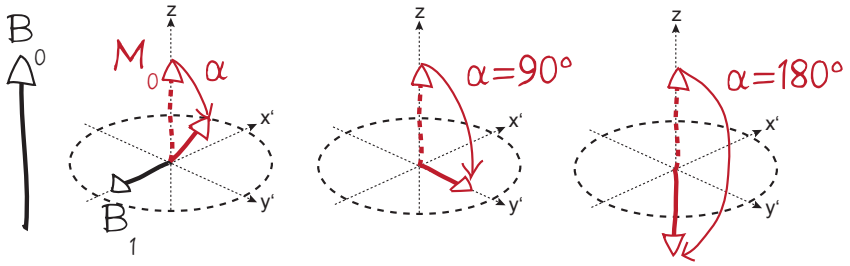

Fig. 2.6: The 90° pulse leads to a complete conversion of the net magnetization to transverse magnetization, and the 180° pulse to opposite net magnetization.

to the transverse plane, the rotating phase-coherent transverse magnetization induces voltage (via the dynamo principle). This decaying signal is the Free Induction Decay (FID) and equals the complex MR signal with its three components: The signal magnitude, the signal frequency and the signal phase (relative to the RF pulse phase) (Brown et al., 2003).

The decay process of the MR signal can be divided into two relaxation types:

The spin-lattice relaxation (or T_1 relaxation) describes the regrowth of the longitudinal magnetization $|\vec{M}_z|$ of the MR signal, after the magnetization has been rotated into the transverse plane $|\vec{M}_{xy}|$. The reason for this relaxation type is the interaction of the spins with their surrounding atomic neighborhood. The time constant of this decay process is T_1, which is the time after a 90°-pulse until 63% of the initial $|\vec{M}_z|$ is recovered. The decay curve is given in Figure 2.7a. Assuming an exponential relaxation process and solving Eq. 2.8 with proper boundary conditions the regrowth of $|\vec{M}_z|$ can be calculated by:

$$|\vec{M}_z(t)| = M_0(1 - (1 - \cos\alpha)\exp(-\frac{t}{T_1})) \tag{2.12}$$

The second relaxation type is the decay of the transversal magnetization (spin-spin relaxation or T_2 relaxation), which can be described as a dephasing[5] of a spin ensemble due to spin-spin interaction. Small differences in the local precession frequency lead to a spin-spin phase dispersion. The time constant T_2 is defined as the value, when $|\vec{M}_{xy}|$ has decayed to 37% of its initial value after a 90°-pulse excitation. The solution of Eq. 2.8 for this decaying process is:

$$|\vec{M}_{xy}(t)| = M_{xy}(0)\exp(-t/T_2) \tag{2.13}$$

Temporally constant field inhomogeneities, such as B_0-imperfections, magnetic field gradients or local susceptibility differences, lead to a faster decay of $|\vec{M}_{xy}|$, which is characterized by the time constant T_2'. The sum of the reciprocals of both relaxation times T_2 and T_2' yields the time constant T_2^*, which characterizes the FID. T_2^* is termed apparent spin-spin relaxation time (Bernstein, 2004). Eq. 2.13 is modified as follows:

$$|\vec{M}_{xy}(t)| = |\vec{M}_{xy}(0)|\exp(-t/T_2^*) \tag{2.14}$$

The time constant T_2^* and the decay of $|\vec{M}_{xy}|$ is shown in 2.7b.

Typical values for both relaxation time constants are presented by Hendrix and Krempe (2008) for different matter: The T_1 relaxation lies within 200ms (fat) and 3s (water), whereas the T_2 relaxation is a faster process

[5] Dephasing is the loss of phase coherence between distinct spins.

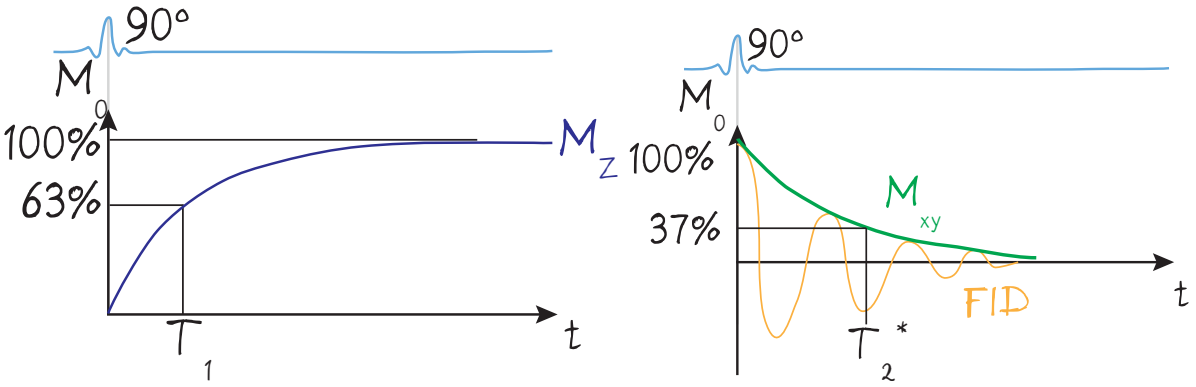

(a) Spin-lattice relaxation of the longitudinal magnetization component

(b) Spin-spin relaxation of the transversal magnetization component

Fig. 2.7: Relaxation types of the longitudinal and transversal magnetization.

with relaxation times between 100ms (fat) and 1.5s (water) for a 1.5 Tesla main magnet.

2.1.5 Echo Generation

As explained above, T_2^* time constants are much shorter than T_2 time constants, due to additional dephasing caused by spatio-temporal constant field inhomogeneities (Weishaupt et al., 2009). These effects can be reversed by applying a 180° pulse. After the 180° pulse is excited an echo of the FID is generated. The duration between the first excitation pulse and the signal echo is the Echo Time (TE). 180° pulses can be repeated several times, with decreasing signal strength at each achieved echo. The envelope to the maxima of the FID and its subsequent echoes gives the real T_2 curve. This is depicted in Fig. 2.8.

The formation of an echoes can be achieved with two different sequence types: Spin Echo (SE) and Gradient Echo (GE).
In SE sequences the spins dephase naturally, after the 90° pulse. A 180° pulse reverses the spins' phases and they start to rephase again. By the time the phases of all spins have realigned on the y'-axis, an echo forms. This process can be repeated several times and is equal to the echo forma-

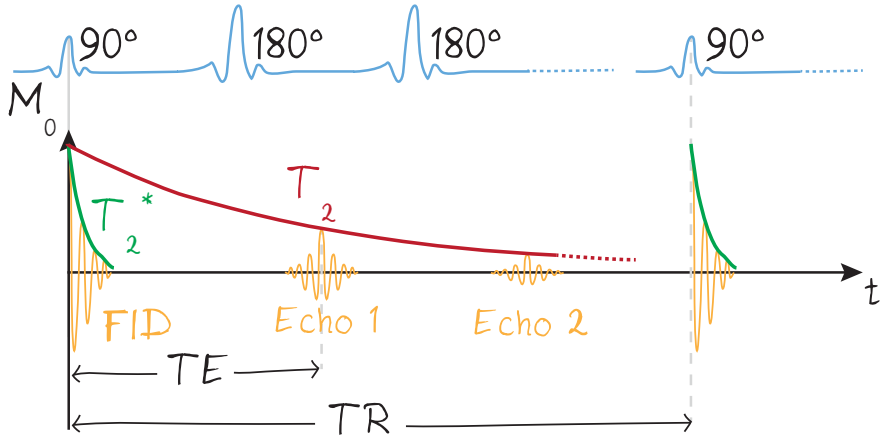

Fig. 2.8: Transversal relaxation with T_2^* and T_2 time constant. Echo formation subsequent to 180° pulses after echo time TE. TR is the repetition time between subsequent excitation pulses.

tion depicted in Fig. 2.8. For this sequence only the radio-frequency unit is needed.

In contrast to the SE sequence, the GE sequence generates the signal echo with the help of the gradient unit; therefore, the sequence is also termed gradient recalled echo sequence. In a GE sequence a negative gradient lobe (dephasing gradient) is switched on just after the RF excitation pulse. This speeds up the dephasing process of the spins and a the transverse magnetization decays faster. This process is reversible by applying a rephasing gradient: a subsequently applied positive gradient lobe with an amplitude of the halve gradient strength of the dephasing gradient but with doubled gradient duration rephases the spins again. A signal echo forms at the halftime of the rephasing gradient. As discussed in section 2.1.7, a magnetic gradient has a spatial orientation in one direction. Typically this gradient is applied in the Frequency Encoding (FE) direction, which is depicted as green lobe in Fig. 2.10.

GE sequences are much faster than SE sequences. In order to enhance speed, the flip angle of the excitation pulse can be reduced (α between 5-60°). With smaller flip angle (than 90°), the longitudinal magnetization can not be fully converted into transverse magnetization, which leads to signal loss. On the contrary, relaxation process of M_z and M_{xy} are much shorter. This leads to a reduction of the duration between subsequent excitation pulses. This duration is known as the repetition time TR. GE sequences can achieve much shorter TE values, than SE sequences.

In several GE sequences the magnitudes of M_z and M_{xy} relax to constant values over many excitation pulses. They reach a steady state or dynamic equilibrium. When M_{xy} relaxes to zero before the next excitation pulse is emitted, the GE sequence is termed spoiled. Spoiling can be accomplished with additional gradients at the end of a sequence or with RF spoiling. An example for a spoiled GE sequence is the FLASH (Fast Low Angle SHot) sequence of Siemens (Erlangen, Germany). If M_{xy} remains nonzero before the next RF excitation pulse arrives, then the GE sequence is called SSFP (Steady-State Free Precession) (Bernstein, 2004).
A detailed discussion about SE or GE sequences can be found in Haacke et al. (1999), Hendrix and Krempe (2008), McRobbie et al. (2002), and Weishaupt et al. (2009).

2.1.6 Contrast

Contrast is essential for MRI and helps to differentiate different tissue. Important for contrast is the composition of the echo time TE and the repetition time TR, which is a function of the used pulse sequence, resulting in different T_1 and T_2 relaxation times. This is called weighting. In the MR image, tissues with high contrast (bright pixels) produce more signal during acquisition than tissues with low contrast (darker pixels). In case of engineering sciences only one fluid is needed and the proton density, T_1 and T_2 are uniformly distributed. Hereby the main purposes are to increase signal and reduce measurement time. This is done with the help of contrast enhancing material.

2.1.6.1 Weighting

In MRI, images can be PD-weighted (Proton Density), T_1-weighted or T_2-weighted. Blood, for instance, has a higher proton density than bone and, hence, has a higher signal intensity. PD-weighted images are often acquired using SE sequences with short TE.

Contrast with T_2 weighting is achieved when long TEs and TRs are applied. This can be done with SE sequences. Tissue with long T_2 values is brighter. That means, that in T_2-weighted images fluids have the highest intensities and water- and fat-based tissues are at mid level. For GE sequences T_2^*-weighting is achieved as the gradient non-uniformities lead to increased spin-spin relaxations. Nevertheless, SE T_2-weighted images and GE T_2^*-weighted images produce the same tissue contrast.
Images with T_1-weighted contrast depict fluids as dark and fat-based tissue as bright areas. Required are short TEs and short TRs. For GE T_1-weighted images the flip angle has more impact on the contrast than TR. α should be chosen high enough to achieve sufficient signal. Due to the short acquisition times GE sequences are T_1 weighted. Furthermore, the signal can be increased by manipulating T_1, T_2 and T_2^* times by doping the measurement fluid with special additives, discussed in the following section.

2.1.6.2 Contrast Enhancement

Matter becomes magnetized, when it is inside a magnetic field. As mentioned above, it produces its own magnetic dipole moment. Materials have different magnetic properties: when the dipole moment vector points parallel to the magnetic field lines the material is paramagnetic. The magnetic susceptibility is positive and the material has unpaired electrons. If the dipole moment vector points antiparallel to the magnetic field lines, the material is diamagnetic and the magnetic susceptibility is negative. These substances have no unpaired electron orbital (Lide, 2014). Ferromagnetic material has a very large positive magnetic susceptibility. In the presence of a non-uniform magnetic field, paramagnetic matter is pulled into the field, whereas diamagnetic matter is pushed away (Griffiths, 1999).
The magnetic susceptibility χ can be derived from Eq. 2.15 for pure protons (Haacke et al., 1999).

$$\chi = \frac{1}{4}\rho_{PD}\frac{\gamma^2\hbar^2}{kT}B_0 \tag{2.15}$$

where, ρ_{PD} is the proton density, γ is gyromagnetic ratio, $\hbar$ is the Planck's constant, k the Boltzmann's constant and T the absolute temperature of the sample.
Typical contrast enhancing material is paramagnetic or superparamagnetic.

Paramagnetic or superparamagnetic ions added to the measurement fluid change the magnetic environment. They speed up the relaxation processes of the water protons, without being measured itself. Paramagnetic ions typically enhance T_1 relaxation, because their additional unpaired electrons lead to strong dipole-dipole interaction with the water protons. Superparamagnetic ions mainly reduce T_2 and T_2^*, due to the introduction of very large local field inhomogeneities, leading to increased dephasing. Both materials have different applications in medical imaging.
For clinical application most used are lanthanide ions like gadolinium (paramagnetic) or metal oxide ions like iron oxide (superparamagnetic). As most lanthanides are toxic when dissolved in water, lanthanide-based contrast agents are embedded in a chemical compound, known as chelate. In this chelate the lanthanide central ion is bound inside a special molecule, which prevents the central ion from interacting with human tissue. A typical contrast agent for human use is gadopentetate dimeglumine (e.g. Magnevist®, Schering AG, Berlin, Germany).
Clinical contrast agents have positive magnetic susceptibilities. In order to enhance contrast, for instance, in fast GE sequences, the time constant T_1 has to be decreased. All time constants are a function of the contrast agent concentration, which has to be adjusted sufficiently.
For technical applications the paramagnetic properties of copper can be used. Easily available is copper(II) sulfate salt ($CuSO_4$) solved in water. Due to its toxicological effects on humans safety precaution should be considered, when handling with $CuSO_4$ and its aqueous solutions.

Hydrocarbons and carbohydrates are measurable with MRI, have a high hydrogen proton density and, hence, provide a sufficient MR signal without needing contrast agents. In medical imaging tissue consists of fat[6] and water. Different techniques can suppress either the water or the fat signal (Haacke et al., 1999; McRobbie et al., 2002), for instance by utilizing the different chemical shift (Poon et al., 1989). Water has a higher chemical shift as fat. This makes mineral or vegetable oils an appropriate alternative to water/contrast-agent solutions, if the increased fluid viscosity is manageable for the pumping system and the required fluid mechanical parameters (Reynolds number) and thermodynamic parameters (heat transfer rate) are reached.

[6] Fat is a chemical compound consisting of triglyceride chains (e.g. -CH_2-CH_2-) (McRobbie et al., 2002).

In contrast to water, fat has no temperature-dependent proton resonance frequency (PRF) shift. This can be utilized for MRT without needing a reference measurement as explained in Sec. 2.2.2. A way of how this technique can be applied is also described in the work of the project partner.

Tab. 2.1 summarizes the most important contrast enhancing substances, their solutions and their magnetic parameters, accordingly.

Tab. 2.1: Table of measurement fluids and contrast agents with according relaxation times T_1 and T_2/T_2^*. Data is taken from Lide (2014) and Schenck (1996).

Material		χ_m	**Effects**
Name	Formula	[10^{-6} cm^3mol^{-1} (cgs)]	
Water	H_2O	-12.96	$T_1 = 3-4$ s, $T_2 = 1-1.2$ s, PRF-shift= $0.01 ppm/°C$
Mineral Oil	-CH_3/-CH_2-	-	$T_1 \approx 140$ ms, $T_2 \approx 27$ ms[7]
Vegetable Oil	-CH_2-	-	$T_1 \approx 250$ ms, $T_2 \approx 35$ ms[8]
Copper(II) sulfate	$CuSO_4$	+1330	$T_1 \downarrow$ $T_2/T_2^* \downarrow$
Copper(II) sulfate pentahydrate	$CuSO_4 \cdot 5H_2O$	+1460	$T_1 \downarrow$ $T_2/T_2^* \downarrow$
1g/l Copper(II) sulfate pentahydrate	$CuSO_4 \cdot 5H_2O$	≈ -12	$T_1 \approx 327$ ms $T_2 \approx 290$ ms[9]
Gadolinium	Gd	+185000	$T_1 \downarrow\downarrow$ $T_2/T_2^* \downarrow$
Gadolinium(III) sulfate octahydrate	$Gd_2(SO_4)_3 \cdot 8H_2O$	+53280	$T_1 \downarrow\downarrow$ $T_2/T_2^* \downarrow$
Iron(II) oxide	FeO	+7200	$T_1 \downarrow$ $T_2/T_2^* \downarrow\downarrow$

[7] $B_0 = 1.5$ T, SE sequence, data from Poon et al. (1989)

[8] $B_0 = 1.5$ T, SE sequence, data from Poon et al. (1989)

[9] measured at 1.5 T

5 mmol/l Praseodymium-2-methoxyethyl-DO3A complex + water	PR-MOE-DO3A + H_2O	-	T_1 =27.6 ms, T_2 =12.8 ms, PRF-shift= $0.13 ppm/°C$[10]

2.1.7 Spatial Encoding

By locally manipulating the proton resonance frequency, it is possible to localize the protons in the measurement field. Additional to the B_0-field, magnetic gradients $\vec{G} = (G_x, G_y, G_z)$ are applied, manipulating the Larmor frequency in space with the spatial position vector $\vec{x} = (x, y, z)$:

$$\omega_0(\vec{x}) = \gamma(B_0 + \vec{G} \cdot \vec{x}) \tag{2.16}$$

As MRI is a tomographic imaging technique, the spatial encoding starts with a slice selective (SS) gradient G_{SS} along the z-axis. This gradient manipulates this direction of the FOV, so that only the spins in a thin slab, perpendicular to the gradient direction, match the resonance condition of the simultaneously applied RF pulse. The central frequency of the RF pulse determines the location. The slice thickness is influenced by the transmitter bandwidth and the slice selection amplitude. In order to save time an acquisition of multiple interleaved slices is common. Thereby G_{SS} stays the same and the slice location is varied with different central frequencies of the RF pulse.

The x-direction of the FOV is manipulated using a frequency encoding (FE) gradient G_{FE}. This gradient is also termed readout gradient, because it is applied during the time the MR signal is received. While G_{FE}, oriented perpendicular to G_{SS}, is present the protons begin to precess at different frequencies along the gradient direction. As a consequence the receiver emits

[10] properties measured with 11.5 T device, from Konstanczak et al. (1997)

signal echoes with a different, but predetermined frequency for every location along the x-axis.

After RF excitation and prior to signal acquisition a phase encoding gradient G_{PE} is switched on for a certain duration t_{PE}. During G_{PE} is present, the spins gain or lose phase, according to their y-location. The resulting phase shift, after the gradient is turned off again and the spins return to their original frequency, depends on the gradient amplitude and duration. One measurement alone does not provide the location in y-direction, because the different phases are sampled simultaneously for one frequency. The phase encoding gradient with modulated amplitude has to be applied multiple times, each time with the same combination of RF pulse, slice selection and frequency encoding gradient. This scheme is called a sequence. Due to that a rate of change of phase is created that, in turn, equals a frequency.

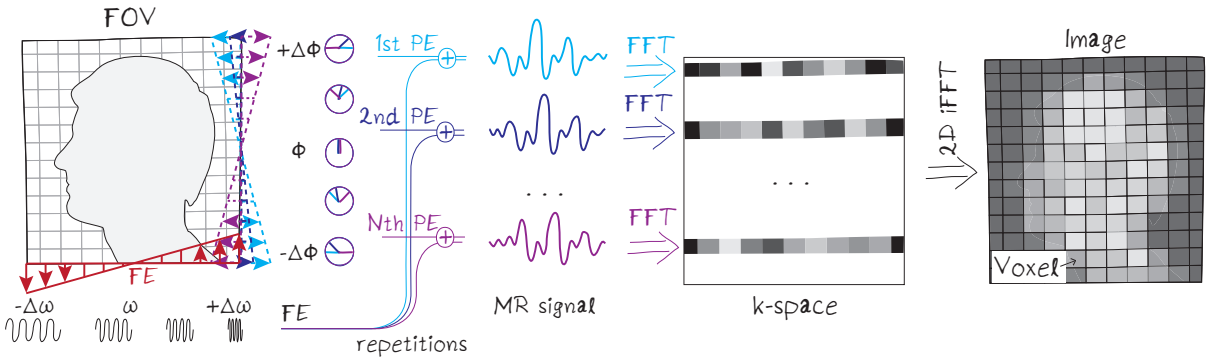

Fig. 2.9: Acquisition scheme for a two-dimensional encoding in frequency encoding (FE) direction and phase encoding (PE) direction. MR data are stored in k-space, each line acquired per PE repetition. An inverse FFT reconstructs the image.

All acquired MR signals are sampled, digitized, Fourier-transformed and stored in a mathematical construction termed k-space. Each line of k-space is obtained with one sequence repetition. The resulting image is obtained by a process called signal and image reconstruction, which is reported in Sec. 2.1.8.
Despite the 2D acquisition shown in Fig. 2.9 3D volumes can be acquired

in two different ways. On the one hand multi slicing acquisition can be applied by repeating the 2D sequence for different slices along the slice selection direction and, thus, achieving a 3D volume subsequently. On the other hand, if an additional phase encoding gradient operates along the slice selection direction a 3D acquisition sequence is used. Advantages of 3D acquisition sequences are that thinner slices are measurable, which is due to the contiguousness of the acquired volume. Additionally, a better Signal-to-Noise Ratio (SNR) is achieved. A longer acquisition time and possible ringing artifacts are the disadvantages (McRobbie et al., 2002). Fig. 2.10 shows a 3D pulse sequence combining the RF excitation, spatial encoding along all three axes and echo generation.

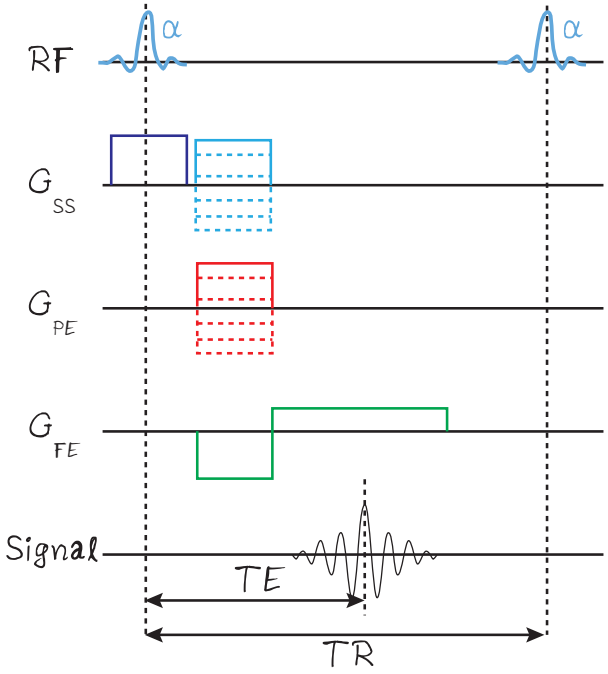

Fig. 2.10: Simple 3D pulse sequence diagram for a gradient recalled echo sequence starting with an excitation pulse at flip angle α simultaneously with a slice selection gradient (dark blue). Subsequently, two phase-encoding gradients are applied along the slice selection (light blue) and phase encoding (red) direction. The phase-encoding gradients (dashed lines) are repeated each excitation but with different gradient strength. The signal echo is generated at halftime of the positive gradient lobe (readout gradient, green) in the remaining direction. This gradient is also responsible for frequency encoding of the signal. TR is the duration between two subsequent excitation pulses. TE is the duration between excitation pulse and signal echo.

2.1.8 Signal and Image Reconstruction

The signal received by the coils is prepared by a variety of treatments, such as pre-amplification, demodulation[11], quadrature detection[12], low pass filtering and so on. The resulting signal $S(t)$ induced in one coil by the rotating transverse magnetization $|\vec{M}_{xy}(\vec{x},t)|$ at phase angle $\Phi(\vec{x},t)$[13] can be given in the time domain (Bernstein, 2004):

$$S(t) = \int |\vec{M}_{xy}(\vec{x},t)||\vec{B}_{xy}(\vec{x},t)|exp(-i\Phi(\vec{x},t))\mathrm{d}x\mathrm{d}y\mathrm{d}z \tag{2.17}$$

$|\vec{B}_{xy}(\vec{x},t)|$ is the transverse component of the receiver coil B_1-field and $\vec{x}$ is the position vector. The signal phase

$$\Phi(\vec{x},t) = \gamma \int_0^t \vec{x} \cdot \vec{G}(t')\mathrm{d}t' \tag{2.18}$$

is a function of the magnetic gradient $\vec{G}(t)$ applied. By defining k-space

$$\vec{k}(t) = \frac{\gamma}{2\pi} \int_0^t \vec{G}(t')\mathrm{d}t' \tag{2.19}$$

Eq. 2.17 can be recast to

$$S(t) = \int |\vec{M}_{xy}(\vec{x},t)|\ |\vec{B}_{xy}(\vec{x},t)|exp(-i2\pi\vec{k}(t) \cdot \vec{x})\mathrm{d}x\mathrm{d}y\mathrm{d}z \tag{2.20}$$

and $S(t)$ in Eq. 2.20 is the Fourier transform of the weighted transverse magnetization $|\vec{M}_{xy}(\vec{x},t)|\ |\vec{B}_{xy}(\vec{x},t)|$. k-Space stands for the accumulated spatial rate of change of phase of stationary spins resulting from the working gradient $\vec{G}(t)$. $\vec{k}(t)$ is the path along which k-space is filled. Most often used is the Cartesian sampling, whereby, each k-space line corresponds to the frequency-encoding readout. This was already explained in Sec. 2.1.7.

---

[11] Larmor precession frequency is removed from the transverse magnetization signal.

[12] FID is converted into a complex signal, which can be processed with a Fourier transformation for image reconstruction.

[13] The phase angle Φ is often termed just signal phase.

After k-space is sampled the data has to be converted into the final image, which is typically done with the help of Fourier reconstruction. As explained above the time domain signal S(t) is the Fourier transform of the transverse magnetization. The MR image can be reconstructed by utilizing an inverse Fourier Transform (iFT). For 3D acquisition a series of 2D-iFTs reconstructs the volumetric data. If the sampling grid is Cartesian then the process can be accelerated using Fast Fourier Transformations (FFTs).
In modern MRI machines it is common to use phased array coils, which enable parallel imaging. Multiple coils are composed to an array covering the same size as a single channel coil. The coils partly overlap and each one has its own receiver channel. In comparison to a single channel coil phased array coils have two major advantages: SNR increases as the sensitive volume of a single channel in the array can be reduced and scan time decreases by leaving out phase-encoding lines in k-space.
For the latter case the spatial sensitivity of each receiver coil channel B_1-field ($|\vec{B}_{xy}(\vec{x},t)|$) is used to prevent or remove aliasing, which occurs when leaving out lines in k-space to save time. Two strategies are common. With SMASH (simultaneous acquisition of spatial harmonics), missing k-space lines are restored utilizing the spatial dependence of the sensitivity. With SENSE (sensitivity encoding), the signal of each channel is inversely Fourier transformed into an image and aliasing is removed by using the coil sensitivities as weighting function. For both strategies calibration is needed to prevent uncorrect aliasing or low SNR. Therefore, additional measurements are required. On the one hand the coil sensitivity can be determined by acquiring a separate calibration scan or from extra lines in k-space (self-calibration). On the other hand weighting functions can be determined for estimating the missing k-space lines without measuring the coil sensitivity. One modification of the SMASH strategy is the GRAPPA (generalized auto-calibrated partially parallel acquisition) proposed by Griswold et al. (2002), which is used in the context of phase-locked 3D-MRV acquisitions (Wassermann et al., 2013).

2.2 Advanced MR Techniques

MRI has the ability to extract a wide variety of measures spatially resolved from an object (tissue, water, etc.) placed inside the FOV. As a measure-

ment tool for fluid mechanics, important quantities are the mean velocity field, the stress tensor (normal + shear stresses), the temperature field and the pressure distribution. Most of these quantities can be extracted from MR data using advanced techniques (Elkins and Alley, 2007). In this work, the estimation of the mean velocity field (MRV) and the temperature field (MRT) from MR data is of great interest. The fluid velocity can be extracted by a technique called flow encoding, which takes advantage of spins receptive to fluid motion while exposed to magnetic gradients. By contrast, the effect of varying fluid temperature on spins has its origins in the properties of water molecules. Both techniques have in common, that the respective quantity is encoded into the phase of the MR signal. Hence, they are termed Phase Contrast Imaging (PCI) techniques. The basics of the techniques and the ways to extract the sought quantity from the signal phase are described in the following sections.

2.2.1 Measuring Flow

Measuring flow using MRV originally comes from medical diagnostics of the cardiovascular system of humans or animals (Bryant et al., 1984; Jung, 2005). Up to the present, a variety of fluid mechanical flows have been measured using this measurement technique. One of the first applications for fluid mechanics was presented by Elkins et al. (2003), measuring the flow inside a turbine blade cooling channel with ribbed walls. Another study showed the highly three-dimensional swirling flow inside a tube with tangential inlets (Grundmann et al., 2012).

2.2.1.1 Flow Encoding

The most important element for the measurement of fluid velocities is the gradient unit as presented in Markl et al. (2003b).
A spin moving along a magnetic gradient $\vec{G}(t)$ with a constant velocity $\vec{v}$ experiences a locally increased Larmor frequency ω_L. This results in a rise of the spin's phase angle Φ. The Larmor frequency as given in Eq. 2.16 can

be extended:

$$\omega_L(\vec{x},t) = \gamma(B_0 + \vec{G}(t)\cdot\vec{x}(t)) \tag{2.21}$$

By integration of Eq. 2.21, the phase angle of the MR signal is achieved, which can be expanded into a Taylor series. The introduction of the position vector $\vec{x}(t) = \vec{x}_0 + \vec{v}(t-t_0)$, whereby t_0 is the time the excitation pulse is emitted, enables to express the following simple equation for Φ:

$$\Phi(\vec{x},TE) = \Phi_0 + \gamma\vec{x}_0 \cdot \underbrace{\int_0^{TE}\vec{G}(t)\mathrm{d}t}_{M_0} + \gamma\vec{v}\cdot\underbrace{\int_0^{TE}\vec{G}(t)t\mathrm{d}t}_{M_1} + O(t^n) \tag{2.22}$$

The first summand Φ_0 is the background phase. The integrals of the following ones are called the n^{th} order gradient moments M_n, whereby $n \in \{0..\infty\}$. The integral of the second summand M_0 describes the influence of the magnetic gradient on the phase of stationary spins positioned at $\vec{x}_0$. The third summand includes the sought velocity vector $\vec{v}$ of constantly moving spins during TE and the first gradient moment M_1. All higher moments are ignored, which is only valid for constant flow (Elkins and Alley, 2007).

The target of flow encoding is to assign the spins in a voxel with a unique phase offset only dependent on the mean flow velocity inside. At first flowing spins have to be separated from stationary spins. This is done with the help of a bipolar gradient (cp. 2.11a). The estimation of the velocity component in one direction is presented in the following.
The bipolar gradient has two gradient lobes, each one with a duration Δt and a gradient amplitude $\pm G_k$. Assuming, that the spins are moving constantly with velocity V along the direction of the magnetic gradient (amplitude $+G_k$), they acquire phase as shown in Figure 2.11a. After duration Δt, the amplitude of the gradient is reversed ($-G_k$). During the reversed gradient duration the same spins lose more phase than they gained in the first halve. After the bipolar gradient, all spins in one voxel acquired a velocity-dependent phase shift

$$\Phi = -\gamma V M_1 \tag{2.23}$$

according to the first moment of the bipolar gradient $M_1 = G_k\Delta t^2$. On the contrary, static spins gain and lose the same amount of phase. They are uninfluenced by flow encoding and the first gradient moment is $M_0 = 0$.

The background phase Φ_0 is still unknown. If the measurement is repeated

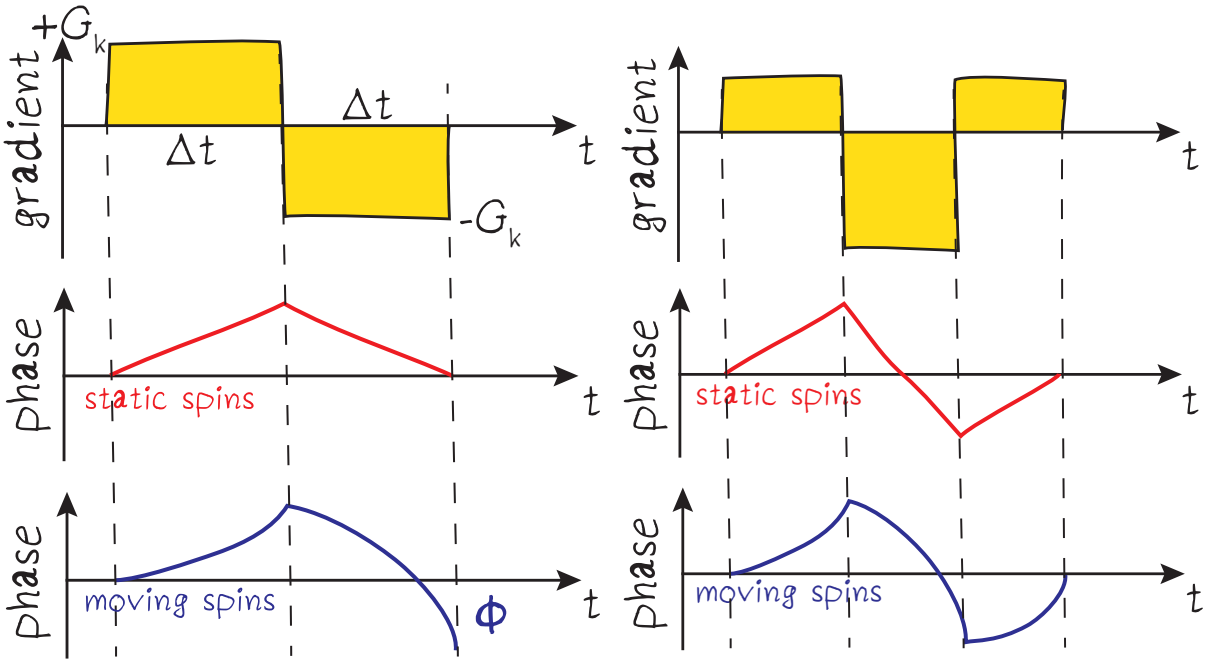

(a) Flow encoding gradient with duration 2Δt and gradient strength G_k. Resulting phase change of the MR signal for static spins and moving spins.

(b) Flow compensation gradient with zero phase change of the MR signal for static spins and moving spins is zero and for moving spins it is $\Delta\Phi$.

Fig. 2.11: Bipolar gradients needed for flow encoding and flow compensation.

with an equal gradient but with opposite polarity, both phase shifts can be subtracted. The resulting phase difference $\Delta\Phi$ of the two scans (superscribed with (1) and (2) for scans 1 and 2, respectively) is:

$$\Delta\Phi = \Phi_1^{(1)} - \Phi_1^{(2)} = \gamma V \left(M_1^{(1)} - M_1^{(2)} \right) = \gamma V \Delta M_1 \tag{2.24}$$

Eq. 2.24 shows, that the phase difference increases with increasing flow velocity V and increasing first gradient moment M_1, which is a function of the gradient strength G_k and the gradient duration Δt. Solving Eq. 2.24 for V and introducing the parameter Venc results in

$$V = \frac{\Delta\Phi}{\pi} \text{Venc} \tag{2.25}$$

where, Venc stands for velocity encoding value[14] and is calculated by

$$\text{Venc} = \frac{\pi}{\gamma \Delta M_1} \tag{2.26}$$

It is a measure for the achievable velocity maximum, that causes a phase shift of ±180° at a given bipolar gradient with first moment difference $\Delta \mathrm{M}_1 = \mathrm{G}_k \Delta \mathrm{t}^2$ and, hence, leads to aliasing artifacts. If the velocity inside a voxel exceeds the Venc the measured phase angle exceeds π and is detected as a negative velocity. Measurement errors resulting from not appropriately chosen values of the Venc are discussed in Sec. 2.3.
An example for a simple one-directional flow encoding sequence is depicted in Fig. 2.12 with application of a pair of bipolar gradients. The sequence is equal to the one shown in Fig. 2.10, except that an additional bipolar gradient is included. Typically TR and TE increase, which can result in additional measurement error (discussed in Sec. 2.3). Applying a bipolar gradient pair is called two-point method (Pelc et al., 1991). Hereby "point" means the acquisition of an entire image with spatial encoding (2D or 3D) and a constant first gradient moment.

There are several strategies how to implement a 3 component (3C) velocity encoding. Pelc et al. (1991) discuss three different methods: the six-point method, the simple four-point method and the balanced four-point method. The six-point method is equal to the two-point method shown in Fig. 2.12 but bipolar gradient pairs in every gradient direction. This means, that six echoes have to be acquired to obtain full 3D velocity data. In contrast to that, the four-point methods are less time-consuming, because they only need four instead of six scans. Therefore, a modified bipolar gradient is needed, known as velocity compensation gradient (illustrated in Figure 2.11b). The result of this gradient is, that both gradient moments M_0 and M_1 are zero. This is also termed gradient moment nulling (Bernstein, 2004). In contrast to the influence of the bipolar gradient, constantly moving spins acquire no additional phase shift. Remaining is the unknown background phase Φ_0. In order to achieve a three-dimensional velocity field four consecutive scans are needed: one flow encoding scan for each direction and one flow compensation scan for background phase subtraction. A disadvantage is that errors in the velocity components are correlated and noise is direction dependent. More advanced is the balanced four-point method. Hereby,

[14] Sometimes the Venc is also referred to as velocity sensitivity.

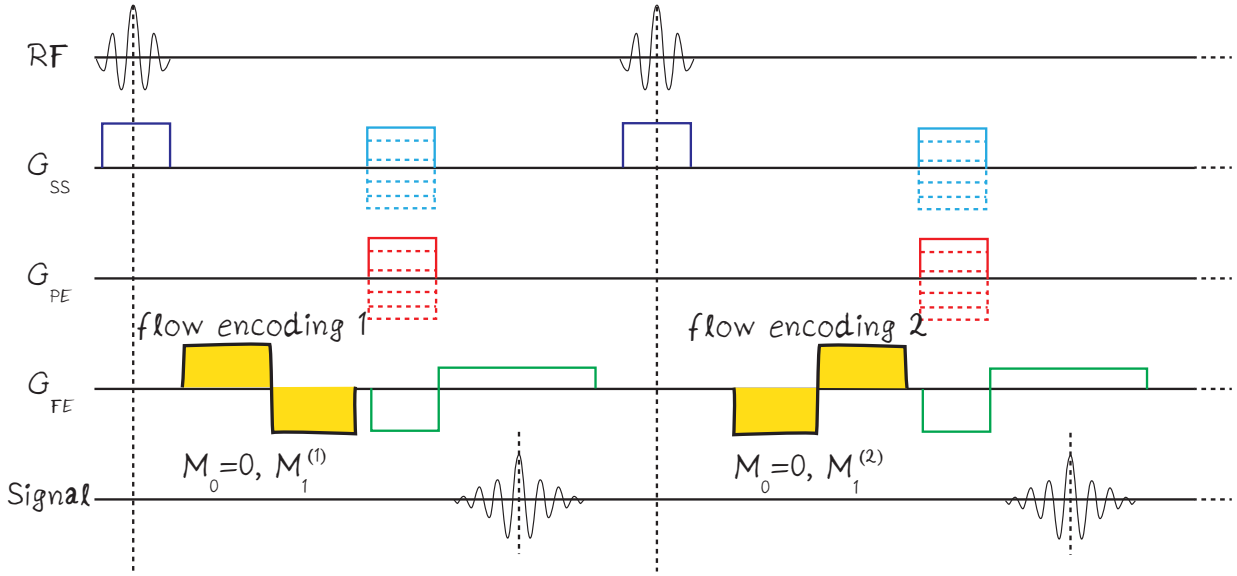

Fig. 2.12: One-direction flow encoding 3D sequence diagram with a gradient recalled echo. In addition to the sequence diagram depicted in Fig. 2.10 bipolar velocity encoding gradient (black and yellow) is included in the FE direction.

the bipolar gradients are toggled on two axes at once. The first scan is still a reference scan with negative first moments in all direction. The velocity components are then calculated by linear combination of the four scans:

$$\begin{aligned} V_{SS} &= \frac{-\Phi^{(1)} + \Phi^{(2)} + \Phi^{(3)} - \Phi^{(4)}}{2\gamma \Delta M_1} \\ V_{PE} &= \frac{-\Phi^{(1)} + \Phi^{(2)} - \Phi^{(3)} + \Phi^{(4)}}{2\gamma \Delta M_1} \\ V_{FE} &= \frac{-\Phi^{(1)} - \Phi^{(2)} + \Phi^{(3)} + \Phi^{(4)}}{2\gamma \Delta M_1} \end{aligned} \tag{2.27}$$

Tab. 2.2 gives an overview over the applied first gradient moments for all three acquisition strategies.

Tab. 2.2: First gradient moments for velocity encoding used in six-point and four-point acquisition strategies. "0" stands for velocity compensated and "-" means that no gradient (encoding or compensation) is applied along this direction.

six-point			
	direction		
scan	SS	PE	FE
1	$+M_1$	$-$	$-$
2	$-M_1$	$-$	$-$
3	$-$	$+M_1$	$-$
4	$-$	$-M_1$	$-$
5	$-$	$-$	$+M_1$
6	$-$	$-$	$-M_1$

simple four-point			
	direction		
scan	SS	PE	FE
1	0	0	0
2	$+M_1$	$-$	$-$
3	$-$	$+M_1$	$-$
4	$-$	$-$	$+M_1$

balanced four-point			
	direction		
scan	SS	PE	FE
1	$-M_1$	$-M_1$	$-M_1$
2	$+M_1$	$+M_1$	$-M_1$
3	$+M_1$	$-M_1$	$+M_1$
4	$-M_1$	$+M_1$	$+M_1$

The balanced four-point method is efficient and the estimated velocities have independent noise as well as direction (Pelc et al., 1991). This is the reason why this method is chosen in state-of-the-art flow encoding protocols.

2.2.2 Measuring Temperature

MR Thermometry is a medical tool for monitoring tissue temperature during minimally invasive thermal therapies, as for example hyperthermia[15] or high-temperature thermal ablation[16]. The advantage of MRI-guiding during these medical therapies is to map the local tissue temperature with sufficient spatial resolution and in real-time (Rieke and Butts Pauly, 2008). Absolute temperatures can be measured when an internal reference is present (Kuroda, 2005).

2.2.2.1 Temperature Sensitivity

There are different MR parameters, showing a sensitivity to temperature (Rieke and Butts Pauly, 2008): the proton density (PD), the relaxation of the longitudinal magnetization (T_1), the relaxation of the transversal magnetization (T_2), the diffusion coefficient (D), the magnetization transfer and the PRF shift. There is also a wide variety of contrast agents which are temperature-sensitive (Rieke and Butts Pauly, 2008). Very promising is PRF thermometry, which utilizes the temperature-dependent hydrogen PRF shift caused by the interaction of the ^1H with other water molecules. Hence, PRF thermometry is the only technique, which is solely determined by the signal frequency and can be detected independently from other parameters (Kuroda, 2005).

[15] 43 - 45 °C, treatment of cancer cells

[16] 50 - 80 °C, induce cell necrosis

2.2.2.2 Hydrogen Bonding

In order to understand the link between the magnetic and the temperature-dependent properties of water molecules an appropriate understanding of hydrogen bonding is necessary. In water, hydrogen bonds develop due to intermolecular dipole-dipole interactions between the proton donor (δ^+, hydrogen) and the proton acceptor (δ^-, oxygen). The larger the hydrogen bond angle Θ[17] and the shorter the bond length L gets, the higher the bond strength is (Jeffrey, 1997). The binding energy of the hydrogen bond is the highest for $\Theta \approx 180°$and $L \approx 2$ angstrom (Song et al., 2014). The hydrogen bond properties influences the molecule´s electronic configuration. Fig. 2.13 shows the bonding between water molecules.

The hydrogen bonds of water molecules are temperature dependent. With

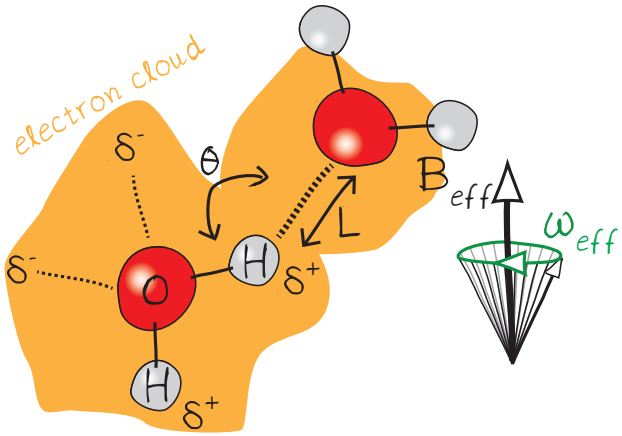

Fig. 2.13: H_2O molecule with hydrogen bonding to another H_2O molecule. The dashed line between the oxygen and the hydrogen is the hydrogen bond. The angle Θ is the bond angle.

increasing water temperature the hydrogen bonds bend, stretch and finally break. This process leads to a rearrangement of the water molecules' electron cloud, which, in the hydrogen bonded state, was displaced from the molecules electric center. The molecular electron cloud has a shielding effect, which is caused by electrical currents that reduce the magnetic field strength B_0 to an effective magnetic field strength B_{eff} (see Fig. 2.13). This

[17] The covalence binding angle between H-O-H is typically fixed at 104.5°(Song et al., 2014).

affects the magnetic configuration of the hydrogen protons. With increasing temperature and, hence, less hydrogen bonds, the electron cloud can shield the hydrogen protons more efficiently (Hindman, 1966). This results in a reduction of the proton resonance frequency. This is also termed proton chemical shift (Kuroda, 2005).

2.2.2.3 Temperature Encoding Using PRF Thermometry

As mentioned in Sec. 2.3.3, the effective local magnetic field B_{eff} depends on the main magnetic field B_0 and is manipulated by the temperature-dependent magnetic susceptibility and the temperature-dependent shielding parameter $\sigma(T)$ (De Poorter et al., 1994):

$$B_{\text{eff}} = B_0(1 - \frac{2}{3}\chi(T) - \sigma(T)) \tag{2.28}$$

Increasing or decreasing fluid temperature changes the shielding parameter of the 1H protons linearly with the proportionality rate[18] α=0.01ppm(°C)$^{-1}$ in the temperature range from -15°C to 100°C for pure water (Hindman, 1966). Kuroda (2005) reports 20°C to 80°C as linear temperature range and a tissue-dependent proportionality rate $0.00739 \leq \alpha \leq 0.0135$ppm(°C)$^{-1}$. The temperature-dependent reduction of the local effective magnetic field B_{eff} leads to a reduction of the effective PRF.
Another property of water is the magnetic susceptibility, which changes in the temperature range from ≈5°C to 60°C about 0.7% (Ergin and Kostrova, 1970). The susceptibility change of water is 0.0026 ppm(°C)$^{-1}$ and, hence, much smaller than the temperature-dependent change of the screening constant. De Poorter (1995) propose, that susceptibility effects in water can be neglected by considering a measurement error of 10%. Artifacts caused by magnetic susceptibility variations are discussed in Sec. 2.3.3.2.
Consequently, the temperature dependence of B_{eff} leads to a temperature dependence of the proton resonance frequency. For a given TE, and according to the actual fluid temperature T, which is assumed to be steadily distributed in each voxel during TE, an MR signal phase angle Φ is acquired:

$$\Phi = \Phi_0 + \Phi_{\text{V}} + \Phi_{\text{other}} + \Phi_{\text{T}} = \omega_{\text{eff}}(T)\text{TE} \tag{2.29}$$

[18] Sometimes referred to as temperature coefficient or chemical shift coefficient.

This phase angle includes the background phase angle offset Φ_0, the velocity induced phase lag Φ_V, phase lags due to other influences Φ_other (higher order moments, susceptibility, et cetera) and the temperature-dependent phase lag Φ_T. The velocity-induced phase lag can be subtracted by applying a velocity compensation gradient. In order to separate the background phase offset and the temperature-dependent phase lag an additional scan is needed. This reference scan is done at a spatially constant fluid temperature $\mathrm{T_{ref}}$. By subtraction of the two MR signal phase angle distributions of the scan with temperature field applied (heat on) $\Phi(T_i)$ and the reference scan (heat off) $\Phi_\mathrm{ref}(T = \mathrm{const})$ the temperature-dependent phase angle lag can be calculated:

$$\begin{aligned} \Delta\Phi &= \Phi_\mathrm{ref}(T_\mathrm{ref}) - \Phi(T_i) \\ &= \gamma \mathrm{TE}(\sigma(T_\mathrm{ref}) - \sigma(T_i))B_0 \\ &= \gamma \mathrm{TE}\alpha\Delta T B_0 \end{aligned} \tag{2.30}$$

After both scans have been obtained, the temperature difference in the FOV can be calculated from the phase difference image (acquisition of $\Delta\Phi$) and the given MR parameter:

$$\Delta T = \frac{\Delta\Phi}{\alpha\gamma \mathrm{TE} B_0} \tag{2.31}$$

If $\mathrm{T_{ref}}$ is known, for example, by a simultaneous measurement of the reference temperature with a MR-suitable temperature sensor (fiber optics) during the reference scan, the absolute temperature field can be estimated, by addition of $\mathrm{T_{ref}}$ and $\Delta\mathrm{T}$.
According to the parameter describing the velocity sensitivity (Venc) of the MRV measurements, the parameter describing the temperature sensitivity of MRT measurements is the echo time TE. The temperature resolution achieved with PRF thermometry is shown to be less than 1°C (Wlodarczyk et al., 1998).
Not yet considered is the phase lag due to other sources Φ_other, which is discussed in Sec. 2.3 and in the work of the project partner as for instance in Buchenberg et al. (2015).

2.2.2.4 MR Thermometry in Technical Flows

In feasibility studies researchers applied MRT to generic fluid mechanical test cases. Elkins et al. (2004) used PRF Thermometry and measured a homogeneous temperature field of a turbulent pipe flow with constant fluid temperature. With the use of a MRI machine with a very strong magnetic field (9.4 Tesla) Small et al. (2009) measured the temperature field inside miniature Shape Memory Polymer (SMP) foam, fed with a constant water flow rate. They also used PRF Thermometry. The foam was locally heated using a laser with a 7 Watt power maximum. One of the most valuable studies in the field of MRT was presented by Sun and Hall (2001). They consider the Graetz problem, which is fundamental in heat exchanger theory. They measured the flow and the temperature distribution inside a tube with constant flow and an applied temperature gradient along the streamwise direction. The flow enters the tube with a water temperature of 40 °C and is then cooled down by water at 2 °C flowing through a jacket surrounding the tube walls. In their study PRF Thermometry is applied simultaneously with MRV within one measurement procedure.

2.2.2.5 Other Advanced MR Thermometry Techniques

Shmatukha et al. (2007) and Soher et al. (2010) propose a PRF technique which does not need an additional background correction scan (reference scan or heat off scan) for mapping correct temperatures. They utilize the non-temperature-dependency of fat and a specialized fat-water separation technique. If one voxel contains sufficient signal of both fat and water, then the phase of the fat signal (containing the background phase) can be subtracted from the phase of the water signal (containing background phase and temperature-dependent phase change). With an appropriate MR sequence and data postprocessing the temperature field can be achieved.
Soher et al. (2010) filled 5×10 inch^2 (diameter×length) plastic cylinders with different ratios of peanut-oil-in-gelatin dispersions. The phantoms were heated using RF antennas. Gradient-echo images were taken in a 1.5 T GE device.

In his PhD Thesis Noeske (2000) introduces a MRT technique they termed thermal probe method, which utilizes the strong temperature-dependent chemical shift of a special contrast agent. This contrast agent consists of a complex with praseodymium as central ion[19]. The three hydrogen protons of the methoxy groups (OCH_3) show a temperature-dependent chemical shift (shielding rate) of $\alpha = 0.13 ppm/°C$ (Frenzel et al., 1996). This value is 10-times higher than pure water and can be used to measure absolute temperatures without needing a reference scan. Therefore, two different frequency shifts of OCH_3 in the PR-MOE-DO3A complex and water are subtracted $\Delta f = f_{OCH_3} - f_{H_20}$. This frequency difference is almost linear in a temperature range from 35 °C to 45 °C. The slope was measured to $\partial \Delta f / \partial T = -14.637 Hz/°C$ for a aqueous solution with 10mM PR-MOE-DO3A added. Hereby, the signal of the methoxy group is much weaker than the water signal, which has to be taken into account by adjusting repetition time, echo time, voxel size and water suppression.

2.2.3 Phase-locked Phase Contrast Imaging

In recent MRI studies, the investigation of the cardiovascular system is of interest. Due to the heart beat, cardiac MRI is associated with the acquisition of pulsatile behavior of flow and tissue. This is achieved by synchronizing the MR sequence to the patient's electrocardiogram (ECG), which is termed ECG gating, Cine Imaging or 4D-PCI. Subdividing the heart cycle into phase steps with equal spacing T_{res}, this series of echoes fills k-space lines subsequently with each ECG. Hence, this method produces phase-averaged or phase-locked data, acquired within the total acquisition time TAT. In the MR community 4D-PCI results are often misinterpreted as time-resolved data. In contrast to that, real-time MRI is based on special acquisition strategies utilizing undersampling of k-space, radial or spiral trajectories of k-space acquisition and nonlinear inverse reconstruction (Bernstein, 2004; Cohen, 2001). A typical scheme for an ECG-triggered 3D flow acquisition of cardiovascular flow is presented by Markl et al. (2003b) and depicted in Fig. 2.14. Phase-locked MRI can also be utilized for 4D-MRT.

[19] Exact chemical term: praseodymium-chelate complex (PR-MOE-DO3A)

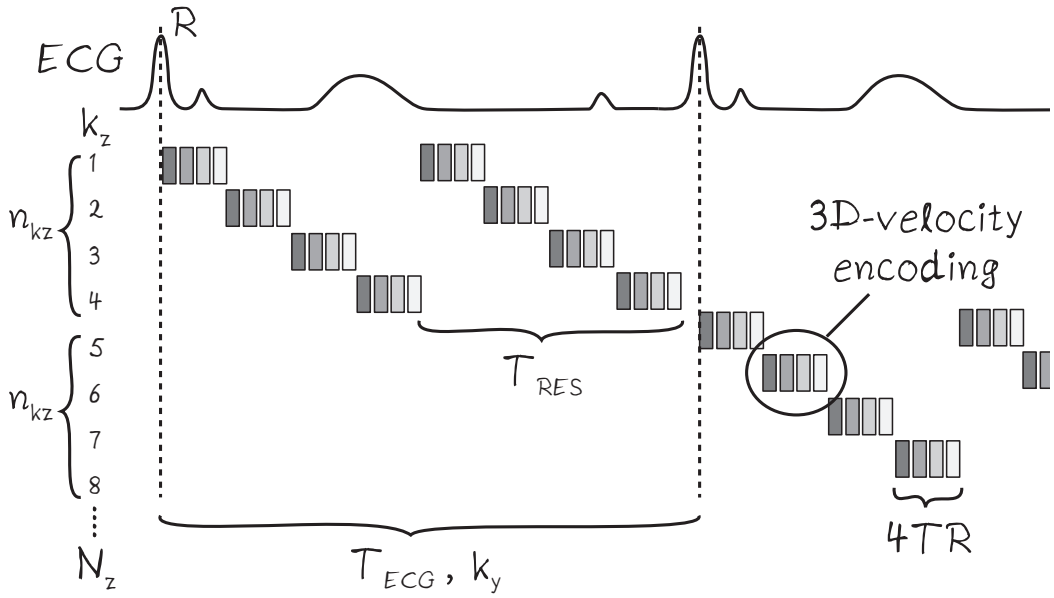

Fig. 2.14: Phase-encoding scheme for an ECG-triggered 4D-MRV acquisition for phase steps with quasi-temporal resolution T_{RES} adapted from Markl et al. (2003b). Every ECG-trigger R of duration T_{ECG}, a number of slices n_{kz} is acquired. This is repeated for several ECG cycles until all slice-encoding steps N_{kz} are obtained. Each slice-encoding step contains a 3D-velocity encoding with four-point acquisition $4TR$. When N_{kz} is reached, the process restarts for the next phase-encoding line k_y.

For in-vitro measurements, the MR system can be triggered by an external source. Wassermann et al. (2013) analyzed the unsteady, cyclic flow inside a bi-stable fluidic oscillator utilizing phase-locked 3D3C MRV. They used an in-situ pressure transducer, which records the jet switching process as pressure curve. This is then fed into a data acquisition unit, processing a trigger signal in real-time with which the MR system is gated.

2.3 Measurement Error

In MRI, different sources of measurement error can occur. One is the signal-to-noise ratio (SNR), which is an overall measure related to the whole FOV. The SNR can be used to estimate the velocity error. As another source,

artifacts are anomalies in the signal intensity and develop in certain parts of the FOV. The origin of artifacts depends on many factors, such as field inhomogeneities, imperfections in the gradient and RF system, fluid motion or object movement, to name only a few.

2.3.1 Signal-to-Noise Ratio

SNR is a measure of the accuracy of the measurement data. Noise describes any signal deviation from its ideal value (Tropea et al., 2007). In MRI, sufficient SNR is needed to differentiate the measured object or distinct tissues from the background (Haacke et al., 1999). For clinical MRI measurements, the value Contrast-to-Noise Ratio (CNR) is used, since different tissue types are determined by different signal magnitudes.
Noise in MRI is mainly generated due to thermal noise in receiver coils, detectable as random voltage fluctuations in the received signal. Macovski (1996) shows, that the SNR is proportional to the voxel volume $\mathrm{V_{voxel}}$ and the square root of the acquisition time $\mathrm{T_{acq}}$:

$$\mathrm{SNR} \propto V_{\mathrm{voxel}} \sqrt{T_{\mathrm{acq}}} \tag{2.32}$$

Increasing the resolution means reducing the voxel size and, hence, reducing SNR. By increasing TE more signal is received as long as TE is shorter than $\mathrm{T_2^*}$ (Haacke et al., 1999).
Furthermore, by averaging multiple acquisitions of the same experiment, the SNR improves by the square root of the number of acquisitions N_{acq}, assuming that the noise is uncorrelated between subsequent experiments (Haacke et al., 1999):

$$\mathrm{SNR} \propto \sqrt{N_{acq}} \tag{2.33}$$

A common method to estimate the SNR from the signal magnitude of only one scan is the signal-background method (McRobbie et al., 2002):

$$\mathrm{SNR_{mag}} = \frac{\mathrm{mean}(\sqrt{\frac{4-\pi}{2}}\mathrm{signal})}{\mathrm{STD(noise)}} \tag{2.34}$$

where two different Regions-Of-Interest (ROI) inside the FOV are defined: ROI1 is chosen inside the water (signal, high magnitude values) and ROI2 is chosen outside the water but still inside the FOV (background, low magnitude values). In order to choose ROI2 enough signal background area has to be acquired. The SNR is then calculated by deriving the mean value of ROI1 and dividing it by the standard deviation (STD) of ROI2. The noise of a single receiver coil follows a Rayleigh distribution. Hence, a conversion factor of $\sqrt{\frac{4-\pi}{2}}$ is needed to calculate the standard deviation (Haacke et al., 1999).
Artifacts can strongly influence the magnitude image and, hence, lead to an underestimation of SNR. A proper choice of the noise ROI and signal ROI is obligatory.
The SNR can be illustrated graphically by plotting the histogram of the magnitude. Therefore, the magnitude value of each voxel is accounted to a bin and summed up. Typically the two distinct peaks are visible. One is the noise peak and one is the signal peak. The histogram plot can help to assess the overall data quality.

2.3.2 Phase Error

The phase error is directly related to $\mathrm{SNR}_{\mathrm{mag}}$ (Haacke et al., 1999). The standard deviation of the signal phase $\sigma(\Phi)$ can be approximated by:

$$\sigma(\Phi) = \frac{1}{\mathrm{SNR}_{\mathrm{mag}}} \tag{2.35}$$

As the velocity data is directly based on the signal phase, Eq. 2.35 can be transformed into a measure for the deviation of the velocity (Bernstein, 2004):

$$\sigma_{\mathrm{vel}} = \frac{2\sqrt{2}\mathrm{Venc}}{\pi} \frac{1}{\mathrm{SNR}_{\mathrm{mag}}} \tag{2.36}$$

It is obvious that high signal strengths lead to increased $\mathrm{SNR}_{\mathrm{mag}}$ and, thus, to a decreased velocity error. Increased signal can be achieved by proper adjustment of imaging parameters, such as TE/TR or signal enhancing contrast agents. High noise, however, reduces $\mathrm{SNR}_{\mathrm{mag}}$ and increases the ve-

locity error. Noise can be reduced by averaging multiple scans, each with equal measurement parameters. Bruschewski et al. (2014) discuss velocity uncertainty of MRV measurements applied on highly turbulent swirling flow. For their setup, SNR is not an appropriate measure to estimate the velocity errors.
Another influence on the velocity error is the Venc, which is inversely proportional to the amplitude G_k and inversely proportional to the square of the duration Δt of the bipolar gradient. The adjustment of the bipolar gradient parameters is important. A Venc chosen as low as possible reduces the velocity error. On the other hand, aliasing can occur, when the flow velocities exceed the Venc. For instance, high positive flow velocities exceeding the Venc $\Delta\Phi > \pi$ are interpreted as negative velocities. In contrary to error minimization, the Venc must be chosen high enough to prevent aliasing (Elkins and Alley, 2007).

2.3.3 Field Inhomogeneity Artifacts

Field inhomogeneities affect the effective local magnetic field strength and, hence, change the proton resonance frequency. This can lead to off resonance conditions, which, in turn leads to signal loss as well as phase errors and promotes the occurrence of other artifacts. Especially gradient echo sequences are sensitive to sources of off-resonance. Peters (2000) names three main sources:

- B_0-field inhomogeneities
- susceptibility variations
- chemical shift

2.3.3.1 Main Field and Gradient Field Inhomogeneities

Geometric distortions can be caused by imperfections in the main magnetic field B_0 or from nonlinearities in the gradient field. Both exist due to the finite size of the magnets. Imperfections in the B_0-field, for instance, arise during the manufacturing process. They can be balanced by shim coils installed in the MR scanner. In a certain range, the magnetic field lines of the magnet are aligned parallel. This region is termed iso-center. Although inhomogeneity artifacts inside the iso-center have rather small influence, geometrical distortions will appear in the resulting image, when the FOV is chosen near the maximum measurable size (Morelli et al., 2011).
Nonlinearities in the gradient field lead to similar geometric distortions. As the gradient field is known, corrections can be applied during image reconstruction or in the post-processing. A typical field distortion artifact, due to too large FOV is depicted in Fig. 2.15.
Field inhomogeneities of the main magnet or the gradient system can develop over time during the measurement. This is then termed B-field drift. A cause for that can be the warming of the magnetic gradient system.

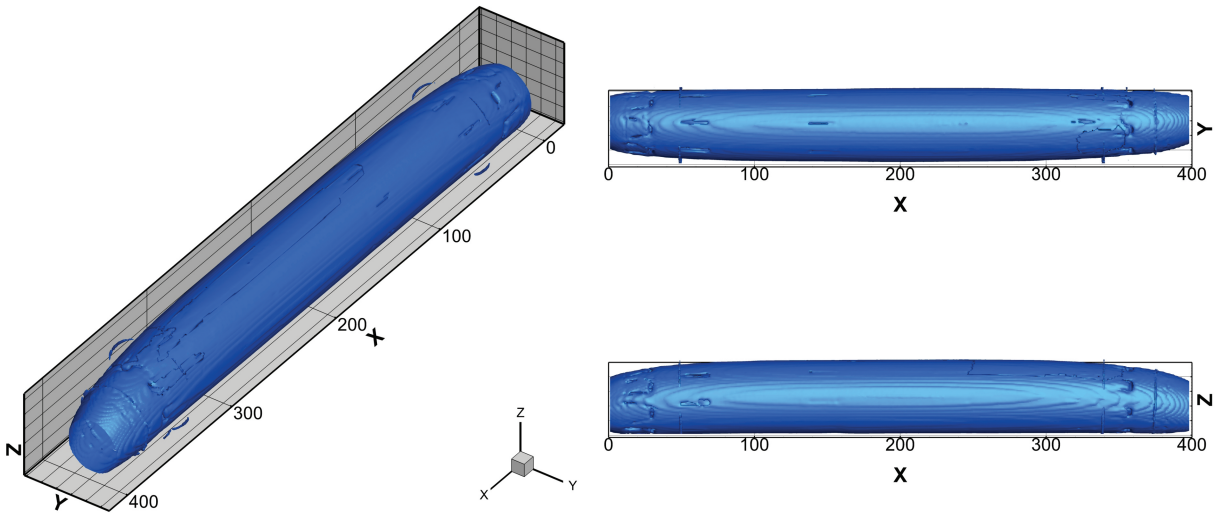

Fig. 2.15: Magnitude image of flow through a pipe (between x=50mm and x=350mm) with parts of the inlet diffuser and outlet nozzle. The FOV was larger than 400mm in x-direction, which corresponds to the direction of the magnetic field lines of the main magnet. Distinct distortions are visible in the image periphery (x-y-plane and x-z-plane). In the image the pipe is crooked at both ends.

2.3.3.2 Susceptibility Artifacts

Inhomogeneities due to magnetic susceptibility effects are mainly present at boundaries between different materials. Different tissues have different magnetization potential, as explained in Sec. 2.1.6.2. Imbalances are caused in the local volume-magnetic susceptibility χ_v. Paramagnetic materials, for instance, strengthen the magnetic field around their location (Morelli et al., 2011). This violates the linear relationship assumed for constant B_0-fields. Especially in more complex experimental setups where different materials are implemented in the flow model, the magnetic field can be distorted locally and cause stationary susceptibility artifacts. Typically, they can be eliminated by background subtraction of two subsequently performed scans, if the material boundaries stay stationary and their environmental conditions (e.g. temperature) keep constant.
However, the magnetic susceptibility of some materials/fluids changes with increasing or decreasing material/fluid temperature. It has to be taken into consideration, when various types of material/fluid each with different temperature-dependent susceptibility are employed in the same setup. Only small changes of the material temperatures, due to variations of the room temperature or fluid temperature can result in variations of the susceptibility. These effects can not be compensated for by background subtraction. Hence, susceptibility artifacts are an important point to consider in MRT measurements, since their effect on the signal phase can be of the same order as the PRF-shift and overlay the temperature information unfavorably (Wlodarczyk et al., 1998). By increasing TE, susceptibility artifacts intensify. An example of the field inhomogeneities produced by this sort of artifact is discussed in Wassermann et al. (2014a).
As ferromagnetic material typically has very large magnetic susceptibilities it becomes clear, that the usage of this material inside an MR scanner leads to strong artifacts and signal dropout. Contrast agents applied in too high concentrations can lead to similar effects, as they are paramagnetic or even superparamagnetic.

2.3.3.3 Chemical Shift Artifacts

Chemical shift artifacts occur due to local changes in the proton resonance frequency leading to a spatial misregistration in the frequency encoding direction (McRobbie et al., 2002). The physical origin of chemical shift is equal to the effect used for PRF thermometry. In medical imaging, chemical shift artifacts typically arise at fat-water interfaces (Morelli et al., 2011).

2.3.4 Flow-induced Artifacts and Errors

Notwithstanding that measurement data can achieve high SNR, imaging artifacts caused by fluid flow can result in a wrong estimation of velocities or displacements in space and, hence, can lead to wrong interpretation of the flow field. Flow artifacts are likely to manifest in all experiments where fluid flow is present.

2.3.4.1 Partial-Volume Effects

Partial volume effects occur in voxels partially consisting of stationary and moving spins. Wrong velocities are calculated due to dispersion of the signal phase between stationary and moving spins. This artifact, which mainly affects phase contrast imaging techniques, depends on the flow type (laminar or turbulent) and can be diminished by decreasing the voxel size. Tang et al. (1993) propose that when encoding is parallel to the flow direction, a minimum of 16 voxels must be acquired to reach a flow accuracy of 10% inside the flow channel. For accurate flow quantification, partial-volume effects are more important than phase-dispersion effects, as discussed in Sec. 2.3.4.4.

2.3.4.2 Time-of-Flight Effects

Time-of-flight effects are present in cases where the velocity distribution changes over time. For instance, this can occur when the flow rate is not held constant or the water temperature changes. The result is a drift in the detected signal phase, which leads to wrong velocity estimation (Elkins and Alley, 2007).

2.3.4.3 Spatial Misalignment

Assuming that the spins travel through voxels with an average velocity U, the spins cover the distance U·TE per TE. If the traveled distance is large and the flow is highly turbulent, wrong velocity values might be interpreted due to spatial misalignment (Elkins et al., 2003). In order to compensate for this error, the model size and flow velocities have to be adjusted with respect to the desired resolution and FOV size.

2.3.4.4 Intravoxel Phase Dispersion

Intravoxel phase dispersions[20] lead to signal cancelation and can occur when TE is chosen too high. This measurement artifact only occurs in highly turbulent flows. Short echo times reduce the time in which the velocity can fluctuate inside one individual voxel, due to turbulence. During a long TE, multiple velocity fluctuations inside a voxel occur, which lead to unwanted signal dephasing, thus, causing a drop of the measurement signal (McRobbie et al., 2002).
Elkins et al. (2003) conduct 4D MRV measurements in a turbulent pipe flow. They define a dephasing parameter DP as:

$$\mathrm{DP} = (u')\mathrm{TE}/X_{\mathrm{voxel}} \tag{2.37}$$

[20] also termed intravoxel dephasing

DP is proportional to the root-mean-square (rms) u' of the average velocity U, the echo time TE and inversely proportional to the voxel dimension X_{voxel}. They propose that signal loss can be expected when DP ≥ 1.
This error occurs, for instance, in experiments with very slow flow velocities. A sufficient resolution of small velocities is accompanied by the choice of a smaller Venc. In order to acquire enough velocity-dependent phase lag, a higher first order moment M_1 has to be applied, leading to increasing TE.

2.3.4.5 Higher-order Moment Artifacts

As mentioned above (see Eq. 2.22), the influence of higher-order moments, such as acceleration, were ignored for velocity encoding. Especially in complex flows or inside the velocity boundary layer, this assumption is wrong and will result in additional velocity errors or spatial misalignment. Shorter TEs and short durations between the bipolar gradient and the signal echo minimize velocity errors, due to higher-order moment dephasing (Elkins et al., 2003).
All effects resulting from too large TE (spatial misalignment, intravoxel phase dispersion or higher-order moment artifacts) especially come into account in flows with separation or strong secondary flows (Elkins et al., 2003).

2.3.4.6 Artifacts due to Oblique Flow

When fluid motion is oblique to the FE and PE direction a displacement artifact occurs. During PE and FE the spins are allocated to a certain position. The temporal lag between PE and FE makes the positions of the moving spins inconsistent. They are allocated to a position they never appeared. This artifact can be reduced by setting the PE gradient as near as possible to the FE gradient (Elkins and Alley, 2007).
Flows with swirl are strongly affected by this measurement error (Bruschewski et al., 2014).

2.3.4.7 Inflow Artifacts

When unsaturated spins enter the first imaging plane, the first RF pulse leads to an increased signal magnitude compared to subsequent slices. After that the spins are saturated in steady-state condition. A pre-saturation pulse diminishes this kind of artifact.

2.3.4.8 Magneto-hydrodynamic Effect

The Magneto-Hydrodynamic Effect (MHD) only occurs when a conducting fluid (containing charged particles or ions) moves with a perpendicular component to the magnetic field $\vec{B}$. A force is produced on the particle charge q moving with velocity $\vec{v}$, described by the Lorentz magnetic force law:

$$\vec{F} = q\vec{v} \times \vec{B} \tag{2.38}$$

The resulting force is perpendicular to the B-field and the fluid velocity and can lead to secondary flows. MHD typically affects the blood flow in vessels, such as the aortic arch (McRobbie et al., 2002).

2.3.5 Other Sources

There are many origins for imaging artifacts, which do not result due to fluid flow or field inhomogeneities, but are likely to occur in most MRV measurements:

Ghosting or smearing occurs, when the imaged object moves during acquisition. This is often present in clinical investigations, when the patient is respiring (ghosting, due to periodic movement) or the eyes are moving (smearing, due to aperiodic movement). The reason for that is an incorrect encoding in the phase direction. k-Space is partly filled with the objects

before and after movement.

Wrap-around artifacts occur, when the imaged object exceeds the dimensions of the FOV. This is caused by under-sampling in the phase encoding direction and can be corrected by enlarging the FOV (which comes with SNR penalty) or by swapping the PE and FE direction (if FOV fits the object).

Eddy currents are induced by time-varying magnetic gradients following the Faraday´s law $\nabla \times \vec{E} = -\frac{\mathrm{d}\vec{B}}{\mathrm{d}t}$ (Griffiths, 1999). They are induced in the magnet, the coils or in other conducting structures present inside the ROI. Eddy currents evoke additional magnetic gradients with small amplitude and opposite polarity. They are induced during the rising or falling slope of the magnetic gradient and, hence, are proportional to the slew rate[21] of the used gradient system (Bernstein, 2004). As a countermeasure gradient slew rates should be chosen as low as possible (decrease $\frac{\mathrm{d}\vec{B}}{\mathrm{d}t}$). They can be compensated by applying a surface fit to the background offset of the phase images in reference phantoms placed around the measurement phantom (Lingamneni et al., 1995).

Maxwell terms or concomitant field-terms result due to the presence of magnetic field gradients. By applying a linear magnetic gradient $\vec{G}$ other magnetic gradients of higher orders are induced as a result of the Maxwell equations (Bernstein, 2004). They produce magnetic field components perpendicular to the B_0-field that can deviate $\vec{M}_z$ from the B_0-field axis. This deviation field is known as c̀oncomitantḿagnetic field. This also affects the signal phase angle (concomitant phase) and, hence, leads to additional errors. The concomitant field strength is proportional to the strength of $\vec{G}$ and inversely proportional to the B_0-field strength (Bernstein, 2004). Artifacts due to Maxwell terms appear as additional shading in the MR image. The Maxwell terms can be diminished or even corrected by applying additional gradients or adequate image reconstructions (Bernstein et al., 1998).

[21] The slew rate is the time the magnetic gradient unit needs to rise and fall to and from full gradient strength.

Gibbs Ringing artifacts or truncation artifacts are bands in the signal magnitude and occur at the object's boundaries, where the signal has a steep gradient. When a step-like profile is discretized, the sampled signal overshoots at the edges. By decreasing the voxel size this artifact can be minimized.

Constant-frequency noise artifacts, Zipper or RF artifacts are present when the RF unit receives unwanted noise from sources with a certain frequency. Origins are improper shielding of a cable located near the scanner, a disability of the Faraday cage shielding (open door) or an RF-controlled electronic device (e.g. radio, light, pump, actuator). In the resulting image, the artifact appears as a white stripe perpendicular to the FE direction. Fig. 2.16 b) shows an example of RF artifacts produced by a piezo-electric linear actuator device (Motor NEXACT N-310, Controller E-861, Physik Instrumente (PI) GmbH & Co. KG, Karlsruhe, Germany) that was especially designed for the use in magnetic high-field environments.

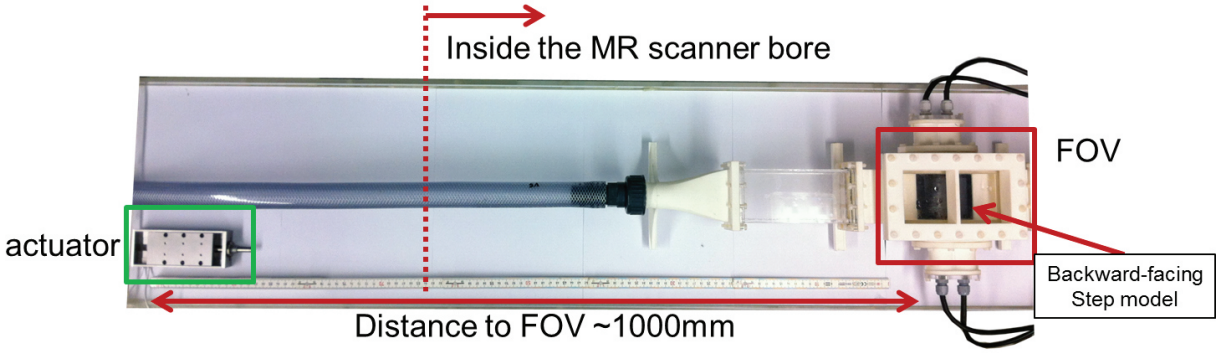

(a) Setup showing the flow model (backward-facing step) and the piezo-electric actor. Activated actuator was positioned outside the scanners bore during an MRV measurement.

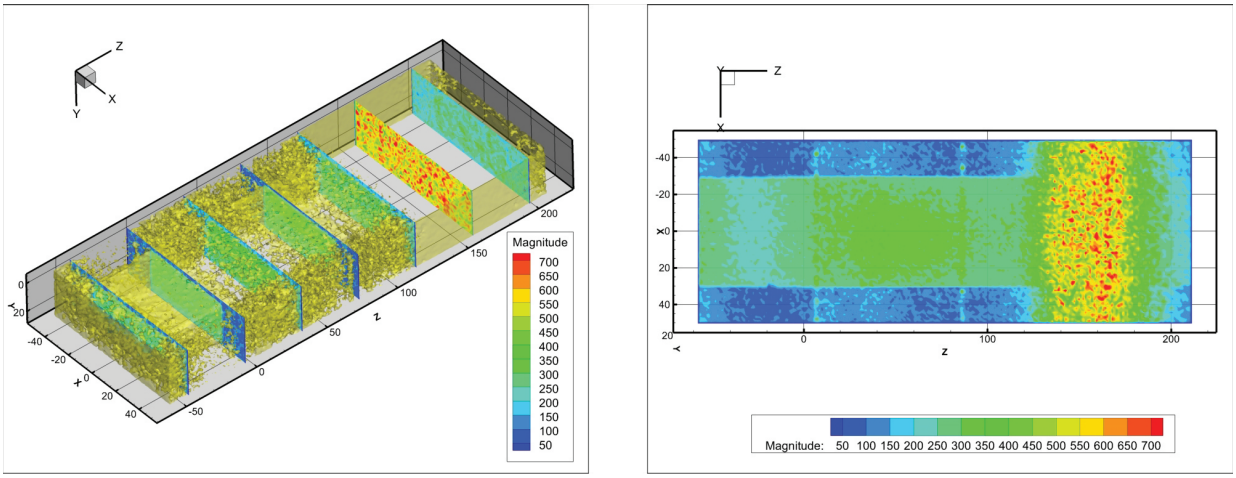

(b) Iso-surface plot (left) and contour plot (right) of signal magnitude acquired during the actor was turned on. Distinct artifacts together with an increased noise level are visible. Over-interpretation of signal in a wide band along the FE direction (z-direction).

Fig. 2.16: Example of high RF noise produced by a piezo-electric actuator operating during an MRV measurement.

Chapter 3

Methodology

3.1 MRI Setup

3.1.1 MRI Device

The systems used for MRI are located at the University Medical Center Freiburg. Two MRI systems are accessible. Detailed information is given in Tab. 3.1. The Siemens Magnetom Prisma system (Erlangen, Germany) is the upgraded version of the Siemens Magnetom Trio system and is used for the majority of measurements. A Siemens Symphony system (1.5 T) is also accessible but not used for the final measurements. It is used for pre-tests.

Tab. 3.1: MRI devices used for MRV/MRTh measurements.

	Siemens Magnetom Trio	**Siemens Magnetom Prisma**
Photo		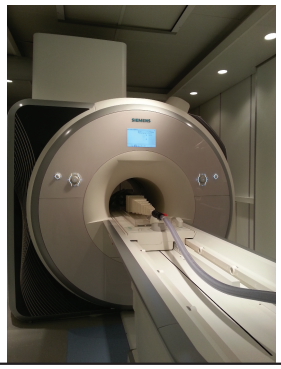
Field strength	3 T	3 T
Maximum gradient strength	40 mT/m	80 mT/m
Gradient slew rate	200 T/(m s)	200 T/(m s)
FOV	500 mm iso	500 mm iso
Bore opening	600 mm	600 mm
Bore length	2 m	2 m
Max. weight	200 kg	250 kg

For each acquisition different coils comprising different numbers of channels can be applied. For the Prisma system the following coils are available: The spine coil is located inside the patient table and comprises 32 channels in total. According to the location of the measured object on the patient table different channel quartets can be selected. A surface body coil can be applied comprising 18 channels, which can be turned on or off in 3 groups at 6 channels each. Additionally, a 1-channel head coil, a small flexible 4-channel coil and a 1-channel wrist coil are available for special purposes.

3.1.2 Measurement Fluid and Contrast Enhancement

For MRV and MRT a measurement fluid is needed. On the one hand the measurement fluid has to be pumped and conditioned with the existing flow supply system. On the other hand it has to have proper MR features, in order to be detectable with the MRI device or to have temperature-dependent properties (for the utilization of PRF thermometry).
For this reason pure or deionized water is the basis. In order to enhance MR capabilities a contrast agent is added to the water. Therefore, a gadolinium-based contrast agent[1] can be used. As this substance is approved for medical use it is rather expensive. Another option is copper(II) sulfate, which was used preferably in this work. Dissolved in water the liquid becomes blue and according to the concentration is acidic. For MRI a very dilute solution is preferred, which is also not deleterious for humans. Nevertheless, all devices coming in contact with the copper sulfate mixture have to be acid-proof. The ratio of contrast agent to water that provides an optimal signal was investigated by the project partner.

3.1.3 MR Data Acquisition and Postprocessing

Different acquisition sequences are implemented on the available MR systems. They can be installed on the scanner software using a special interface. For PCI measurements a 3D gradient echo FLASH sequence is installed. Simple fully Cartesian sampling is achieved for all acquisitions. With the interface all sequence parameter can be modified and adjusted prior to a scan. Typical parameter are the FOV, the Venc, TE, TR, et cetera. The sequences used were programmed and developed by the project partner.
Another important feature is the field distortion correction. This correction method is useful for the acquisition of very large FOVs. By enabling the correction mode, the bending of the B-field is corrected during image reconstruction in FE and PE direction. The measured object is stretched according to an internal correction algorithm and additional voxels are added

[1] e.g. Magnevist®by Schering AG

at the edges of the FOV.
After the scan is finished the data are exported as images in the `dicom` format. Each image is two-dimensional with a height according to the FE steps and a width according to the PE steps. As information each voxel contains grey level values of either the signal magnitude or the signal phase. A complete 3D data set comprises an image per slice-selection step.
When using a multi-channel coil, the data can either be saved, combined or uncombined. If the uncombined mode is chosen, one data set per channel is saved. This can increase the amount of capacity needed on the hard disk. If the data are saved in combined mode, then the scanner composes one data set from all channels using the sum of squares reconstruction.

3.1.3.1 MRV Procedure

For velocity measurements a simple four-point acquisition strategy is implemented as explained in Sec. 2.2.1. In order to reduce the gradient strength needed, only halved first gradient moments are applied, shown in Tab. 3.2. From the four scans one magnitude image is composed by averaging the

Tab. 3.2: First gradient moments for the simple four-point acquisition scheme implemented on the available MR machines.

	direction		
scan	SS	PE	FE
1	$-\frac{1}{2}M_1$	$-\frac{1}{2}M_1$	$-\frac{1}{2}M_1$
2	$+\frac{1}{2}M_1$	$-\frac{1}{2}M_1$	$-\frac{1}{2}M_1$
3	$-\frac{1}{2}M_1$	$+\frac{1}{2}M_1$	$-\frac{1}{2}M_1$
4	$-\frac{1}{2}M_1$	$-\frac{1}{2}M_1$	$+\frac{1}{2}M_1$

four magnitudes. The four signal phases yield three phase difference images by pairwise subtraction:

$$\begin{aligned} \Delta\Phi_{SS} &= \frac{\Phi^{(2)} - \Phi^{(1)}}{\gamma M_1} \\ \Delta\Phi_{PE} &= \frac{\Phi^{(3)} - \Phi^{(1)}}{\gamma M_1} \\ \Delta\Phi_{FE} &= \frac{\Phi^{(4)} - \Phi^{(1)}}{\gamma M_1} \end{aligned} \tag{3.1}$$

It is also possible to reconstruct the images "unsubtracted". Then all four single phase images are stored.
In order to enhance SNR, multiple scans with identical parameters can be acquired. The dicom images are converted into Matlab (The MathWorks, Massachusetts, USA) structs using the Velomap Tool (©Martin Bruschewski, TU Darmstadt, Darmstadt, Germany). In this program the velocity components are calculated according to Eq. 2.25. Furthermore, data can be exported into Tecplot 360 (Tecplot, Washington, USA) format.

3.1.3.2 MRT Procedure

MRT is performed utilizing the PRF method. A similar sequence as applied for MRV is used with different parameters. The sequence and the data processing strategy has been developed by the project partner and presented in Buchenberg et al. (2015). A short summary shall be given in the following. Contrary to the four-point velocity encoding, only one scan with flow compensation in all directions is performed to ensure no phase shifts are induced due to fluid motion. In the sequence the most important parameter to adjust is TE which determines the temperature resolution. The sequence should be tuned by choice of appropriate parameters according to Buchenberg et al. (2015). The optimal parameters have to be determined for each setup individually, which was done by the project partner. As explained in Sec. 2.2.2, temperature maps can be derived from the single phase images of two consecutive scans: a scan with temperature distribution T and a scan at constant reference temperature T_{ref}. Both are then subtracted in the post-processing by combining the data from all channels of the phased array coils. Therefore, a post-processing strategy has been developed by the project partner with which single channel images are combined using the complex coil signals acquired at T_{ref} and T. The temperature maps are

then calculated according to Eq. 2.31 and saved as Matlab struct. In order to achieve correct temperature maps background corrections have to be performed.

When using distilled water with added copper sulfate to increase contrast, the screening constant α of pure water can be affected. Hence, α has to be experimentally determined in a separate experiment according to Peters et al. (1998). This was done experimentally by the project partner and a value of $\alpha = -1.03 \pm 0.02 \cdot 10^{-8}/°\mathrm{C}$ could be determined.

3.1.3.3 4D-MRI Procedure

The 4D procedure can be applied to MRV as well as MRT. A program was implemented in the scanner software by the personnel of the University Medical Center Freiburg. A requirement for the procedure is to provide a 5V Transistor-Transistor-Logic (TTL) signal as trigger emulating the underlying flow or heating cycle. The TTL is produced with a Real-Time PXI-1031 DC system (National Instruments, Austin, Texas, USA), equipped with a NI PXI-8106 embedded controller card and a NI PXI-6259 multifunctional DAQ card, running under the LabVIEW Real-time operating system and fed into the MR system through a chinch connector.
Prior to a scan, important parameters have to be chosen. The scan-cycle duration SD has to be selected according to the trigger and segmented into phase steps PS, yielding the temporal spacing $\mathrm{T_{Res}}$ between two phase steps. An experimental setup utilizing the 4D-procedure with MRV has been presented in Wassermann et al. (2013).

3.1.3.4 Background Corrections

For PC-MRI, corrections of gradient field distortions are required, as they affect the first order gradient moments and, hence, the velocity measurement. Markl et al. (2003a) provide the *generalized reconstruction algorithm*, with which the phase shift due to spatial wrapping can be calculated and

corrected. This is implemented in the acquisition programme of the used MRI devices.

Background phase errors can arise due to eddy currents, Maxwell terms and B-field drifts as discussed in Sec. 2.3. Undesired spatial variations in the background phase are the result. They are different for every MRI system and for each experimental setup. A post-processing step has to be employed to correct the background phase errors.
For MRV measurements, Elkins and Alley (2007) describe a method for which two subsequent scans have to be performed: One scan with flow turned on (flow on scan) and one scan with flow turned off (flow off scan) are necessary. The flow off scan measures the background phase shift but not the velocity-induced phase shift. Subtracting the flow on scan with the flow off scan removes these errors.
Another method especially useful for PRF thermometry is utilized by the project partner and based on De Poorter (1995). It utilizes the background phase shift measured in reference phantoms positioned outside the phantom and, thus, allows the correction of B_0-field drifts. The FOV has to be enlarged in order to cover the phantoms, as well as the reference phantoms. More details are presented in detail in the work of the project partner.
The background phase can approximated with a 3D fit routine provided by Testud and Zaitsev (2009). This routine is based on spherical harmonics that can be solved with Legendre polynomials (Roméo and Hoult, 1984). Another method proposed by the project partner utilizes these polynomials to calculate the background phase shift in the reference phantoms or from a flow off scan. It can be used to calculate a three-dimensional residual phase map of the whole FOV. This estimated correction field is then subtracted from the phase difference map. The method is especially useful, when a flow off scan is not possible (e.g. moving parts, heated measurements for MRT are not possible to measure without flow) or in order to reduce scan time. Another big advantage is, that the Legendre-fitted background phase map is free of noise. After subtraction the SNR of the resulting phase map does not increase, as it does for the standard flow off scan subtraction.

3.2 Flow Model Design

Flow model development and construction is a major task in this PhD thesis. In the jargon of MR physics a model is termed *phantom*.

3.2.1 MR Considerations

In this section important consideration of MR physics background are transferred to the engineering design and construction process of flow models used for MRT. These recommendations are based on the work of Schenck (1996) and further extensive research done cooperatively by both project partners. As this was an iterative process, design rules achieved by project partner were included into the engineering construction process. In the following a summary of the main MR considerations is given without discussion. Their consequences for the engineering part of the project are worked out subsequently.

The main points proposed by and discussed in the work of the project partner (important points achieved by the project partner were already presented in Buchenberg et al. (2015)) consider:

1. *the model shape*

- Avoid air bubbles and other air-water surfaces of complex shape inside the FOV.
- Avoid sharp edges (especially at material boundaries) and sudden changes of the cross-sectional area (e.g. flanges) inside the FOV.
- Consider the orientation of walls and structures in relation to the B_0-field. Circularly-shaped or ovally-shaped models aligned parallel to the B_0-field are optimal applicable (Schenck, 1996).
- Avoid additions to the flow model (e.g. probe inlets) inside the FOV.

2. *the model material*

   - Use materials with a good susceptibility matching to water or the used measurement fluid (Schenck, 1996) (see Tab. 3.3).
   - The susceptibility of materials outside an object (mostly in the surrounding air) should be zero or should have the same value as the surrounding fluid.
   - Prevent undesired contaminants. In ceramics, iron oxides can be incorporated into the binding matrix. After machining with steel cutting tools the work piece surface can be contaminated. Semi-finished products can contain undesired iron particles.
   - Electrical conductive material can screen the B_1-field of the RF excitation pulse (Faraday cage).

3. *the model placement inside the FOV*

   - Other objects (e.g. reference phantoms) should be placed with appropriate distance to the flow model.
   - Place the ROI of the flow model inside the iso-center.

4. *the flow conditions*

   - Prevent strong fluid accelerations or deceleration, when no acceleration compensation is performed.
   - Avoid strong unsteady fluid flow.
   - Obtain stable experimental conditions.

Considering the model shape this implies for the fluid mechanical design of a flow model that an appropriate flow preparation has to be present to prevent flow-induced air-water surfaces. Every model should comprise air vents at several positions throughout the flow channel. Especially behind sudden expansions of the channel cross-section where flow-induced separa-

tion regions occur, air vents can be necessary. However, according to the model shape considerations, air vents can cause errors. Hence, they should be avoided inside the ROI.

Schenck (1996) points out two parameters which characterize the MR-suitability of a material: the magnetic susceptibility χ and the inherent magnetization M_{inh}. M_{inh} is greater than zero for permanent magnetic material (e.g. neodymium-iron-boron magnets), which cannot be used for MRI (hard magnetic material). Only material with $M_{inh} = 0$ is suitable for application in MR-environment. Materials with large magnetic susceptibilities (soft magnetic material) experience forces inside a strong magnetic field. Contrary, materials with very small magnetic susceptibilities (nonmagnetic materials) experience no forces. Hence, Schenck (1996) can categorize the materials. Important for the classification is the difference of the susceptibilities of one material χ_{mat1} compared to water χ_{water}, as water is mainly measured in MR experiments. Schenck (1996) proposes a perfect susceptibility matching, when $\chi_{mat1} - \chi_{water} = 0$. These materials are recommended for MR usage. This categorization is independent of whether the material is paramagnetic ($\chi > 0$) or diamagnetic ($\chi < 0$).
From the engineering perspective, the model material recommendations proposed by Schenck (1996) and the project partner have to be linked to the available manufacturing processes and the fluid mechanical and thermodynamical boundary conditions determined by the application. Hence, Tab. 3.3 summarizes thermal and magnetic properties of important technical materials (metals, ceramics, polymers and other material), which are accessible on the market and are processable with available tools. On the one hand materials are listed, which have a good susceptibility matching to water and on the other hand the thermal conductivity is listed, which is needed for thermofluid applications where heat transfer through surface conduction is applied.

Tab. 3.3: Thermal and magnetic properties of different non-organic and organic materials for the use in MR-environment. λ is the thermal conductivity, χ_v is the volume magnetic susceptibility, χ_m is the molar magnetic susceptibility.

Mat.	$\boldsymbol{\lambda}$[2] [W/mK]	$\boldsymbol{\chi_v}$[3] [10^{-6} (SI)]	$\boldsymbol{\chi_m}$[4] [10^{-6} cm^3mol^{-1} (cgs)]	**machinability**[5]
Ag	407	-24	-19.5	good
Cu	384	-9.63/-10.43 [6]	-5.46	very good
Al	204	20.7	16.5	very good
Fe	81	200,000×10^6	ferro.	fair
AlN	100-200	-	-	poor
Al_2O_3	20-30	-18.1	-37	fair
Si_3N_4	20-40	-9.0	-	poor
SiO_2 (quartz)	12	-16.3/-14.326 [7]	-	poor
TiO_2	9-13	-	-	good
PA	0.25-0.35	-8.13 [8]	-	very good
PE	0.33-0.57	-9.47 [9]	-	very good
PMMA	0.19	-9.01 [10]/-40.715 [11]	-	good
PET	0.24	-	-	very good
CH_4	-	-	-17.4	-
H_2O (37 °C)	0.58	-9.05	-12.96	-

[2] data taken from Kalweit (2006) and Lide (2014)

[3] data taken from Schenck (1996)

[4] data taken from Lide (2014)

[5] These qualitative statements are based on personal experiences working with these materials and on experiences of the institute´s tool shop.

[6] at 300 °K, from Bowers (1956)

[7] Duh et al., 2003.

[8] Marcon et al., 2011.

[9] Carlsson, 2009.

[10] Carlsson, 2009.

[11] Duh et al., 2003.

3. Methodology

From a combined MR physics and engineering perspective copper, polyamide (PA), polyethylene (PE) and acrylic glass (poly(methyl methacrylate) - PMMA) have a good susceptibility matching to water (group 1 in Schenck (1996)), are freely available as semi-finished products and are easy to machine. Especially PMMA has the advantage that it is optical translucent. Care has to be taken when machining or gluing PMMA parts. Unwanted tensions inside occur, which can lead to cracks and, thus, have to be removed by a temperature treatment. Models made of PA are primary formable using laser-sintering techniques. This enables the design of models with complex geometries. Hence, PA and PMMA are the choice as primary model material. Certain MRT flow models need increased thermal conductivity on specific channel walls in order to achieve an appropriate surface heat flux into the measurement fluid. Due to their high thermal conductivity copper, aluminium and aluminium nitride would be the choice. Additionally considering the susceptibility matching copper would be the best choice. It is also easy to machine. If copper or other applicable metal materials are used, then the recommendations considering the model shape proposed by the project partner have to be taken into account. Silicon nitride (Si_3N_4) has a good susceptibility matching but a thermal conductivity that is only 10% of the value of copper, as well as limited mechanical machinability. It is solely available in simple pre-product forms. Hence, only models with a simple geometry could obtained.
Materials often used in model fabrication are alumina (Al_2O_3) and silicon, which are assigned by Schenck (1996) to group 2 and, thus, should only be second choice in flow model design. Alumina has the advantage that it is easy to machine and can withstand high temperatures. Ceramics based on alumina silicate[12] are easily machinable, whereas they have a comparably small thermal conductivity (≈1 W/mK). No magnetic susceptibility values could be found in literature.
Besides their good susceptibility matching, most ceramics and polymers have the advantage of not being electrical conductive and, hence, not screening electromagnetic radiation. Models made of these materials will not shield the B_1-field from entering and the MR signal from exiting it and can be used as material for the flow channel.
The use of electrically conducting cables (e.g. sensor cables, power supply) inside the MR scanners bore have to be considered carefully. As explained in Sec. 2.3 RF artifacts can be evoked, which are typically appearing very

[12] e.g. Rescor 902™available from Polytec PT (Waldbronn, Germany)

locally in the MR image.

Another important point proposed by the project partner considers the model flow conditions. The steadiness and stability of the inlet conditions are mainly influenced by the flow apparatus presented in Sec. 3.3. The steadiness of the flow, the turbulence level and accerleration/deceleration within the flow model are part of the engineering design process and have to be assessed using dimensionless numbers and comparison to other literature.

3.2.2 Fluid Mechanics and Thermodynamics Considerations

Fluid mechanical and thermodynamical processes in a flow model are characterized by the experimental parameters and coefficients as well as the material properties. They are presented in Sec. A.3.1. Most important for the comparison to other experiments are the characteristic dimensionless numbers, which are explained in Sec. A.3.2.

In this thesis only a selection of the parameters listed in Tab. A.1 and the dimensionless numbers given in Tab. A.3 and Tab. A.4 is necessary. This comprises the Reynolds number characterizing the flow, the Nusselt number characterizing the heat transfer and the Grashof and the Richardson numbers both characterizing the influence of buoyancy forces. For many setups empirical correlations have been achieved, which are summarized in design rule books. In order to calculate the dimensionless parameters the material properties are necessary, which include the density ρ, the dynamic viscosity η, the specific heat capacity c_p, the thermal diffusivity a, the thermal conductivity λ and the thermal expansion coefficient β as well as their combinations. Values for the properties of water are listed in Tab. C.1 as a function of the temperature. Additionally, the variables fluid velocity U and fluid temperature T are necessary. For heat transfer processes the heat transfer rate $\dot{Q}$, the wall heat flux $\dot{q}_W$ and the heat transfer coefficient α are important. They are typically a function of the temperature, the velocity, and the experimental setup.

3.2.3 Model Manufacturing

All flow model investigated within the scope of this PhD thesis were developed and manufactured at the Institute of Fluid Mechanics and Aerodynamics at Technische Universität Darmstadt.
In the development phase each model was designed using the CAD software NX (Siemens PLM Software, California, USA).
Complex parts were mainly manufactured from PA using an EOS Formiga P100 direct laser sintering machine (EOS, Krailling, Germany). During the sintering process a model is built up slice by slice. The process temperature is set just below the melting point of the PA powder. In each step a 0.1 mm thick layer of PA powder is applied over a vertically traversable table (200 mm × 250 mm) and a laser beam (thickness 0.4 mm) shoots the cross-section of the model. After all slices have been achieved (maximum height 330 mm), the entire manufacturing space has to cool. During the cooling duration the model shrinks. Depending on the machine´s calibration an accuracy of <0.5 mm is possible.
Parts, where optical access was desired, were made of PMMA pre-products (main vendor Evonik Industries, Essen, Germany). They were machined manually or using a 2-axis laser cutter (skylaser 9060, Pfeifer technology & innovation, Plauen, Germany). PMMA pre-products are typically primary formed in a cast or extruded. PMMA pipes used in this thesis have a typical fabrication tolerance of ±0.5 to 1 mm for the outer diameter and ±0.25 to 0.4 mm for the wall-thickness[13].
Components of a flow model were mated using PA screws. Rough surfaces of a model made of PA (flanges) were treated with abrasive paper. O-rings made of nitrile rubber (NBR) were used for sealing. To increase sealing performance, silicone, grease or vaseline was applied on the sealing surfaces.

[13] Values taken from http://www.plexiglas.de/product/plexiglas/Documents/BHB/BHB-PLEXIGLAS-de.pdf.

3.3 Flow Apparatus

3.3.1 Flow Supply Systems

Providing water flow with conditioned and monitored flow rate, temperature and pressure is crucial for every MRV and MRT experiment. This is also important in order to achieve constant and reproducible bulk dimensionless numbers. Hence, portable systems were developed capable of feeding the experiment with conditioned flow of adjustable Reynolds numbers. One system was described before in Grundmann et al. (2012) or developed and constructed with the help of Basbug et al. (2012) and Siebner (2013). Details are given in Tab. 3.4.

Tab. 3.4: Flow supply systems designed for different applications and flow rates.

	Large system	**Small system**
Photo	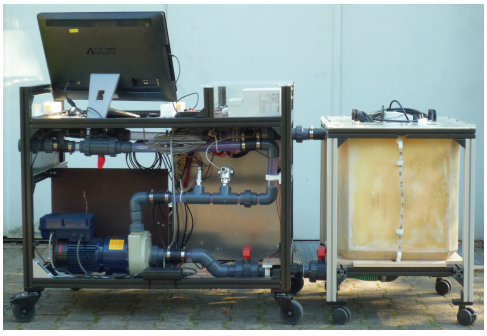	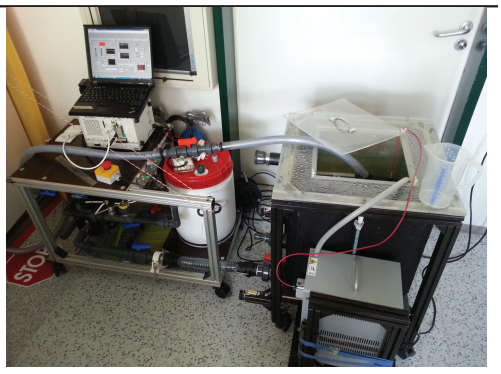
Pump	Sondermann RM-MS1 with variable frequency drive EMGR Mini 4.8 (1.1 kW)	Grundfos CME3-2 A-R-I-V-AQQE (3.7 m^3/h nominal flow rate)
Flow sensor	2 × Systec Controls Deltawave C-F / ultrasound converter XUC-FW F21	2 × Bürkert 8030 DN15 & DN20, paddle wheel flow meter (hall sensor)
Pressure sensor	Laboom CB7500 ECO (0-4 bar)	Jumo Midas 401001
Temperature sensor	Pt100	Pt100

Controls	Potentiometer (analog), NI Labview / DAQ6002 USB	NI Labview / DAQ6009 USB or PXI-1031
Water supply	100 l (big tank, external)	30 l (small tank, internal), 100 l (big tank, external)
Flow rate range	1-200 L/min	1-85 L/min
Pressure range	up to 2.8 bar	up to 2.7 bar
Temperature range	5-60 °C	5-60 °C
Flow error	±0.5 L/min (50 L/min) precision / ±1.6 L/min (taken from manual)	±1 L/min
Temperature error	±0.3 K (50 L/min)	±0.3 K (50 L/min)
Application	MRV, 4D-MRV (determined trigger), MRTh	MRV, 4D-MRV (in-situ triggering), MRTh, 4D-MRTh

Inside the flow supply systems, all components (pump, flow rate / pressure / temperature sensors) are fluidically connected using polyvinyl chloride (PVC) tubes and PVC fittings. PVC is cheap, easy to use and compatible to many chemicals.

The measurement fluid is led to the flow model through standard PVC supply hoses. They are fabric reinforced to ensure stability against bending at higher temperatures and to withstand high internal pressures. The temperature working range is -20 to 60 °C and a maximum internal pressure of 9 bar at 40 °C. The hoses are connected to the pumping carts and flow models with PVC screw connectors.

In order to feed an experiment with very low flow rates ($\dot{V} < 10$ L/min) a circuit control valve (Oventrop Hydrocontrol VTR DN32 or Oventrop Hycocon VTZ DN20, Olsberg, Germany) can be adjusted in the flow circuit. It is recommended to install the valve downstream the flow experiment and inside the scanner console room. Closing the valve at a fixed pump control voltage induces a pressure rise and, hence, reduces the flow rate. This

method enables a precise adjustment of the flow rate. Due to the increased control voltage, the pump runs at a more stable state. The increased system pressure can lead to leakage in the flow model. This should be tested beforehand and, if necessary, extra sealing provided.

3.3.2 Temperature Conditioning Systems

In order to condition the flow temperature of the primary circuit a heater or cooler can be applied. If the tank temperature should be kept at or below ambient temperature an immersion cooler of the type Julabo FT402 (Julabo, Seelbach, Germany) can be inserted into the water tank. The immersion cooler has a built-in temperature control, measuring the tank temperature with an external pt100 sensor. If the tank temperature has to be increased above ambient temperature an ohmic heating foil (resistance 25.5 Ohm) with polyimide insulation of type MINCO HK5600R25.5L12A (Minco, Minneapolis, Minnesota, USA) can be applied. The foil dimensions are 279.4 $\times$ 381.0 mm^2 with a maximum power consumption of 2kW. A thermostat with pt100 sensor controls the tank temperature by switching on/off the electrical power supply of the heating foil. For appropriate fluid mixing a self-built stirrer propelled by a DC electro motor and controlled by a servo tester can be applied.

The pressure supply and fluid conditioning for a secondary flow circuit is achieved with two different devices: If the temperature of the secondary flow is desired to be higher than the temperature of the primary circuit a Julabo SE, class III immersion heating circulator (Julabo, Seelbach, Germany) is applied. It has a maximum heating capacity of 1.3 kW. The device is set on a self-built plexiglas reservoir containing 10 liters of water. The provided flow rate depends on the pump pressure (4 adjustment levels) and the pressure loss in the secondary flow circuit.
If the temperature of the secondary flow is desired to be lower than the temperature of the primary circuit a Julabo FC1200T recirculating cooler (Julabo, Seelbach, Germany) is connected. It has a maximum cooling capacity of 1.3 kW and provides a constant flow rate of $\approx$25 L/min (up to 3.5

bar pressure loss). The device has an internal water reservoir containing 10 liters of water. The device is also capable of heating the fluid with a heating capacity of 1.2 kW.
Connected to the secondary circuit of the small system the flow rate can be measured for both devices.

All flow devices are connected to the flow model with 25.4 mm ID PVC hoses (primary circuit) and 19.05 mm ID hoses (secondary circuit).

3.3.3 In-situ Ohmic Heating

Applying Ohmic heating to a flow model which is situated inside the MR environment is a challenging task. Therefore, special heating elements fabricated of ceramic material were tested and selected. A heating system was constructed, which is capable of controlling the heating elements in a pulsatile mode and adjusting the heating power.

3.3.3.1 Heating Ceramics

Heating ceramics with different forms and with different materials were tested for usage in MR environment. Photos of the original elements and their modifications are shown in Fig. 3.1.
One vendor is Bach Resistor Ceramics GmbH (Seefeld, Germany). Their ceramic elements consist of an electrical conducting heating ceramic surrounded by an insulating ceramic based on silicon nitride. The junctions are made of copper. Two geometries were chosen: one cylindrical-shaped heating cartridge with an OD of 7.8 mm (Fig. 3.1 1)) and a heated length of 33 mm and a rectangular-shaped glow igniter with the heating area dimensions of $50 \times 14.6 \times 4.3$ mm (Fig. 3.1 2)). Both elements are powered with 230 VAC and have an electrical heating power of approximately 200 W. All ceramics were tested unheated using a GE sequence and no artifacts

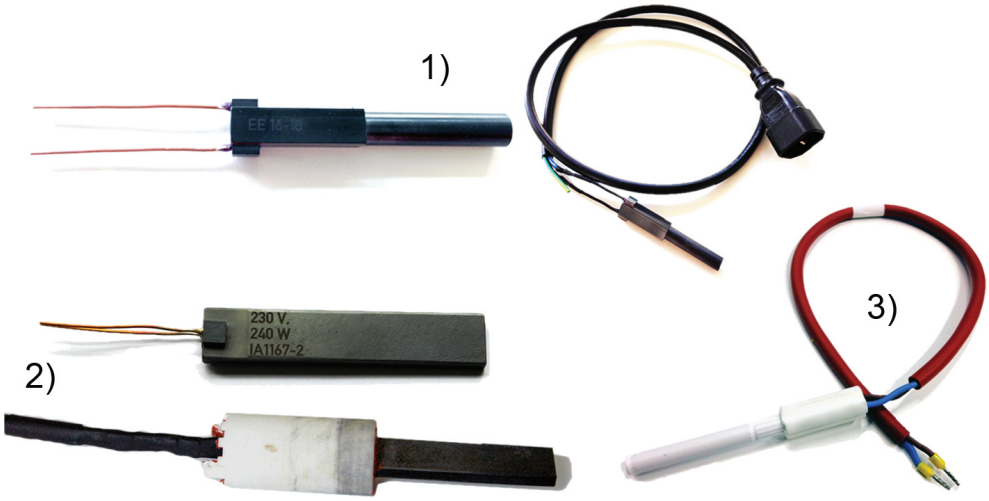

Fig. 3.1: Ceramic heating elements: 1) Bach RC heating cartridge; 2) Bach RC heating glow igniter; 3) Rauschert GmbH heating cartridge.

or other objections were found.
Another vendor is Rauschert GmbH (Steinbach am Wald, Germany). They manufacture heating elements based on an aluminium oxide (Al_2O_3) insulation with integrated platinum heating conductor, which are also powered by 230 VAC. One cylindrical-shaped element was tested with an OD of 7.9 mm and a heating length of 54 mm (Fig. 3.1 3)). Due to the heating conductor made of platinum the elements produced large artifacts when measured with a GE sequence. Hence, these type of elements cannot be used for in-situ heating.

Implementing a heating element into a flow model without producing an electrical short circuit is an important task. Therefore, the junctions have to be insulated and an appropriate sealing has to be applied. Therefore, Freudenhammer (2012) developed a procedure for sealing the glow igniter ceramic. The result is depicted in Fig. 3.1 2). First the junctions are painted with a temperature-resistant lacquer based on silicon. Then the two copper junctions are covered with shrink-on tubes. The painted area is coated with additional high-temperature silicon. The covered copper junctions are contacted with a longer cable[14], which is connected to an International Electronics Commission (IEC) power connector. Finally, the end of the heating

[14] The cable consisted copper wires which can lead to RF-artifacts discussed in Sec. 2.3.

ceramic where the junctions are is fixed into a cylindrical mold and filled with a white cast ceramic based on Al_2O_3. The heating ceramic is now electrically connected and insulated.

3.3.3.2 4D-triggered Heating Element Control

Although the heating ceramics are directly applicable for the unheated case, electrical currents inside a magnetic field induce disturbances and artifacts. Hence, proper data can only be achieved when no electrical charge is moving through the heating conductor during a measurement. During heating the measured data will be corrupted by artifacts. The solution for that is the utilization of the 4D-MRI sequence. The scan-cycle duration SD of the 4D sequence is divided into a measurement cycle (MC), where data is collected and a duty cycle (DC), where heating is applied. The result is a pulsed heating, whereby SD, MC and DC have to be adjusted so that a constant heating process is achieved. Furthermore, the heating power has to be adjustable in order to prevent local over-heating and, hence, bulk boiling. The procedure is sketched in Fig. 3.2.

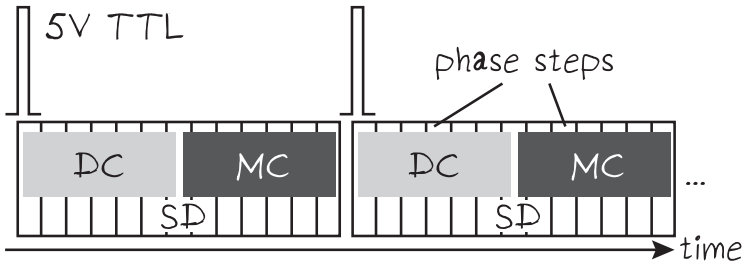

Fig. 3.2: 4D-triggered procedure for heating duty cycle (DC) and measurement cycle (MC). The entire scan has the duration SD and is divided into phase steps acoording to the adjusted measurement parameter.

A 4D-triggered heating element control system was developed by Freudenhammer (2012). The heating elements are supplied by a current toggled on/off by an electrical relay. The relay is connected to a triac unit controlling the transferred electrical power and an optical coupler which ultimately

disconnects the electrical supply. Everything is mounted on a DIN rail and for safety precautions a Residual Current-operated Circuit Brake (RCCB) is included. The triac output is controlled by a 0-10 V heating elements voltage U_{HE} and the optical coupler is switched by a 5V-TTL signal. The system is controlled by a Labview program, which provides the 5V-TTL signal for a chosen SD and the durations for MC and DC, as well as U_{HE}. Fig. 3.3 depicts the parts of the explained system.

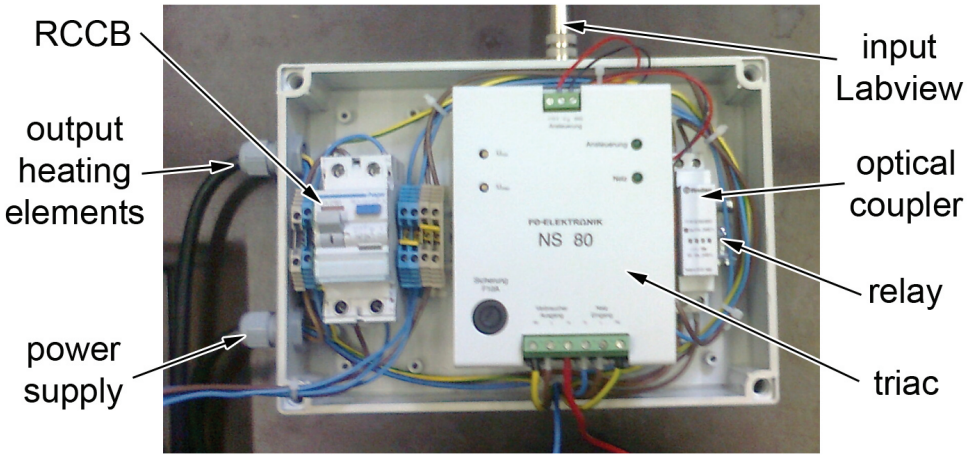

Fig. 3.3: Components of the 4D-triggered heating element control system. The photograph is taken from Freudenhammer (2012).

During the 4D sequence the MR system acquires data in both cycle parts, the MC and the DC. All phase steps in the DC have to be discarded, due to the artifacts. The phase steps acquired during MC can be averaged to one resulting data set (magnitude and phase).

3.3.4 Flow Preparation

Important for the inflow conditions of the flow models is not only the Reynolds number (as a function of the flow rate, temperature and pressure) but also the inlet velocity profile. As the supply hoses have a smaller cross-sectional area than the flow models, the flow has to be transferred to

an increased cross-section. In order to achieve an appropriate quality of the inflow profile into the flow model the flow should be accelerated. This is typically done with a combination of a diffuser, a settling chamber and a nozzle.

The diffuser is the most crucial component and difficult to design. Regarding the continuity and momentum conservation equations, fluid flowing through a channel with increasing cross-sectional area experiences decreasing velocities, while the pressure increases. The kinetic energy is transformed into pressure energy. Especially in the vicinity of the channel wall the fluid velocity inside the boundary layer is even smaller and the kinetic energy of the fluid particles is too low to further move against the adverse pressure gradient. In one point in the flow, when the wall slope is too high the flow separates from the surface. Downstream the flow separation a flow recirculation can occur. The boundary layer separation artificially reduces the cross-section and the mean flow velocity is higher than expected when no separation occurs. A separated diffuser does not recover the pressure ideally. A critical design value is the diffuser opening angle δ. In literature a diffuser is considered separation free, when the equivalent cone opening angle is $\delta < 5°$ (Spurk and Aksel, 2010). Another important design parameter is the expansion ration ER, which describes the ratio of outlet cross-sectional area to inlet cross-sectional area. Now the problem of standard diffusers becomes clear: Designing a conical diffuser with ER $= 2$ and $\delta = 5°$ means achieving a length of 22-times the radius. For MR application in most cases this is far too long. Utilizing $\delta > 6°$ wide-angle diffusers are investigated by Mehta (1977). Inserting grids at distinct positions and with determined open-area ratios β into the diffuser prevents the flow separation. Each grid generates a pressure loss distribution, which is varying according to the local flow velocity (Seltsam, 1995). In regions where the flow has the highest velocities the grid evokes the highest pressure loss and vice versa.
Two wide-angle diffusers were realized: One expands the flow from 25.4 mm ID to a rectangular cross-section of 150×150 mm^2 within a length of 800 mm. It was designed, tested and verified within the work of Bauer (2013). A second diffuser expanding from 25.4 mm ID to a circular cross-section of 150 mm ID within a length of 500 mm was developed and constructed with equal design parameters by the author.
Downstream the diffuser the settling chamber is mounted. It comprises a de-aeration hole to remove trapped air. Optionally honeycombs can be inserted to further homogenize the flow and take out large scale turbulence.

For setups with low flow rates the honeycombs are removed. The settling chamber was kept as short as possible to prevent the velocity boundary layer to become too thick. A length of 100 mm could be realized.
According to the cross-sectional area of the test section a nozzle is mounted which accelerates the flow and, hence, removes flow turbulence. For most setups the nozzle has a length of 200 mm. The nozzle outlet cross-section is adapted to the inlet cross-section of the flow model.
All parts of the flow preparation setup are laser-sintered of PA. This gives the opportunity to easily include features such as de-aeration holes or probe inlets in the flow preparation section.

3.4 Conventional and in-situ Measurement Techniques

3.4.1 Temperature

For in-vitro temperature logging inside the MR device, as well as validation measurements in laboratory environment a fiber optical temperature measurement system based on the temperature-dependent band edge of the gallium arsenide crystal is utilized (FOTEMP 4, probe TS2, Optocon AG, Dresden, Germany). Four Fiber Optical Probes (FOPs) can be instrumented and the temperature logged. For in-situ measurements each probe has to be calibrated beforehand inside the B_0-field according to Buchenberg et al. (2014).

A second system utilizing thermocouples (TCs) is available for point-wise temperature measurements in laboratory environment. TCs with different diameters (d = 0.5/1 mm) and of different materials (type K and type T) are available. They are connected to a NI-SCC-TC02 module (National Instruments, Austin, Texas, USA), which comprises a built-in thermistor for cold-junction-compensation with an accuracy of ±0.4 °C. The TC02 module is plugged into a carrier module NI-SC-2345, which is connected to the PXI-1031 DC system (embedded controller card NI PXI-8106). A LabVIEW program logs and monitors the measured data from five TCs.

3.4.2 Velocity

A Dantec Dynamics LDV system is used for comparative studies of the fluid velocity. It comprises an optical head (Dantec Dynamics Flow Explorer) consisting of two lasers (650nm @120mW and 730nm @ 120mW), the beam splitters, the Bragg cells, the front lens (300mm focal length) and the receiving optics in backscatter mode. A signal processor with built-in photomultiplier (Dantec Dynamics BSA F60) receives and processes the optical data. A three-axis lightweight traverse (Isel Germany AG) moves the optical head to a distinct place with a minimum increment of 1/80 mm. The laser head is mounted on a plate which can be rotated and fixed at an angular position between $\pm 60°$. The LDV system and the traverse system are controlled with the Dantec Dynamics Flow BSA software installed on a Laptop computer.

Chapter 4

MRV Experiments

This chapter presents experiments within the scope of thermofluid applications that utilize MRV data for the analysis. Two experimental setups were designed and are described. Both have in common that they are associated with forced convection heat transfer and comprise complex internal structures. This makes the flow field measurement challenging with conventional measurement techniques.

4.1 Tetradecahedral Grid

Increasing the performance of modern heat exchangers has two foci: Enhancement of the local convective heat transfer and reduction of flow-induced pressure loss. Hereby, the optimization function is the cost function, which considers the transferred heat over pressure loss. At the same time, heat exchangers face the requirement to be minimized in size. A promising solution is the application of customized internal structures, as for instance open-cell metal foams. In general, these foams are a porous medium, which consist of many cells with either regular/calculable morphology (e.g. Tetradecahedrons) or statistically determined morphology. Internal structures increase turbulence locally, which, in turn, increases heat convection but also pressure loss. Finding the best solution means being able to obtain information about the flow and temperature field inside the heat exchanger.

In addition the heat conduction process inside the struts is important. The porous medium has to be designed so that the heat is transported to regions were the convection is strongest. These are challenging design targets.
Lu et al. (1998) analyze the heat transfer in open-cell metal foams by an empirical model. They estimate that heat radiation at aluminium-based cylinders in turbulent flow is usually one order smaller than heat convection and can therefore be neglected when the temperature is rather low. Natural convection is negligible in metal foams with cell diameters less than 10mm.
Onstad et al. (2011) present an extensive study analyzing a foam comprising stochastic cells as internal structure in future compact heat exchangers. They apply MRV and measure the full 3D3C velocity data in a replica of an open-celled metal foam manufactured in plastic by multijet modeling. As one important parameter for heat transfer they identify the coherence length of streamwise and transverse jets. When a jet impinges on a downstream lying foam ligament heat transfer increases at that position. Throughout the foam a continuous process of fluid impingement on ligaments produces high RMS values in the transverse velocity component and leads to fluid renewal. They achieve a mechanical dispersion coefficient which is based on the transverse displacement of streamlines. Onstad et al. (2011) further calculate the coherence length of jets passing through the cells from power spectra of the streamwise velocity component. They found that 2 cell diameters in streamwise and 1 cell diameter in transverse direction is the typical jet coherence length for the investigated structure. Mixing abilities were analyzed by calculating streamlines and tracking their spanwise and vertical displacement.
Rezaey et al. (2013) compare a foam based on a cubic cell with a foam composed of tetradecahedral (TDH) cells. Both structures had equal strut diameter but different porosities (cubic 0.76, TDH 0.89). They use digital manometers and thermocouples to measure the pressure drop and the local heat transfer characteristics. They observe that the TDH foam has higher average Nusselt numbers and less pressure loss than the cubic structure.

The presented investigations show that heat exchangers composed of foams with more advanced cell structures can have fluid mechanical and/or thermodynamical advantages. By analyzing the internal flow field in such a foam, many features that are an indicator for heat transfer advancement can be worked out. Characterizations achieved by the measurement of integral quantities can be explained in detail by considering the internal flow struc-

ture. This is also the goal of investigations, which were achieved from an interdisciplinary cooperation group with researchers from the Department of Mathematics (Prof. Herbert Egger), the Graduate School of Computational Engineering (Felix Loosmann, M.Sc.) and the Institute of Fluid Mechanics and Aerodynamics (Prof. Cameron Tropea), all associated to the Technische Universität Darmstadt. The following section summarizes these efforts, which were also presented in Wassermann et al. (2014b).

4.1.1 Experimental Setup, Measurement Parameter and Data Quality

Based on the experiments presented in Rezaey et al. (2013), the flow field inside a channel regularly filled with tetradecahedrons (TDH) is measured using MRV and compared to LDV measurements and numerical results conducted with OpenFOAM[1].
The TDH grid (factor 3.94 scaled version of Rezaey et al. (2013)) consists of $3 \times 3 \times 7$ (Y×Z×X) TDH elements, with a strut diameter of 3.94 mm. It was manufactured from PA using direct laser sintering. The grid is held inside a PMMA test section (100×100 mm^2 cross-section and 200 mm length). Fig. 4.1 shows the grid dimensions, the MRV FOVs and the LDV acquisition lines. For appropriate in-flow conditions upstream the test section a converging nozzle and a diffuser as described in Sec. 3.3.4 were applied. A second nozzle is fixed downstream the test section. The hoses that lead the measurement fluid back to the flow supply system can be connected.

Two MRV data sets were acquired, whereby water flow was achieved by the small flow supply system at two flow rates: 62 L/min (termed TDH1) and 32 L/min (termed TDH2). The tank temperature was maintained at 30 °C for both flow rates using an immersion heater. This resulted in Reynolds numbers of 5,000 and 10,000 referred to the bulk channel width.
MRV measurements were conducted at the Siemens Magnetom Tim Trio 3T device. The measurement fluid was deionized water with a Gadolinium-

[1] The CFD simulations in OpenFOAM were performed by Felix Loosmann, M.Sc., Technische Universität Darmstadt.

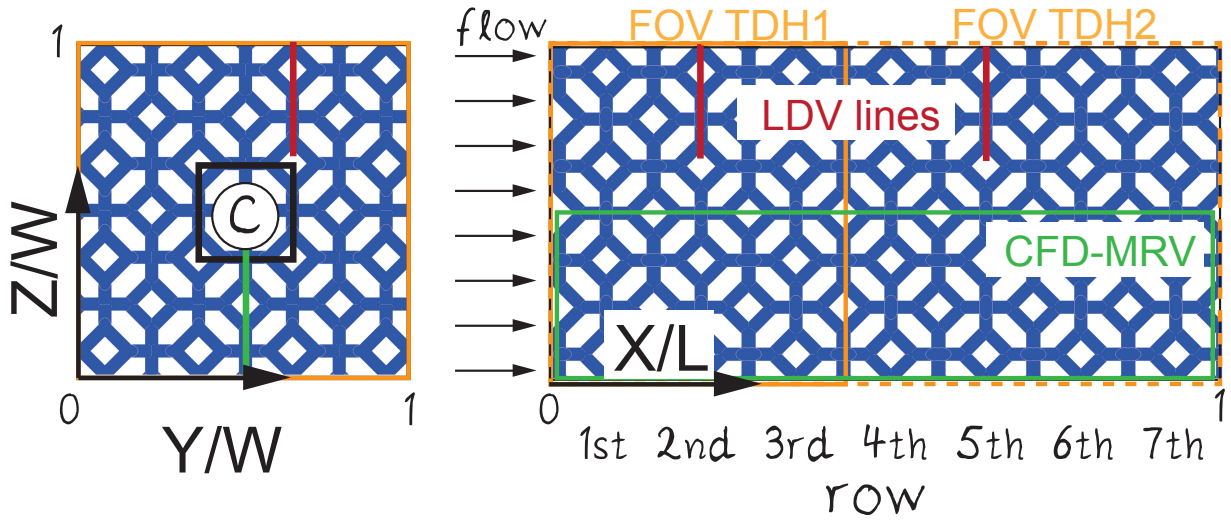

Fig. 4.1: Visualization of the TDH grid showing the coordinate system, the MRV FOVs for TDH1 (orange, solid line) and TDH2 (orange, dashed line), the LDV acquisition lines (red) in rows 2 and 5 and the plane for CFD and MRV comparison.

based contrast agent added. The MR parameter are listed in Tab. 4.1. The acquired FOV of TDH1 covered a large part of the upstream nozzle. Due to strong field distortions at the ends only 3 rows of the TDH grid could be used for data analysis. The FOV chosen for TDH2 covers the entire grid section. Field distortions have to be taken into account in the periphery regions.

The data quality can be assessed by calculating the SNR value from the signal magnitude. Therefore, a histogram plot is displayed for TDH1 in Fig. 4.2. Hereby, the magnitude threshold was set to 100, dividing the signal and the background noise. In the noise two peaks are present which is not typical. A reason for that could not be found. As listed in Tab. 4.1 a $\mathrm{SNR}_{\mathrm{mag}}$ of 15.1 was derived from the magnitude data according to Eq. 2.34. Applying Eq. 2.36 a phase noise of $\sigma_{\mathrm{vel}} = 0.015$ m/s as measure for the velocity uncertainty resulting from the MR setup could be derived. Both values were derived for the TDH2 MRV data and listed in Tab. 4.1, accordingly.

Tab. 4.1: Imaging parameters and MR settings of the MRV measurements both measurements TDH1 and TDH2.

Parameters	**MRV-TDH1**	**MRV-TDH2**
TR/TE [ms]	26.8/4.0	29.2/4.6
flip angle [°]	15	25
pixel bandwidth [Hz/pixel]	457	456
voxel dimension [mm]	1 isotropic	1 isotropic
FExPE lines	288x216	224x168
slices	176	176
channels	21	18
total acquisition time [min]	17	14
averages	3	3
Venc	0.25	0.15
SNR	15.1	14.3
σ_{vel}	0.015 m/s	0.01 m/s

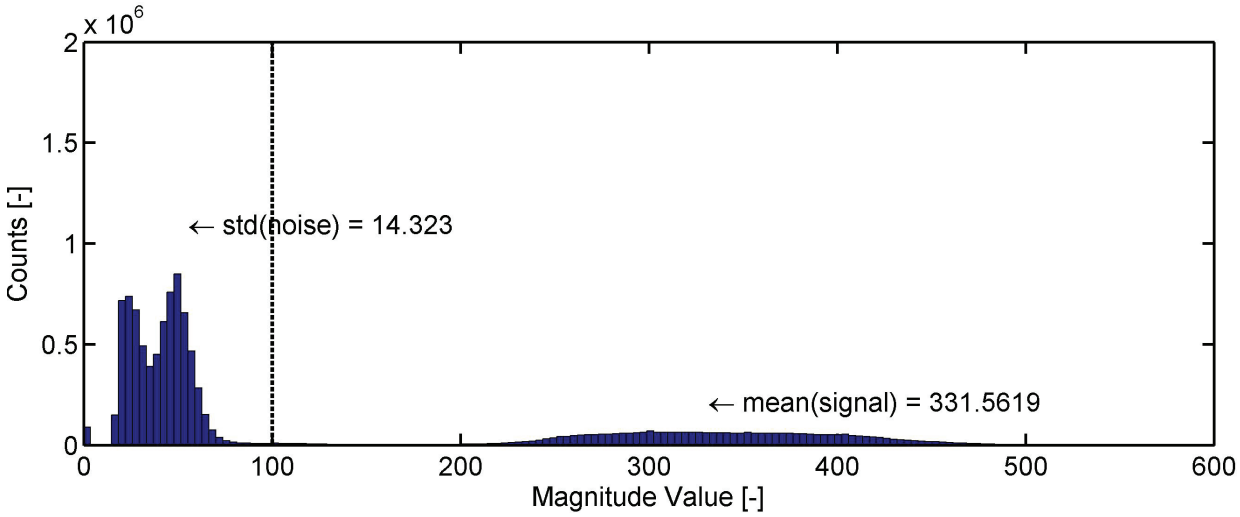

Fig. 4.2: Histogram plot of the signal magnitude of the TDH1 MRV measurement.

4.1.2 Results and Discussion

4.1.2.1 TDH1 Data Set

For reason of better visualization the entire flow field has been reduced to the TDH center element and different graphics displayed in Fig. 4.3. The flow field on the vertical center plane of the TDH center element is depicted in Fig. 4.3 a). Obvious is the development of high speed flow (jets) in parts of the TDH, where strong changes in the cross-sectional area lead to flow acceleration. As the plot begins for a streamwise position of 0, the development of the center jet is visible, which reduces in size and strength with increasing X/L values. With the third row the flow field is fully developed. Additionally, Fig. 4.3 b) depicts the flow field at the border to the neighboring elements. The formation of high speed jets, but also flow recirculations with negative streamwise velocity values, becomes obvious. Characteristic for the TDH structure is a continuous fluid acceleration and deceleration with a regular pattern. The presence of high speed jets evokes high turbulent mixing in the shear layers. The location of the jet is fixed on the center line. Fluid can move through the structure without obstruction. Streamlines depicted in Fig. 4.3 c) that were seeded in the center area show this behavior. In the periphery of the TDH the flow is varying stronger as the jets pass and hit the struts of the following structure. This becomes obvious when considering Fig. 4.3 d). Streamlines have been seeded in the lower left corner of the depicted slice. The streamlines are more compressed and expanded and only a small number remains at $X/L > 0.5$. Streamlines end at a discontinuity or at a stagnation point in the velocity field. Discontinuities are present in a non-smooth velocity field, which is a result of a too coarse resolution. As a consequence, a discontinuity in the velocity field must be due to increased noise or due to a strong velocity gradient between adjacent voxels. Hence, in those regions of the TDH grid where the streamlines abruptly end increased turbulence is expected which is an indicator for increased fluid mixing. This is also expected to be advantageous for heat transfer. In the flow recirculations behind the wakes of the TDH struts it is expected that hot fluid can be trapped. This is not desirable as this can lead to material failure and less heat transfer.

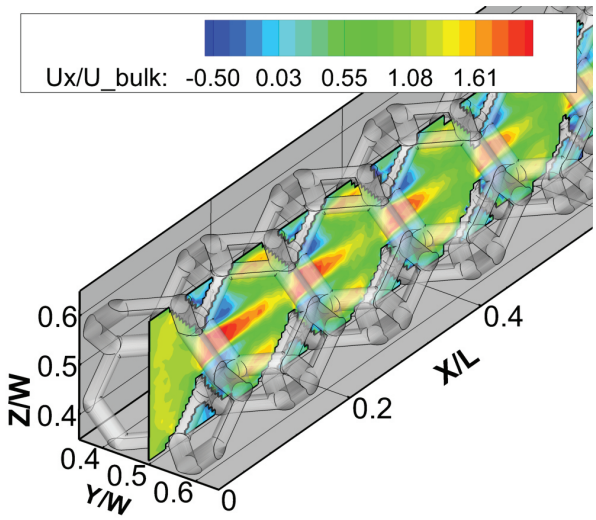

(a) Contour plot on the vertical center plane of the center TDH element showing the streamwise velocity component U referred to the bulk velocity U_{bulk}.

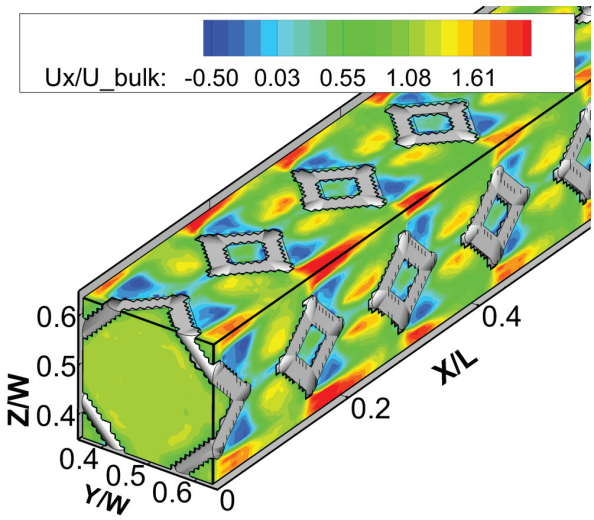

(b) Visualization of the streamwise velocity at border of the TDH center element to the neighboring TDH cells. U is referred to the bulk velocity U_{bulk}.

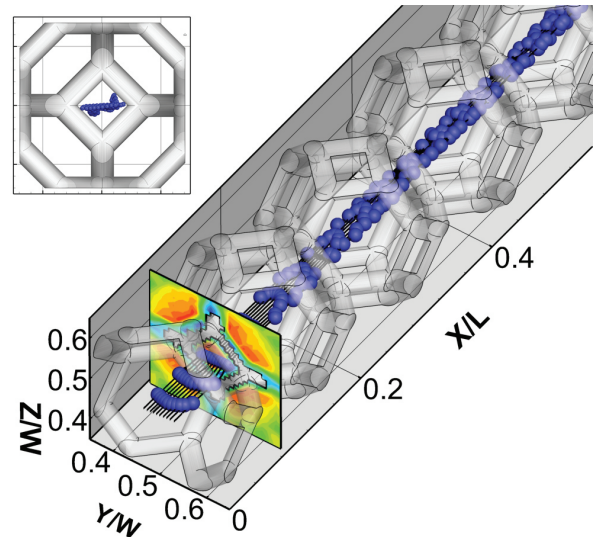

(c) Streamlines seeded in the area around the centerline of the TDH from the depicted slice.

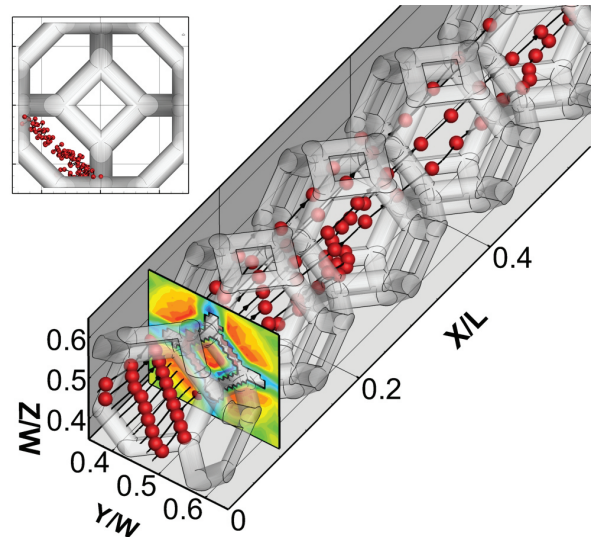

(d) Streamlines seeded in the lower left corner of the TDH element from the depicted slice.

Fig. 4.3: Visualizations of the flow field measured with MRV extracted for the center element of the TDH structure.

For data comparison LDV was accomplished utilizing the system explained in Sec. 3.4. Data was acquired in a wall-near TDH element at two X-direction positions on vertical (Z-direction) measurement lines (depicted

in Fig. 4.1) with 0.5 mm distance between subsequent measurement points. Data was collected for two flow rates (10 L/min and 40 L/min resulting in bulk channel Reynolds numbers of 1,600 and 6,600) and compared to the MRV data set TDH1. The flow rates which are differing from the MRV values where chosen in order to assess the influence of the Reynolds number on the flow development.
For data evaluation Fig. 4.4 compares the average streamwise velocity referred to the bulk velocity acquired with LDV and MRV at different vertical lines shown in Fig. 4.1. Although the flow rates are different and the data was extracted for different rows, the comparison shows good qualitative and quantitative agreement, which means that the flow in this location is independent of the Reynolds number and, thus, fully developed. Different behavior is obvious in the wall-near region ($0.9 \leq \mathrm{Z/W} \leq 1$) for the 10 L/min case. The LDV data shows a higher peak. Due to the low bulk channel Reynolds number the flow is expected to be laminar. This can have a significant influence on the flow development, which seems to be still in a development phase in row 2 for the 10 L/min case.
The flow profiles ($\mathrm{U}_x/\mathrm{U}_{\mathrm{bulk}}$) are equal for the 40 L/min (LDV) and the 60 L/min (MRV) case. It is expected that the flow through the TDH grid is independent of the Reynolds number for the presented velocity region. In addition to that, the LDV data acquired in row 5 shows similar behavior. This implies that the flow is fully developed after row 2 for these Reynolds numbers.

4.1.2.2 TDH2 Data Set

During the project, preliminary numerical calculations (CFD) have been conducted using a SimpleFOAM[2] solver for laminar flow. The simulation was performed by Felix Loosmann for air flow (flow rate = 100 L/min), resulting in a bulk channel Reynolds number of 5,100. Additional MRV measurements were obtained matching this Reynolds number. The resulting TDH2 data set has a comparable Reynolds number of 5,000. The CFD data were calculated only for the lower left quarter (Y/W and Z/W = 0.5) of the channel to save resources.

[2] 'Simple' stands for semi-implicit method for pressure-linked equations.

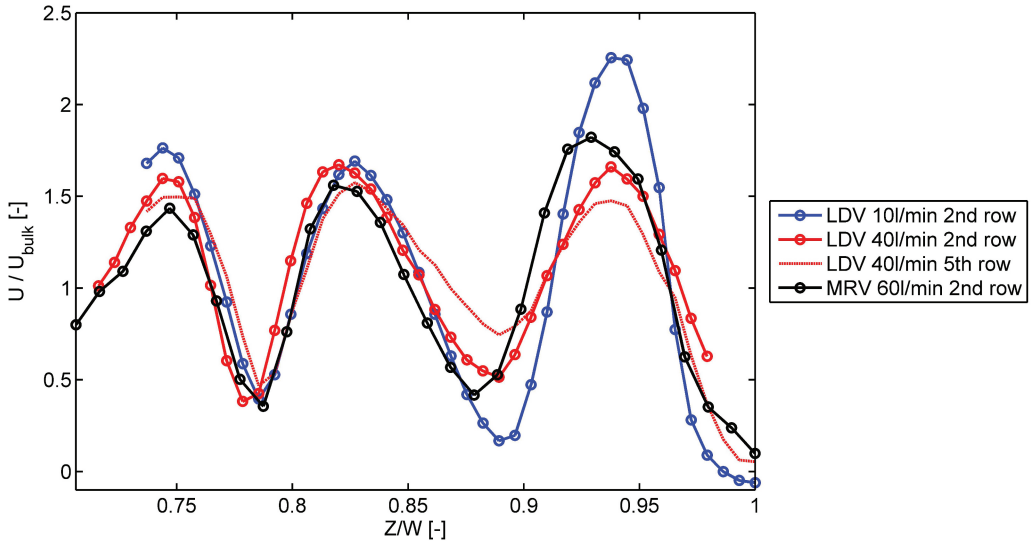

Fig. 4.4: Comparison of MRV and LDV measurements at different positions inside the TDH grid.

Fig. 4.5 shows a comparison of MRV (Fig. 4.5 a)) and CFD (Fig. 4.5 b)). Contour plots of the streamwise velocity field (snap shot for CFD, temporal-average for MRV) with absolute values are presented for the vertical TDH midplane at Y/W = 0.5 marked in Fig. 4.1. The main flow features are similar for MRV and CFD. High speed flow (jets) develop in the center of the TDH element and in parts where the flow is accelerated due to the presence of struts. Downstream of each strut recirculation regions occur with flow reversal. Maximum and minimum velocity values are in good agreement for both data sets. Since the CFD results were calculated for laminar, incompressible and stationary flow conditions the turbulent processes are not considered. It is assumed that the flow development process is different for turbulent and laminar flow. Turbulent CFD simulations have already been conducted but are not considered in this thesis. Further details of the simulations can be found in Wassermann et al. (2014b).

Onstad et al. (2011) conclude that the special flow features in porous media are the source of enhanced convective heat transfer. Especially the formation of high-speed jets impinging on surfaces increases turbulent mixing; hence, heat transfer. The MRV data was used to simulate heat transfer

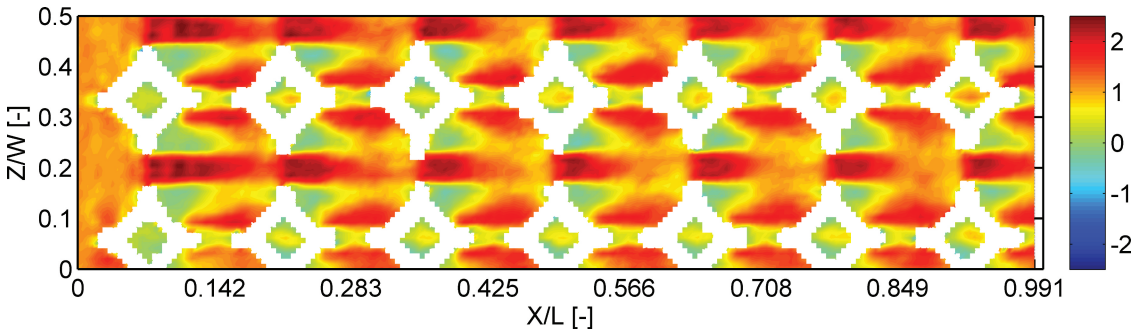

(a) MRV data

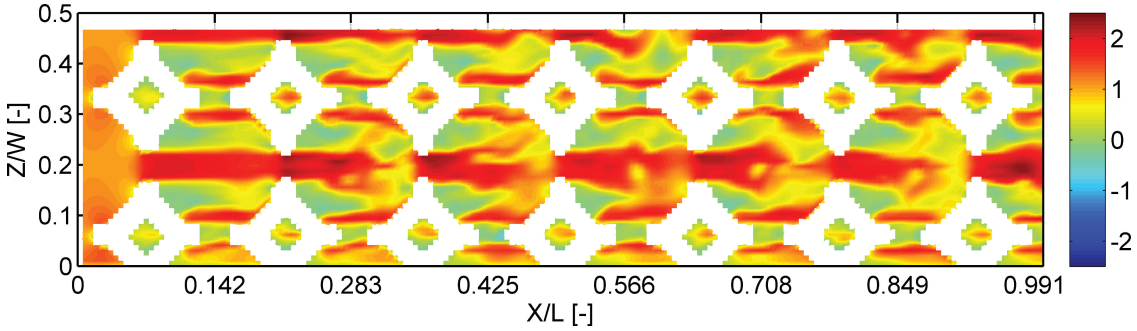

(b) CFD data

Fig. 4.5: Comparison of MRV and CFD: a contour slice plot shows the absolute streamwise velocity value taken for a middle cross section of the halve Y-direction TDH grid. These images are taken from Wassermann et al. (2014b).

according to an approach that was reported before by Elkins et al. (2004)[3]. It is assumed that the velocity field does not alter with temperature changes. This is why the temperature can be treated as a passive scalar and calculated with the conservative form of the energy equation. As a starting condition the struts, the channel walls and the enclosed fluid were set to a constant temperature. Volumetric information about the grid was taken from the signal magnitude exceeding a threshold. For the temperature calculations, flow was applied according to the TDH2 MRV data and the flow inlet temperature was set to a lower value. More details are given in Wassermann et al. (2014b).

The qualitative cooling process within the first second is depicted in Fig. 4.6 for different streamwise positions and time steps. The TDH structure is clearly observable in the derived temperature field. A temperature stratifi-

[3] The heat transfer simulation was performed by Prof. Dr. Herbert Egger, Technische Universität Darmstadt.

cation develops for all time steps. After the first second the cooling process would not be in a steady-state condition. Nevertheless, some important observations can be made. The temperature boundary layer at the channel side walls seems to be in a fully developed state after 0.4s and has a thickness of half a TDH diameter. This also means that no replacement of hot fluid into other areas occurs. For optimal heat transfer a high fluid mixing and fluid renewal at the side walls would be desirable. Obvious in the image at t = 1.0 s and z = 50 mm is the development of the high speed jets, which carry cold fluid through the center of each TDH element. This is also not desirable, since heat transfer into fluid elements moving with the jet can only be accomplished by heat conduction. Notwithstanding the above, the TDH structure shows promising performance, since no other direct passages are obvious.
This approach has not yet been validated, but illustrates how spatially resolved data with access to the velocity field and grid information can be used for additional analysis.
In Rezaey et al. (2013), the performance of the TDH grid was found to be superior to the performance of the simple cubic grid. Especially the friction factor and the pressure drop were found to be lower and the overall Nusselt number was found to be higher. The above presented flow field investigations provide additional insights that revealed basic flow features. This serves as a basis for further research in the field of compact heat exchangers filled with complex structures.

4.1.3 Conclusions

Analyzing the internal flow field in porous media and applying advanced post-processing approaches is a first step in understanding heat transfer processes without needing access to the temperature field. Variations of geometric parameters of the porous medium directly result in flow field alterations, which MRV is capable of measuring. This enables to use the data for integral characterization as well as quantitative analysis of local events.
LDV measurements showed good quantitative agreement to the MRV data. Additionally performed CFD simulations reproduce flow features such as jets or flow recirculation in size and in strength. For future considerations

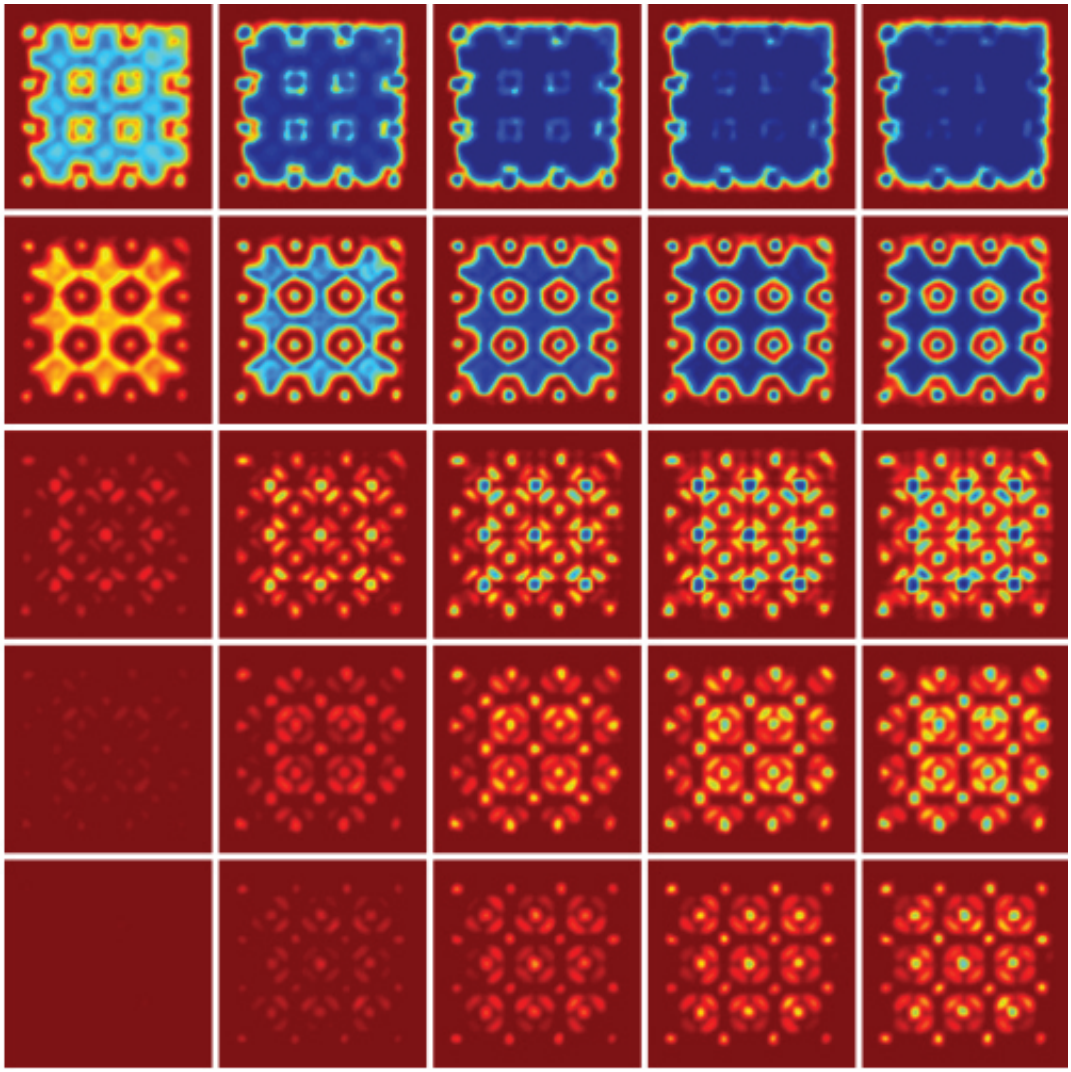

Fig. 4.6: Simulated temperature field depicted for different time steps t = 0.2/0.4/0.6/0.8/1.0 s (left to right) and different streamwise cross-sections z = 10/20/30/40/50 mm (top to bottom), taken from (Wassermann et al., 2014b). In the upper left plot cold fluid enters the hot channel and mixes with the existing hot fluid. In the lower left plot still and only hot fluid is present at z = 50 mm. Following the plots from left to right the evolution over the first second is visible. This image was created by Prof. Dr. Herbert Egger, Technische Universität Darmstadt and presented in Wassermann et al. (2014b).

MRV is able to validate CFD. On the other hand CFD is able to solve the transport equations necessary to simulate the temperature field.
As an innovative approach the heat transfer performance of the TDH grid could be estimated by numerically deriving the temperature field from the

convective energy equation. This was done by combining the MRV data (grid and velocity information) with a finite-element method.

4.2 Fuel Bundle

The following section presents results that were achieved in a joint research project of the Institute of Fluid Mechanics and Aerodynamics, Technische Universität Darmstadt and Canada Nuclear Laboratories (CNL). In thermal hydraulics, the fluid is under high pressure, so that high fluid temperatures near or exceeding the boiling point at atmospheric pressure can be reached without gasification. A typical application is the coolant flow through the primary loop of a water cooled nuclear reactor. One specific design is the CANDU (CANadian Uranium Deuterium) nuclear power reactor. Classified as Pressurized Heavy Water Reactor (PHWR), the CANDU reactor has a unique fuel channel (which contains the coolant) configuration that is horizontal, as opposed to many vertically oriented designs. In the primary loop, the heavy water (D_2O) coolant flows through the reactor core, where thermal energy is produced due to nuclear fission to generate steam in a secondary loop, which drives a turbine.
A CANDU fuel bundle is a cylindrical arrangement of several fuel elements[4] of cylindrical shape with an outer diameter ≈ 10 mm. They are held on both sides by end plates, which keep them in position. The fuel elements and end plates are together referred to as fuel bundle, which is about 500 mm long and 100 mm in diameter. Fuel bundles are inserted into the pressure tube, which in turn is held inside a cylindrical container termed calandria tube filled with the D_2O moderator. This configuration is the CANDU fuel channel. Each fuel element consists of a zirconium-alloyed sheath. Inside it is filled with the uranium dioxide pellets, which produce heat due to nuclear fission. The fuel elements have spacer pads joined on the outer wall keeping the distance between adjacent elements. Additional bearing pads prevent the sheath of the outer elements from touching the pressure tube's wall. A typical CANDU design is a 37-element fuel bundle shown in Fig. 4.7.

[4] The number of fuel elements depends on the specific reactor design.

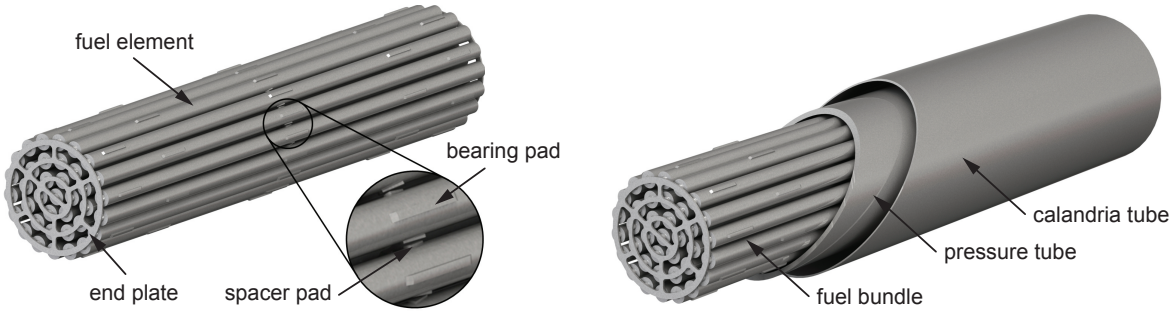

(a) CANDU 37 element fuel bundle showing bearing and spacer pads.

(b) CANDU fuel channel with fuel bundle inserted into the pressure tube held inside the calandria tube.

Fig. 4.7: CANDU configuration was taken from Piro et al. (2015).

The coolant flow led through the pressure tube is mainly influenced and altered by the presence of the fuel bundle. Hence, the flow development in the annulus between the fuel elements, termed subchannels, is of great interest. Especially the development of the velocity boundary layers can lead to a blockage in certain subchannels. This is critical because the redistribution of the flow can lead to a partly decreased supply of coolant to certain fuel elements with a great risk of failure. Additional flow alterations can occur due to obstructions such as the presence of foreign debris (undesired material in the coolant). They can lead to unwanted flow recirculations (potential hot spots) or the production of swirl (increase of pressure loss). In summary, the analysis of the entire flow field of an intact fuel bundle is the basis for further research.
For future CANDU safety considerations, different scenarios are important to investigate. The horizontal arrangement of the reactor core implies that the fuel elements in a CANDU reactor face gravitational forces that are not aligned with axis of the fuel element with an increased potential to deform under load. Under the conditions of a postulated Large Break Loss of Coolant Accident (LB-LOCA), the nuclear fuel can be partly uncooled leading to decreased material strength. Hereby, only certain fuel elements can bend or the entire fuel bundle can conceivably collapse. Although an LB-LOCA has never occurred in A CANDU reactor, this scenario needs further experimental and numerical investigation, which was requested by the Canadian Nuclear Safety Commision (CNSC) (Piro et al., 2014; Piro et al., 2015). With the help of 3D rapid prototyping techniques and bundle deformation simulations, a deformed fuel bundle can be realized and mea-

sured with MRV.
Last but not least the pressure tube can deform due to thermal radiation induced creep. A crept pressure tube has a larger bulk area. Flow bypass can occur, also leading to partly uncooled fuel elements. This can induce the negative consequences as explained with the previous scenarios. Hence, the flow through an intact fuel bundle surrounded by a crept pressure tube is another potential research field. Such a setup can be easily realized by substituting the original pressure tube with a tube of increased inner diameter.

MRV is a suitable method for the investigation of the foregoing fluid flow problems. All scenarios are safety relevant and not sufficiently measurable with other measurement techniques. The results could be used for direct analysis or validation of CFD simulations. This has already been shown for a preliminary experiment, where the entry flow field in a scaled-up replica of an undeformed 8-element fuel bundle was investigated utilizing MRV and CFD by Piro et al. (2015) and Wassermann et al. (2014c). In the following section, further progress within this research project is shown, which is proposed to be helpful for future investigations. The goal is to understand the flow field inside an additive manufactured replica of an intact CANDU bundle. This has been done by utilizing MRV with multiple FOVs.

4.2.0.1 Experimental Setup and Measurement Parameters

The CANDU fuel bundle design was provided by CNL and consists of 37 fuel elements. Each element has a sheath outer diameter of $D_s = 13.1$ mm. The elements are equipped with spacer and bearing pads as depicted in Fig. 4.7. The endplates holding the fuel elements have a thickness of 1.5 mm. The complete bundle has a length of 495.3 mm with an outer diameter of 102 mm. The replica was manufactured in two halves using direct PA laser sintering. At the ends´ of the half elements a tongue and groove was applied, so that both parts could be mated using an adhesive. During the manufacturing process, the sintered parts experience a thermal shrinkage, especially for the in-plane dimension. The final sheath diameter measured with a vernier calliper was $D_s = 12.9$ mm. During a preliminary measurement residues of PA powder were found in the magnitude image at several

positions throughout the fuel bundle. The debris was removed by an additional cleaning procedure.
Like the pressure tube, the current bundle is surrounded by a tube with ID = 102 and OD = 110 mm made of PMMA. Due to the fabrication tolerances, the ID was measured to be 102.5 mm with a vernier calliper. The fuel bundle is axially fixed with a pin attached to the downstream end nozzle. Upstream, the fuel bundle nozzle converges the flow coming from the settling chamber with an ID of 150 mm. Both, the settling chamber and the end nozzle comprise de-aeration holes, which are important to achieve a uniform velocity profile. For flow preparation, a wide-angle diffuser as described in Sec. 3.3.4 is fixed upstream the settling chamber. The entire flow model is depicted in Fig. 4.8.

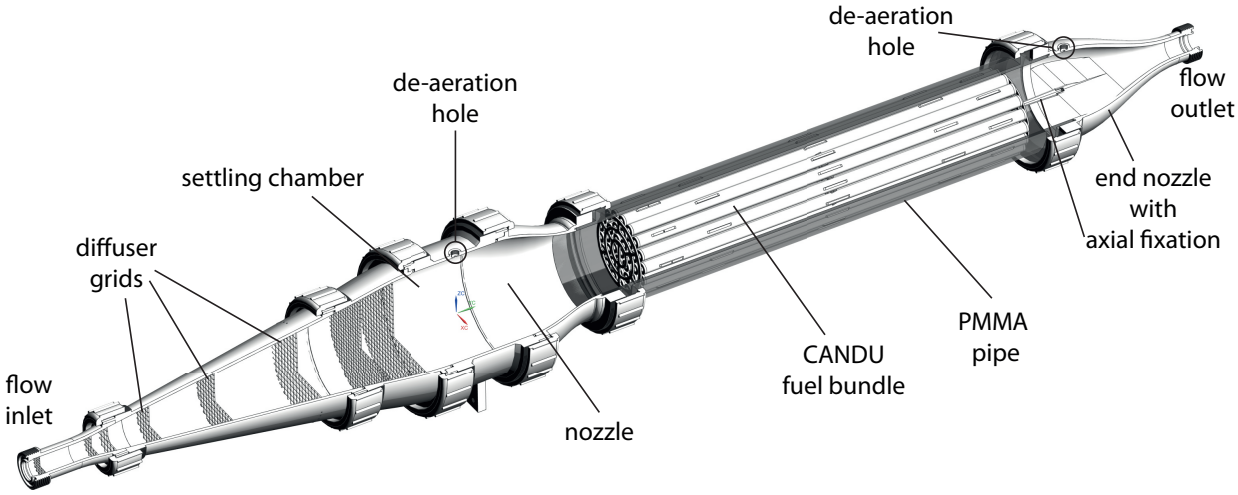

Fig. 4.8: Cross-sectional cut through the CAD drawing showing components and features of the flow model. The CANDU fuel bundle is inserted into the PMMA pipe.

The measurement medium was deionized water with copper sulfate as a contrast agent. The flow was prepared by the large flow supply system and adjusted to 60 L/min. The fluid temperature was kept constant at 21 °C using the Julabo immersion cooler inserted into the water reservoir.
For MRV measurements, the Siemens Tim Prisma system was utilized. Due to the length of the fuel bundle and to prevent image distortions due to the bending of the magnetic field lines, five separate FOVs were acquired with equal MR settings, which are given in Tab. 4.2. For each FOV the patient

table was moved 100 mm by the scanner console and the coils were adapted to the table position. One resulting data set for the complete fuel bundle was composed during post-processing of data resulting from five acquisitions.
Another important point is the voxel size. On the one hand it has to be chosen small enough to sufficiently capture the fuel bundle geometry. On the other hand with decreasing voxel size the acquisition time increases and the SNR decreases. An appropriate value was chosen according to the preliminary experiments performed in Wassermann et al. (2014c).
For background corrections, an additional flow off scan was performed from which the background phase residuals were calculated utilizing Legendre polynomials. The result was then subtracted from the flow on data set.

Tab. 4.2: Imaging parameters and MR settings of the MRV measurements for the CANDU fuel bundle.

Parameters	**MRV**
TR/TE [ms]	36.8/5.2
flip angle [°]	15
pixel bandwidth [Hz/pixel]	445
voxel dimension [mm]	0.8 isotropic
FExPE lines	256x144
slices	144
channels	14
total acquisition time [min]	15
averages	1(2 for FOV 1)
Venc	0.5
SNR	13.1
σ_{vel}	0.03 m/s

4.2.1 Results and Discussion

4.2.1.1 MR Data Consistency

As the data set has been composed of five different acquisitions (FOV1 to FOV5), the data quality and data consistency have to be assessed. At first, a measure for the data quality is the SNR value. The signal magnitude histogram composed of the five FOVs is displayed in Fig. 4.9. For further considerations, a signal magnitude threshold of 60 was chosen because it separates the noise from the signal peak. The threshold is plotted as dotted line in Fig. 4.9. An SNR_{mag} of 13.1 could be derived according to Eq. 2.34. With the help of Eq. 2.36 an estimated velocity error due to phase noise of $\sigma_{vel} = 0.03$ m/s can be given. Both values were already given in Tab. 4.2.

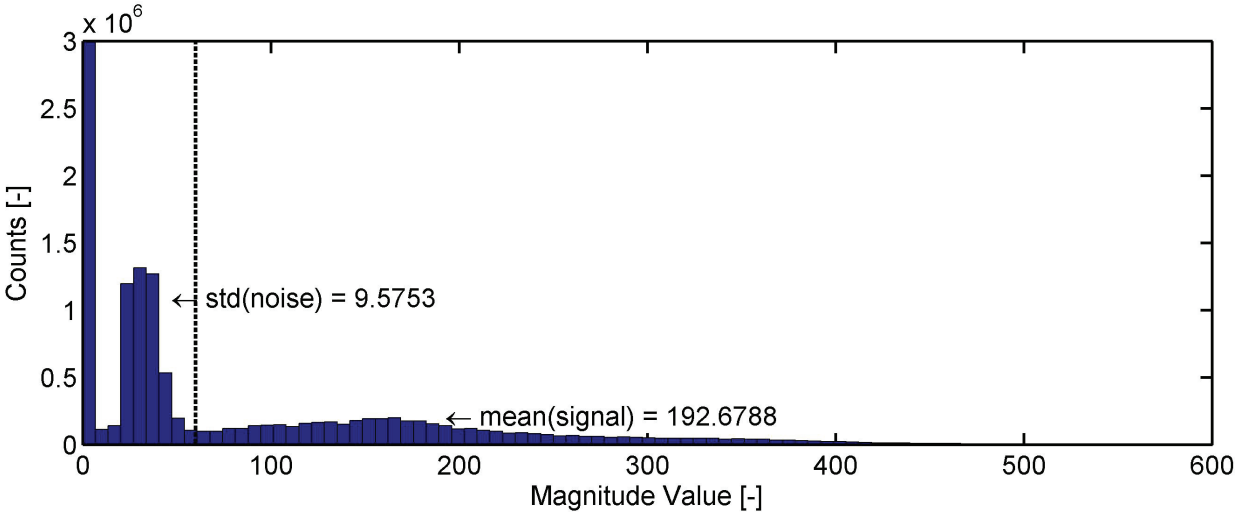

Fig. 4.9: Histogram plot of the signal magnitude taken from the entire MRV data set for FOV1 to FOV5.

Another way of assessing data consistency is the cross-sectional integration of different quantities. The cross-sectional flow-through area can be integrated by utilizing the signal magnitude. Therefore, all voxels (each voxel has an area of 0.8×0.8 mm^2) per cross-section were summarized, which have a signal magnitude value higher than the chosen threshold of 60. The sum resembles the flow-through area. The result is shown in Fig. 4.10. The

cross-sectional integrated flow-through area is compared to the calculated bulk pressure pipe area ($A_{bulk} = \pi \mathrm{ID}^2/4$) and the calculated flow-through area ($A_{bulk} - 37\pi \mathrm{D}_s^2/4$[5]).

Fig. 4.10 a) shows that the integrated flow-through area is very constant throughout the entire fuel bundle and in the upstream part. Distortions arising from bending B_0-field lines or gradient fields outside the iso-center, which lead to a relative decrease of the cross-sectional area towards the FOV´s ends could be avoided by applying the distortion correction for the FE-PE-plane. Additionally by reducing the FOVs to 100 mm in the streamwise direction, effects arising from the through-plane distortion (SS-direction) could be minimized. Only for FOV1 and FOV5 a small reduction of the integrated flow-through area towards the ends is detectable.

Affecting all FOVs, the integrated flow-through area is biased compared to the calculated flow-through area. One explanation for that could be the rough and porous surface of the laser-sintered PA elements. The measurement fluid enters the first 0.2 mm of the fuel elements´ surface. The MR sequence also detects voxels that are only partly filled (typically with a decrease in the magnitude value). As the smallest distance between neighboring elements is 1.8 mm and the chosen resolution would only yield 2 voxels within that distance, the detection of an additional voxel would noticeably increase the area and, hence, lead to such a global offset.

Reductions of the integrated flow-through area due to the presence of spacer and bearing pads are only partly recognizable. In some Z-positions, a small reduction is visible in Fig. 4.10 a) at the beginnings and ends of the bearing pads. Due to their relative size they do not affect the integration, whereas they are clearly visible in the magnitude plot shown in Fig. 4.10 b2).

A non-physical behavior is obvious for Z $\approx$ 320mm (streamwise middle position in FOV3). A sudden increase in the flow-through area is present. This is caused by water ingestion between the groove and tongue. As it was impossible to remove remaining adhesive from the mating surfaces of the inner fuel elements, glue was applied only sparsely. Hence, measurement fluid could enter the voids, which was detected by the scanner. This part should be left unconsidered for velocity integration or averaging, whereas the velocity vectors measured in the flow-through area are presumed to be unaffected.

A decrease of the integrated flow-through area is visible towards the ends of FOV2 and FOV4. The reason for that becomes obvious when consider-

[5] This equation is an approximate that does not consider geometric feature like the bearing and spacer pads or the end plates.

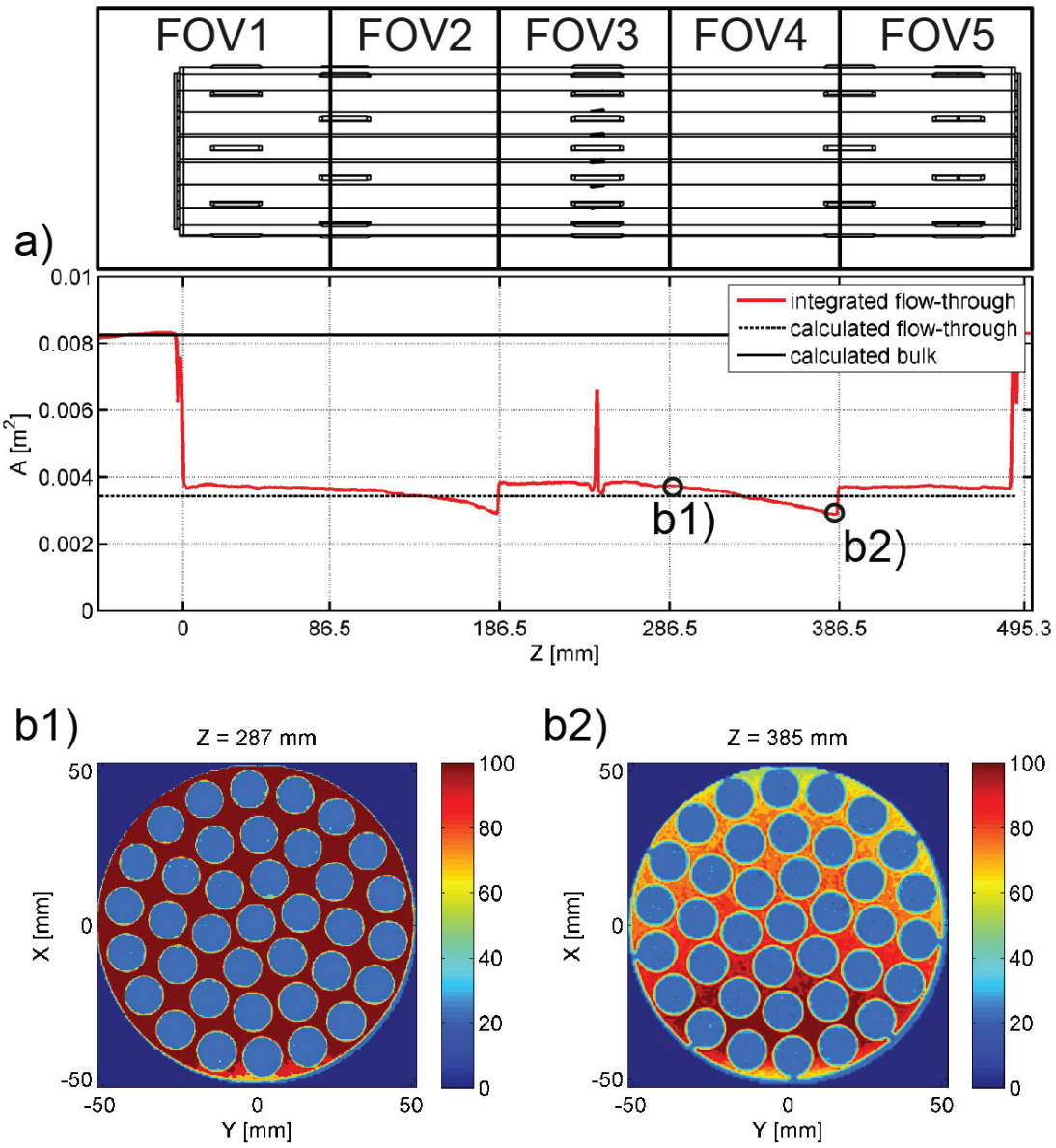

Fig. 4.10: a) Cross-sectional integrated flow-through area, calculated flow-through area and bulk pressure pipe area. The five FOVs are marked in the CAD sketch displayed at the top of the image. b1) and b2) show contour plots of the signal magnitude at two Z-locations marked with ◯ in the area plot.

ing the magnitude contour plots depicted in Figures 4.10 b1) and b2) for the two marked Z-locations. In Fig. 4.10 b1) the magnitude is evenly distributed with values > 100. Only at the bottom and in the vicinity of the fuel elements a decrease below a value of 100 is obvious. In Fig. 4.10 b2) the magnitude drops below 100 for a vast majority of the voxels. At the top the

values even decrease below the threshold of 60. Hence, these voxels are not considered for the flow-through area integration. The reason for the partial signal loss are insufficiently chosen receiver coil channels. Prior to the measurements, the surface coils had to be positioned and fixed above the flow model. This is important to gain adequate MR signal. For each FOV, the patient table was moved 100 mm so that each FOV was positioned in the scanners´ iso-center. In order to gain sufficient signal, only the covering channels directly above or below the FOV part had to be toggled on. This was done manually and, in case of FOV2 and FOV4, the correct channels could not be selected due to the coil position. This implies that the magnitude data as well as the velocity data have to be considered carefully in those regions. A decreased signal magnitude with unchanged noise results in an increased phase error and, thus, an increased velocity uncertainty. The described signal decrease towards the ends of FOV2 and FOV4 may also corrupt the local velocity values.

For this reason and to show data consistency of the velocity data, the cross-sectional averaged velocity components U_X, U_Y and U_Z (streamwise component) were computed, as well as the cross-sectional integrated flow rate. The results are displayed in Fig. 4.11, whereby the flow rate is compared to the adjusted flow rate by the flow supply system.
At first, in Fig. 4.11 a) the cross-sectional average of the cross-stream components (X- and Y-direction) are considered. Both components are balanced around zero. This means, that the inflow was well conditioned and that the applied background phase correction was done properly, which also affects the U_Z-component.
Secondly, Fig. 4.11 a) shows the progress of the cross-sectional averaged streamwise velocity component U_Z, as well as the overall average (dashed line). This is an important test showing data continuity. The cross-sectional average and the overall average agree over a wide range of the Z-coordinate. Similar behavior as shown in Fig. 4.10 a) for the flow-through area is obvious for FOV2 and FOV4, where the cross-sectional average increases towards the ends. Therefore, Figures 4.11 b1) and b2) show contour plots of the streamwise velocity component at Z = 385 mm (last slice of FOV4) and Z = 387 mm (second slice of FOV5). It is obvious, that for Fig. 4.11 b1) the fuel elements appear larger in diameter compared to Fig. 4.11 b2), which is physically not possible as each bundle half was manufactured in one process. For Fig. 4.11 b1) the gaps between neighboring elements are smaller and the

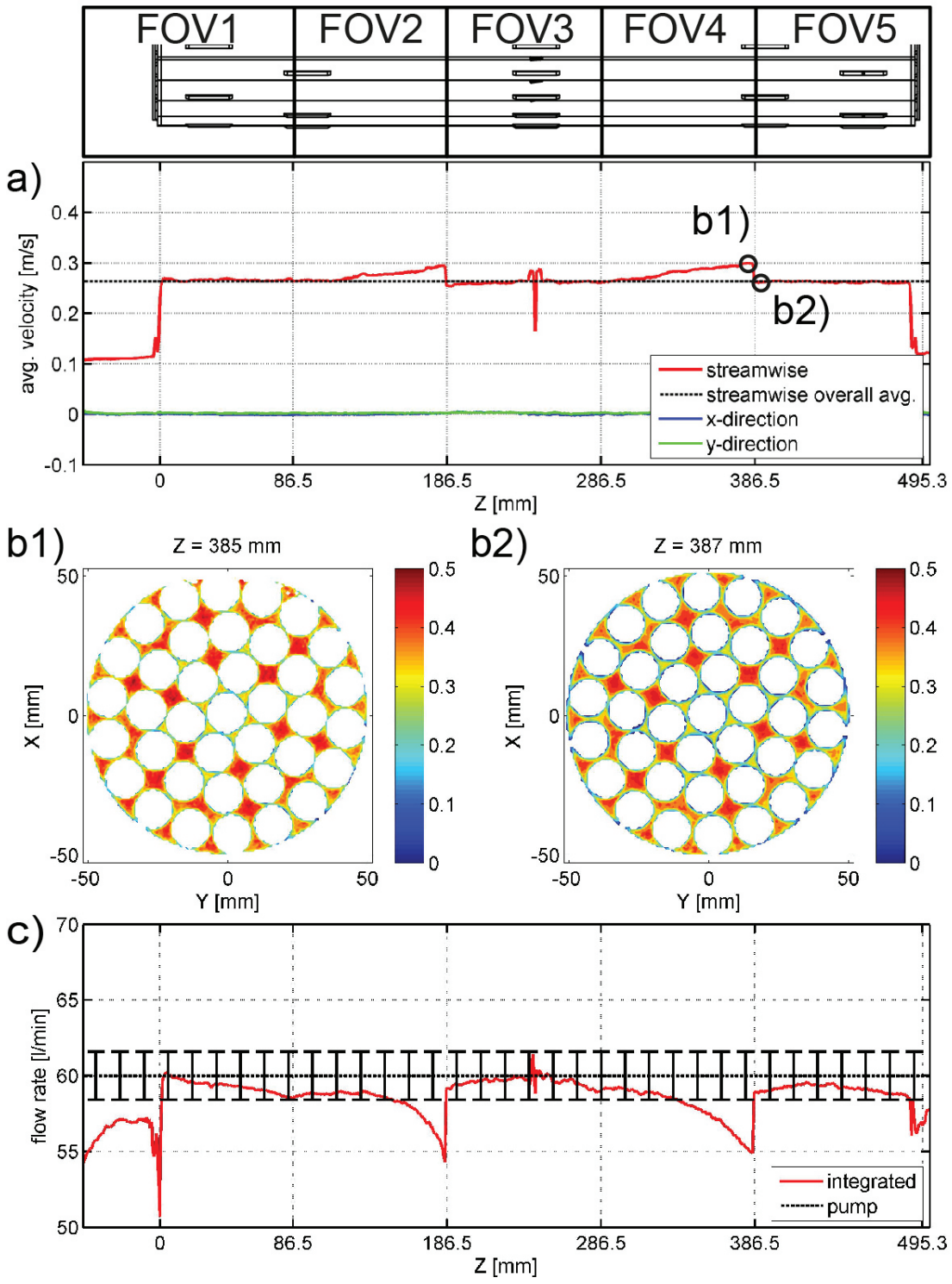

Fig. 4.11: a) Cross-sectional averaged velocity components in X-, Y- and Z-direction (streamwise). Additionally, the overall average of the streamwise velocity component is displayed (dashed line). b1) and b2) show contour plots of the streamwise velocity U_Z at two Z-locations marked with ◯ in plot a). c) Cross-sectional integrated flow rate and flow rate provided by the flow supply system. The five FOVs are marked in the CAD sketch, which shows a side-view of the halve CANDU bundle.

boundary layers do not appear. Due to the drop in the signal magnitude, partial volume artifacts increase in strength. This means, that voxels partially containing measurement fluid and solid material produce less signal magnitude and, thus, fall under the chosen signal magnitude threshold. This also explains the increase of the cross-sectional average of U_Z illustrated in Fig. 4.10 a) for FOV2 and FOV4. The voxels adjacent to the walls typically have smaller velocity values as they coincide with the velocity boundary layer. If these voxels are excluded, the average of U_Z increases. Nevertheless, the local velocity values look equal for both contour plots, which means that MRV did not acquire incorrect values. The improper coil adjustment affects the signal magnitude and the acquired voxels likewise.
Fig. 4.10 c) shows the integrated flow rate compared to the flow rate provided by the flow supply system (denoted by pump). Good agreement is found and the integrated flow rate lies within the error bars (taken from Tab. 3.4) over a wide range of the Z-coordinate. A small underestimation is obvious, which corresponds to the bias discussed for the integrated flow-through area depicted in Fig. 4.10 a). The flow rate decrease towards the ends of FOV2 and FOV4 is less pronounced, as the drop of the integrated flow-through area and the rise of the averaged streamwise velocity component work against each other. A non-physical drop of the flow rate occurs in the middle section of FOV3, which was already discussed above. Additionally, when the flow passes the end plates the flow rate also decreases. This effect is based on improper resolution and the strong flow acceleration. For further flow rate considerations these areas should be ignored.

4.2.1.2 Results - Integrative Measures

The CANDU fuel bundle consists of 37 fuel elements, which are concentrically aligned around the center element in three rings. The space between neighboring elements is termed a subchannel, through which the coolant is flowing. For good convective heat transfer high turbulence, small velocity boundary layers and a high convection speed are advantageous. By subdividing the fuel bundle into four concentric subchannel rings and calculating the cross-sectional averaged streamwise velocity and the cross-sectional integrated flow rate insights about the flow distribution can be achieved. Fig. 4.12 a) shows the four subchannel rings with the values for the outer diameters in millimeter. Each ring has a certain color (red, light blue, green

and dark blue), which is used to mark the corresponding graphs in Figures 4.12 b) and c). Z-positions highlighted with light orange have to be considered carefully, due to abnormalities in the acquisition process.
In Fig. 4.12 b), the cross-sectional averaged streamwise velocity relative to the overall average of the streamwise velocity (in the following termed bulk velocity) is depicted for the four calculation areas. Throughout the fuel bundle, the cross-sectional average of U_Z is equal to the bulk velocity for the light blue area, is slightly exceeding the bulk velocity for the green area and slightly below the bulk velocity for the dark blue area. All three start with the same value at Z = 0mm. Afterwards the dark blue graph is decreasing and the green increasing. Just after the streamwise center position, where the strongest cross-section obstruction due to spacer and bearing pads is present, the light blue, green and dark blue graphs are leveled again and the progress repeats for the second half of the fuel bundle. Hence, the strong obstruction beginning at Z $\approx$ 235 mm leads to a velocity re-distribution, which is positive for the areas A2, A3 and A4. Interesting is the progress of the red graph resembling the average streamwise velocity of A1 around the center element. It becomes clear, that the streamwise velocities decrease throughout the fuel bundle. An explanation for that is the increasing thickness of the velocity boundary layers, which increasingly obstruct the subchannels of A1. In addition, these subchannels are smaller then in the other rings. This acts negatively on the cooling of the center element.

In combination with that the cross-sectional integrated flow rate, relative to the overall flow rate value is plotted in Fig. 4.12 c) for A1 to A4. For sake of completeness, the flow rate values of A1 to A4 are summarized and displayed as the dashed line, which lies around 100%. Approximately 40% of the flow rate passes through the green area (A3) that also has the highest value. Following is A4 with $\approx$30%, A2 with $\approx$20% and, finally, A1 with $\approx$10%. The graphs show a similar behavior as discussed for the relative cross-sectional averaged streamwise velocity.
Another interesting point is obvious for Z $<$ 0 mm. The red, light blue and green curve start with a drop in the flow rate over the front end plate, whereas the dark blue curve experiences a rise. This is due to the sudden cross-sectional area reduction, starting with the front end plate, where the flow has to evade the downstream obstruction. For A1 to A3 the flow has to funnel through the small segments of the end plate. On the pressure pipe wall upstream of the fuel bundle a significant velocity boundary layer has

developed. Hence, the flow can evade into these regions and reduce the velocity boundary layer. This is also the reason why the flow rate increases for A4 just downstream the front end plate.

A general conclusion from the presented results is that all subchannels are able to communicate with each other. With appropriate passive flow control devices (e.g. vanes) a redistribution of the flow is possible. For the given CANDU fuel bundle this is already achieved by the spacer and bearing pads. Critical is the flow through the center area A1 and around the center element. The average streamwise velocities are up to 30% lower than the bulk velocity. When assuming constant material properties, this also implies that the local Reynolds number decreases. This can lead to a reduction of flow turbulence or even flow relaminarization, which would lead to a decreased cooling.

4.2.1.3 Results - Flow Field

The distribution of the streamwise velocity component U_Z for different streamwise positions is shown in Fig. 4.13. The streamwise positions can be allocated to the features of the CANDU bundle as depicted in Fig. 4.10 a). Starting with Z = -10 mm, the flow upstream the front end plate is very homogeneous with a small boundary layer at the pressure pipe wall. For Z = 10 mm, a flow field has developed in each subchannel, where the maximum velocity values are present in area A1. In all other areas, U_Z is more evenly distributed. Only small boundary layers surrounding the elements and at the pressure pipe wall are visible (size of a voxel or less). Effects resulting from the obstruction of the front end plate are still observable in the flow field. Following the slices further downstream (Z = 50 mm, Z = 100 mm and Z = 200 mm), the maximum velocity values increase in the areas A2 to A4 and decrease in the area A1. This behavior was already observed in the section before. The maximum velocities are not evenly distributed as for Z = 10 mm. In some subchannels, higher U_Z values develop as in other sub channels. Concurrently, the boundary layers increase in size. At Z = 250 mm, the maximum streamwise velocities in the entire flow field develop which is caused by the minimum cross-sectional area that is reached due to the presence of the spacer pads. As shown above, the spacer pads are ap-

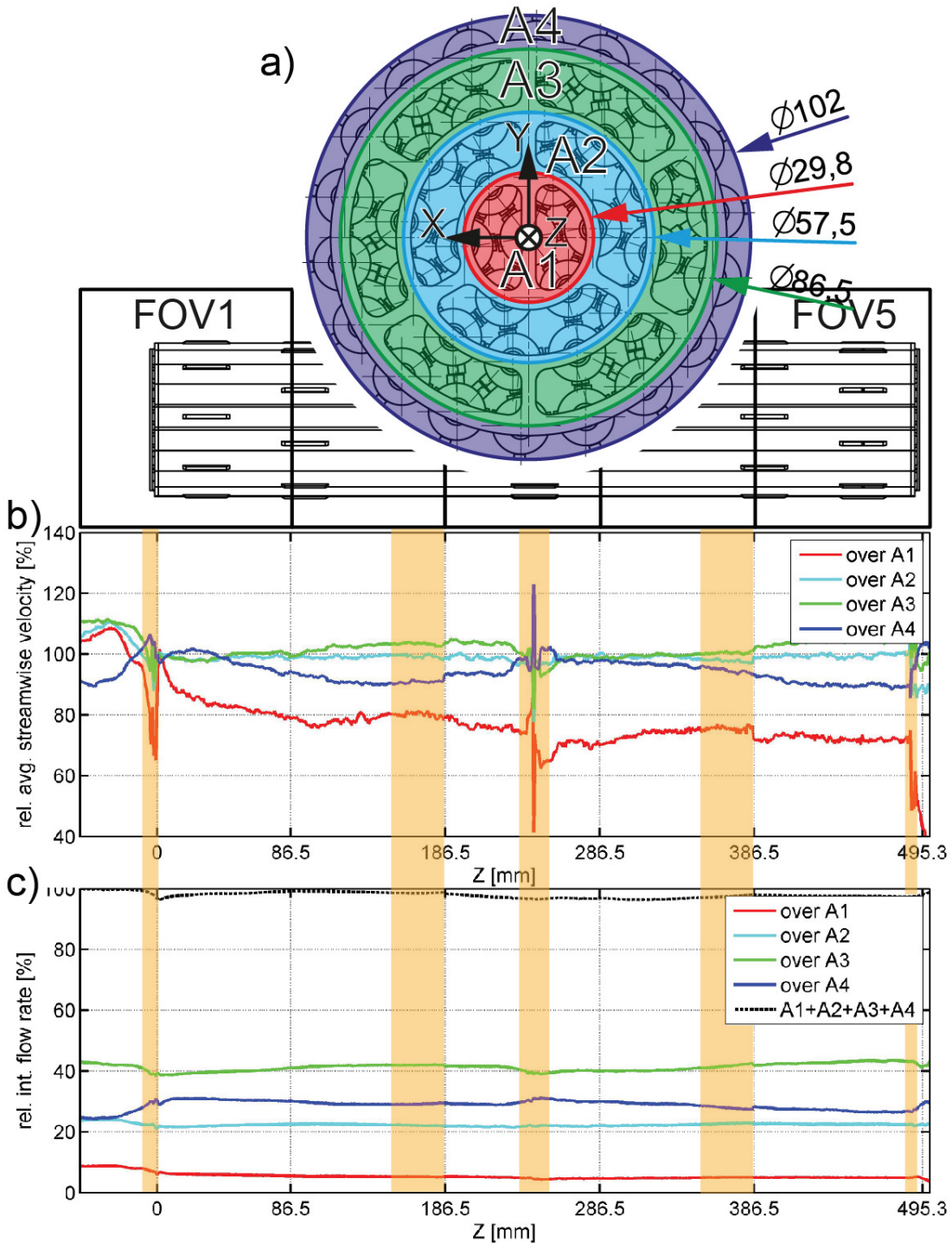

Fig. 4.12: a) Front view on the CAD drawing of the CANDU fuel bundle depicting the four subchannel integration areas. b) Cross-sectional averaged streamwise velocity relative to the overall average of the streamwise velocity derived for the four color-coded areas marked in the sketch above with A1 to A4. c) Cross-sectional integrated flow rate relative to the total flow rate derived for the four color-coded areas marked in the sketch above with A1 to A4. The dashed line marks the sum of the flow rates over the four areas. Marked in light orange are the Z-positions which have an increased error.

plied at the half length of the CANDU fuel bundle. Additionally, the form of the spacer pads induces a deflection of the main flow in the radial and angular direction. These effects are observable in the cross-stream velocity components.

As the CANDU fuel bundle has a certain rotational symmetry, it is valuable to transform the cross-stream velocity components into a radial velocity U_R and an angular velocity U_Φ. This enables the observation of a redistribution in the R-direction that is associated with fluid movement from one area A1 to A4 into the neighboring area. With U_Φ a swirling motion or a fluid movement within a subchannel ring is identifiable. Fig. 4.14 depicts different contour slices showing the U_R and U_Φ fields for critical Z-positions before and after the front end plate and during the presence of the spacer pads. The displayed coordinate system gives the direction for U_R and U_Φ. For Z = -5 mm the U_R plot shows that the flow is deflected by the front end plate and the presence of the fuel bundle. The radial redistribution of the flow is maximum for area A4 in the positive R-direction. This redistribution was already observed in the previous section for the flow rate integration over area A4. The radial movement in the negative R-direction is only slightly visible. In addition to that U_Φ depicts the deflection produced by the radial struts of the front end plate. The angular deflection is much weaker than the radial deflection. The contour plots for Z = 5 mm show the strong interaction between the radial subchannel rings. The radial velocity is a maximum right after the small gaps of each ring. Like before, the radial movement in positive R-direction is stronger than the negative one. Examination of the U_Φ plot for this Z-location shows that high angular velocity values are only present where the radial struts are located upstream. Another critical Z-location was the region where the spacer pads are installed, which corresponds to Z = 242 mm. Again, strong radial movement especially from A3 to A4 and A1 to A2 is present. At positions where spacer pads are present and the streamwise velocity value is high, increased angular movement is observable. This is mainly present in the third ring (area A3).

The last important critical location is the out-flow profile on the downstream end of the CANDU fuel bundle. In the pressure tube of a CANDU reactor core one fuel bundle follows the next one in a row without an axial gap between two subsequent end plates. This is not simulated in the present

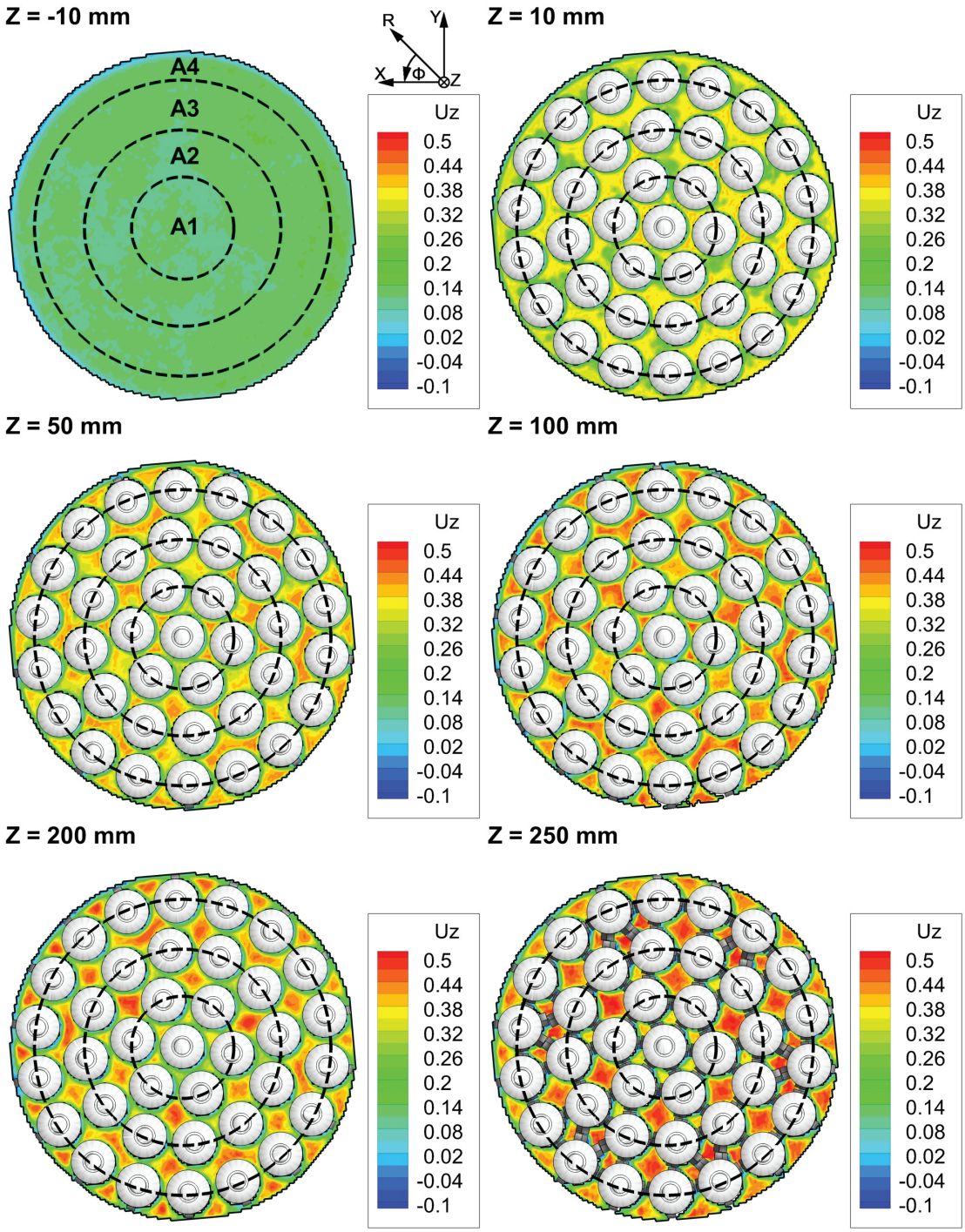

Fig. 4.13: Contour slice plots of the streamwise velocity component U_Z for different Z-positions. The dashed concentric rings symbolize the center line of the rings of the front end plate. Additionally, they segment the cross-section into the four integration areas A1 to A4. The fuel elements are displayed as original CAD model.

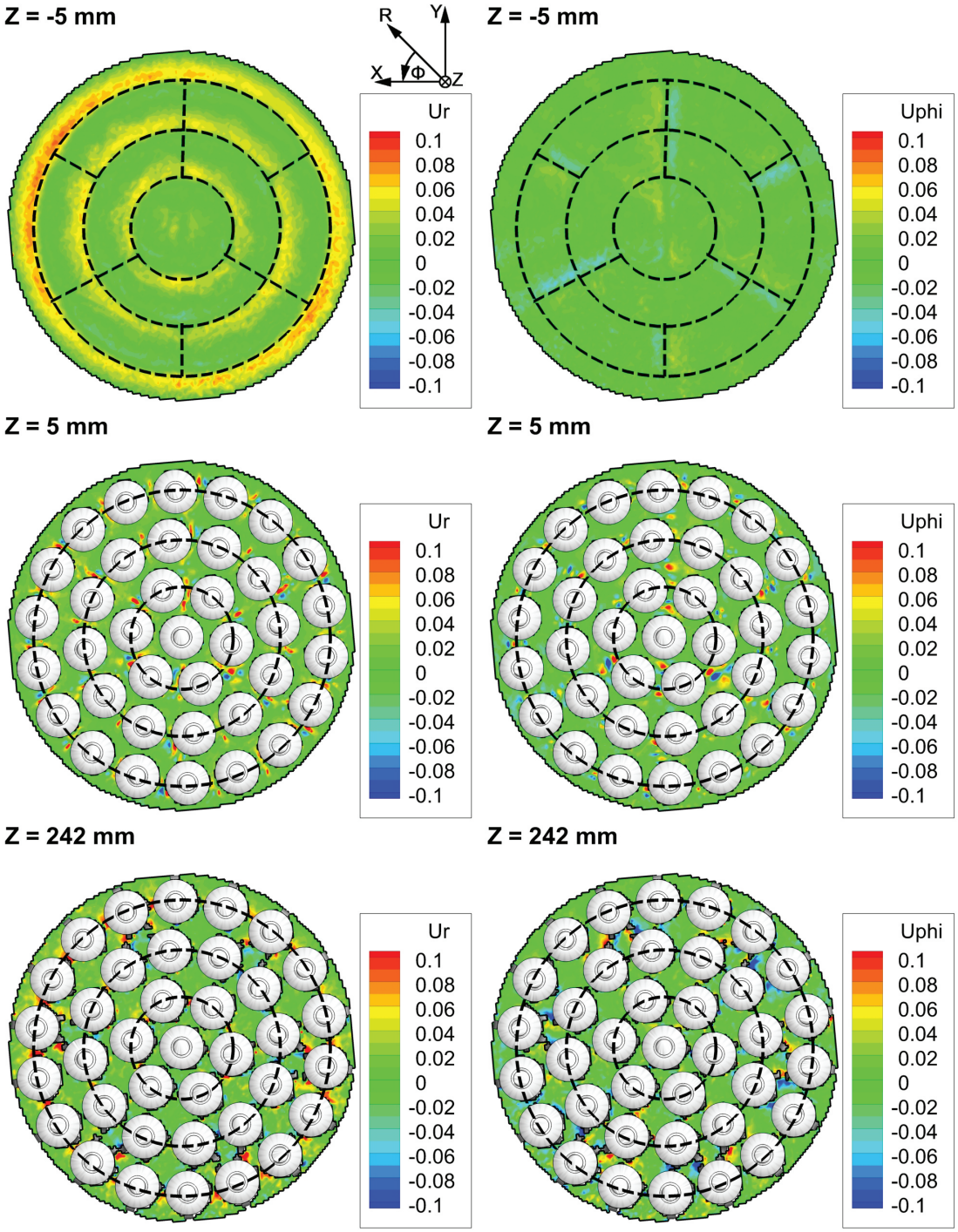

Fig. 4.14: Contour slice plots of the radial velocity component U_R and the angular velocity component U_Φ for different Z-positions. The dashed concentric rings symbolize the center line of the rings of the front end plate. Additionally, they segment the cross-section into the four integration areas A1 to A4. The dashed radial lines show the presence of the front end plate struts. The fuel elements are displayed as original CAD model.

study. Nevertheless, an impression of how the exiting flow field would look like is depicted for Z = 500 mm in Fig. 4.15 for the streamwise velocity component. Behind the radial struts of the exit end plate large wakes with recirculating fluid are present. Additionally, jets with high speed fluid develop from the subchannels of areas A2 to A4. In comparison to that, the velocities in the center area A1 are low.
One critical result of such a flow profile would be flow structure interactions. As the downstream following fuel bundle is not angularly aligned with the foregoing fuel bundle, a very complex flow deflection would be present. This could lead to increased mechanical loads on the front end plate and fuel element heads.
Another potential scenario resulting from the uneven out-flow profile and the complex interaction with the entry region of the downstream fuel bundle would be the undersupply of certain subchannels with coolant flow. As shown above, a fluidic interaction between the subchannels in angular and radial position is possible. Nevertheless, the redistribution of coolant in radial direction is not very intensive. As a worst case, and in conjunction with increasing boundary layers across the fuel bundle length, a blockage of subchannels could be the result. The fuel elements in these subchannels would suffer from insufficient cooling as the flow rate does not change significantly over the subchannel rings. The possibility of this scenario could be increased if debris or other unwanted material would present in these subchannels.
Especially the center area A1 is a candidate for coolant undersupply. As discussed above, this region only deflects flow rate to the next subchannel ring over the bundle length. A downstream lying fuel bundle fed with the reduced flow rate of A1 would certainly not recover the full flow rate. Too low coolant renewal or even blockage would be the result. Insufficient cooling of the center element and the surrounding ones leads to higher thermal and mechanical loads.
Due to the horizontal arrangement, the fuel bundles face gravitational loads over the entire length. In combination with increased thermal loads resulting from improper cooling and leading to non-uniform material properties, the advancement of bundle deformation processes is possible. Under these circumstances even more critical events could be evoked, as discussed in the introduction part of this section.

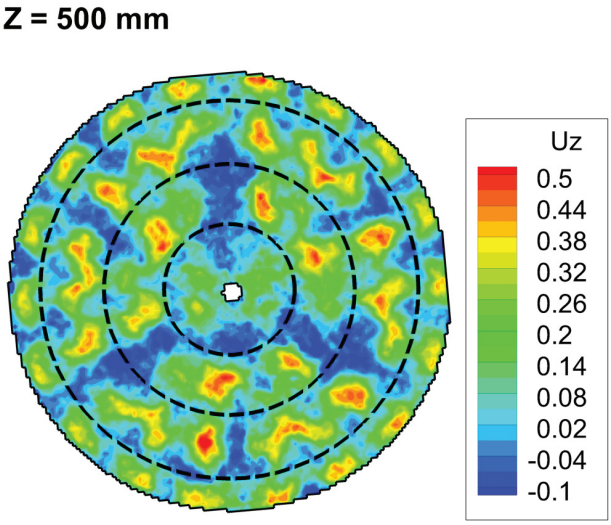

Fig. 4.15: Contour slice plot of the streamwise velocity component U_Z for Z = 500 mm. The dashed concentric rings symbolize the center line of the rings of the front end plate. Additionally, they segment the cross-section into the four integration areas A1 to A4. The dot in the middle shows the axial fixation pin.

4.2.2 Conclusions

Summarizing all the above mentioned observations shows that the flow field of a CANDU fuel bundle is very complex and mainly affected by the structure itself (end plate, spacer pads) or by fluid mechanic nature (boundary layer development). Potentially critical points could be worked out by deriving integral values and by observing the overall development of the flow field. This novel approach was only possible due to the 3D3C nature of the MRV data. Other critical regions in the flow that were pointed out are important for future safety considerations and justify additional research in this field.
MRV provides data with sufficient resolution. Additionally, they are achieved in an excellent acquisition time. Using complex flow models also increases the error proneness. As explained above, in a preliminary measurement undesired PA powder residing in subchannels was detected and finally removed. Although this "human factor" due to improper cleaning is correctable, it is hard to detect if optical access is limited. This inspection is even more important for future projects investigating a deformed fuel bundle. Parts of the FOV which showed improper signal behavior could

be detected. The background phase correction using Legendre polynomials applied on the flow off-scan showed good results and prevented a decrease in SNR, which would be obligatory when using the standard subtraction method.
By slight modification of the existing setup, proposed scenarios like the crept pressure tube are easily implemented for further research.

Chapter 5

MRT Experiments

This chapter presents experiments utilizing MRT. It starts with a short review on thermofluid applications which are suitable for further investigations. Then preliminary experiments are presented, which were conducted to explore the possibilities and limitations of MRT. Finally, the double pipe experiments are presented and a detailed discussion on the applicability of MRT is provided.

5.1 Review on Selected Thermofluid Applications

5.1.1 Mixing of Fluids

Mixing of fluids occurs in many natural as well as in technical environments. In this context mixing is understood to be the fusion process of two or more single-phase fluids with different physical properties, such as temperature or density. Not considered here is the mixture process of multi-phase flows. In this review, the mixing process of two fluid streams is discussed, which can subdivided into the mixing of two parallel aligned flows or the injection of a secondary flow into a primary flow at a certain angle. The presented literature review to this topic was prepared with the help of Kiekebusch

et al. (2015).

Considering the mixing of a primary flow at a low temperature with a secondary flow at a higher temperature and oriented perpendicular to the primary flow direction leads one to the heating, ventilation and air-conditioning unit (HVAC) in cars and other vehicles. Fresh air from the outside is pressurized by a fan and led to an evaporator, which cools and dehumidifies the air. Afterwards the cold air flow is divided by an air-mix valve and partly led through a heater core, which heats the air to 80 °C. In the area downstream the hot air impinges perpendicular onto the bypassed cold air and strong turbulent thermal mixing occurs. In literature this mixing process is simulated in a test channel termed T-junction, which comprises a primary rectangular channel with cold flow and perpendicularly oriented rectangular channel (also termed branch channel) of hot fluid. According to the main flow and cross-flow Reynolds numbers strong three-dimensional flow and temperature distributions occur. Especially in turbulent mixing, flow and temperature fluctuations occur, which need to be understood for further HVAC design. Investigations measuring the velocity field and turbulent velocity fluctuations using LDV and PIV, as well as measuring the temperature field using a thermocouple rake are presented in Hirota et al. (2010) and Hirota et al. (2006).
Dedicated to thermal hydraulic systems in power plants a similar setup is present in pipes with mixing tees. In the nuclear power community investigations of T-junctions are common as those components are safety relevant. Structural damage results from thermal fatigue (e.g. thermal striping) caused by temperature fluctuations. The primary and the secondary channel are of circular shape. Such setups with different pipe diameters and Reynolds numbers were investigated experimentally using TCs (Tang et al., 1993), LDV and point-wise TCs (Westin et al., 2008), PIV and a TC tree (Kamide et al., 2009; Kimura et al., 2010).

The investigation of two mixing parallel flows of different temperature is motivated by many different applications, where the mixing layer is induced by a free shear flow. This can be the merging of two rivers or the mixture of air and fuel in industrial combustion systems. For laminar flow conditions the Rayleigh-Taylor instabilities were investigated utilizing PIV and thermocouples by Ramaprabhu and Andrews (2004). The investigation of buoyancy effects on the flow dynamics utilizing Constant Temperature

Anemometry (CTA), Hot Wire Anemometry (HWA) and PIV was presented by Sodjavi and Carlier (2013).
With a turbulent flow condition, parallel mixing was investigated by Benson et al. (2010) utilizing the Magnetic Resonance Concentration (MRC) technique and the results were compared to Planar Laser-Induced Fluorescence (PLIF) measurements. Since then a variety of MRC investigations analyzing different flow mixing setups have been performed (Benson et al., 2012; Yapa et al., 2014).

Analyzing an inclined jet injected into cross-flow at a Reynolds number of 3,000 was investigated using MRT by Burton et al. (2014). Thereby, the jet was conditioned to 48 °C fluid temperature and the cross flow to 18 °C. A GE 3T Signa Magnet was utilized to perform PRF thermometry with a TE of 16 ms. The measured temperature data were compared to MRC data and encouraging agreement was found.

Fluid mixing processes are common in many engineering applications. Especially the knowledge of three-dimensional temperature and velocity fields, as well as their fluctuations is crucial for further component design. MRI measurements utilizing the MRC and MRT technique have already been performed to analyze mixing processes. Hence, mixing processes are promising thermo-fluids test cases for the the application to MRI techniques.

5.1.2 Backward-facing Step

In many thermofluids applications flow separation and flow reattachment is of great interest. Typical examples are flow through valves, coolant flow in internal turbine blade cooling channels, cooling of nuclear reactors or flows in diffusers with steep opening angles. Especially in heat exchangers the occurrence of flow separation and reattachment influences energy transport significantly (Eaton and Johnston, 1981; Nie, 2002; Saldana et al., 2005).

5. MRT Experiments

Separation and reattachment phenomena are present in a Backward-Facing Step (BFS), which consists of a channel with a sudden expansion. The geometry is defined by the step height S, the inlet channel height h, the outlet channel height H, the channel length L and the channel width W. These parameter are shown in Figure 5.1a. Important dimensionless parameters are the expansion ratio ER= $\frac{H}{h}$ and the aspect ratio AR= $\frac{W}{S}$. Both have different influences on the flow. The ER characterizes the size and the strength of the flow separation. The AR charaterizes the effects of the side-walls on the flow field; hence, is a measure for three-dimensionality. Two-dimensionality at the centerline can be assumed if AR$\geq$ 16 for laminar flow (Iwai and Nakabe, 2000), whereas Armaly et al. (1983) measure two-dimensional flow in a BFS with an AR of 18 for Re$<$ 600 or Re$>$ 8,000. Another important measure is the reattachment length x_r, which depends on the Reynolds number, the ER and the AR. In a BFS with low AR, three-dimensional flow develops. Typical is, that the reattachment line is curved and vortices develop resulting from side-wall interactions and lead to a down-wash zone (Iwai and Nakabe, 2000; Nie, 2002). These phenomena are qualitatively sketched in Figure 5.1b.
If an additional heating/cooling source is applied on the bottom wall (heating length L_h) mixed convection phenomena occur. Saldana et al. (2005), for instance, demonstrate that buoyancy forces can have a significant influence on the 3D velocity and temperature field. For mixed convection with Ri = 1 the reattachment line is further downstream then for the pure forced convection case (Ri = 0). If Ri is large (Ri = 3), then the reattachment line is further upstream then in the forced convection case. Further investigations are experimentally and numerically presented by Aung (1983), Iwai et al. (1999), Nie and Armaly (2003), Nie (2002), Saldana et al. (2005), and Tsay et al. (2004) for laminar and by Avancha and Pletcher (2002), Keating et al. (2004), and Vogel and Eaton (1985) for turbulent mixed convection flow.

The BFS geometry is a well-known test case for validating numerical code and turbulence models. There are still few experimental data available of the 3D velocity field and 3D temperature field. Additionally to the 3D behavior in a BFS with low AR, a setup with heated bottom wall has further advantages. As the hot fluid is entrapped in the flow separation zone and heats up due to continuous flow recirculation, low heat transfer rates are needed to generate comparably high temperature differences. Hence, this setup is potentially applicable for the MRT technique.

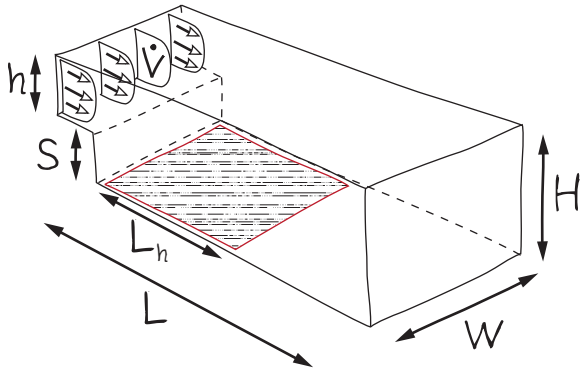

(a) Geometric parameters of the backward-facing step.

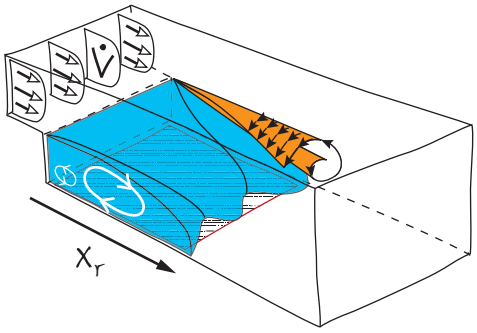

(b) Qualitative sketch of the shape of the recirculation zone. W-shape of the reattachment line denoted with reattachment length x_r.

Fig. 5.1: Backward-facing step flow phenomena and reattachment line x_r.

5.1.3 Double Pipe Heat Exchanger

The double pipe is the most simple setup exchanging heat between two fluid flows of different temperature (Incropera et al., 2006). It consists of two concentrically aligned pipes. The inner pipe is thermally conductive and the outer pipe is thermally isolating. If the two fluids flow in the same direction, then this arrangement is termed co-current flow. If the two fluids flow in opposite direction to each other a counter-current arrangement is achieved.

Typically the double pipe heat exchanger is supplied with high pressurized fluid. The flow is then turbulent and heat is solely transferred due to forced convection. In this case natural convection is negligible. The developed temperature field is not coupled to the velocity field and has a two-dimensional behavior. This makes this experimental configuration less interesting for the utilization of MRT. Experimental research utilizing this configuration is presently of decreasing interest. Nevertheless, the double pipe with turbulent heat transfer is still an important component in many applications. Research deals with the increase of heat transfer due to modifications of the setup. Basically, in double pipe heat exchangers heat transfer enhancement is achieved by increasing flow turbulence or modifying the ve-

locity profile. This is, for instance, done by covering the inner pipe with porous substrates Alkam and Al-Nimr, 1999, inserting a louvered strip inside the inner pipe Eiamsa-ard et al., 2008 or by introducing swirl flow in the inner pipe Durmus et al., 2002.

In most convective flows a combination of both natural and forced convection occurs. When buoyancy forces are of the same order as inertia forces and the flow is laminar, temperature and velocity fields are coupled and exhibit strong three-dimensional behavior. In this case one speaks of laminar mixed convection. Research within this area subdivides two regions of interest: One considers the region where the flow is hydrodynamically and thermally developed. The other one is the entry region where the temperature field and sometimes also the velocity develops.
One setup frequently considered is the flow through a horizontally aligned annular duct with heat flux through the inner walls. In experiments this setup is achieved by applying the concentric double pipe setup and transferring heat through the inner pipe, by means of electrical or fluidic heating or cooling. Through the annulus between the inner and outer pipe laminar flow is achieved by a constant pressure gradient and appropriate upstream flow preparation.
Hattori and Kotake (1978) did one of the first and few experiments in a double pipe supplied with water flow. They varied the tube diameter ratios and fluid viscosities and determined the wall temperature at the inner and outer pipe using TCs. Another experimental investigation is provided by Mohammed et al. (2010). They focus on the thermal entry region of a concentric double pipe arrangement in laminar mixed convection air flow by measuring wall temperatures. They propose that the developing secondary flow due to buoyancy forces significantly increases heat transfer rates. They observe more intense secondary flow patterns on the upper half of the annulus' cross-section.
Nguyen et al. (1983) present a theoretical approach for a similar setup and calculate the velocity field. They describe that the axial flow pattern is strongly influenced by natural convection. Nieckele and Patankar (1985) conduct a numerical experiment. In their horizontal concentric annulus setup they consider laminar mixed convection with heat transfer at the inner wall. They present cross-section plots of the annulus depicting streamlines and isotherms for different adjustments of natural to forced convection. With their study they find out, that a stable temperature stratification

inside the annulus is present, which is also a sign for highly nonuniform heat transfer. In their numerical study Zerari et al. (2013) investigate the laminar mixed convection water flow through an annulus achieved by two concentrically aligned elliptical cylinders. The focus was set on the comparison of the hydrodynamical and thermal development for either constant or temperature-dependent thermophysical fluid properties. They show the three-dimensional nature of the annulus flow by observing the cross-sectional velocity and temperature fields at different streamwise positions. A review of different experimental and numerical studies is presented by Togun et al. (2014).
As shown in this short review, most research concerning the double pipe with laminar mixed convection flow is of numerical background. There are only a few experimental studies available presenting validation data. They do not present appropriate three-dimensionally resolved data. For future research the experimental acquisition of temperature and velocity fields with appropriate spatial resolution is desirable.

5.2 Preliminary MRT Tests

5.2.1 Straight Pipe

A first preliminary experiment was designed and measured with MRT. The flow model was a simple straight pipe. The goal was to explore the possibilities and limits of the applied PRF method with this simple setup and to produce temperature maps for simple experimental conditions (constant flow rates and constant fluid temperatures). Results were already presented and discussed in Wassermann et al. (2014a), whereas results considering the MR applicability were achieved by the project partner.

5.2.1.1 Experimental Setup and Measurement Parameters

The model consists of a PA wide-angle diffuser[1] including three internal grids, a PMMA pipe (50 mm ID) and a PA end nozzle (Fig. 5.2). Both ends are connected to PVC hoses. Two temperature probes can be inserted into an upstream and downstream probe inlet. Each one is included into a PA adapter part.

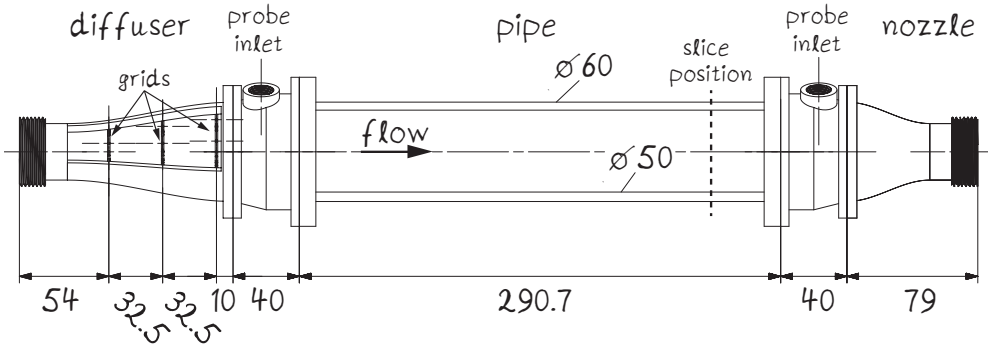

Fig. 5.2: CAD sketch of the straight pipe showing components and features of the flow model. The position is marked for which results are depicted. The image was taken from Wassermann et al. (2014a).

The small flow supply system was used to provide the desired flow rates. To achieve constant fluid temperature the tank temperature was controlled with the help of the Julabo immersion cooler (for maintaining the tank temperature at room temperature) and with the MINCO heating foil (for tank temperatures maintained above room temperature). The measurement fluid was distilled water with 1 g/l copper sulfate added.

The MR machine used was the Siemens Magnetom Trio system. To enhance signal a spine coil and a surface body coil were applied. For field drift corrections reference phantoms were placed around the flow model.
In-situ temperature monitoring was performed with the thermometer system utilizing fiber optical probes. Therefore, one probe was inserted into

[1] constructed after the design rules presented in Sec. 3.3.4

the downstream inlet and two into the reference phantoms.

A PRF sequence was obtained to measure a 2D transversal slice at the location depicted in Fig. 5.2. Two different sets of scans were performed: the first set had a high TE of 20 ms (leading to maximum measurable temperature difference of $\Delta \mathrm{T}_{max} \approx \pm 20K$) and the second set had a TE of 10 ms ($\Delta \mathrm{T}_{max} \approx \pm 40K$). For each set a reference scan at room temperature ($\mathrm{T}_{ref} \approx 20°C$) and three scans with increased fluid temperature (T - T_{ref} = $+5K/+10K/+15K$) were performed. Three different flow rates (20, 40 and 60 L/min) were achieved for the second set, resulting in Reynolds numbers in the range of 9,500 $\leq \mathrm{RE}_d \leq$ 35,000. This resulted in 9 different cases for the second set. Fig. 5.3 was prepared by the project partner and already presented in Wassermann et al. (2014a). It shows a magnitude image of the setup comprising the flow model and the reference phantoms. The red and green regions of interest (ROI) show areas, which were used for FOP temperature averaging (red - pipe) or background phase fitting (green - reference phantoms).

5.2.1.2 Results and Discussion

Fig. 5.4 gives an exemplary temperature map achieved with a long TE of 20ms. It was achieved by the project partner, who marked critical areas showing artifacts, which arise for TEs which were chosen too long. They appear as false temperature difference distributions. A detailed discussion is presented in the work of the project partner. The main points important for further engineering considerations are: the positioning of the reference phantoms, the presence of temperature probes, the accumulation of phantoms with different shapes resulting in B_0-field distortions (Schenck, 1996) and the presence of air bubbles or air-water interfaces (especially in combination with sharp edges at the boundaries). The marked background phase slope that can be seen in the large reference phantoms shows the need for background correction. These important findings achieved by the project partner were already listed in Sec. 3.2.1.

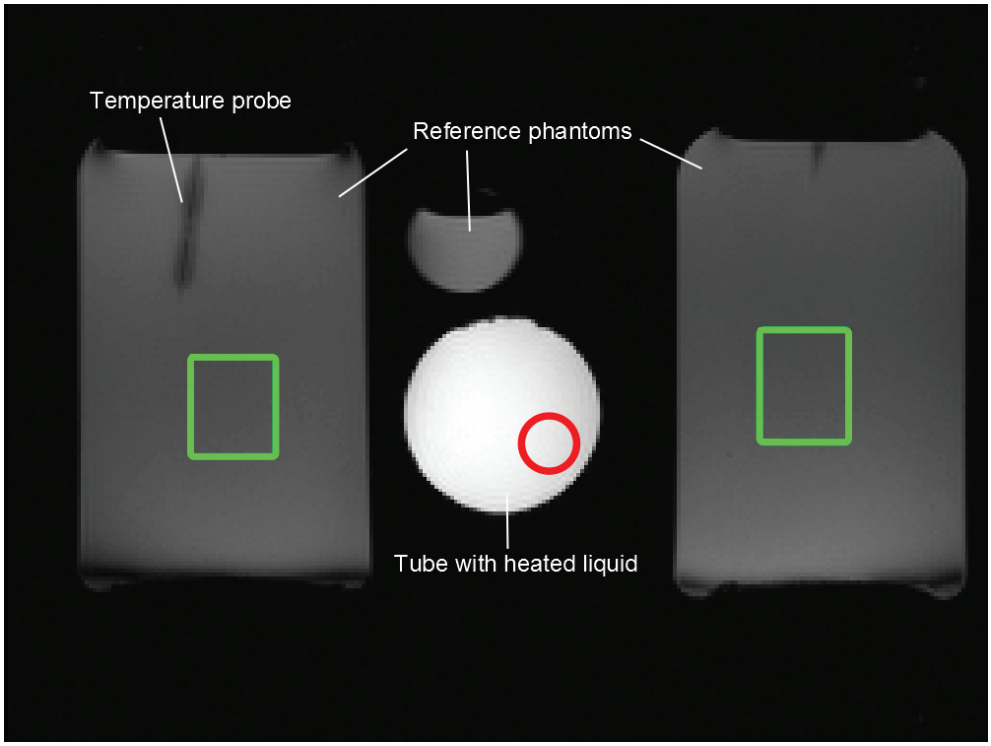

Fig. 5.3: Magnitude image showing the setup inside the scanner. The pipe (middle circular object) is surrounded by reference phantoms. The red ROI represents the area averaged for temperature measurements. The green ROIs represent the areas used for background phase fitting and subtraction. This image is intellectual property of the project partner and was taken from Wassermann et al. (2014a).

Fig. 5.5 was prepared by the project partner and presents temperature maps measured with a short TE of 10ms. In general, temperature changes measured with MRT compare well with values measured by the FOP and differ with maximum of 1.2K for all cases. Increasing the flow rate does not significantly alter the temperature maps. As the Reynolds numbers imply that the flow is turbulent for all cases, the turbulence level seems not to influence the temperature map significantly. Only the erroneous hot spots at the top of the pipe disappear with increasing flow rate. For shorter TEs the susceptibility artifacts are less pronounced. Nevertheless, the temperature distribution within the pipe is clearly inhomogeneous and other artifacts as described appear (e.g. air bubbles, too close reference phantoms).

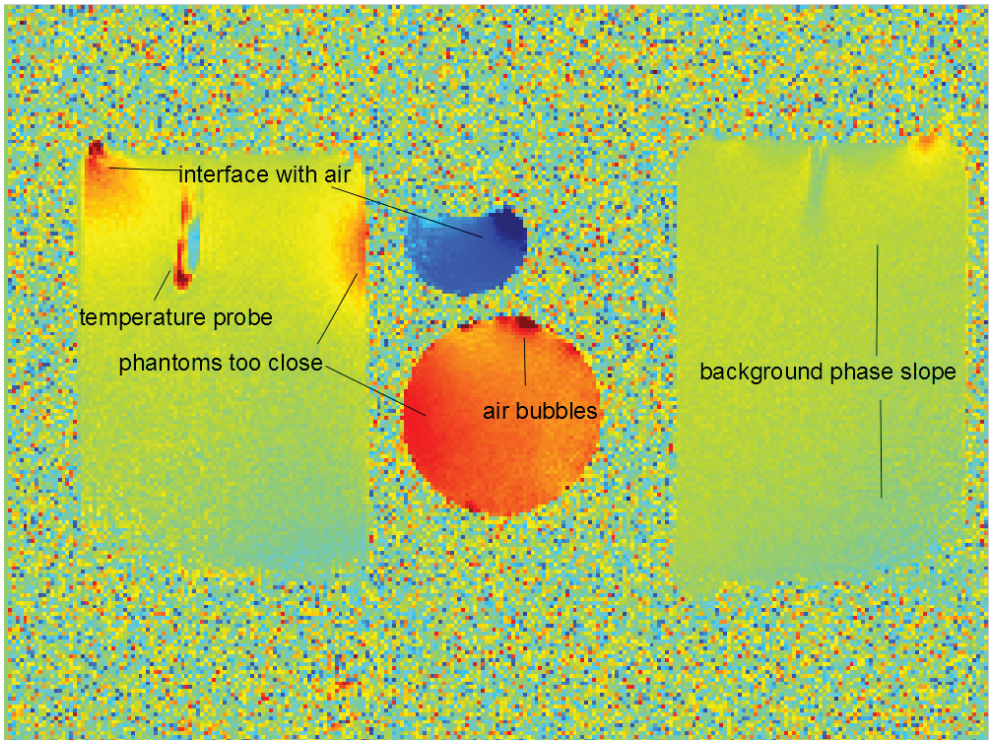

Fig. 5.4: Uncorrected example temperature map for TE = 20 ms showing unwanted field inhomogeneities. Locally varying magnetization potential (susceptibility) cause errors in the temperature maps. A background slope is visible in the reference phantoms. These errors need to be carefully considered during experimental design. This image is intellectual property of the project partner and was taken from Wassermann et al. (2014a).

5.2.1.3 Lessons Learned

The straight pipe experiments showed a successful application of MRT. With this investigation important points could be addressed by the project partner helping to improve the design of further experimental setups. Some of the points are already listed in Sec. 3.2.1.

- Flow compensation preventing unwanted shifts in the signal phase due to fluid movement (see Sec. 3.1.3.2) works sufficiently for the applied cases. This was proved by achieving temperature maps for three different flow rates.

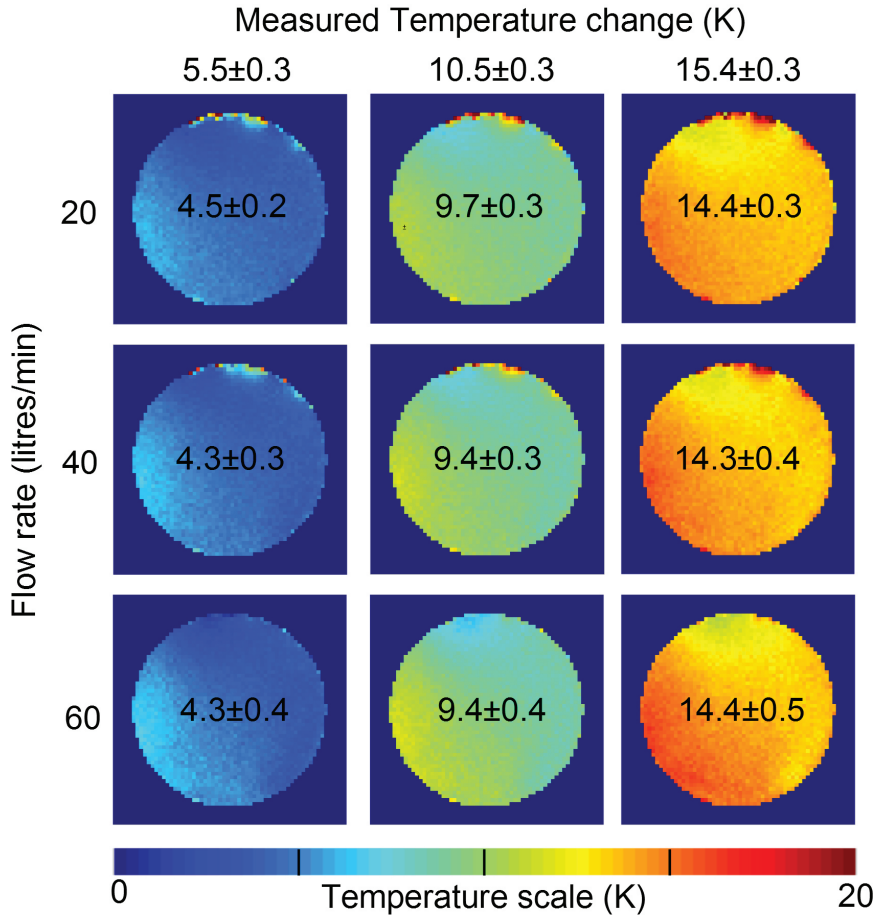

Fig. 5.5: Temperature maps acquired for TE = 10 ms for three different fluid temperatures and three different flow rates. The mean and standard deviation of the temperature change (values taken from the ROI marked in red in Fig. 5.3) are displayed within the pipe. The temperatures measured with the optical probes are shown above each column. This image is intellectual property of the project partner and was taken from Wassermann et al. (2014a).

- Reference phantoms are necessary for background phase correction and have to be included in the measurement volume.
- Reference phantoms and other B_0-field affecting bodies should be placed so that they do not influence each other.
- Air bubbles and sharp edges at air-water boundaries should be avoided.
- Optical probes as used in this investigation, produce signal loss due to partial volume effects and small artifacts.

- Decreasing TE leads to decreased intensity of susceptibility-related artifacts and a decreased temperature resolution.

5.2.2 Backward Facing Step

The importance of the BFS flow and temperature field in literature has been surveyed in Sec. 5.1. This section presents an experimental setup utilizing ceramic heating elements at the bottom wall downstream of the step. The main goal of this preliminary experiment was to show the influence of heating elements during 4D-MRV and 4D-MRT acquisitions. The BFS setup was prepared in cooperation with Freudenhammer (2012).

5.2.2.1 Experimental Setup and Measurement Parameters

The BFS parameter as defined in Sec. 5.1 are listed in Tab. 5.1. The model is manufactured using PA direct laser sintering. For in-situ heating four rectangular ceramic heating elements, as explained in Sec. 3.3.3.1, are used. Two at a time are combined in one heating element module. The two existing modules are slid into opening on the side walls of the BFS. When completely inserted, the heating elements are interleaved and provide a heated area of 0.05×0.06 m^2 (width$\times$length). Below the heating elements a ceramic insulation block made of Al_2O_3 is installed which protects the PA material from the hot heating element surfaces.
The flow model setup is depicted in Fig. 5.6. The flow enters upstream of the diffuser (contains internal grids). Further downstream, a nozzle guides the flow to the BFS. On the top part of the BFS an acrylic glass plate is inserted for visual inspection. Downstream of the BFS an acrylic glass channel section is attached and a nozzle converges the flow to the size of the hose diameter.

The flow was provided by the small flow supply system. As the measurement fluid deionized water mixed with Gadolinium contrast agent was used.

Tab. 5.1: Parameter describing the investigated BFS as defined in Chap. 1.

Parameter	Value
S [m]	0.015
W [m]	0.06
H [m]	0.03
h [m]	0.015
ER	2
AR_s	4
d_h [m]	0.024

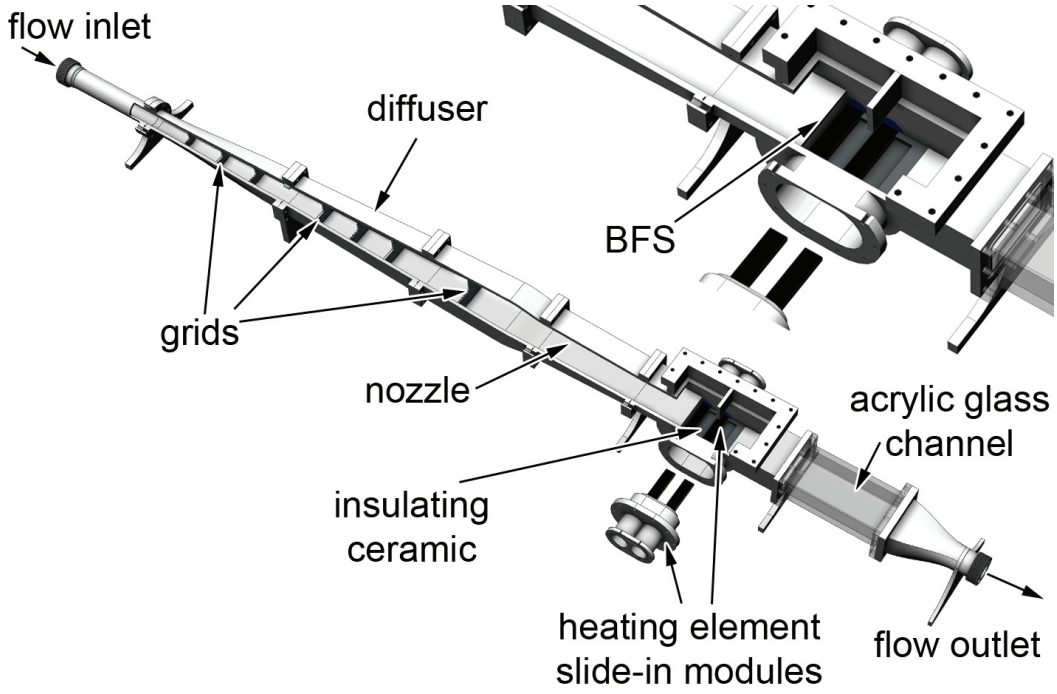

Fig. 5.6: CAD drawing showing the components of the BFS flow model and setup. One of the heating element modules is shown in exploded view.

The temperature in the supply tank was increased to 30 °C[2]. The flow rate was set to 16.5 L/min, which resulted in a bulk flow Reynolds number of 5,600 based on the step height.
For all measurements the SD was 1050 ms, the DC was 500 ms and U_{HE}

[2] During these measurements no water cooling system was available. The introduced heat by the heating elements was removed by free convection to the cooler ambient air.

was set to 5.6 V. This resulted in an average electrical heating power of approximately 255 W. Preceding thermocouple measurements for different streamwise positions showed, that with this configuration a stationary temperature profile develops due to the high thermal capacity of ceramic material. A maximum temperature difference of 15 K compared to the temperature measured in bulk flow develops 1 mm above the second downstream heating element. The results of the thermocouple measurements are given in Tab. 5.2 for three different streamwise positions and different distances above the heating elements. In order to characterize the influence of buoy-

Tab. 5.2: Thermocouple measurements at three streamwise positions for different vertical distances above the heating element, measured on the channel center line. The temperature differences were derived by subtraction of the temperature measured 10 mm upstream the step in the bulk flow. T_1 is 5 mm, T_2 is 20 mm and T_3 is 65 mm downstream the step. The results were obtained by Freudenhammer (2012).

Vertical distance	$\Delta T_1 \pm \sigma$	$\Delta T_2 \pm \sigma$	$\Delta T_3 \pm \sigma$
1mm	9.04 ± 3.77 K	15.56 ± 3.98 K	0.37 ± 0.10 K
2mm	6.40 ± 2.32 K	6.53 ± 2.43 K	0.36 ± 0.09 K
4mm	5.59 ± 1.91 K	5.03 ± 2.24 K	0.35 ± 0.10 K
6mm	4.86 ± 1.69 K	4.51 ± 1.45 K	0.39 ± 0.13 K
8mm	3.33 ± 1.63 K	3.97 ± 1.24 K	0.40 ± 0.11 K

ancy forces on the development of the flow field, a Richardson number of ≈0.01 according to Tab. A.4 could be estimated. Hence, the flow field is not strongly influenced by heating.

For all measurements a Siemens Trio MR device was used.
At first MRV data were obtained applying a 4D GE FLASH sequence. The resolution was set to 1.2 mm isotropic with an acquisition matrix of 224×84×44 (FE×PE×SS). The flip angle was 15°. 8 phase steps were acquired with a SD of 1050 ms. For velocity encoding a Venc of 0.1 m/s was used and phase wrapping was corrected during post-processing in the Velomap tool. This resulted in a TE of 5.03 ms, a TR of 30.8 ms and a total acquisition time per scan of 15:42 min. MRV data was achieved for the three cases flow on / heat off (2 scans), flow on / heat on (3 scans) and

flow off / heat off (1 scan). For the flow on / heat on case four phase steps during MC were averaged. For the other cases all phase steps were averaged. Afterwards, the velocity data were subtracted with the flow off data to correct for background drifts. All velocity components were referenced by $U_{bulk} = 0.3$ m/s.
For MRT, the PRF method was applied utilizing a 2D phase-locked gradient echo FLASH sequence. The resolution was 1.04 mm isotropic with a 288×288 (FE×PE) acquisition matrix. The flip angle was 15°. 37 phase steps with a SD of 1050 ms were acquired. The sequence was flow-compensated and the flow-compensation gradient stretched to maximum length. The TE was set to 10 ms in order to achieve sufficient temperature resolution. The TR was 25.4 ms and the total acquisition time was 2:25 min. The 2D temperature map was achieved by subtraction of a reference scan without heating and a scan with heating applied. For background phase correction reference phantoms were placed around the BFS model. Their location and their geometry (bottle on top and tube below) can be seen in Fig. 5.7.

5.2.2.2 Results and Discussion

In Fig. 5.7 magnitude images of one phase step of the MRT data are shown. Obvious is the presence of strong artifacts during the DC. These artifacts arise due to the presence of moving charges in the electrical conductors of the heating elements. They lead to signal loss and smearing. The artifacts affec the entire PE direction and are present in regions of the FE direction, where the heating elements are. Another artifact is present in both cycles MC and DC. These are RF artifacts resulting from received frequencies arising from cables inside the FOV. They are present as a white stripe along PE direction for a distinct FE position. These artifacts cannot be compensated. Improved cable shielding can help to reduce RF artifacts.

Fig. 5.8 shows flow field visualizations of the 4D-MRV measurements in the BFS for the case with heating (flow on / heat on). In the upper graphic a top-view of the iso-velocity surface for $U/U_{bulk} = 0$ is given, showing the size of the flow separation zone. In the lower graphic a contour slice displayed at the middle axis with additional streamlines are depicted.
No additional artifacts are visible due to the electrical heating. This means,

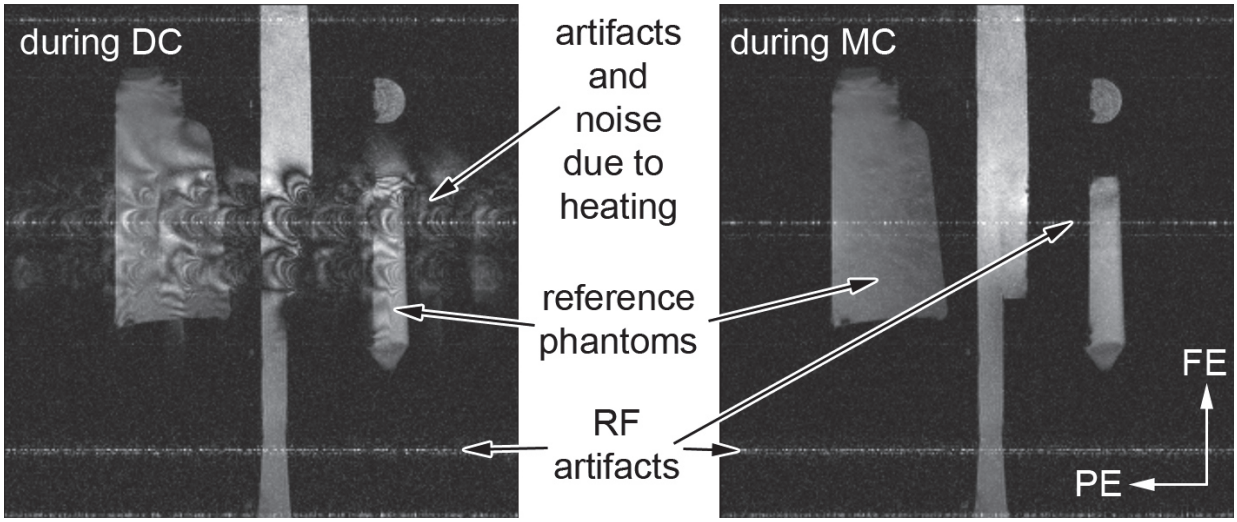

Fig. 5.7: Magnitude images of 2D phase-locked MRT data showing the BFS and the reference phantoms during MC and DC.

that the MRV measurements are not corrupted by the heating elements and the data acquired during MC can be used.
The 3D shape of the separation zone is clearly visible observing the iso-velocity surface. The reattachment line is w-shaped and lies between 6 to 7 step lengths downstream the step. This corresponds well with values presented by Saldana et al. (2005).

A preliminary MRT measurement is depicted in Fig. 5.9 showing a qualitative temperature difference map. The color green is a ΔT of 0 K and in this case equals room temperature, blue is a $\Delta T < 0$ and yellow/red a $\Delta T > 0$. Throughout the BFS anomalies in the temperature map are obvious. In the channel inlet (left side) the temperature is higher than in the channel outlet (right side). Around the step and in the lower reference phantom negative temperatures are measured. Immediately behind the step and further downstream of the last heating element hot spots are visible. These phenomena are physically not possible; hence they must be an effect of strong artifacts. In the upper phantom a reasonable homogeneous temperature distribution with $\Delta T = 0$ K is measured.
The artifacts are presumed to result from susceptibility changes induced by the heating elements and the insulation ceramic. According to Sec. 3.2.1, the heating elements made of silicon nitride have a good susceptibility matching with water. The aluminium oxide of the insulation ceramic has less sufficient

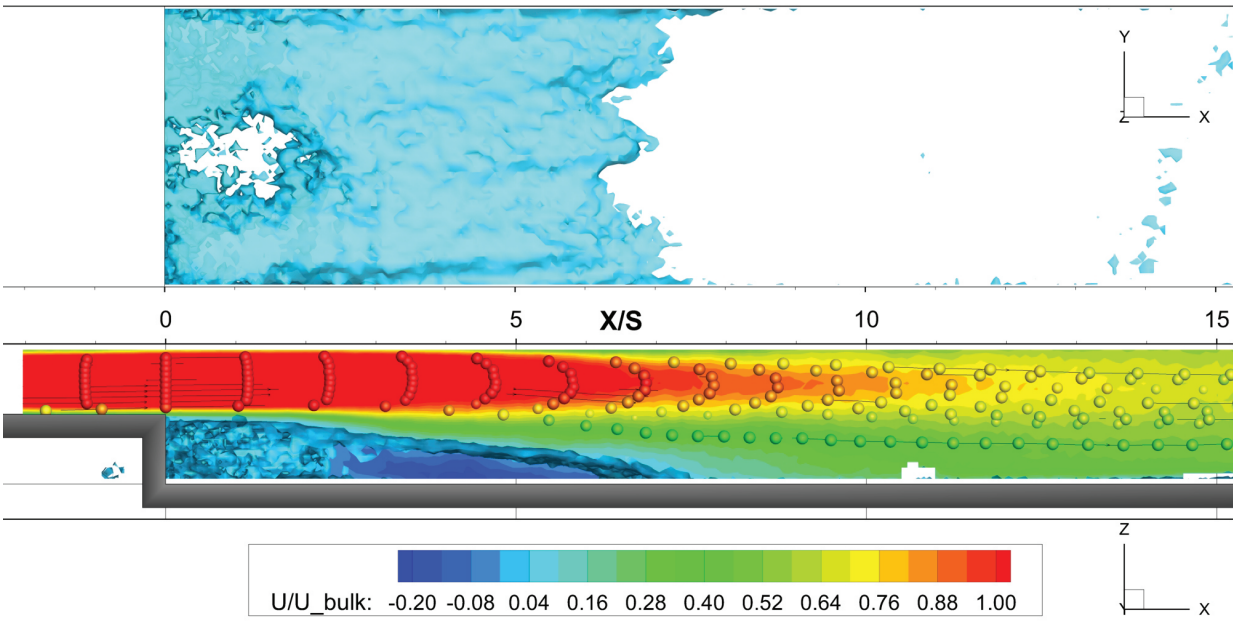

Fig. 5.8: MRV results for the case flow on / heat on. The flow field is visualized in a X-Y-view (upper image) showing an iso-velocity surface for $U/U_{bulk} = 0$ and in a X-Z-view (lower image) depicting a contour slice through the middle axis with streamlines applied. The spheres show the particle progress (time-averaged flow data) along the streamlines starting at $X/S = 0$.

matching. However, the silicon nitride seems to have a strong temperature-dependency of the susceptibility. This means, that the susceptibility-induced phase change is different for the reference case and for the case with heating. By subtraction of both data sets errors occur, which cannot be compensated for by additional measurements. In comparison to the MRV measurements, TE is much longer for MRT. By increasing TE susceptibility artifacts intensify, as explained in Sec. 2.3.3.2. To achieve sufficient temperature resolution a comparably long TE is needed. Increasing the heating power leads to local boiling, which, in turn produces strong artifacts. Hence, the utilization of heating elements with strong temperature-dependent susceptibility is not possible without sufficient correction methods. These are conclusions drawn by the project partner.

De Poorter (1995) presented a way to model the susceptibility effects of different tissue and geometry. For the presented BFS setup, two 2D simu-

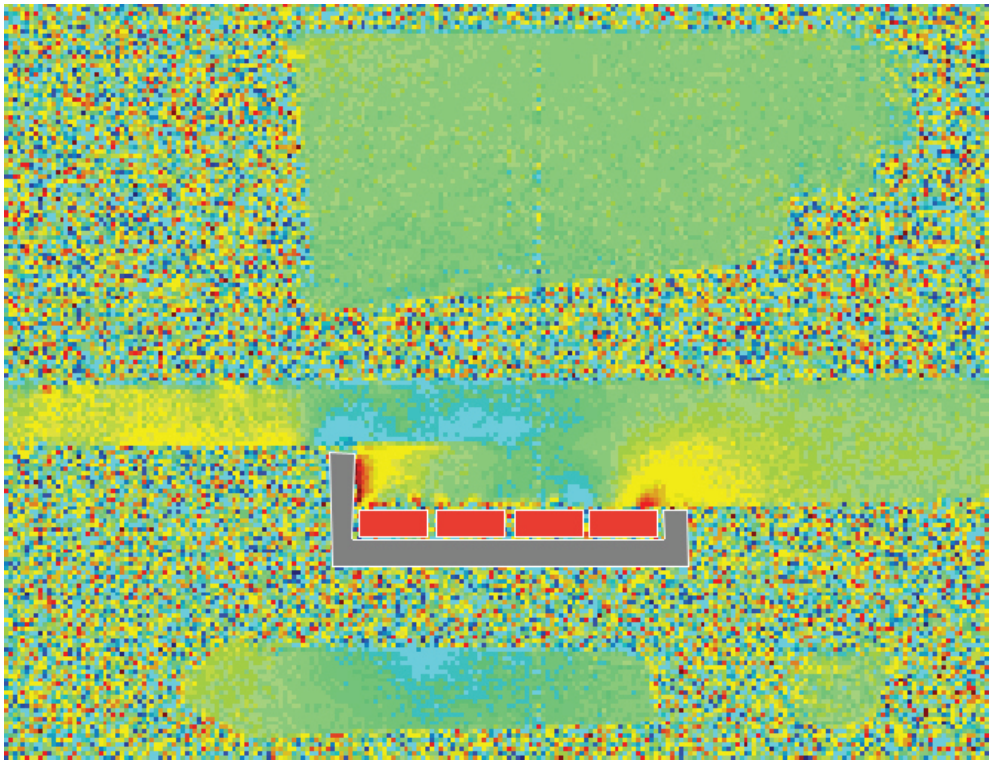

Fig. 5.9: Contour plot showing the uncorrected results of the MRT measurements. The insulating ceramic is displayed in grey and the heating ceramics in red. This image is intellectual property of Dr. Robin Simpson, University Medical Center Freiburg.

lations of the susceptibility-induced phase changes were performed for the insulation ceramic and the heating elements by Dr. Robin Simpson, University Medical Center Freiburg. Each simulated phase change map was converted into a temperature difference map according to the given MRT parameter. The results of both simulations were summarized and finally subtracted from the uncorrected temperature map (as depicted in Fig. 5.9). The results of both simulations, as well as the corrected temperature map are shown in Fig. 5.10.
In the corrected image small regions downstream the heating elements showing negative ΔT are left. In the channel inlet, as well as channel outlet the temperature difference is almost zero, which seems more realistic than before. In addition to that, the artifacts in the lower reference phantom were removed. In the region above the heating elements, which also coincides with flow separation, an increased and distributed ΔT is observable. There are still some hot spots in the vicinity of the heating elements left, which seem to be erroneous. These results show the possibility that a correction can be

performed, if the geometry and the material´s susceptibility is known. A more improved simulation model has to be developed, taking into account the real geometry and 3D effects.

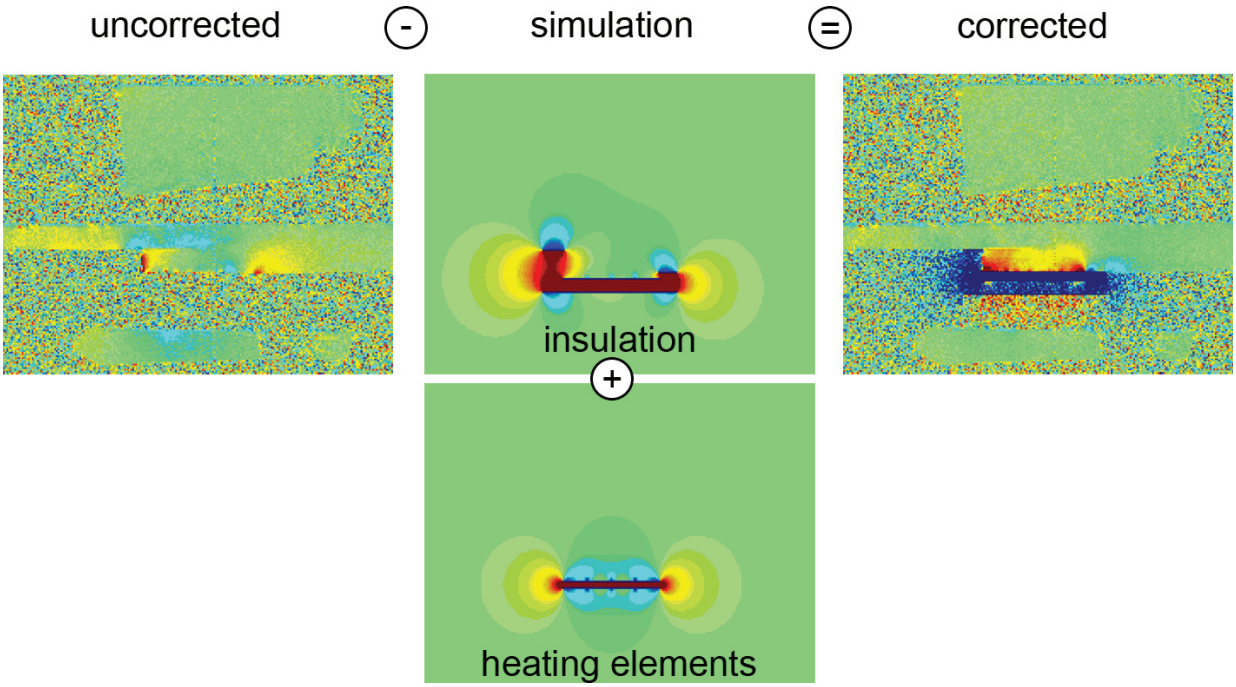

Fig. 5.10: Correction method of susceptibility-induced phase artifacts as proposed by the project partners [The presented images are intellectual property of Dr. Robin Simpson, University Medical Center Freiburg].

5.2.2.3 Lessons Learned

The preliminary results of the BFS experiments show a successful utilization of ceramic heating elements within the MR machine. The data taken in phase steps during the measurement cycle of 4D-triggered MRV measurements were uninfluenced, whereas MRT measurements were strongly disturbed by susceptibility artifacts. Nevertheless, a correction method was applied that shows a first way to correct the measurements. The investigations pointed out the following suggestions:

- Ceramic material and ceramic heating elements can be used in MR environment. During DC the images are corrupted. Cables produce RF artifacts.

- Pulsatile heating of the heating elements works sufficiently and the MR system can be triggered to the heating cycle.

- The BFS setup shows sufficient temperature differences in the separation regions above the heating elements.

- MRV measurements for the case with heating applied showed good results without the occurrence of stronger artifacts.

- MRT measurements showed strong artifacts which are presumed to result from susceptibility-induced phase changes from the ceramic material.

- Simulations of the susceptibility-induced phase changes for the insulation ceramic and heating elements could correct the majority of artifacts. Still some artifacts remain. An improvement of the method is required.

5.3 Double Pipe Experiments

As an initial test case for the application of MRT in combination with MRV a counter-current double pipe heat exchanger was chosen. The test case and first MRT results were already presented in Buchenberg et al. (2015). In this section data achieved with additional MRV and MRT measurements are discussed.
The double pipe is an arrangement of an inner pipe surrounded by a concentrically aligned outer pipe. This builds an annulus through which laminar flow (here termed bulk flow) at a certain temperature is flowing. Through the inner pipe, which has a high thermal conductivity, turbulent flow (here termed inner flow) at a constant higher or lower temperature compared to the bulk flow is applied. Due to heat transport between the bulk flow and the inner flow the temperature and velocity fields develop a three-dimensional nature, which is a result of the presence of strong buoyancy effects. This was described by many authors as reviewed in Sec. 5.1.

The described double pipe arrangement is expected to be reproducible in flow and temperature development. This can be achieved by applying constant fluid inlet conditions in the bulk and inner flow, for which the tools explained in Sec. 3.3 were used. Due its simplicity, the design rules proposed by Schenck (1996), the consideration provided by the project partner (see Sec. 3.2.1) and the lessons learned from preliminary experiments (see Sec. 5.2) the double pipe arrangement was designed to meet MR requirements. Hence, the presented experimental setup was chosen as an appropriate thermofluid test case to successively apply MRT.

5.3.1 Experimental Setup

5.3.1.1 Flow Model

The flow model consists of two pipes that are concentrically arranged. Heat is transferred through the inner pipe by means of fluidic heating or cooling achieved by the inner flow circuit. A second pipe surrounding the inner pipe builds an annulus through which fluid is pumped by the primary flow circuit. A counterflow arrangement was chosen, so that the two fluids move in opposite direction to each other. The inner pipe is made of copper (bulk diameter (OD= 15 mm, wall thickness 1 mm); hence, it has a high thermal conductivity and a good susceptibility matching with the measurement fluid as explained in Sec. 3.2.1. The bulk pipe is made of PMMA (inner diameter ID= 50 mm, wall thickness 5 mm), which can be assumed to be thermally isolating (adiabatic) due to the low thermal conductivity of PMMA.

In order to provide appropriate inlet velocity profiles the flow model has a flow preparation section as explained in Sec. 3.3.4 comprising a diffusor and a settling chamber.
The nozzle has different functions: It fixes the copper pipe and the PMMA pipe axially and radially. It reduces flow turbulence by accelerating the bulk flow and it builds the exit port for the inner flow. Probe inlets are included to measure the bulk temperature $T_{bulk,in}$ and the inner flow outlet temperature $T_{inner,out}$. The end nozzle fixes the two pipes from the other side and comprises the bulk flow outlet, the inner flow inlet and an additional tem-

perature probe port ($T_{inner,in}$). All parts of the double pipe arrangement as described in the foregoing text and the dimensions of the setup are depicted in Fig. 5.11.

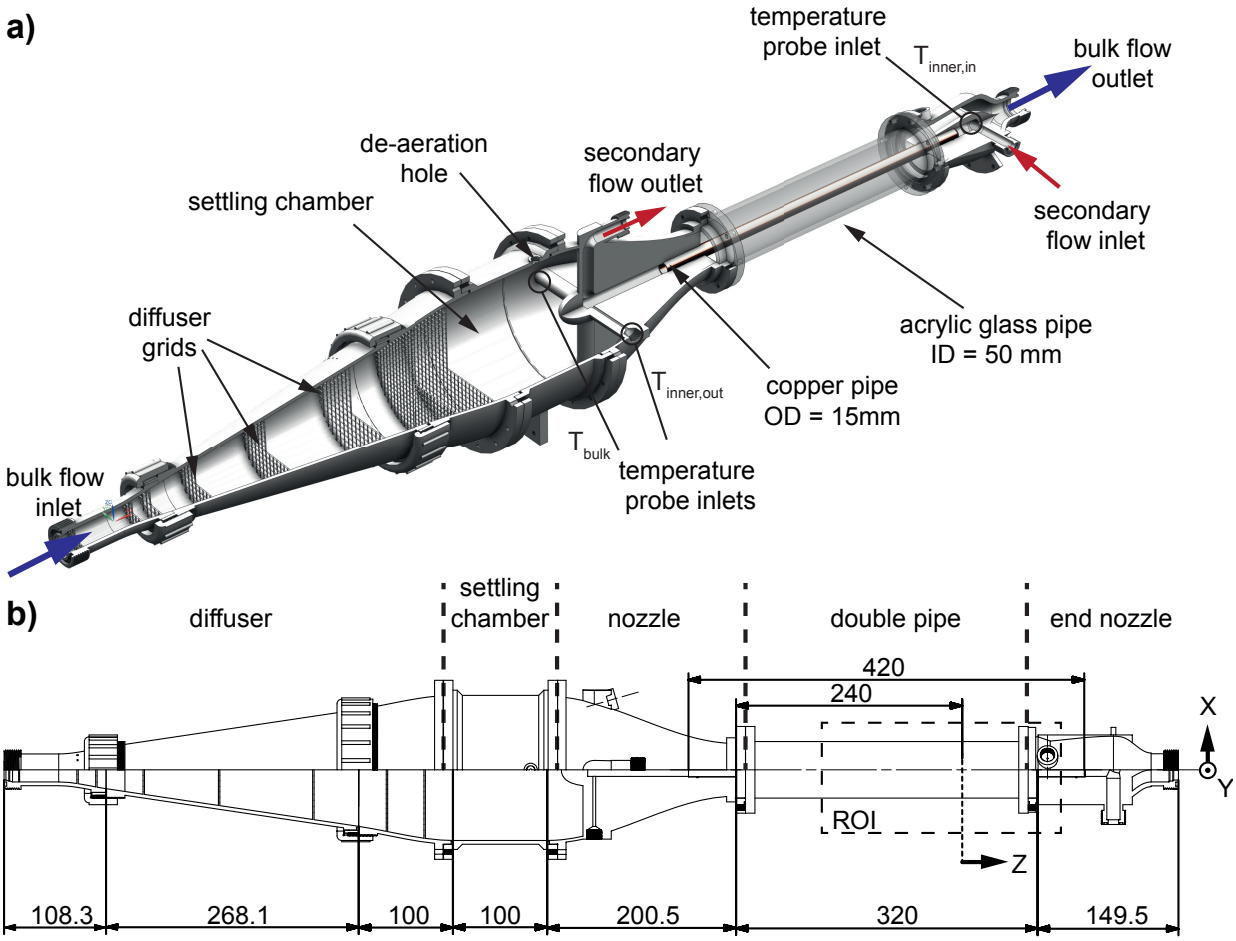

Fig. 5.11: (a) Cross-sectional cut through the CAD drawing showing components and features of the flow model. (b) Top-view of the CAD drawing showing the measures of length and the coordinate system used for the results (adapted from Buchenberg et al. (2015)).

For B_0-field drift correction thermally isolated reference phantoms[3] are positioned within the FOV according to the recommendations proposed by the project partner.

[3] The phantoms are of cylindrical shape with 7 cm inner diameter and 13 cm height. Each phantom is filled with distilled water mixed with 5% hydroxyethylcellulose to increase viscosity and 1 g/l CuSO4 to increase signal.

During data acquisition the FOPs were utilized for measuring and logging the temperature at the probe ports for the bulk flow inlet temperature $T_{bulk,in}$, the inner flow inlet temperature $T_{inner,in}$ and the inner flow outlet temperature $T_{inner,out}$. A fourth probe was used to measure the reference phantom temperature or the ambient room temperature.

5.3.1.2 Flow Apparatus

In this section all components needed for the preparation of appropriate flow and temperature conditions in the bulk and inner flow are summarized.
The MR experiments were conducted with deionized water mixed with 1 g/l copper sulfate salt. For experiments the large flow supply system described in Sec. 3.3 was used for the bulk flow circuit. The flow rate was adjusted by adjusting the pump control voltage and by adjusting additional pressure loss by closing a valve downstream the flow model. The tank temperature holding the measurement fluid was kept at a constant value using the Julabo FT402 immersion cooler or the MINCO heating foil.
In the MR environment the inner flow with increased temperature was achieved by the Julabo SE, class III immersion heating circulator, which was operating at a flow rate of $\approx$ 20 L/min[4]. For inner flow temperatures below or at ambient room temperature the Julabo FC1200T circulation cooler with a flow rate of $\approx$ 25 L/min was used. For measurements in a laboratory environment, the small system was utilized to prepare the inner flow at an increased temperature.
Fig. 5.12 shows a schematic of the flow apparatus used for MR measurements. The blue circuit marks the bulk flow and the red circuit the inner flow. The flow model position inside the MR scanner and the locations of the FOPs (in addition to Fig. 5.11) are marked.

[4] This was measured in the laboratory with the help of the second flow rate sensor installed in the small flow supply system.

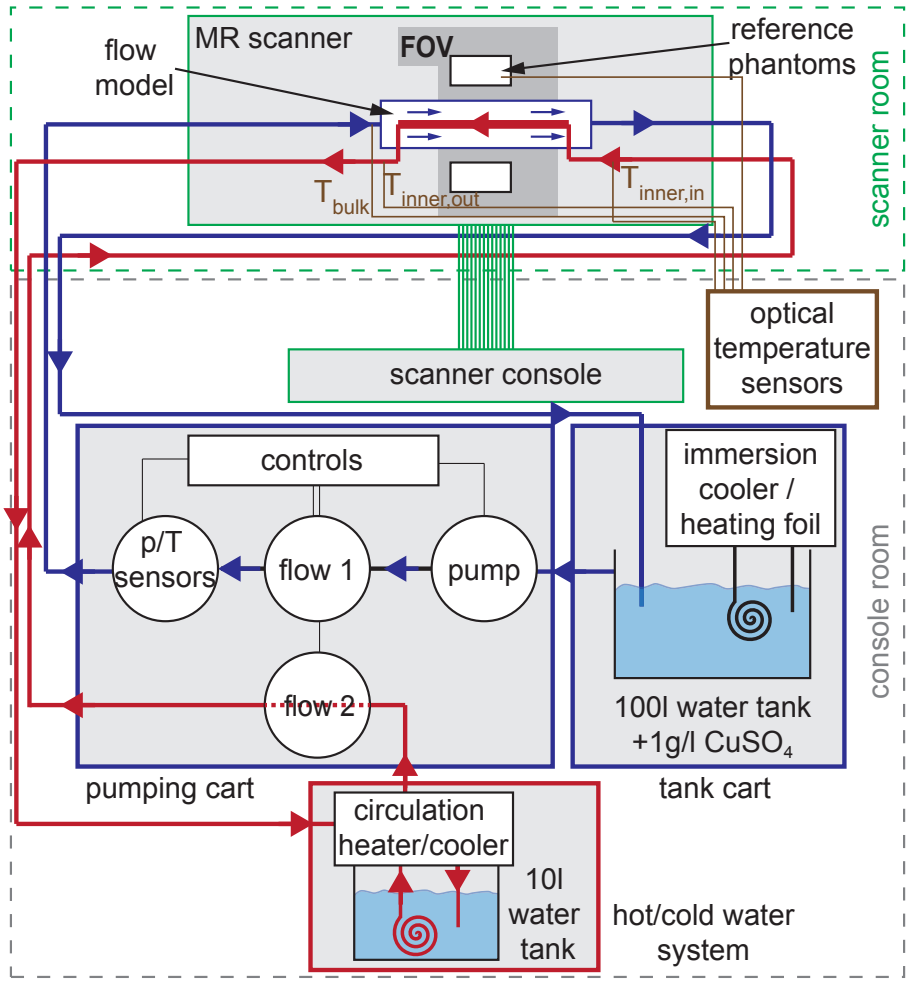

Fig. 5.12: Schematic of the flow apparatus and the flow model setup in MR environment. The black lines show the bulk flow circuit and the orange lines the inner circuit. The positions of the temperature probes are marked in brown (adapted from Buchenberg et al. (2015)).

5.3.1.3 MR Settings and Post-Processing

For MR measurements a Siemens Magnetom Prisma system was utilized as explained in Chap. 3. A typical arrangement of all necessary components as set up in the scanner and console room is given in Fig. 5.13. The MR settings were adjusted according to the parameters given in the table of each result section.

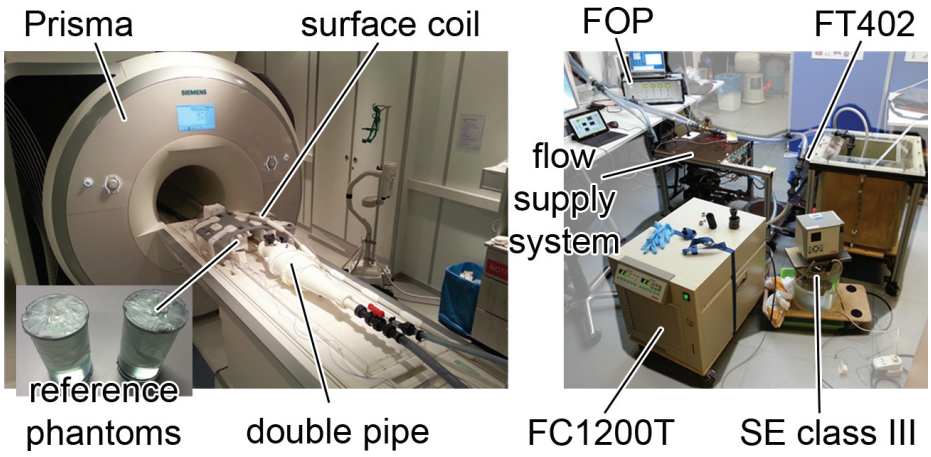

Fig. 5.13: Left - photo of the double pipe setup arranged on the patient table of the Prisma scanner with reference phantoms and surface coil applied. Right - photo of the flow apparatus and fiber optical probes (FOP) adjusted in the console room.

The raw images (dicoms) were converted using the Velomap tool. The whole temperature data obtained with MRT were composed according to Sec. 3.1.3.2 and corrected using a 0^{th} order correction (constant value across the imaging volume). This was done by the project partner. MRV data were achieved according to Sec. 3.1.3.1 and corrected using the Legendre polynomial tool with 1^{st} order correction.
Calculations and graphical visualization of the final data were done with Matlab. Tecplot was used for more advanced three-dimensional visualizations.

5.3.1.4 Cases

In order to exploit the capabilities of MRT and the double pipe setup, three different cases were created by varying the bulk flow temperature condition and the inner flow temperature condition as explained in Buchenberg et al. (2015): the *homogeneously heated case*, the *heated case* and the *cooled case*. For all cases the bulk flow rate was kept constant. In order to calculate the temperature difference field two scans with equal MRT adjustments but different temperature conditions were conducted: For the reference scan the bulk and inner flow were held at a constant temperature

T_{ref} =$T_{bulk,in}$ =$T_{inner,in}$ = 21°C, which was chosen according to the room temperature. Following this, a second scan with different temperature conditions was performed according to the case under investigation. For the *homogeneously heated case* the bulk and the inner flow temperatures were held at a constant but increased temperature $T_{bulk,in}$ =$T_{inner,in}$ = 31°C. As this case was discussed adequately in Buchenberg et al. (2015) and it is not further interesting for heat transfer considerations it is not presented here. For the *heated case* the bulk flow temperature was set to at room temperature ($T_{bulk,in}$ = 21°C) and the inner flow was increased to $T_{inner,in}$ = 50°C. Limited by the performance of the conditioning systems for the *cooled case* the bulk flow temperature was increased to $T_{bulk,in}$ = 31°C and the inner flow was decreased to $T_{inner,in}$ = 9°C. In order to achieve information about the velocity fields the MRT measurements were embraced by MRV measurements. The following list gives an exemplary acquisition scheme for the heated case:

1. MRV at homogeneous temperature $T_{bulk,in}$ =$T_{inner,in}$ = 21 °C
2. MRT at homogeneous temperature $T_{bulk,in}$ =$T_{inner,in}$ = 21 °C
3. MRT with $T_{bulk,in}$ = 21 °C and $T_{inner,in}$ = 50 °C
4. MRV with $T_{bulk,in}$ = 21 °C and $T_{inner,in}$ = 50 °C

A final data set consists of a temperature difference scalar field and the accompanying velocity vector field. The time between subsequent measurements was kept as short as possible to avoid background effects discussed by the project partner (Buchenberg et al., 2015). For the cooled case, heating $T_{bulk,in}$ to 31 °C took the longest time period with about 30 min.

For all three cases the pump control voltage was adjusted at a constant value yielding a flow rate of 5.6 L/min. To correct the high systematic error of the flow rate sensor, the stopwatch-bucket method was applied.

5.3.1.5 Data Comparison

The MR data quality and consistency were checked by comparisons to design rules found in literature and to data achieved with conventional measurement techniques. This is comparison is presented for the heated case.

During MRT measurements temperature measurements were conducted utilizing the FOPs. In addition to that temperature measurements outside the scanner were conducted using TCs. Velocity measurements were performed using the LDV system. All systems are explained in detail in Sec. 3.4. Data was compared for the streamwise position Z = 0 mm, as marked in Fig. 5.11.

The temperature comparison of MRT and TC data was reported in Buchenberg et al. (2015). Good agreement was found at different radial and angular lines. Additional comparisons are shown in this thesis.

For velocity comparison the LDV head was traversed to Z = 0 mm, such that both LDV beams entered the PMMA pipe radially. In order to avoid reflections a small area ($\approx$ 4 cm^2) of the surface of the copper pipe was painted matt black. Radial velocity profiles between $7.5mm < r < 25mm$ were acquired at three different angular positions 0°, 22.5° and 45°. A spatial resolution of 0.5 mm in the radial direction was adjusted.
Since the laser beams of the cross-streamwise LDV velocity component entered through the curved surface of the PMMA pipe a positioning error occurs. This error is not linear for different radial positions. According to the recommendations found in *LDA and PDA Reference Manual* (2011), the LDV system was set to non-coincidence mode. The cross-streamwise velocity component was not considered in the data comparison. The following LDV operation parameter were chosen: The record mode was set to auto adaptive and the sensitivity was 1000. The center velocity for the streamwise measurement component was set to 0.05 m/s with a velocity span of $\pm$ 0.05 m/s. The center velocity of the cross-streamwise component was set to 0 m/s with a velocity span of 0.2 m/s. Data was sampled for 20 s or 20,000 bursts for each LDV component.

5.3.2 Results Heated Case

The heated case was chosen to be presented and discussed at first because it is the most often measured case. At first the measurement settings for MRT and MRV are given and the resulting data sets are discussed according to their data quality and consistency. Then the MRT and MRV data are presented and important features in the flow and temperature field are depicted and discussed. Finally, the MR data set is compared to data calculated using design rules and to data achieved by conventional measurement techniques.

5.3.2.1 MR Settings and Data Field

The MR system settings for these measurements are given in Tab. 5.3.

Tab. 5.3: Imaging parameters and MR settings of MRV and MRT measurements used for the heated case.

Parameters	**MRV**	**MRT**
TR/TE [ms]	56.8/10.2	29.1/20.0
flip angle [°]	7	7
pixel bandwidth [Hz/pixel]	455	455
voxel dimensions [mm]	1.1 isotropic	1.1 isotropic
FExPE lines	224x280	224x280
slices	64	64
channels	30	30
total acquisition time [min]	17	8
averages	1	1
Venc [m/s]	0.2	-
SNR	13	-
σ_{vel} [m/s]	0.014	-

Figure 5.14a shows the magnitude data of the complete FOV. The axes display the acquisition steps in FE, PE and SS direction (224×280×64). Between 0 ≤PE≤ 60 and 220 ≤PE≤ 280 the reference phantoms are placed. Figure 5.14b shows the magnitude data of the reduced FOV (176×47×46). Hereby, the area outside of the double pipe has been removed in order to save memory and for better data visualization. In FE direction (Z-direction) data was removed at the beginning (first four slices) and the end of the pipe (last 44 slices) due to the presence of artifacts. In the end region of the tube susceptibility artifacts arise which are caused by the PMMA flanges. These artifacts are mainly visible in the phase images of the MRT data caused and intensify by increasing TE. The FOV shows negligible artifacts in the magnitude data, which reflects the good quality of the setup.

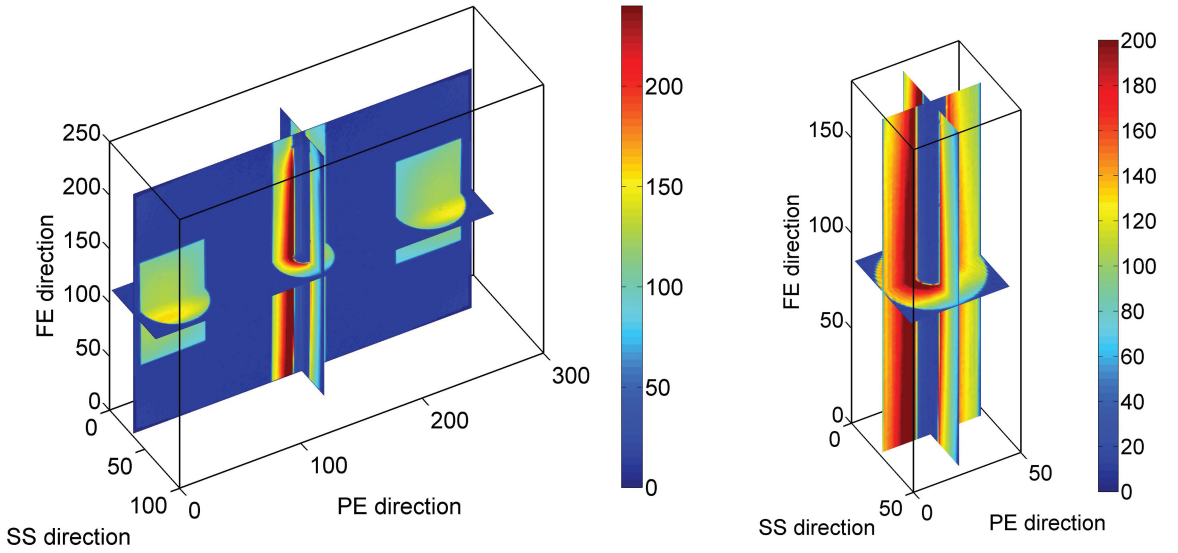

(a) Complete FOV.

(b) Reduced FOV (double pipe only, without reference phantoms).

Fig. 5.14: Slice plot of the signal magnitude taken from the MRV data acquired for the heated case.

5.3.2.2 Quality and Consistency of MRV Data

In order to assess quality of the achieved data, the SNR was defined in Sec. 2.3. The signal magnitude of the MRV data displayed as histogram plots is presented in Fig. 5.15 for the heated case. In Fig. 5.15a the complete FOV as shown in Fig. 5.14a was used, depicting a large peak for the signal background (magnitude value between 0 and 50) and a secondary, broader peak for the signal (magnitude value > 50). The bin around the magnitude value of 0 is populated, which is a result of the applied field distortion correction. Figure 5.15b shows the magnitude histogram of the reduced FOV (as given in Fig. 5.14b). Hereby, values for the average signal magnitude value and the standard deviation of the signal background are given. An SNR value of 13 results, according to Eq. 2.34, which is an appropriate value for this setup. Due to the Gaussian-like distribution of the signal peak a magnitude value of 50 was used as a threshold to separate the signal from the background. According to Eq. 2.36, the SNR value results in a phase noise error of $\sigma_{vel} = 0.014$ m/s. This value is relatively high.

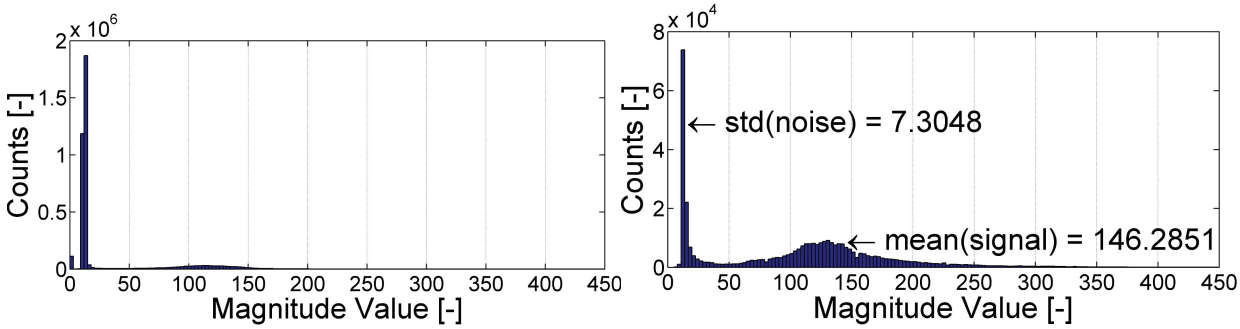

(a) Complete FOV.

(b) Reduced FOV (double pipe only, without reference phantoms).

Fig. 5.15: Histogram plot of the signal magnitude taken from the MRV data acquired for the heated case.

In order to show data consistency several integral values can be derived by spatial integration of the data. An estimate of how appropriate the flow model geometry is captured can be given by integration of the cross-sectional area. Therefore, all values exceeding the magnitude threshold are summed up. Fig. 5.16 shows the voxel-wise integrated cross-sectional area A_{int} re-

ferred to the calculated area $A_{calc} = \frac{\pi}{4}(D_o{}^2 - D_i{}^2)$. In this plot $\frac{A_{int}}{A_{calc}}$ is maximum 5% above 1 along the Z-coordinate. Hence, the applied spatial resolution and the magnitude threshold were chosen correctly. Nevertheless, the curve bends towards the ends and has no plateau. The general overestimation of the calculated area is caused by partial-volume artifacts. This affects the voxels at the walls partially containing water and material. The bending of the curve displayed in Fig. 5.16 is caused by inhomogeneities of the B_0-field. Even though the MR scanner used in this study provides highest quality of the magnetic field, the homogeneity of the B_0-field is spatially limited and drops with increasing spatial distance from the iso-center of the magnet. In a similar manner, the gradient field is inhomogeneous. Bending B-field lines are the result. As a countermeasure a field distortion correction can be applied which compensates the bending in FE and PE direction. As the distortion is not corrected in SS direction the curve shown in Fig. 5.16 is bend.

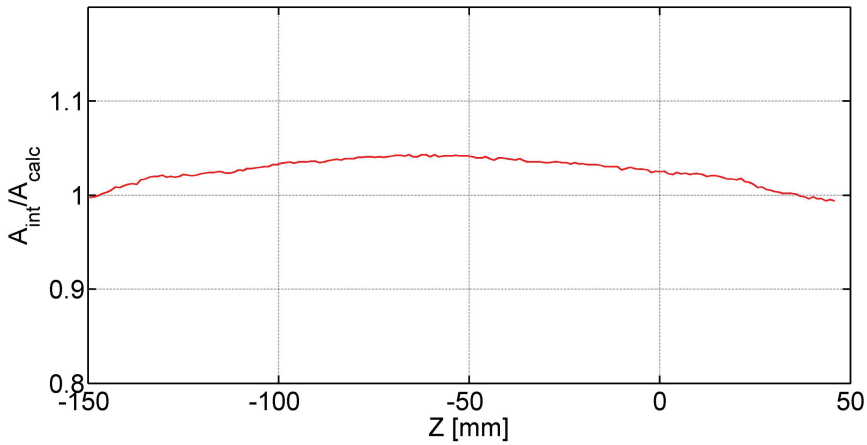

Fig. 5.16: Average of the voxel-wise integrated cross-sectional area A_{int} referred to the calculated area A_{calc}.

A quantity showing data consistency of the velocity data can be derived by averaging the velocity components U_x, U_y and U_z over the cross-section. The results are displayed in Fig. 5.17. As expected, the components in cross-stream direction and buoyancy direction U_x and U_y are zero. The streamwise component U_z attains an overall average of 0.051 m/s, which matches the calculated bulk velocity provided by the pump. Multiplied with the

cross-sectional area shows that the measured flow rate $\dot{V}_{bulk,meas} = 5.7$ L/min is slightly higher than the flow rate provided by the flow supply system. This deviation is less than 2%. The velocity measurements are equally affected by the field distortions as explained for the integrated cross-sectional area. Due to the averaging instead of integration the effects are less pronounced. A bending can be seen in the cross-sectional average U_z curve towards the ends.
As explained in Sec. 3.1.3 the velocity data was corrected using a 1st order correction algorithm utilizing the background phase image of the reference phantoms. To show the effects of the correction, equal calculations as for Fig. 5.17 have been performed for the uncorrected data set. The results are depicted in Fig. B.1 of Sec. B.2, which show that a background correction is obligatory.

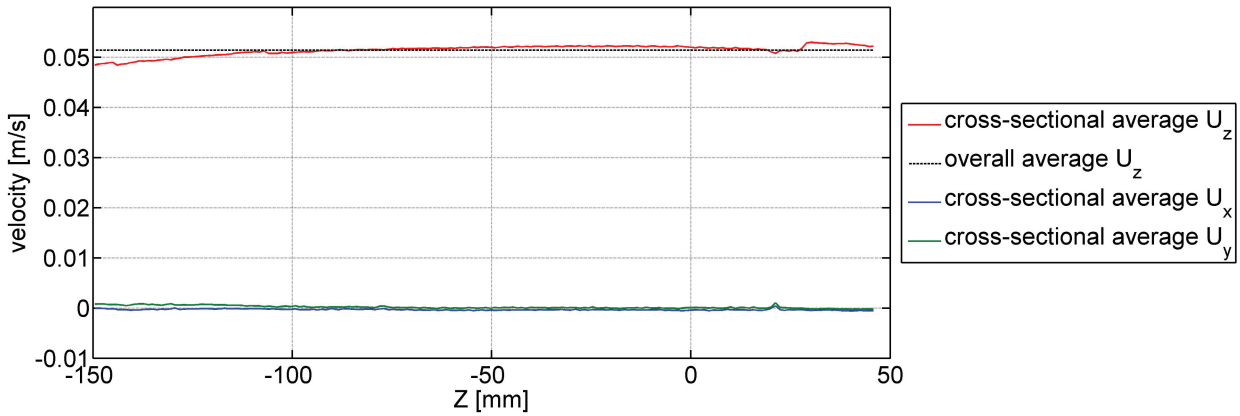

Fig. 5.17: Cross-sectional average of the velocity components U in X- ,Y- and Z-direction.

5.3.2.3 Consistency of MRT Data

Proving data consistency for MRT data is more complicated since many influences cause local discrepancies in the measured temperature field. In comparison to MRV, MRT is in general more sensitive to artifacts as TE is much longer.
Measurement errors mainly arise from susceptibility artifacts which are caused by field inhomogeneities (see Sec. 2.3.3.2). Objects positioned in

the vicinity of the flow model can alter the B_0-field. Hence, the reference phantoms were positioned in a certain distance to the flow model, which was found to be optimal. PMMA flanges also influence the magnetic field. MRT data acquired around the flanges cannot be used. Another source of artifacts arises from fluid acceleration. The measurement sequence is not acceleration compensated. The acceleration can be calculated using the material derivative of the velocity field given with Eq. A.9. As the velocity field is steady the partial derivative of the time can be neglected. The voxel-wise acceleration was derived for all velocity components and a maximum $\frac{\mathrm{D}U_z}{\mathrm{D}t} = 1.91 \frac{m}{s^2}$ was found. This is less than 10% of the acceleration sensitivity of the used MRT sequence. All possible errors are a main part of the work of the project partner and, hence, are not discussed in detail. An error discussion was already presented in Buchenberg et al. (2015).

Averaging over the streamwise cross-sections has been performed for the temperature difference field ΔT. In Fig. 5.18 the results are plotted versus the streamwise coordinate. The red curve shows the averaged ΔT progress averaged over an entire cross section. For this curve a two-point extrapolation line between the points Z=-150mm and Z=-130mm has been derived and plotted as black dashed line. Additionally, depicted as blue curve, an integration of ΔT has been performed for the region marked with ROI.
The ΔT curve has linear parts between -150 mm $\leq$ Z $\leq$ -130 mm and be-

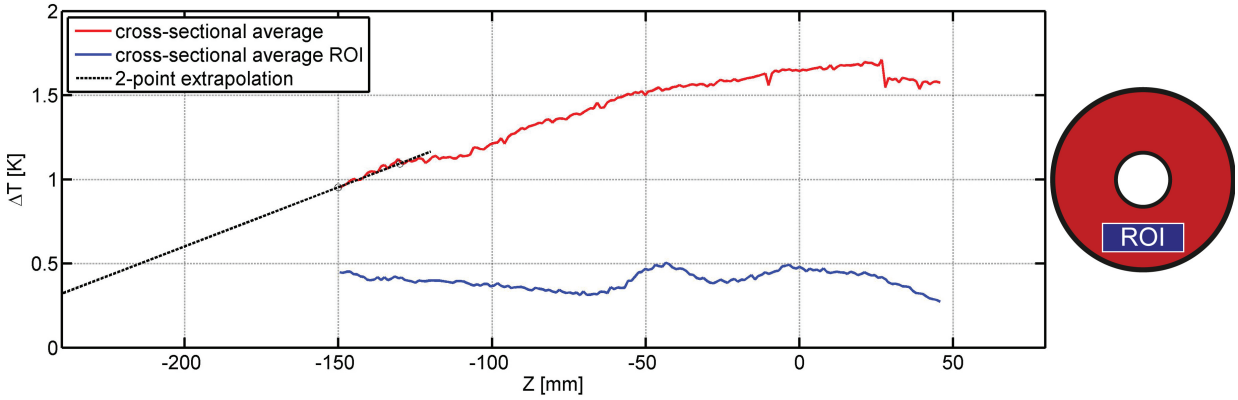

Fig. 5.18: Cross-sectional average of ΔT with two-point extrapolation and the average of the temperature difference field inside the region marked with ROI.

tween -100 mm $\leq$ Z $\leq$ -50 mm. At the end of the measurement region (Z =

40 mm) it converges to a fixed value. At Z > 25 mm a sudden temperature drop occurs, which is physically not possible. This is caused by the upstream located PMMA flange. Assuming that the wall temperature stays constant throughout the copper pipe, the cross-sectional average of ΔT is supposed to have an asymptotic behavior towards the beginning. This is discussed in Sec. A.2.5 for a constant wall temperature boundary condition. Hence, the performed extrapolation would not be valid. Nevertheless, following the extrapolation line to Z = -240 mm, an offset of $\approx$ 0.35 K remains.
A temperature offset is also obvious in the distribution derived by averaging ΔT over the region marked with ROI. The curve is colored blue in Fig. 5.18. The ROI is located below the copper pipe. In this region ΔT is expected to be 0 which was proved by additional measurements done with TCs and FOPs. Furthermore, the blue curve is not constant. Fig. 5.19 shows the cross-sectional ΔT distribution for two Z-locations Z = -80 mm and Z = -45 mm and depicts the location of the ROI. For Z = -80 mm the average ΔT value in the ROI is 0.32 K. For Z = 0 mm the average ΔT value is slightly higher at 0.43 K. Just below the copper pipe two areas with increased ΔT values are visible which are not connected to the hot area around the copper pipe. As the temperature is not increasing monotonically this cannot be caused by heat conduction. It is expected that these anomalies are caused by local artifacts which could be the effect of contaminants in the copper material or due to eddy currents. Yet the origin is not clear and part of the work of the project partner. Nevertheless, throughout the copper pipe an offset of approximately 0.3 to 0.4 K is present.
The discussion above leads to the assumption that the 0th order correction,

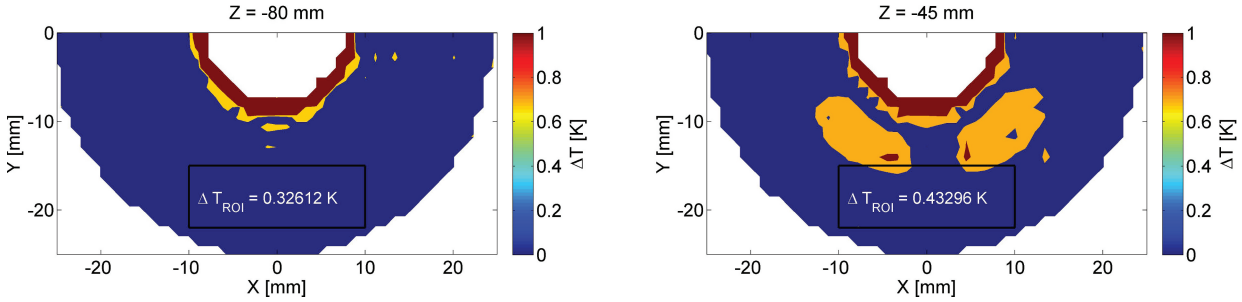

Fig. 5.19: Lower half of the cross-sectional ΔT distribution depicted for Z = -80 mm and Z = -45 mm. The ROI is displayed as black rectangle. The average ΔT value is listed inside the ROI.

utilizing the background offset of the reference phantoms, is not sufficient.

Furthermore, it is expected that the background phase of the MRT measurements is not constant. A linear correction has been applied for the MRV data set. A correction methods with which the MRT data can be corrected sufficiently is still an issue. Further suggestions are to be found in the work of the project partner.

Additionally, the integral values can be compared to values measured with conventional temperature probes or by comparison to analytical calculation rules as presented in Sec. 5.3.2.5. The energy equation for a simple heat exchanger is given with Eq. A.37. The overall heat transfer rate $\dot{Q}$ can be measured by measuring the flow rate $\dot{V}$ and the temperature difference ΔT:

$$\dot{Q} = \rho \dot{V} c_p \Delta T \tag{5.1}$$

In Eq. 5.1 ρ is the fluid density and c_p the fluid´s specific heat capacity. For the bulk flow a flow rate of 5.6 L/min was measured. The overall ΔT was measured utilizing TCs in the bulk probe port and in a port downstream the double pipe after a flow mixing device[5]. A ΔT of 1.1 K was measured resulting in a heat transfer rate transferred into the bulk flow of $\dot{Q}_{bulk,TC} \approx 440$ W. In the inner flow a temperature drop of 0.35 K was measured utilizing the FOPs. A flow rate of 20 L/min was measured. The amount of heat transferred from the inner flow was $\dot{Q}_{inner,FOP} \approx 480$ W. Both values of $\dot{Q}$ are in good agreement. As the PMMA pipe and the PA parts are not perfectly adiabatic a heat transfer loss over the channel walls can be expected.
Assuming that $\dot{Q}_{inner,FOP}$ is transferred into the bulk flow without losses, an overall ΔT of approximately 1.7 K is obtained throughout the double pipe. This value would be possible by extrapolating the cross-sectional averaged ΔT distribution shown in Fig. 5.18. Hence, from a thermodynamical point-of-view, the measured temperature maps are assumed to be trustworthy. This stands in contrast to the temperature offset present in the lower part of the double pipe and has to be considered in future studies.

[5] This mixing device was a pipe containing different grids which enhance flow mixing and, hence, a temperature mixing. This device was used only for the TC measurements.

5.3.2.4 Temperature and Velocity Field

In order to understand the characteristics of the temperature and velocity fields contour plots of the three velocity components and the temperature difference are depicted in Fig. 5.20 for Z = 0 mm.
In Fig. 5.20a the temperature difference distribution is shown. Typical patterns occurring in free and mixed convection flows as described in Chap. 1 are present. At fist the thermal boundary layer surrounding the copper pipe is visible. Herein, at the top of the copper pipe the highest temperature differences are measured with $\Delta T_{max} = 21$ K. The thin stripe of high ΔT marked with (I) is termed plume. At the upper PMMA wall hot fluid is present in two eccentrically aligned lobes, which are symmetrical to the Y-axis. This secondary temperature pattern is denoted with (II). The three velocity components are given in Figures 5.20b, 5.20c and 5.20d, respectively. In the regions of the plume and the secondary temperature pattern, U_z is decreased. In the temperature boundary layer it becomes zero. The U_z-plot reveals that the velocity boundary layer at the PMMA pipe wall is larger than the one at the copper pipe wall. Likewise ΔT, U_z is symmetric to the Y-axis. As the values of U_x and U_y are relatively small compared to the Venc, both components are very noisy. Nevertheless, positive velocity values in buoyancy direction (Y-direction) are visible. This upward motion coincides spatially with the plume and the temperature boundary layer and can be interpreted as a result of the buoyancy forces resulting from the density differences. These structures can be observed in detail in Fig. 5.21, showing the temperature difference contour overlayed with the in-plane velocity vectors. Coinciding with the secondary temperature pattern is a vortex pair. The formation of the vortex pair is obvious in all three velocity components shown in Fig. 5.20. In the area around the copper pipe the fluid particles heat up and form the plume. Inside the plume the fluid particles are accelerated and form a jet. This part has the lowest U_z values. During their upward motion inside the plume the fluid particles lose their high temperature and mix with the surrounding fluid. At the top wall, the fluid jet splits and feeds the vortex pair and the secondary temperature pattern.

The development of temperature and velocity field at Z = -150 mm is shown in Fig. 5.22. As the inlet velocity profile into the double pipe was not within the FOV, an impression can be given by focussing on the streamwise velocity distribution shown in Fig. 5.22 b). Inside the nozzle the flow is

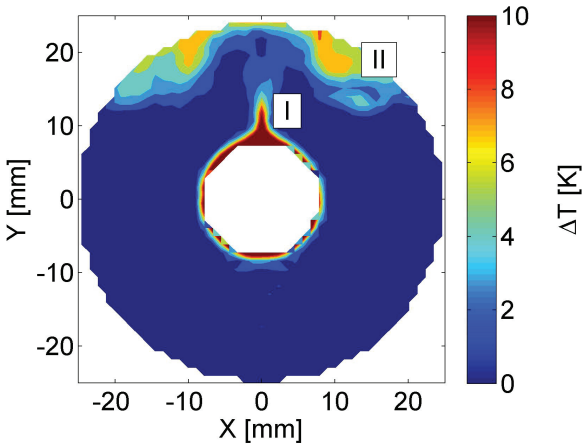

(a) Temperature difference. (I) marks the plume and (II) the secondary temperature pattern.

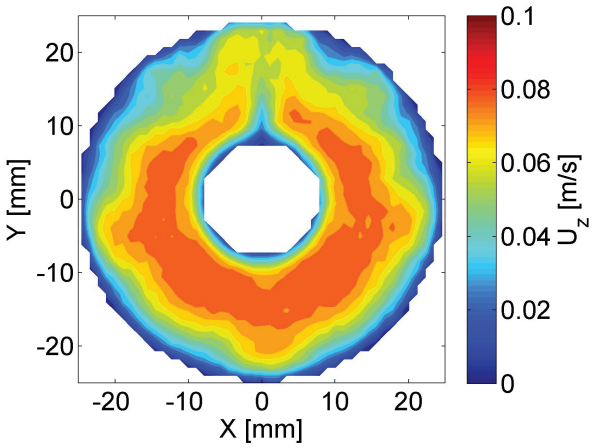

(b) Velocity component in Z-direction

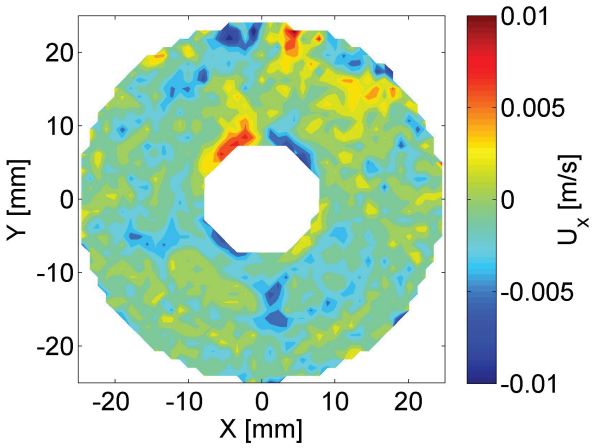

(c) Velocity component in X-direction.

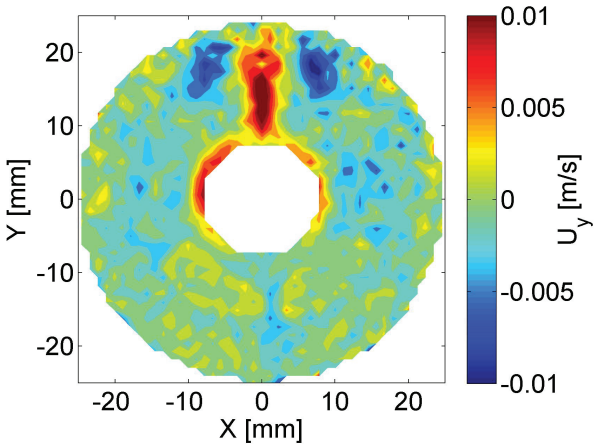

(d) Velocity component in Y-direction.

Fig. 5.20: Color coded temperature difference contours and velocity component contours extracted at the streamwise position Z = 0 mm.

separated into four segments due to the struts that hold the conjunctions for the copper pipe and the inner flow outlet. The velocity boundary layer thickness has to grow along the struts. This leads to shear layers and the formation of wakes downstream the struts. U_z is distributed symmetrically at the beginning of the double pipe but not uniformly. With increasing Z the wakes at three, six and nine o'clock diminish and finally recover the velocity value of the bulk flow. This can be seen in Figure 5.20b. The U_z values in the wake at twelve o'clock are smaller than in the wakes at three, six and

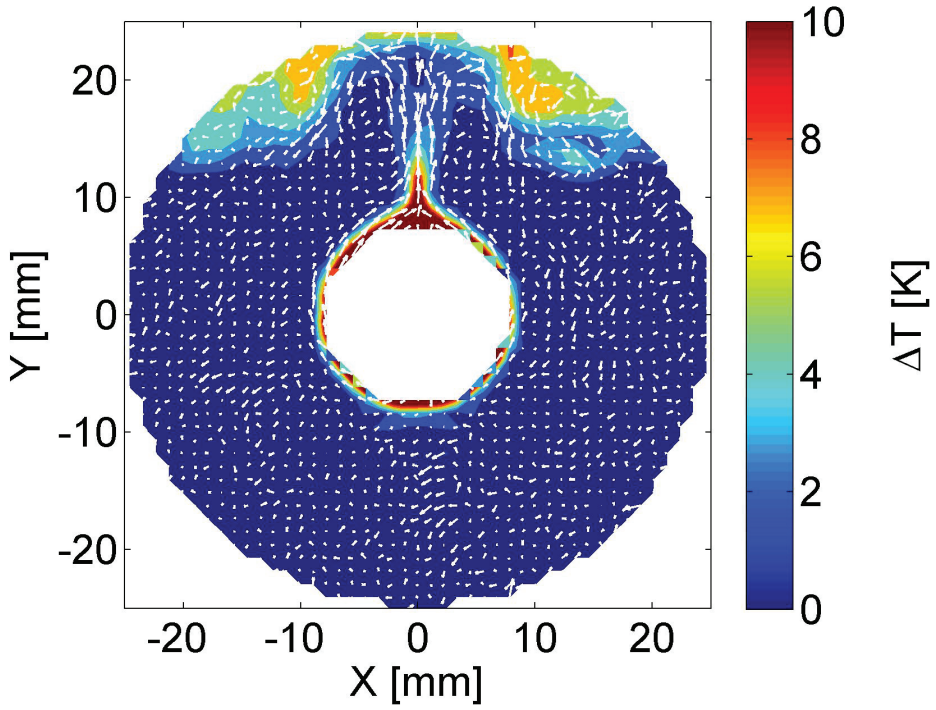

Fig. 5.21: Color coded temperature difference contours with overlaid in-plane velocity vectors extracted at the streamwise position Z = 0 mm.

nine o'clock. Starting with the exposure of the copper pipe to the bulk flow the thermal boundary layer start to develop. This evokes buoyancy forces and the formation of the plume. The plume, in turn, has the effect of an obstruction in the flow and, thus, has a strong influence on the velocity field. This prevents the wake at twelve o'clock from recovering. The velocity values further decrease in that area. This corresponds to the shape of the plume visible in Fig. 5.22 a). In this plot also the secondary temperature pattern develops. Two small lobes right at the top wall of the PMMA tube have formed at that streamwise position.

In order to follow the development progress of the temperature and velocity field a visualization of U_z and ΔT is shown in Fig. 5.23. Contours of slices at different Z positions from Z = -125 mm to Z = 25 mm are depicted. The U_z flow pattern shown in Figure 5.23a is similar at all Z-positions. Most obvious is the regression of the wakes, which is completed in the third slice (Z ≈ -75 mm) and the proceeding reduction of the velocities in the wall-near region of the secondary temperature pattern. In Fig.

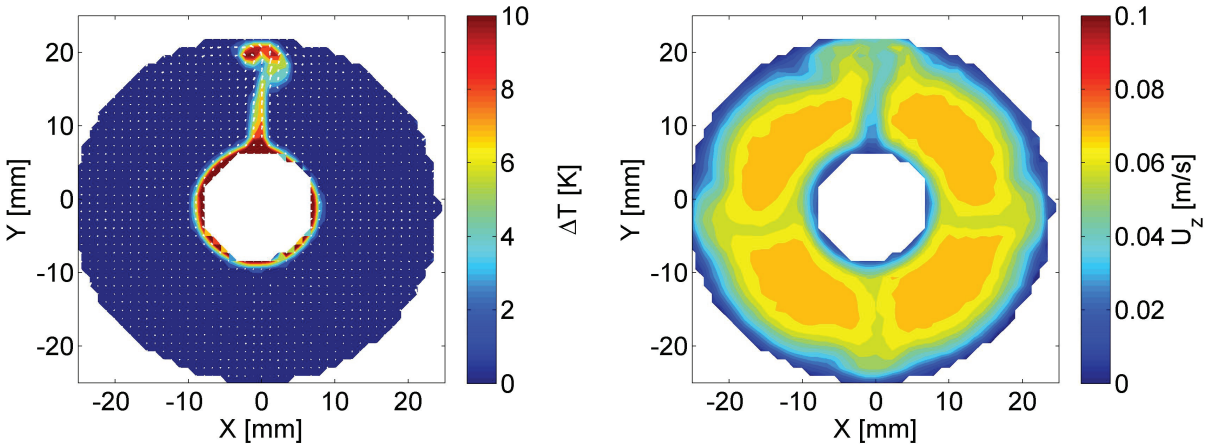

(a) Temperature difference with in-plane velocity vectors.

(b) Velocity component in Z-direction

Fig. 5.22: Temperature difference contour plot and velocity component contour plot extracted at the streamwise position Z = -150 mm.

5.23b the development of the temperature difference field is shown. Further upstream the plume is a very distinct line, which reaches from the PMMA pipe to the wall. Note that the double pipe begins at Z = -240 mm. At Z = -25 mm the upper part of the plume starts to spread and becomes more diffuse, which indicates enhanced mixing in this region. At the beginning of the double pipe the secondary temperature structure is centered at the tubeś cross section. With increasing Z, both structures shift symmetrical along the wall curvature. Thereby, they expand in space.

An additional illustration of the temperature difference field (Fig. 5.24)shows this development. At the beginning (Z = -125 mm) the development of the secondary temperature pattern is obvious. In an early stage the plume is characterized by high ΔT values and increased velocities in Y-direction. This changes at a certain downstream Z-position (Z $\approx$ -25 mm). Ar first, the plume feeds the secondary temperature pattern with hot fluid. Further downstream the distinct plume line decreases in size. Additionally, the velocity component in the Y-direction reduces. Between the copper pipe and the PMMA pipe wall, the ΔT-field has a stronger mixing than further upstream. This leads to the assumption that at that point the velocity field changes from laminar to transitional or even turbulent. A measure for that can be the local Reynolds number calculated for each voxel. This was depicted as contour plots in Fig. B.2 in Sec. B.2. The local Reynolds number was de-

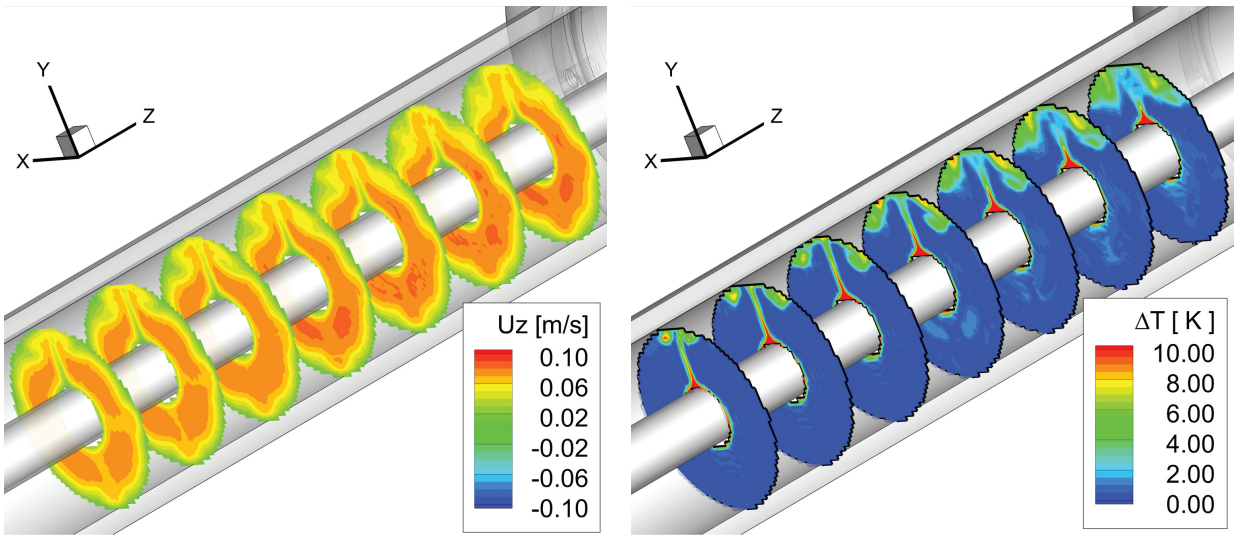

(a) Velocity component in Z-direction. (b) Temperature difference map.

Fig. 5.23: Visualization of streamwise velocity component and temperature difference contours at subsequent slices between -125 mm $\leq$ Z $\leq$ 25 mm.

rived with the streamwise velocity value and the temperature-dependent kinematic viscosity (temperature taken from the ΔT maps) for each voxel. The redistribution of the Re number with increasing Z can be seen. An increasing Reynolds in certain regions

5.3.2.5 Comparison to Calculation Rules

In literature many calculation rules are available, with which the estimation of heat transfer coefficients for different kinds of heat exchangers is possible (Stephan, 1962). One of these rules has been developed by Stephan (1962) for the concentric annulus. They can be applied for laminar or turbulent flow and for either solely heat transfer over the walls of the inner or bulk pipe or heat transfer over both pipe walls. For laminar flow the rules were derived analytically from basic thermodynamic and fluid mechanic equations. Additionally, the thermal and hydrodynamical entry region can be considered. The manner in which calculations were performed is shown in Sec. B.1.
In the context of the presented analysis it is insightful to compare the es-

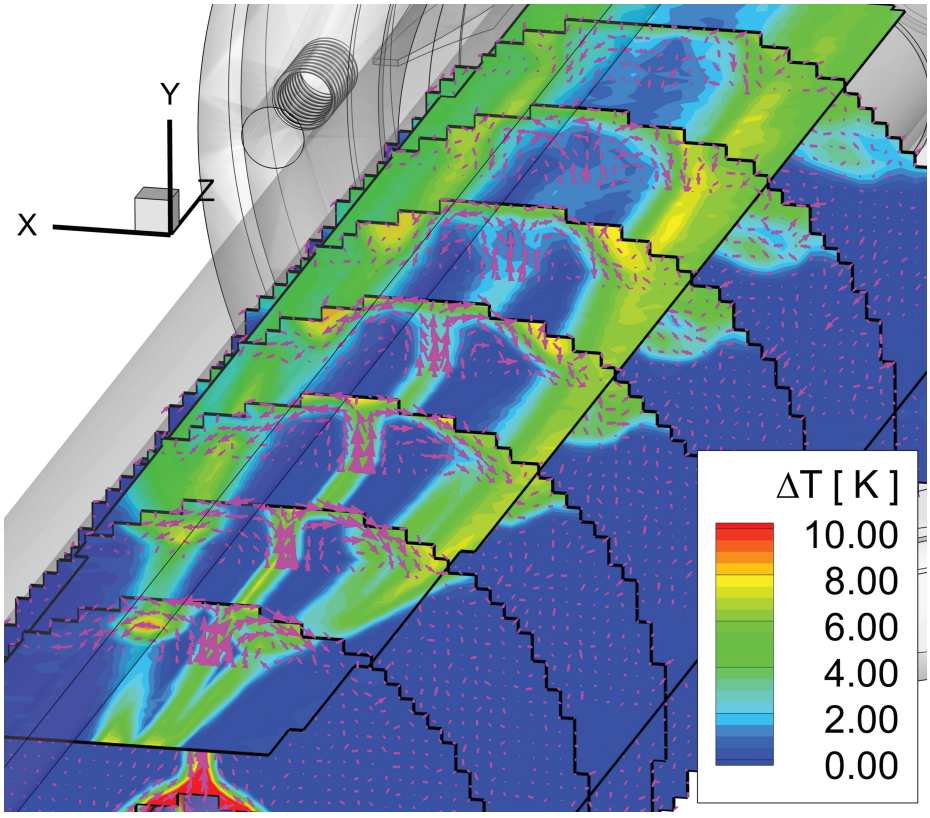

Fig. 5.24: Visualization of the temperature difference contours at subsequent slices between -125 mm $\leq$ Z $\leq$ 25 mm. In-plane velocity vectors were applied and an additional slice was inserted in the X-Z-plane at Y = 18 mm.

timated thermodynamic parameters with data measured with MRT/MRV, data measured with in-situ applied FOPs and data monitored with the systems of the flow apparatus. In order to do so, temperature-dependent fluid properties (e.g. ν, Pr, ρ, etc.) of water at a constant pressure of 1 bar are needed. They were taken from VDI (2010) and Wagner and Kretzschmar (2008). An excerpt of the fluid properties of water is given in Tab. C.1.

Three length scales are important, which characterize the thermodynamics of the presented double pipe setup. The hydraulic diameter is defined as

$$D_h = D_o - D_i \tag{5.2}$$

where D_o is the inner diameter of the outer pipe and D_i is the outer diameter of the inner pipe. The pipe length L can be nondimensionalized by division of the hydraulic diameter and the Péclet number, yielding

$$L^+ = \frac{L}{D_h Pe} = \frac{L}{D_h RePr}. \tag{5.3}$$

Nondimensionalizing L^+ with the Péclet number considers the heat transport due to convection versus the heat transport due to conduction. The higher Pe gets, the smaller L^+ becomes (all other parameters are unchanged), which leads to an increase of the Nusselt number. This relation can be seen in Fig. 5.25. Furthermore, the diameter ratio

$$k = \frac{D_i}{D_o} \tag{5.4}$$

can be defined. The presented length scales influence the heat transfer process and, hence, the Nu number with Nu=f(1/L$^+$, k). Assuming laminar mixed convection, the Nu number can be assessed graphically from Fig. 5.25 for a given L$^+$ and k. For the presented setup L$^+$ is 7.2·10^{-4} and a k is 0.3, which results in an expected Nu number between 20 and 30.

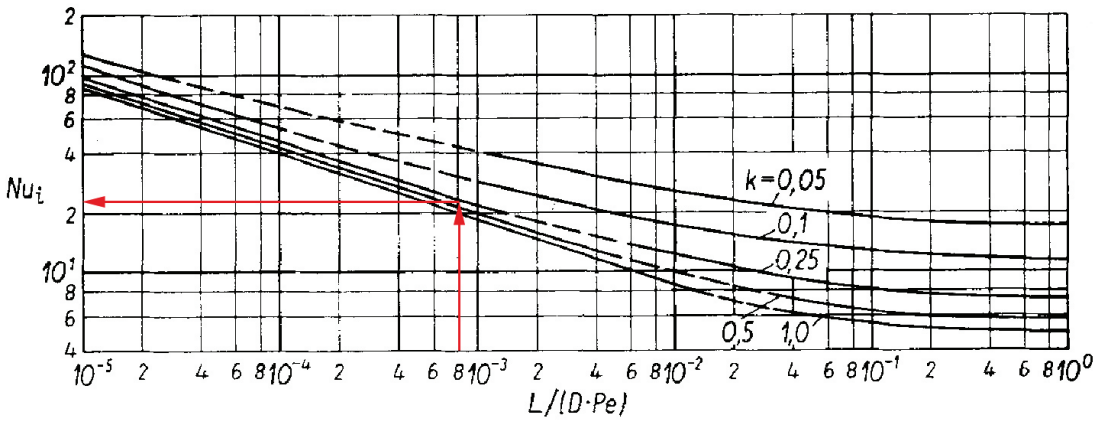

Fig. 5.25: Nu number over modified dimensionless length. Graphic taken from Stephan (1962). This image is reused with permission from John Wiley and Sons. Arrows show the path how to graphically obtain the Nusselt number for the given setting.

For the heated case characteristic parameters were derived from the measured data[6] or estimated using the proposed calculation rules. Additionally, important dimensionless numbers as presented in A are calculated from the measured or estimated data. One special value is the wall temperature of the copper pipe T_w, which could not be measured with TCs or FOPs. Hence, for all calculations T_w was chosen to 50 °C. All results are composed in Tab. 5.4.
In general an encouraging agreement is found between the MRV/MRT data and the estimated values using the proposed calculation rules. Especially the values of $T_{bulk,out}$, $\dot{Q}_{bulk}$, ΔT_{ln}, Nu_{bulk}, α_{bulk}, Ri and Gr are similar. This shows that both the measured data and the proposed calculation rules are comparable.

5.3.2.6 Comparison MRV and LDV

There is only limited research applying MRT in combination with MRV found in current literature. As the presence of a temperature distribution also alters the flow profile, a comparison of MRV data with LDV measurements was achieved using the system described in Sec. 3.4 with equal flow and temperature conditions.
Data was collected along radial lines for the heated and homogeneously heated case. This was done at the streamwise position of Z = 0 mm. The results are presented in Fig. 5.26 showing line plots of the streamwise velocity component U_z over the radial position R. The LDV RMS values were added as an error envelope.
For both cases the acquired LDV data show good qualitative and quantitative agreement with the MRV data. Only in the heated case (Fig. 5.26b) between 7.5 mm $\leq$ R $\leq$ 9 mm a slight deviation between LDV and MRV is obvious. A possible reason for this can be a wrong data extraction. Furthermore, in this area the velocity error of the MRV data due to phase noise is of the same magnitude as the measured velocity.

[6] The measured flow rate was taken from the flow supply system and the temperature data from the FOP system. All values displayed in red color are measured with MRV and MRT.

Tab. 5.4: Characteristic values of the double pipe setup achieved for the heated case. The second column shows experimental (exp.) parameters, which are predetermined by the geometry or by the flow apparatus adjustments. The third column shows values which are calculated (calc.) from the first column or derived from measured data. The values displayed in red are from the presented MRV and MRT data. The forth column depicts estimated (est.) values, which were achieved utilizing the calculation rules given in Sec. B.1.

Characteristics	**Exp. Parameter**	**Calc. Values**	**Est. Values**
L	320 mm		
L^+		$7.2{\cdot}10^{-4}$	
D_i	15 mm		
D_o	50 mm		
D_h	35 mm		
k		0.3	
$\dot{V}_{bulk}$	5.6/5.7 L/min		
U_{bulk}		0.05/0.052 m/s	
$\dot{V}_{inner}$	20 L/min		
U_s		2.17 m/s	
$T_{bulk,in}$	21 °C		
$T_{bulk,out}$	22.2 °C		22.2 °C
$T_{inner,in}$	50 °C		
$T_{inner,out}$	49.65 °C		
T_w			50 °C
ΔT_{ln}		28.4	28.4 K
$\dot{Q}_s$		480 W	
$\dot{Q}_{bulk}$		470 W	481 W
Re_{bulk}		1,900/1,900	
Re_{inner}		55,000	
Nu_{bulk}		27	28
α_{bulk}		470 W/m^{2}K	482 W/m^{2}K
Gr		$2.8{\cdot}10^6$	$2.9{\cdot}10^6$
Ri		0.8	0.8

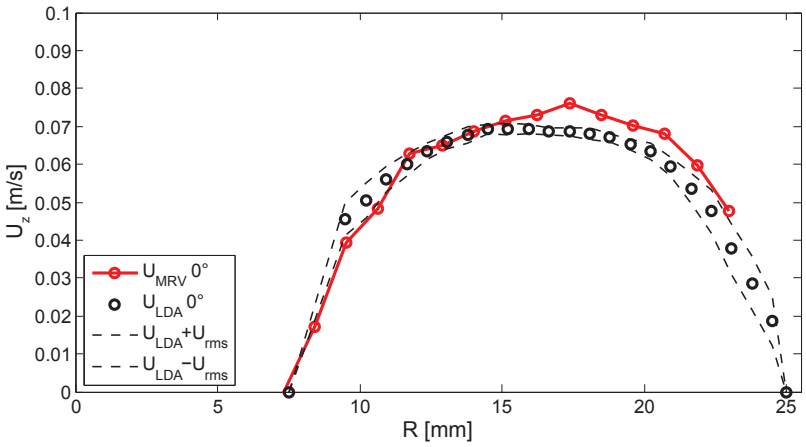

(a) Homogeneously heated case, MRV and LDV at 0°

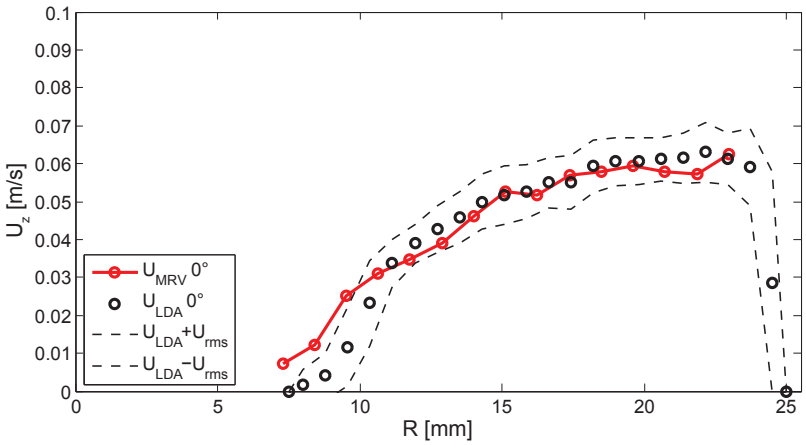

(b) Heated case, MRV and LDV at 0°

Fig. 5.26: Comparison of the streamwise velocity component U_z for MRV and LDV. Data was obtained for the heated and the homogeneous case at Z = 0 mm.

5.3.2.7 Comparison MRT and TC/FOP

Conventional temperature measurement systems as explained in Sec. 3.4 have been used for temperature monitoring and evaluation, as well as data comparison. Therefore, FOPs were utilized during MRT measurements at different fixed locations of the double pipe model marked in Fig. 5.11. Results have already been used for the calculations shown above. In Buchenberg et al. (2015) FOP data were used for temperature error quantification of the homogeneous test case. A temperature Root Mean Square Deviation

(RMSD) of 0.5 K was calculated for this case and a radially and angularly fixed FOP position.

Additionally, the TC system was used for temperature measurements in a modified double pipe setup during the work of this PhD thesis. A second PMMA pipe was constructed comprising an elongated hole positioned downstream of Z = 0 mm. Through this inlet an L-shaped TC was inserted so that the probe head was positioned at Z = 0 mm facing the flow. The TC could be traversed radially into and out of the inlet and the PMMA pipe could be rotated to achieve different angular positions. Due to the L-shape of the TC sheath, a maximum radial position of 23 mm could be traversed. Two radial lines and one angular line were obtained using TCs in the upper half of the PMMA pipe. The measurement positions of the TC and the points that were extracted from the MRT data are shown in Fig. 5.27. For each measurement position, data was sampled for at least 60 s with a

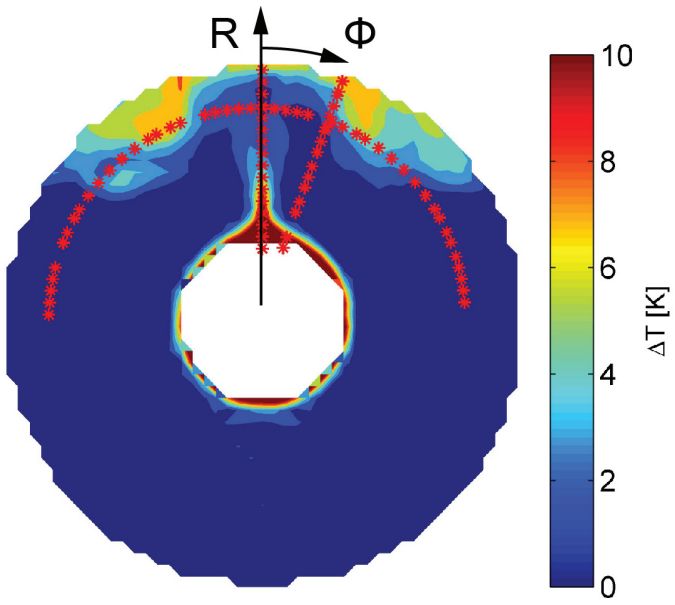

Fig. 5.27: Radial and angular lines extracted from MRT data and obtained with thermocouples. Radial and angular coordinate vectors are depicted.

sampling frequency of 10 Hz and averaged during the post-processing. Additionally, the RMS value could be calculated and is depicted as error bar. Between traversing and acquisition a pause was made to allow the flow and temperature field to settle to initial conditions.

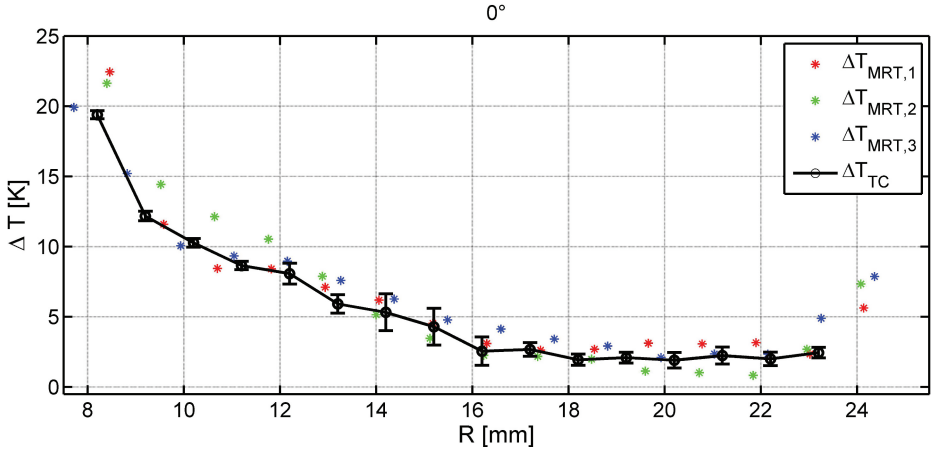

(a) Comparison of MRT data and TC data for a radial line at $\Phi = 0°$.

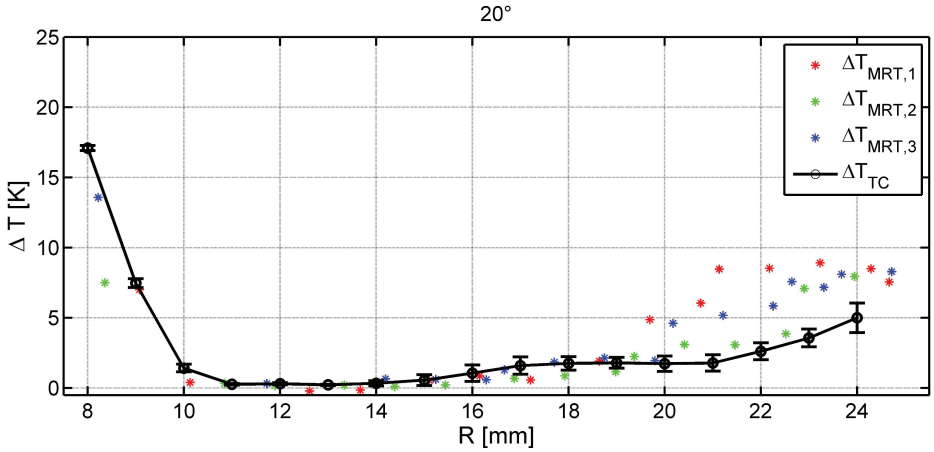

(b) Comparison of MRT data and TC data for a radial line at $\Phi = 20°$.

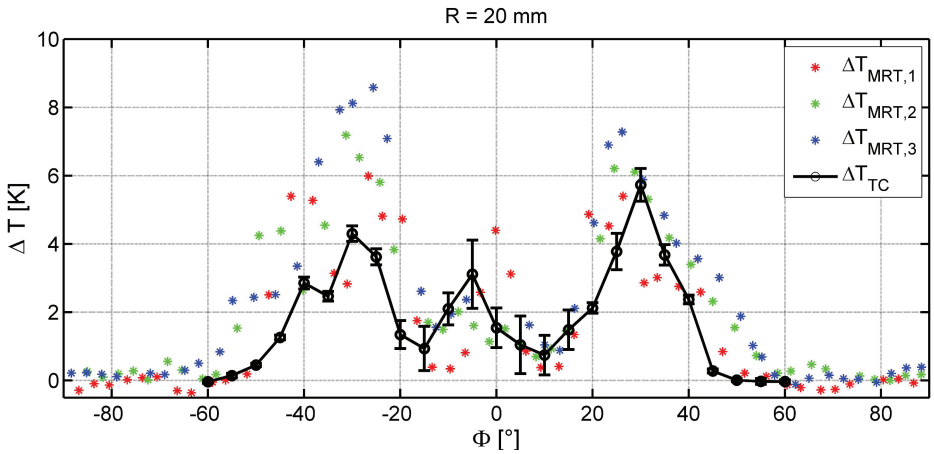

(c) Comparison of MRT data and TC data for an angular line at R = 20 mm.

Fig. 5.28: Radial and angular line comparisons of MRT data and TC data measured at the streamwise position Z = 0 mm (adapted from Buchenberg et al. (2015)).

The TC data and the MRT data set $\Delta T_{MRT,1}$ in Figure 5.28a and Figure 5.28c were already presented in Buchenberg et al. (2015). The data shown in Figure 5.28b was not shown before. Additional MRT data ($\Delta T_{MRT,2}$ and $\Delta T_{MRT,3}$) obtained at different days with similar MR settings were added. $\Delta T_{MRT,2}$ equals the measurement data presented in this chapter.
Good qualitative and quantitative agreement between MRT and TC data is found for the radial line plots. The data depicted in Figure 5.28a match well for all positions. The ΔT increase towards the end is not captured by the TC data. A good qualitative and quantitative agreement can be observed in Figure 5.28c for R ¡ 20 mm. Towards the outer radius, ΔT increases stronger for the MRT data than for the TC data. The MRT data set $\Delta T_{MRT,2}$ follows the TC curve until R = 23 mm. Figure 5.28b shows a good qualitative agreement. Both techniques capture the w-shape of the temperature distribution. A sufficient quantitative agreement is found for the right lobe (20°$< \Phi <$ 60°). Larger discrepancies are found for the left lobe (-60°$< \Phi <$ -20°) and the center region (-20°$< \Phi <$ 20°). In the left lobe the MRT data exceeds the TC curve with a maximum of 4 K. The peak in the center region (plume) is shifted towards negative Φ. Hereby, the MRT data sets show different behavior. $\Delta T_{MRT,1}$ is centered, whereas $\Delta T_{MRT,2}$ and $\Delta T_{MRT,3}$ are also shifted towards negative Φ.
According to Buchenberg et al. (2015), a measure of how good the MRT data curve fits to the TC data curve is the RMSD value calculated for the ΔT profiles:

$$\mathrm{RMSD} = \sqrt{\frac{\sum_{i=1}^{n} \left(\Delta T_{MRT,k}(i) - \Delta T_{TC}(i)\right)^2}{n}} \quad \text{with } k = 1, 2, 3 \tag{5.5}$$

In order to do so, the MRT data were interpolated on the same radial or angular grid as the TC data. The results are listed in Tab. 5.5. The calculated RMSD values lie between 1.00 and 2.71 K for all data sets, which is above the RMSD value calculated for the homogeneous case with the FOP data measured at a fixed position in the flow field. The $\Delta T_{MRT,2}$ data set shows the best overall fit. The lowest RMSD values are found for the radial curves at $\Phi = 0°$. All three MRT data sets have similar values. The reason for that could be the reduced streamwise velocity values compared to the other regions in the flow field. Still, other reasons for the temperature deviation have to be discussed.

Tab. 5.5: ΔT-RMSD values in [K] calculated with Eq. 5.5 for the $\Delta T_{MRT,k}$-data and ΔT_{TC}-data.

	$\Delta T_{MRT,1}$	$\Delta T_{MRT,2}$	$\Delta T_{MRT,3}$
$\Phi = 0°$	1.00	1.67	1.18
$\Phi = 20°$	2.71	1.19	1.79
R = 20 mm	1.57	1.61	2.22

In Buchenberg et al. (2015) an extensive discussion of the sources of errors was presented. The addressed points were errors due to noise, susceptibility, displacement, acceleration and the experimental stability. They come to the conclusion that the majority of the proposed errors are small for the presented experimental setup. Errors due to field drifts are expected to be the main error source. The ΔT progress of the MRT data presented in Fig. 5.28 is very similar for all data sets, although they were acquired on different days. This supports the assumption that the experimental setup is stable and MRT is repeatable. Assumed that distinct errors are present in all MRT data sets, the errors are reproduced in every MRT acquisition. This implies, that the errors are systematic and, hence, can be corrected by an improved calibration. This is still an issue for further work.
On the other hand, measurement errors are produced by using invasive measurement techniques as reviewed in Sec. 1.3.2.1. The presence of the TC head and sheath as well as the modifications of the PMMA pipe can alter the flow profile significantly. This also influences the temperature field, which can lead to wrong temperature measurements. Measurement uncertainties arising from positioning errors of the TC head are not quantifiable. Co-registering the TC data with the MRT data is difficult. Picking the corresponding line from the MRT data is nearly impossible. In addition to that the fine structures in the temperature field have to be captured by the rather thick head of the TC (approximately 1 mm^2). For the double pipe setup it is recommended to apply a more suitable temperature validation technique, such as PIT or TSP.
However, the results shown in Fig. 5.28 and the ΔT-RMSD values listed in Tab. 5.5 are promising and show a good qualitative and a quantitative agreement within a temperature range of 1 to 3 K. Additionally, the difficulty of using invasive probes becomes obvious and the need for further validation and calibration of the MRT data. Nevertheless, the double pipe is expected

to be a suitable experiment for utilizing MRT because main sources of error due to fluid motion (displacement and acceleration) are small.

5.3.3 Results Cooled Case

The cooled case was chosen because it has certain advantages over the heated case. Since the measurement fluid is likely to degas at the hot copper pipe wall air bubbles can emerge. They lead to local susceptibility changes and, hence, to measurement errors. This is not taking place when the copper pipe is fed with cold fluid compared to the bulk flow.
According to the heated case, a similar but bottom-up flow and temperature field is expected. Hot fluid is lifted. Cold fluid sinks to the bottom. A short analysis and discussion for the cooled case is given in the following section.

5.3.3.1 MR Settings and MR Data

The MR system settings are given in Tab. 5.6. For these measurements the whisper gradient settings were applied, which reduced the maximum gradient slew rate to 50 mT/m/ms in order to reduce eddy current artifacts. This leads to an elongation of TR and, hence, of the total acquisition time. For the MRT measurements the bandwidth was decreased to reduce noise. The very low Venc value leads to aliasing in the U_z velocity component. These artifacts could be corrected using the Velomap tool. Equal correction methods as applied in the heated case were used for the velocity and temperature fields.

Plots showing the voxel-wise integrated values (area, U, ΔT) are given in Fig. B.3, Fig. B.4 and Fig. B.5 in Sec. B.2. An average streamwise velocity of $U_{bulk} = 0.047$ m/s results in an overall volume flow rate of 5.3 L/min. The bulk flow outlet temperature is derived from the ΔT data to $T_{bulk,out} = 29.03°C$. This results in an overall heat transfer rate of $\dot{Q}_{bulk} = -348$W.

Tab. 5.6: Imaging parameters and MR settings of MRV and MRT measurements acquired for the heated case.

Parameters	**MRV**	**MRT**
TR/TE [ms]	62/11.5	32.1/20.0
flip angle [°]	7	7
pixel bandwidth [Hz/pixel]	455	120
voxel dimensions [mm]	1.1 isotropic	1.1 isotropic
FExPE lines	224x280	224x280
slices	72	72
channels	24	24
total acquisition time [min]	21	11
averages	1	1
Venc	0.05	-
SNR	9	-

5.3.3.2 Temperature and Velocity Field

Fig. 5.29 shows contour plots for the temperature difference field and the three velocity components. As expected, all distributions are similar to the heated case but mirrored on the horizontal line. Additional to that, The ΔT field is inverted with the minimum temperature present in the plume and in secondary temperature pattern. The velocity fields coincide with the plume. They show a downward motion of the fluid towards the bottom side of the copper pipe. The size of the secondary temperature pattern is less pronounced compared to the heated case, whereas the in-plane velocity components are of the same order. The components U_x and U_y are less noisy, which is an effect of the low Venc.

Due to the high quality the velocity components U_x and U_y can be transformed into the radial velocity component U_R and the angular velocity component U_Φ. The associated contour plots are depicted in Fig. 5.30 for the polar coordinate system displayed in the left contour plot.
This provides a better understanding of the in-plane fluid motion. Focussing on the U_Φ-component, the plume is fed by warm fluid passing the copper pipe in an angular motion. A downwash at $\Phi = 270°$ is obvious in

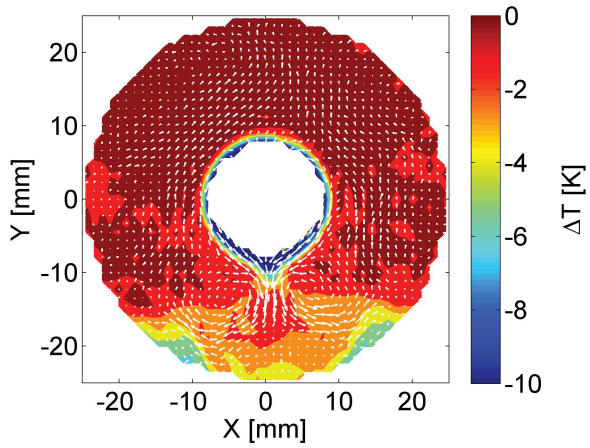

(a) Temperature difference with in-plane velocity vectors.

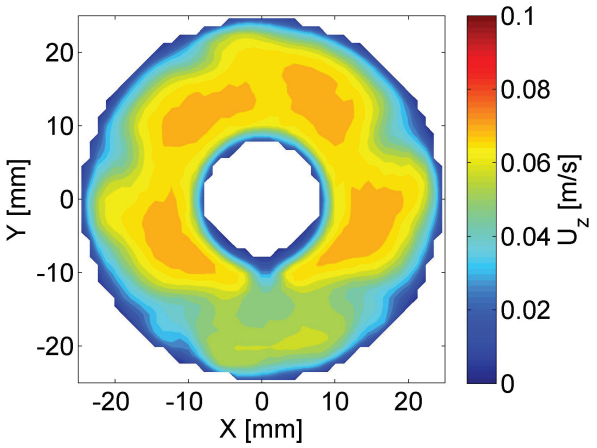

(b) Velocity component in Z-direction

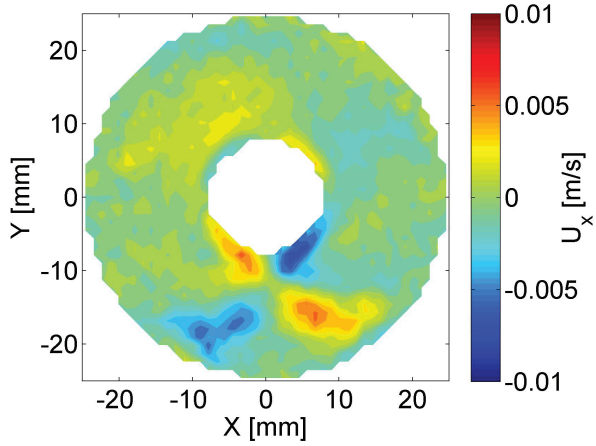

(c) Velocity component in X-direction.

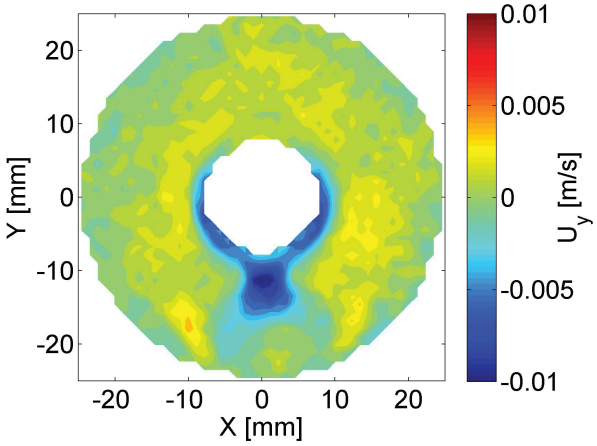

(d) Velocity component in Y-direction.

Fig. 5.29: Temperature difference contour plot and velocity components contour plots extracted at streamwise position Z = 0 mm.

the U_R-component. The fluid splits in to two vortices which leads to the development of the secondary temperature pattern. Due to the kinematic boundary condition at the PMMA pipe wall the downwash flow is deflected. U_Φ changes its sign and fluid moves in the opposite angular direction. A large scale vortex system develops. In the region between $\Phi = -45°$ and $\Phi = 45°$ (and mirrored on the other side), the plume is fed from the re-circulating fluid. The radial velocities are negative in this region. This is similar to the observations done in literature about the concentric annulus applied with pure free convection. In the present double pipe setup, the

vortex system is convected downstream with U_z. This is the reason for the three-dimensionality of the flow and the development of a complex mixed convection pattern.

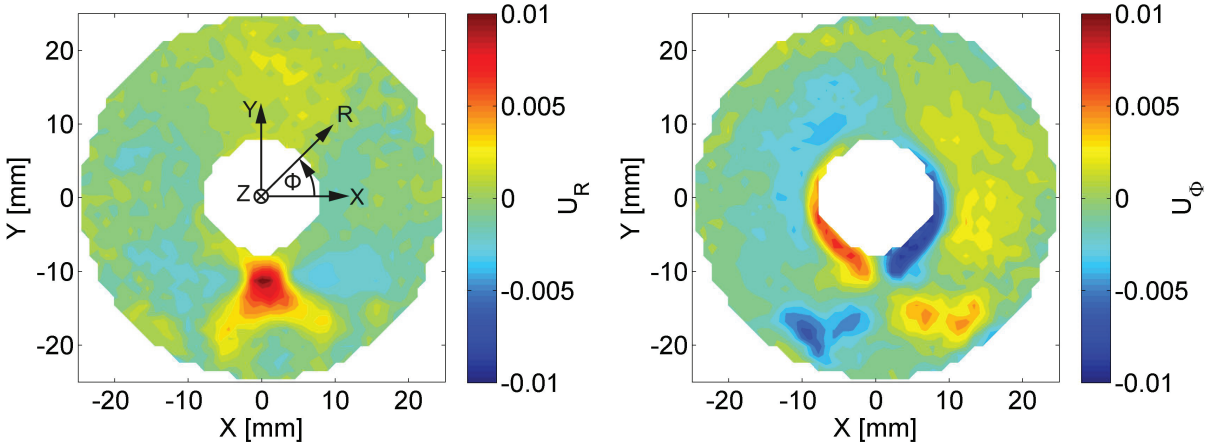

(a) Velocity component in R-direction. (b) Velocity component in Φ-direction.

Fig. 5.30: Contour plots of the radial and angular velocity component derived at streamwise position Z = 0 mm.

5.3.4 Conclusions

In this section a double pipe setup was explained. MRV and MRT measurements were acquired for a heated and a cooled case. For the heated case different fluid mechanical and thermodynamical integral quantities were calculated and compared to values taken from literature. Additional LDV and TC measurements were conducted and compared to the MRV/MRT data. A good agreement of the results was found. ΔT-RMSD values lie between 1 and 3 K. The flow and the temperature field were analyzed for the hot and the cooled case. The development of the three-dimensional temperature pattern is linked to the presence of a complex vortex system, which is typical for most mixed convection flows. Issues with the MRT data were addressed. This involved the background correction method and the data validation. Considering the main error sources proposed by Buchenberg et al. (2015)

the double pipe is expected to be an adequate setup for applying MRT. This supports the trustworthiness of MRT and MRV for future thermofluid setups.

Chapter 6

Closing Remarks

6.1 Summary and Conclusions

State-of-the-art MRI techniques applied to thermofluid applications were described in this thesis. The results showed that MRV and MRT are applicable to a variety of different situations important to the engineering sciences and industries.

From a technological point-of-view, a variety of flow and temperature measurement techniques are available, each one with certain advantages and limitations. One main advantage of MRI is the possibility to measure in flow models with arbitrary complex geometries. In some problems the complexity is extremely high. Hence, conventional measurement techniques can only be utilized with an unreasonable experimental effort. The high spatial resolution of MRI in combination with the fast acquisition time was found to be superior than conventional techniques. However, MRI has certain limitations. In order to understand the features of MRI, the physical principles were summarized from an engineering perspective. MRV and MRT, as well as the accompanying procedures were explained. Limitations result from imaging artifacts that appear as local and/or spatial errors in the measurement data. The main sources are present due to disturbances in the magnetic and electro-magnetic environment of the MR machine. Major influences were the use of inadequately selected material, the improper

design or positioning of the flow model or insufficiently chosen MR parameters. MR techniques are still mainly a tool for medical diagnostics; thus, optimized for human use. The restriction to measure the proton of the ^{1}H isotope is at the current stage only reasonably for water flows. Optimal results are obtained when the experimental parameters can be adjusted so that they fit the spatial and temporal scales of the human as well as the flow and the temperature range. This limits the measurable applications, although the utilized MRI machines are state-of-the-art. Furthermore, MRI machines are not freely accessible as they are situated in medical centers. However, within the scope of this work cooperation with a medical center and medical physicists was established. Access to MRI machines was possible with restrictions in the temporal availability. Detailed knowledge about MR physics is obligatory for further improvements and the design of novel MR procedures. On the other hand, if procedures (e.g. MRV) are well-established, MRI is easy to apply, since elaborate calibrations or adjustments are not necessary. In addition to the conventional measurement techniques MRI techniques are a powerful engineering measurement tool.

The methodology chapter presented the components utilized during the experiments. The MRI system and the MR procedures were introduced and important considerations (mainly proposed by the project partner) concerning the flow model design were given. This was then transferred to the engineering perspective. All design rules were considered during the flow model construction. For the models used for MRT, different in-situ heating principles and their implementations were introduced. By evaluating the dimensionless quantities, a characterization of the fluid mechanical and thermodynamical setting was possible. A complex flow apparatus was a part of each experimental setup. This also included the upstream and downstream components of the flow model as well as several tools needed for temperature conditioning and secondary flow support.

Results were presented in two chapters. In the first chapter MRV was applied to thermofluid test cases with complex internal structures.
As a potential candidate for future compact heat exchangers, the flow through a tetradecahedral grid was measured. Important flow features were worked out that are important for heat transfer processes. The flow field was compared to LDV and CFD data and good agreement was found. A novel post processing approach was presented that utilized the MRV data to

estimate the temperature field. Thereby, the signal magnitude data served to separate the fluid from the structure and the velocity field was used as forced convection flow. This was found to be another unique feature of MRI, that information about the structure can be extracted from the data. The structure was prescribed with a certain surface temperature. The surface temperature was conducted into the fluid and finally convected downstream according to the measured velocity field. This approach showed promising results presenting further insights into forced convection flows.
As a second test case the flow through a one-to-one replica of a CANDU nuclear fuel bundle was presented. An MRV data set in this detail and that size has never been shown before for such an application. This is also the first time that a 3D3C velocity field of a CANDU fuel bundle was measured. By partially integrating the MRV data, integral flow rates through different fuel bundle regions were measured. Flow-induced mechanisms could be worked out, possibly limiting the coolability in certain regions of the CANDU fuel bundle. Such an approach needs 3D flow data with high spatial resolution. Critical points in the flow were analyzed that have to be considered for future designs. This is important for safety analyses in future research.
The second results chapter describes novel experimental setups for the utilization of MRT. Preliminary experiments are described that were performed to obtain first experience with MRT and to explore the capabilities and limitations of this novel technique. A simple pipe flow setup applied with different flow rates and different homogeneous fluid temperatures showed promising MRT results. Sources of artifacts which are pronounced when using MRT were identified and design considerations for future setups were made. A backward-facing step flow model utilizing ceramic heating elements was operated inside the MRI machine. The use of electric heating elements based on ceramics, in combination with a phase-locked MRI acquisition, was presented for the first time in literature. This alternative heating method worked well in the MR environment. Good results were obtained with 4D-MRV measurements. 4D-MRT measurements also worked, but the measured data were corrupted by strong susceptibility artifacts. A method for correcting these artifacts by modeling the susceptibility-induced phase changes of the ceramic parts was introduced. An exemplary two-dimensional temperature map showed good results.
A double pipe flow model was designed and applied to MRT and MRV. A copper pipe was used as an inner pipe. It showed an excellent MR applicability. Additionally, copper has an optimal thermal conductivity. The quality and consistency of the presented MRT and MRV results were assessed from

a fluid mechanics perspective. Integral quantities were derived from MRT and MRV data and compared to data acquired with LDV and TC measurement techniques. Furthermore, the results were compared to data calculated with analytical calculation rules. A good qualitative agreement was found for all comparisons. Important to mention is, that different MRT acquisition reproduced similar temperature fields. A quantitative comparison between TC data and MRT data was possible by computing the temperature RMSD. The values were between 1 and 3 K. For the homogeneous case the RMSD between MRT data and FOP data was 0.5 K (Buchenberg et al., 2015). One error source was attributed to the magnetic field drifts for which the employed correction method was found to be insufficient. Problems using invasive probes in such a sensitive mixed convection flow were addressed. An extensive error analysis given in Buchenberg et al. (2015) and in detail in the work of the project partner supports the assumption, that MRT is trustworthy for the double pipe setup and the measured ΔT maps are correct. Analyzing the flow and the temperature field of the double pipe revealed complex three-dimensional vortex structures and temperature patterns. They are unique for this setup and have never been discussed before in the literature. This shows the capabilities of MRV and MRT and the unique features of MRI techniques, which encourages to use these measurement techniques for future research in the field of thermofluids.

6.2 Outlook

MRI currently plays an important role in medical diagnostics of human or animal tissue. In future it will be crucial for the assessment of the human cardio-vascular system or as guidance tool in thermal therapy treatments. MRT for clinical use is still in a state of development.
MRI techniques proved their usability and applicability as a measurement tool for engineering problems. The utilization of MRT and the possibility to obtain three-dimensional temperature fields in complex flow models corroborates MRI as a tool for thermofluid sciences.

This thesis also prompts questions for further consideration. Unanswered points viewed from a technological perspective are as follows.

One major issue is the error quantification of MRI techniques. The signal-to-noise ratio is still an important quantity as it can be easily derived from the signal magnitude. In the past, research has been done to quantify the phase error of PCI acquisitions. Measurement errors (artifacts) arising from the interaction of the experiment with the MR system are still not quantifiable. An automatic detection and correction would be desired. In the current state, imaging artifacts have to be treated manually and are dealt with in a best practice manner. The choice of an MR-suitable flow model design as well as appropriate flow and temperature conditions are the solution used in this thesis to avoid measurement errors. Measurement errors arising from flow acceleration or high flow turbulence have not been considered and are the subject of research of the project partner. In order to do so, other experimental parameters have to be applied to the presented flow models or novel flow models developed. Accuracy and precision of MRT measurements have to be evaluated in a future study.
Despite the extensive error discussion and the comparison to invasive temperature measurement techniques, MRT data should be compared with data measured with non-invasive temperature measurement techniques, such as PIT.
The applied methods that are necessary for background phase correction are also a point. Correcting MRV flow data by applying Legendre polynomials on the flow off scan data showed excellent background phase compensation. The zeroth order correction method used for MRT background phase correction provided only acceptable results. Other correction procedures such as the implementation of a first order correction using multiple reference phantoms have to be considered in the design of future setups.
As presented in the review on MRT, additional alternative methods are available. Some methods utilize contrast agents with higher thermal sensitivity. Other applications include multi-phase fluids (e.g. oil and water). These special fluids are often not applicable in-vivo without causing severe health damage. However, they can be applied to in-vitro applications.
In the current state, MRI is a medical diagnostic tool and not a dedicated engineering measurement tool. MRI machines are available in a variety of versions with different field strengths and designed for different applications. It is expected that crucial improvements can be achieved if the MR device is exclusively used for engineering purposes. This would enable to create a built-in flow facility equal to a wind tunnel with optimal flow preparation. With appropriate add-ons, more advanced MRI techniques would be applicable, such as MRC measurements, MR turbulence measurements, real-time

MRI or MRI utilizing hyperpolarized gas as measurement fluid. The capabilities of MRV and MRT can be improved by enhanced positioning inside the bore or by improved receiving and transmitting coil design.

Unanswered points can also be given from an application perspective. In this thesis, heat transfer in a flow model was accomplished by the use of ceramic heating elements and by utilizing a secondary flow circuit providing hot or cold fluid. Another method would be the injection of hot or cold fluid directly into the measurement fluid. Mixing processes could be investigated which covers a wide range of thermofluid applications. The experimental setup would be much more complicating, since the mixed fluid has to be separated and conditioned. Additionally, mixing processes are characterized by strong flow turbulence and fluid acceleration, which is still an issue for MRT. Nevertheless, results could be compared to data obtained with MRC measurements. Thus, heat and mass transfer analogies could be demonstrated.
Electrical heating of the measurement fluid inside the MR scanner could decrease the experimental effort and open up the design of even more complex applications that are not possible with fluidic heating methods. Ceramic elements operated in a pulsed mode were used for fluid heating in a backward facing step model. MRT in combination with the 4D-MRI procedure was applied and temperature maps could be measured. The temperature maps were corrupted by strong susceptibility artifacts arising from the setup. The applied correction method showed promising results. Yet no further investigations have been accomplished. It is the sincere hope of the author that this preliminary study leads to further efforts utilizing electrical heating elements. Additionally, the development of a 3D susceptibility modeling tool would be necessary to correct the evoked artifacts.
CFD is capable of resolving 3D3C velocity and temperature fields in complex geometries. Such simulations need the availability of immense computing resources. The efficacy of turbulence models is restricted to a certain amount of applications. MR techniques at it´s current development state would be the perfect validation technique for CFD simulations for mean velocity and temperature fields. This thesis showed comparisons between MRV and CFD. Furthermore, approaches were proposed of how to use data sets with high spatial resolution. Therefore, spatially integrated quantities were derived. Such an approach could be used in future studies to compare MRI data with CFD data. On the other hand, a direct comparison method

would be desirable. More advanced methods are necessary for future investigations that sufficiently and efficiently compare MRI and CFD data.
The post-processing method shown for the tetradecahedral grid is an insightful approach. It uses MRV data to calculate the convective temperature field. This method was applied in a basic version and has not been validated yet. This also leads to novel post-processing steps which improve the measured MRI data. Data filtering based on fluid mechanical or thermodynamical laws would be required to decrease SNR and remove measurement errors. MRI data could be extended by resolving the velocity or temperature boundary layer with the help of CFD. This would further increase the applicability of MR data.
The applicability of materials that are not commonly used in MR environment have been discussed in this thesis. For MRT important material features are the B-field shielding, the susceptibility matching to the measurement fluid and the thermal conductivity. Nevertheless, there is still a variety of materials which are not investigated. Especially, ceramic materials show a good MR suitability as well as adequate machinability and availability. Other materials mentioned in this thesis have to be tested. State-of-the-art manufacturing processes enable the manufacturing of complex structures made of polymeric or ceramic material. With 3D printing functional materials like conducting wires or even receiver coils can be implemented into the structure. The availability of such manufacturing techniques would further increase the complexity, applicability and MR suitability of future flow models.

Appendix A

Fundamentals of Fluid Mechanics, Thermodynamics and Heat Transfer

This chapter summarizes important equations and knowledge of fluid mechanics and thermodynamics in order to introduce heat transfer processes.

A.1 Fundamental Laws and Basic Equations

A.1.1 Continuity Equation

The conservation of mass can be expressed as 'the mass of the bounded part of the fluid must remain constant in time' (Spurk and Aksel, 2010):

$$\frac{\mathrm{D}m}{\mathrm{D}t} = 0 \tag{A.1}$$

Using Reynolds transport theorem the differential form of the conservation of mass can be given:

$$\frac{\mathrm{d}\rho}{\mathrm{d}t} = \frac{\partial \rho}{\partial t} + \frac{\partial(\rho u_i)}{\partial x_i} = 0 \tag{A.2}$$

Describing an incompressible flow and constant fluid density in time and space $\rho = \text{const}$, Eq. A.2 simplifies to:

$$\frac{\partial u_i}{\partial x_i} = 0 \tag{A.3}$$

By integrating Eq. A.2 over an arbitrary integration region V the conservation law can be given in integral form:

$$\iiint\limits_{(V)} \left[\frac{\partial \rho}{\partial t} + \frac{\partial (\rho u_i)}{\partial x_i} \right] \mathrm{d}V = 0 \tag{A.4}$$

For flows with constant fluid density the volume integral of the divergence in Eq. A.4 can be transformed into to the surface S perpendicular fluxes $u_i n_i$ bounding the control volume V with the help of Gauss' theorem:

$$\iint\limits_{(S)} \rho u_i n_i \mathrm{d}S = 0 \tag{A.5}$$

By calculating the flux through an infinitesimally thin control volume with surface S_{out} the mass flow rate $\dot{m}$ can be calulated:

$$\dot{m} = \iint\limits_{(S_{out})} \rho u_i n_i \mathrm{d}S \tag{A.6}$$

For constant density flows the mass flow rate is proportional to the volume flow rate $\dot{V}$ times the fluid density: $\dot{m} = \rho \dot{V}$.

A.1.2 Balance of Momentum

Each infinitesimal mass element dm transports momentum in a flow. According to Newton's second law the change of momentum with time equals the sum of all forces acting on the body. These forces can be divided into body forces affecting all particles (e.g. gravity) and surface forces working in the boundary layer between flow and the body's surface (e.g. shear stresses). Also known as Cauchy's first law of motion the balance of momentum can be given in the differential form as follows:

$$\rho \frac{\mathrm{D}u_i}{\mathrm{D}t} = \rho k_i + \frac{\partial \tau_{ji}}{\partial x_j} \tag{A.7}$$

Hereby, k_i are the body forces and τ_{ji} is the stress tensor, which can be decomposed into:

$$\tau_{ji} = -p\delta_{ji} + P_{ji} \tag{A.8}$$

The term p is the pressure, δ_{ji} symbolizes the Kronecker delta and P_{ji} is the frictional stress tensor. The term $\frac{\mathrm{D}u_i}{\mathrm{D}t}$ is the material derivative of the velocity field, i.e. the acceleration:

$$\frac{\mathrm{D}u_i}{\mathrm{D}t} = \frac{\partial u_i}{\partial t} + u_j \frac{\partial u_i}{\partial x_j} \tag{A.9}$$

The first summand is the local temporal derivative and the second summand is the convective term.
When the calculation of integral forces on a certain body within a control volume is desired, the integral form of the momentum balance is used:

$$\iiint\limits_{(V)} \frac{\partial(\rho u_i)}{\partial t} \mathrm{d}V + \iint\limits_{(S)} \rho u_i (u_j n_j) \mathrm{d}S = \iiint\limits_{(V)} \rho k_i \mathrm{d}V + \iint\limits_{(S)} \frac{\partial \tau_{ji}}{\partial x_j} \mathrm{d}S \tag{A.10}$$

A.1.3 Navier-Stokes Equation

Considering Newtonian fluids a constitutive relation can be given for the stress tensor:

$$\tau_{ji} = -p\delta_{ji} + \lambda^* e_{kk} \delta ji + 2\eta e_{ji} \tag{A.11}$$

Additional to Eq. A.8, λ^* is the first Lamé parameter, $e_{ji} = \frac{1}{2}\left(\frac{\partial u_j}{\partial x_i} + \frac{\partial u_i}{\partial x_j}\right)$ is the deformation velocity tensor (or strain tensor), e_{kk} stands for the diagonal elements of the strain tensor and η the dynamic viscosity.
Inserting Eq. A.11 into Eq. A.7 and assuming $\eta = \text{const}$ the Navier-Stokes equation can be derived in differential form:

$$\rho \frac{\mathrm{D}u_i}{\mathrm{D}t} = \rho k_i - \frac{\partial p}{\partial x_i} + (\lambda^* + \eta) \frac{\partial}{\partial x_i} \left[\frac{\partial u_k}{\partial x_k}\right] + \eta \left[\frac{\partial^2 u_i}{\partial x_j \partial x_j}\right] \tag{A.12}$$

For an incompressible fluid the term e_{kk} of Eq. A.12 is zero, which simplifies the given equation to:

$$\rho \frac{\mathrm{D}u_i}{\mathrm{D}t} = \rho k_i - \frac{\partial p}{\partial x_i} + \eta \left[\frac{\partial^2 u_i}{\partial x_j \partial x_j} \right] \tag{A.13}$$

A.1.4 Balance of Energy

The first law of thermodynamics states, that the energy in an isolated system is conserved and can neither be destroyed nor created. In other words: the sum of all changes of energy in an isolated system is zero:

$$\mathrm{d}E_{tot} = \mathrm{d}Q + \mathrm{d}W = 0 \tag{A.14}$$

The total energy $\mathrm{E}_{tot} = \iiint_{V(t)} e\rho \mathrm{d}V$, which is the integral of the internal energy of a material particle $e\mathrm{d}m$ over the region V(t), has different forms (heat Q, work W), which can be transformed into each other. Work can be subdivided into mechanical work, pressure-volume work, shaft work, electric work and so on. Furthermore, energy can be subdivided into internal energy E_{int}, kinetic energy E_{kin} and potential energy E_{pot}, yielding:

$$\mathrm{d}E_{tot} = \mathrm{d}E_{int} + \mathrm{d}E_{kin} + \mathrm{d}E_{pot} = \mathrm{d}Q + \mathrm{d}W \tag{A.15}$$

Hereby, the kinetic and the potential energy together can be termed mechanical energy E_{mech}. The internal energy summarizes energy, which is stored inside the system. It can be imagined as kinetic energy (rotation, translation, oscillation) of single molecules.
For open systems an additional energy form E_m, due to transport of matter over the system boundary $\mathrm{d}M$ has to be considered. Fig. A.1 describes such an open system with all energy forms. The energy balance given in Eq. A.14 can be extended to the following form Stephan (2013):

$$\mathrm{d}E_{tot} = \underbrace{\mathrm{d}Q}_{\text{heat}} + \underbrace{\mathrm{d}W}_{\text{work}} + \underbrace{\sum_{k=1}^{n} \mathrm{d}M_k (e_k + \frac{u_k^2}{2} + g z_k)}_{\substack{\text{sum of energy } E_m \\ \text{transported with matter}}} \tag{A.16}$$

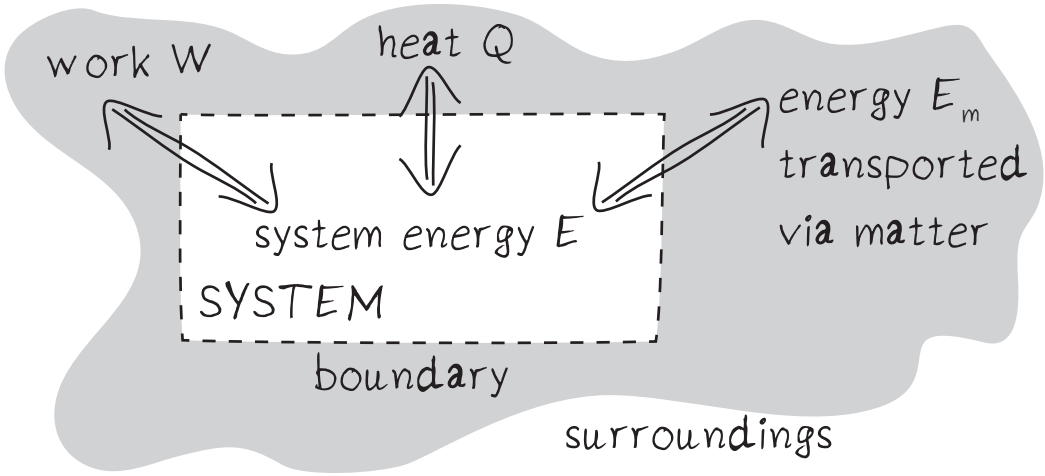

Fig. A.1: Thermodynamic open system with different energy forms.

In Eq. A.16 e_k is the specific internal energy. The specific internal energy is a caloric measure of state and a function of the temperature T and the specific volume v. The term $\frac{u_k^2}{2}$ is the kinetic energy and the term gz_k is the potential energy. With the introduction of the specific enthalpy $h = e + pv$ the pressure-volume work $W_v = pv\rho dV$, which is bound to material transport, can be extracted from the general work W. The result is the technical work W_t, which can be found in a recast version of Eq. A.16:

$$dE_{tot} = dQ + dW_t + \sum_{k=1}^{n} dM_k(h_k + \frac{u_k^2}{2} + gz_k) \tag{A.17}$$

By differentiating Eq. A.17 by time t, the energy balance can be applied on a continuous process for a system described in Fig. A.1:

$$\begin{aligned} \frac{DE_{tot}}{Dt} = \dot{Q} + P + \sum_{in} \dot{M}_{in}(h_{in} + \frac{u_{in}^2}{2} + gz_{in}) \\ - \sum_{out} \dot{M}_{out}(h_{out} + \frac{u_{out}^2}{2} + gz_{out}) \end{aligned} \tag{A.18}$$

$\dot{Q} = \frac{dQ}{dt} = -dV\frac{\partial \dot{q}_i}{\partial x_i}$ is the heat transfer rate proportional to the divergence of the heat flux vector $\dot{q}_i$, $P = \frac{dW_t}{dt} = dV\rho u_i k_i + dV\frac{\partial}{\partial x_j}(u_i\tau_{ji})$ is the power resulting from body forces and surface forces and $\dot{M}$ the mass flow with

which energy is transported into ($*_{in}$) or out ($*_{out}$) of the system.

Considering that the system with total energy E_{tot} consists of small material particle with mass $dm = \rho dV$ the energy equation can be given in differential form:

$$\rho \frac{D}{Dt}\left(e + \frac{1}{2}u_i u_i\right) = \rho k_i u_i + \frac{\partial}{\partial x_j}\left(u_i \tau_{ji}\right) - \frac{\partial \dot{q}_i}{\partial x_i} \tag{A.19}$$

The left side of the equation stands for the change of the specific internal energy e and the kinetic energy $\frac{u_i u_i}{2}$ of each particle. This must be equal to the sum of the power through body forces $\rho u_i k_i$, the power through surface forces $\frac{\partial}{\partial x_j}\left(u_i \tau_{ji}\right)$[1] and the transferred heat flux $-\frac{\partial \dot{q}_i}{\partial x_i}$.
Decomposing Eq. A.19 leads to the mechanical energy equation, which is identical to the momentum balance given with Eq. A.7 (here multiplied with u_i):

$$\rho u_i \frac{D(u_i)}{Dt} = \rho k_i u_i + u_i \frac{\partial \tau_{ji}}{x_j} \tag{A.20}$$

and the thermal energy equation:

$$\rho \frac{De}{Dt} = \tau_{ji} \frac{\partial u_i}{\partial x_j} - \frac{\partial \dot{q}_i}{\partial x_i} \tag{A.21}$$

The first summand comprises the reversible and irreversible work. By implementing Eq. A.8 into Eq. A.21 and decomposing $\frac{\partial u_i}{\partial x_j} = e_{ij} + \Omega_{ij}$[2] leads to:

$$\rho \frac{De}{Dt} = -p \frac{\partial u_i}{\partial x_i} + P_{ij} e_{ij} - \frac{\partial \dot{q}_i}{\partial x_i} \tag{A.22}$$

The term $P_{ij} e_{ij}$ is often referred to as dissipation function Φ and describes the deformation work which is irreversibly transformed into heat, due to friction stresses. The first term $-p\frac{\partial u_i}{\partial x_i}$ is the reversible compression work and only present when the density is not constant. For a constant density Eq. A.3 holds and the term is zero. Replacing the specific energy with the specific enthalpy in Eq. A.22 yields another form of the thermal energy equation:

[1] τ_{ji} is the stress tensor
[2] $\Omega_{ij} = \frac{1}{2}\left(\frac{\partial u_i}{\partial x_j} - \frac{\partial u_j}{\partial x_i}\right)$ is the anti-symmetric rotational tensor.

$$\rho \frac{\mathrm{D}h}{\mathrm{D}t} = \frac{\mathrm{D}p}{\mathrm{D}t} + P_{ij} e_{ij} - \frac{\partial \dot{q}_i}{\partial x_i} \tag{A.23}$$

Introducing Fourier´s law for isotropic materials with thermal conductivity λ, the heat flux vector $\dot{q}_i$ can be expressed as follows:

$$\dot{q}_i = -\lambda \frac{\partial T}{\partial x_i} \tag{A.24}$$

Two equations of state coupling the temperature field T with the internal energy e or the enthalpy h can be given for an ideal gas. The total differential of the specific internal energy e can be given by:

$$\mathrm{d}e(T, v) = \left(\frac{\partial e}{\partial T}\right)_v \mathrm{d}T + \left(\frac{\partial e}{\partial v}\right)_T \mathrm{d}v \tag{A.25}$$

Hereby, the term $\left(\frac{\partial e}{\partial T}\right)_v = c_v$ is the specific heat capacity at constant volume (isochoric). The total differential of the specific enthalpy h yields:

$$\mathrm{d}h(T, p) = \left(\frac{\partial h}{\partial T}\right)_p \mathrm{d}T + \left(\frac{\partial h}{\partial p}\right)_T \mathrm{d}p \tag{A.26}$$

The term $\left(\frac{\partial h}{\partial T}\right)_p = c_p$ is the specific heat capacity at constant pressure (isobaric). A valid assumption is, that liquids are incompressible. This means, that the specific volume v does not change when external forces are applied ($\mathrm{d}v = 0$) and Eq. A.25 simplifies to

$$\mathrm{d}e = c_v \mathrm{d}T \tag{A.27}$$

and with $h = e + pv$ Eq. A.26 can be rewritten

$$\mathrm{d}h = c_p \mathrm{d}T + v \mathrm{d}p \tag{A.28}$$

In this case one can approximate, that both heat capacities have the same value ($c_v \approx c_p = c$). The specific heat capacity is a material property and connects heat and temperature: It describes the amount of heat that is needed to increase the temperature of a volume V with density ρ about the value $\mathrm{d}T$:

$$\mathrm{d}Q = \rho V c \mathrm{d}T \tag{A.29}$$

Setting Eq. A.24 and the equation of state for the internal energy of Eq. A.27 into Eq. A.22, substituting the friction stress tensor P_{ij} for an incompressible Newtonian fluid and assuming constant material properties, the thermal energy equation can be expressed just through the temperature, pressure and velocity field:

$$\rho c_v \frac{\mathrm{D}T}{\mathrm{D}t} = -p\frac{\partial u_i}{\partial x_i} + \frac{1}{2}\eta\left(\frac{\partial u_j}{\partial x_i} + \frac{\partial u_i}{\partial x_j}\right)^2 + \lambda\frac{\partial^2 T}{\partial x_i^2} \tag{A.30}$$

The total energy equation (Eq. A.19) can be recast with equal assumptions as used before:

$$\rho c_p \frac{\mathrm{D}T}{\mathrm{D}t} = \rho k_i u_i - \frac{\partial(p u_j)}{\partial x_j} + 2\eta\frac{\partial}{\partial x_j}\left(u_i\left(\frac{\partial u_i}{\partial x_j} + \frac{\partial u_j}{\partial x_i}\right)\right) + \lambda\frac{\partial^2 T}{\partial x_i^2} \tag{A.31}$$

This also yields the third and last important form of the thermal energy equation building the material derivative of Eq. A.28 and introducing the thermal expansion coefficient β:

$$\rho c_p \frac{\mathrm{D}T}{\mathrm{D}t} = \beta T\frac{\mathrm{D}p}{\mathrm{D}t} + P_{ij}e_{ij} - \lambda\frac{\partial^2 T}{\partial x_i^2} \tag{A.32}$$

A.2 Heat Transfer

Heat is a basic measure in thermodynamics and is defined as the energy crossing the boundary of a system Baehr (2006). It is part of the internal energy, which, in turn, can be divided into thermal, chemical and nuclear internal energy Stephan (2013). Heat transfer describes the process how internal energy is transported over the boundary of a system. Thereby, the process is driven by a temperature difference between the system and its boundary. In contrast to thermodynamics, heat transfer is a continuum theory, in which energy can be transferred as heat between small individual systems. This enables the usage of field measures such as heat flux vector field or temperature field. Heat transfer can be divided into three categories Baehr (2006):

- *Heat conduction* is the energy transfer between neighboring molecules due to a temperature difference.
- *Heat convection* is the transport and mixing of energy, due to direct movement of the molecules among themselves.
- *Heat radiation* is the energy transfer via electromagnetic waves.

Heat conduction and heat convection can only be present in matter or between different matter in contact with each other. As radiation is electromagnetic, heat transfer through radiation can be transferred between matter separated from each other by vacuum. Gases and liquids are usually transparent, which makes them less receptive for radiative heat transfer. In conventional heat exchangers thermal energy is predominantly transferred by heat conduction and heat convection processes between the exchanger walls and the coolant (e.g. air, water,...).

A.2.1 Heat Conduction

Heat transfer through conduction is a molecular energy transport mechanism driven by the temperature gradient ∇T. Characteristic for this process is the thermal conductivity $\lambda = \lambda(T, p)$, which is a material property and only dependent on the temperature and the pressure, defined for isotropic material.
Considering a closed thermodynamic system without fluid movement ($u_i = 0$), Eq. A.31 simplifies to the differential equation characterizing the temperature field through heat conduction:

$$\rho c_p \frac{\partial T}{\partial t} = +\lambda \frac{\partial^2 T}{\partial x_i^2} \tag{A.33}$$

By division with the product ρc_p the thermal diffusivity $a = \frac{\lambda}{\rho c_p}$[3] can be given.
If the heat conduction process is steady Eq. A.33 further simplifies to the

[3] In English literature denoted with α

Laplacian of the temperature field $\frac{\partial^2 T}{\partial x_i^2} = 0$. Setting proper thermal boundary conditions one-dimensional heat conduction problems can be solved analytically.

A.2.2 Heat Convection

Heat convection can be subdivided into free or natural convection and forced convection.

A.2.2.1 Natural Convection

Natural convection only occurs when gravitational forces are present. The velocity field is generated due to lift forces emanating from density differences in the fluid. Hydrostatic equilibrium means that density and pressure gradient are parallel and can be derived by applying the curl operator ($\nabla\times$) on Eq. A.13 and setting $u_i \equiv 0$:

$$0 = -\underbrace{\nabla \times \nabla}_{=0} p + \nabla\rho \times \vec{k} + \rho \underbrace{\nabla \times \vec{k}}_{\substack{=0 \text{ if } \vec{k} \\ \text{is a potential}}} \tag{A.34}$$

In earth environment $\vec{k}$ is equal to the gravity force $-\vec{g}$. If $\nabla\rho$ is then parallel to $\vec{k}$, no free convection flow develops and a temperature distribution arises just as function of heat conduction. If the density gradient $\nabla\rho$ is at an angle to $\vec{k}$, then the hydrostatic equilibrium is violated and a convection flow must develop. This is termed direct natural convection and is typically the reason for an inclined heated wall at angle θ, for which the component of the gravity force $-|\vec{g}| \sin\theta$ is strong enough. In contrast to that indirect natural convection occurs at horizontally arranged heated walls. Due to the density gradient above the heated wall the hydrostatic pressure is lower than in the area before or after the wall. The isobaric lines fall in this region, which

leads to a wall parallel force. A fluid particle within this area experiences is accelerated parallel to the wall and a natural convection flow develops. Indirect natural convection is often present in meteorology.
In natural convection flows the density variation reasons from varying fluid temperature. Hence, the temperature and the velocity field are coupled.

A.2.2.2 Forced Convection

In contrast to natural convection, temperature and velocity field are assumed independent in forced convection flow. Hereby, the flow is maintained by a pressure source (e.g. pump). The fluid properties are assumed to be constant. This also implies, that both, velocity and temperature field, do not influence each other. Furthermore, forced convection can take place in internal flows (e.g. channels, pipes) or external flows (flat plate, bluff bodies).
If no flow is maintained energy will be transported perpendicular to the heated wall solely due to heat conduction. When flow is present a heated fluid particle will be taken away parallel to the wall. Heat is solely transferred from the wall (which is at a different temperature T_W compared to the mean fluid temperature T_F) into the first layer of the fluid via heat conduction (thermal conductivity of fluid λ_F), due to the fact that no flow is present at the wall (no-slip condition). Temperature changes only happen in the temperature boundary layer (thickness δ_T). Inside the velocity boundary layer (thickness δ_V) fluid particles and, hence, heat in form of internal energy, are accelerated and carried away with the flow parallel to the wall (bulk velocity U_0). This means that the wall parallel energy transport is more effective the higher the bulk mass flow rate is. Another important point for high convective heat transfer is a thin velocity boundary layer at the walls and appropriate mixing within the flow. Increasing the Reynolds number means to decrease the velocity boundary layer thickness. At a certain Reynolds number each flow becomes turbulent, which implies that the velocity profile becomes fuller. Additionally, fluid mixing occurs due to turbulent diffusion. Impulse and internal energy transfer between fluid particles increases. As a result the temperature boundary layer thickness reduces leading to an increase of the driving temperature gradient. Hence, the heat transfer improves in comparison to laminar flow.

As the heat transfer rate $\dot{Q}$ describes the quantity of transferred thermal energy over the boundaries of an arbitrary thermodynamic system, the quality of heat transfer can only be assessed for a specific system introducing the heat transfer coefficient α[4] in Newton's law of cooling:

$$\dot{Q} = \dot{q}_W A = \alpha A \Delta T \tag{A.35}$$

It connects the wall heat flux $\dot{q}_W$ with the driving temperature difference $\Delta \mathrm{T} = \mathrm{T}_W - \mathrm{T}_F$ and the heat transfer coefficient α:

$$\alpha = \frac{\dot{q}_W}{\Delta T} \tag{A.36}$$

All parameters describing convective heat transfer are depicted in Fig. A.2.

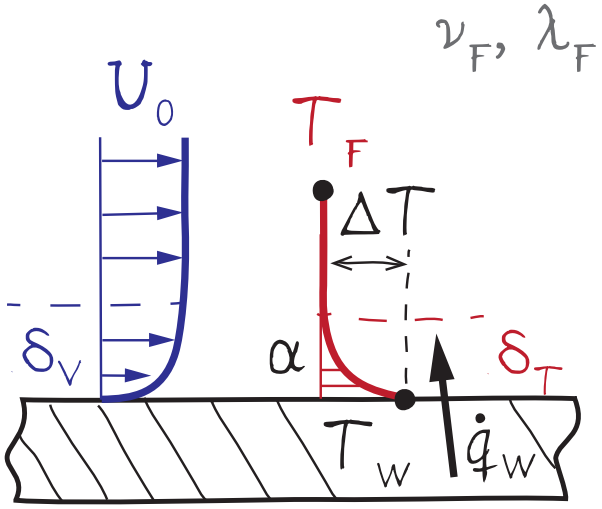

Fig. A.2: Convective heat transfer between wall and fluid. U_0 is the bulk flow velocity, δ_V the velocity boundary layer thickness, T_W is the wall temperature, T_F the fluid temperature, $\Delta \mathrm{T}$ is the temperature difference, δ_T is the thermal boundary layer, α is the convective heat transfer coefficient, λ_F the fluid thermal conductivity and ν_F the fluid viscosity.

A disadvantage using heat transfer coefficients is, that every coefficient has to be determined empirically and is then valid for this unique setup. As explained in Sec. A.3.2, more information can be transported and different

[4] In American literature denoted with k

experimental setups compared by utilizing dimensionless quantities such as the Reynolds number or Nusselt number.

A.2.3 Combined Forced and Natural Convection

In internal, as well as external convection flows, both types of convection exist, which is then called mixed or combined convection (Incropera et al., 2006; Schlichting, 2000). A decision criterion weather the influence of natural convection can be neglected or not provide dimensionless numbers, such as the Grashof number, Rayleigh number and their ratio to the Reynolds number. These dimensionless quantities are discussed in detail in Sec. A.3.2.

In order to assess the impact of buoyancy on heat transfer Incropera et al. (2006) categorize three cases, which characterize the direction of buoyancy force relative to the forced flow direction. *Assisting* flow is present when buoyancy force and forced fluid motion points in the same direction, whereas *opposed* flow occurs when both point in opposite direction. When buoyancy and forced flow are perpendicular to each other, then one speaks of *transverse* flow.
In the assisting and transverse flow case the buoyancy forces enhance heat transfer rates, when the flow is laminar.

A.2.4 Thermal Boundary Conditions

In order to compare theory and experiment detailed information about the thermal conditions at the boundaries of the thermodynamic system are important. Herwig and Moschallski (2009) give three different boundary conditions:
A *constant temperature at system boundary* is present when T_W is held constant. The temperature gradient and the heat flux is then unknown. In the

experiment this condition can be achieved approximately, when the system is surrounded by a material with high thermal conductivity held at a constant wall temperature (e.g. fluidic heating).
Constant heat flux at system boundary means, that $\dot{q}_W$ =constant. The wall temperature is variable and unknown. One solution is the adiabatic wall, for which $\dot{q}_W = 0$. This condition can be realized experimentally only with the help of an electrical heating device. Over the heating surface the resistance has to be constant, as well as the electrical current distribution.
The last and more theoretic condition implies a *constant heat transfer coefficient at system boundary* and the ratio $\frac{\dot{q}_W}{\Delta T}$ is held constant. Hereby, temperature gradient and wall heat flux are unknown but coupled. In the experiment a constant heat transfer coefficient can be present, when a phase change occurs (e.g. boiling).
In general the realization of constant boundary conditions in the experiment is complicating and often not realizable.

A.2.5 Internal Convection Flow

Focussing on internal flows, a simple heat exchanger is a channel with heated walls as sketched in Fig. A.3. The energy equation for this setup fed with constant volumetric flow rate ($\dot{V} = \frac{\dot{m}}{\rho} = \text{const}$) of an incompressible fluid (density ρ and specific heat capacity c) can be given setting Eq. A.35 into Eq. A.18:

$$\dot{m}(h_{out} - h_{in}) = \dot{q}_W A_W \tag{A.37}$$

$$\rho \dot{V} c(T_F - T_0) = \alpha A_W (T_W - T_F) \tag{A.38}$$

Applying boundary condition $\dot{q}_W = \text{const}$ for this setup, it is obvious, that the mean fluid temperature T_F increases linear with the streamwise direction z, when the flow is hydrodynamically developed. This also implies, that the higher α is lower is the required temperature difference $T_W - T_F$ to transfer the heat from the wall into the flow. Improving heat transfer means to decrease the wall temperature. The non-linear part at the beginning of the heated region is called the entry region.

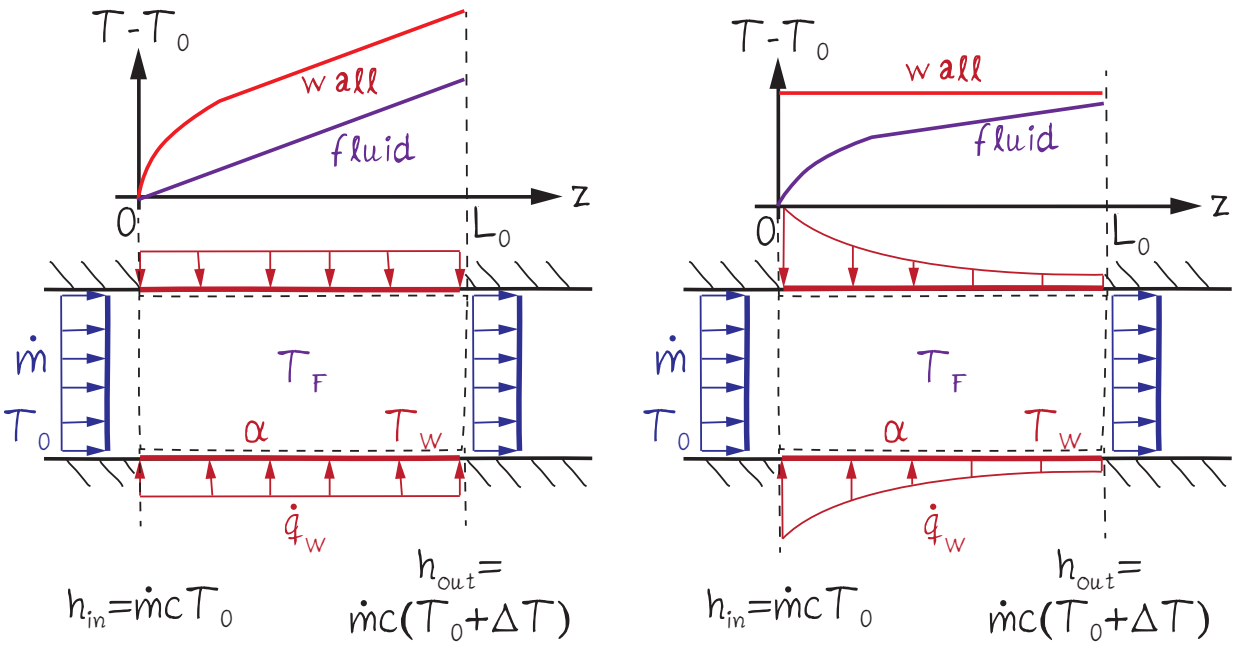

(a) constant wall heat flux $\dot{q}_W$ (b) constant wall temperature T_W

Fig. A.3: Simple heat exchanger arrangement of a channel with heated walls at different conditions.

For boundary condition T_W=const. the mean fluid temperature increases from $T_F = T_0$ at $z = 0$ to $T_F = T_W$ for $z \to \infty$. Typically the maximum achievable temperature is reached after a finite distance z^*, for instance when $T_F = 99\%\ T_W$. Increasing α and, hence, heat transfer decreases z^*, due to an increase of the local heat flux. The development of the temperature profile in this case is called Graetz problem (Gersten and Herwig, 1992).

For simple heat exchangers heat transfer characteristics can assessed. By measuring the volumetric flow rate, the inlet temperature T_{in} and the mean fluid temperature at the outlet $T_{F,out}$ of a heat exchanging device this simple equation can be used to estimate the overall heat transferred into the fluid between inlet and outlet. Moreover, by measuring the wall temperature T_W the heat transfer coefficient α can be calculated. Hence, the overall heat transfer quality can be assessed. A prediction on local heat transport phenomena is still not possible to give. Therefore, local wall and fluid temperatures, as well as heat fluxes, along the streamwise flow direction in the channel (here z-direction) have to be recorded. Then α_z can be given

as a function of the z-direction:

$$\alpha_z = \frac{\dot{q}_W(z)}{T_W(z) - T_F(z)} \tag{A.39}$$

Integrating α_z over the channel length L yields the overall heat transfer coefficient:

$$\alpha = \frac{1}{L}\int_0^L \alpha_z \mathrm{d}z \tag{A.40}$$

These estimates are only valid for constant thermal boundary conditions and fully-developed flow profiles throughout the control volume. Especially in the entry region of a channel with constant wall heat flux, as shown in Fig. A.3, the boundary conditions are not constant. This gets even more complex if the velocity profile is not hydrodynamically developed. This situation is typical when heat exchanger design becomes more sophisticated. For instance, when the wall contour is shaped in a complex way or complex internal structures are present. Additionally, parts in the heat exchanger where natural convection dominates can not be neglected. Then appropriate experimental setups and measurement techniques are necessary and heat transfer phenomena have to be assessed locally.

A.3 Similitude and Model Theory

Similitude is a concept of engineering sciences, which enables the researcher to compare a model with a real application. Each realistic application has a typical shape (geometry), material properties and boundary conditions. Surrounded by a certain fluid with different material properties and boundary conditions the application is then moved, heated or cooled, fluid flow is applied or combinations of these are performed. The goal is to understand the complex interaction between the application and the fluid by measuring appropriate physical quantities. As this is typically not achievable for the realistic case, a scaled experimental setup is developed which has to reproduce equal physical behavior. This means that all boundary conditions have to be adjusted accordingly to achieve similarity.
This is done by nondimensionalizing the characteristic parameter of the real

application. Dimensionless quantities reduce the experimental effort, due to similarity between different experiments. In model theory experiments with different geometry, different boundary conditions (such as bulk flow, wall heat flux,...) can be compared with each other, when they have equal dimensionless quantities. Therefore, dimensionless numbers are important for comparing the model with the real application or with other experiments of different geometry and fluid properties. If the characterizing quantities of a fluid mechanical problem are known, then the dimensionless numbers can be developed by dimension analysis Herwig (2006).

A.3.1 Model Parameters and Properties

The first step is to define the quantities characterizing the physics of the problem. For thermofluid applications this is typically a combination of a length scale, a velocity, a temperature and pressure. If the processes are unsteady, then the time or the frequency have to be considered. Tab. A.1 presents variables and properties which are used to define a model.

A.3.2 Dimensionless Numbers

Dimensionless numbers result when the basic equations of fluid mechanics and thermodynamics are cast with dimensionless dependent variables. They characterize the physics of the given setup. The fundamental equations of fluid mechanics and thermodynamics built the theoretical background needed to understand mass and heat transfer processes in fluid flow. For fluid mechanical considerations important equations are the continuity equation, the momentum balance and the Navier-Stokes equation, which includes the constitutive relations for Newtonian fluids. For heat transfer processes the energy balance is relevant, as well as Fourier´s law for heat conduction processes and Netwon´s law of cooling for heat convection processes. All fundamental equations have already been presented in many

Tab. A.1: List of variables and material properties, which are important to formulate dimensionless quantities.

Variables	**Description**	**Unit**	**Examples**
L	length	m	tube diameter D, channel hydraulic diameter d_h, chord length of an airfoil c
U	velocity	$\frac{m}{s}$	bulk inlet channel velocity U_{bulk}
T	temperature	K	bulk inlet temperature T_{bulk} or T_0 / wall temperature T_W
$\dot{q}$	heat flux	$\frac{W}{m^2}$	wall heat flux $\dot{q}_W$
p	pressure	$\frac{kg}{m\ s^2}$	stagnation pressure p_0
t	time	s	starting time of process t_0
Property			**Function of**
g	gravity force	$\frac{m}{s^2}$	-
ρ	density	$\frac{kg}{m^3}$	T, p
η	dynamic viscosity	$\frac{kg}{m\ s}$	T, p
ν	kinematic viscosity	$\frac{m^2}{s}$	T, p
c_p	specific heat capacity	$\frac{kJ}{kg\ K}$	T, p
λ_F	thermal conductivity of fluid	$\frac{W}{m\ K}$	T
λ_S	thermal conductivity of solid	$\frac{W}{m\ K}$	T
$a = \frac{\lambda}{\rho c_p}$	thermal diffusivity	$\frac{m^2}{s}$	T
β	thermal expansion coefficient	$\frac{1}{K}$	T, p
α	convective heat transfer coefficient	$\frac{W}{m^2 K}$	T, fluid, flow

works and are not further given here. Some of the important works are Spurk and Aksel (2010), Schlichting (2000), Stephan (2013), Baehr (2006), Gersten and Herwig (1992) and Herwig (2006).

Dimensionless numbers form when the basic equations are divided by reference quantities, which characterize the geometry, material properties and flow parameters. The most important quantities were already presented in Tab. A.1. Some examples of the dimensionless variables are given in Tab. A.2. In order to separate them from variables with dimension they are superscribed with a "+".

Tab. A.2: Dimensionless variables describing the geometry and flow parameters of a fluid mechanical problem.

Name	**aka**	**Formula**	**Characteristic for**
dimensionless coordinate	x^+	$\frac{x}{L_0}$	models with spatial dimension
dimensionless velocity	U^+	$\frac{U}{U_0}$	models with flow
dimensionless temperature	T^+	$\frac{T-T_0}{\Delta T_0}$	models with heat flux or varying temperature
dimensionless pressure	p^+	$\frac{p}{\rho_0 * U_0^2}$	models with varying flow fields
dimensionless time	t^+	$\frac{tU_0}{L_0}$	unsteady, time-dependent flow field

Most important is the dimensionless form of the incompressible Navier-Stokes equation without body forces:

$$\frac{\mathrm{D}u_i^+}{\mathrm{D}t^+} = -\frac{\partial p^+}{\partial x_i^+} + Re^{-1}\left[\frac{\partial^2 u_i^+}{\partial x_j^+ \partial x_j^+}\right] \tag{A.41}$$

Hereby, the well-known Reynolds number Re occurs:

$$Re = \frac{UL}{\nu} \tag{A.42}$$

The Reynolds number characterizes the flow field and provides a criterion for whether the flow is laminar or turbulent. Most of the dimensionless numbers can be interpreted descriptively by considering extreme small or extreme large values. For Re$\rightarrow$ 0 creeping flows occur, which are likely for flows with low flow velocities or high fluid viscosities. In this case inertia forces are small compared to viscous forces. When Re$\rightarrow \infty$ the flow can be treated inviscid and potential theory can be applied. Only within the velocity boundary layer viscosity and, hence, shear forces play an important role. This area cannot be represented with potential theory.

The energy equation can be given in dimensionless form as follows:

$$\frac{\mathrm{D}T^+}{\mathrm{D}t^+} = Ec\ k_i^+ u_i^+ + Re^{-1} Ec \frac{\partial}{\partial x_j^+}\left(u_i^+\left(\frac{\partial u_i^+}{\partial u_j^+} + \frac{\partial u_j^+}{\partial u_i^+}\right)\right) - Pe^{-1}\frac{\partial^2 T^+}{\partial (x_i^+)^2} \tag{A.43}$$

Eq. A.43 provides two new dimensionless numbers. The Eckert number

$$Ec = \frac{U^2}{c_p \Delta T} \tag{A.44}$$

is the ratio of kinetic energy to enthalpy across the thermal boundary layer. It is a measure for how strong the temperature field is influenced by viscous dissipation. Ec and the corresponding term in the energy equation is important for flows with high fluid velocities. Then considerable warming occurs due to friction.
The Peclet number

$$Pe = \frac{\rho U L c_p}{\lambda} \tag{A.45}$$

is an important dimensionless number for heat transfer. It is a measure for convective heat transport versus conductive heat transport. By expanding and recasting the fraction of Eq. A.45 with the dynamic viscosity η

$$Pe = \frac{\rho U L c_p}{\lambda} = \frac{\rho U L}{\eta}\frac{c_p \eta}{\lambda} = \frac{UL}{\nu}\frac{\nu}{a} = Re \cdot Pr \tag{A.46}$$

it becomes clear that Pe is a combination of two dimensionless numbers, namely, Reynolds number and Prandtl number Pr. Pr is a material property and an important characteristic for heat transfer in all convection flows. It can be interpreted graphically as the ratios of the velocity boundary layer

δ_V and the temperature boundary layer δ_T as depicted in Fig. A.4.
Convective heat transfer is characterized by the convective heat transfer co-

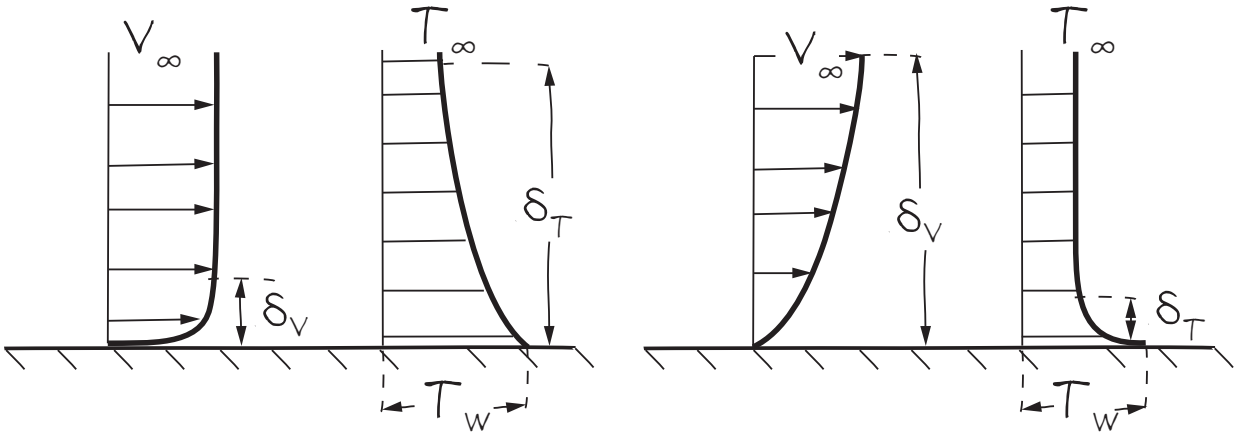

(a) Pr→ 0 (e.g. liquid metals) (b) Pr→ ∞ (e.g. oil)

Fig. A.4: Graphical interpretation of small and large Prandtl numbers.

efficient α. By nondimensionalizing the energy equation including Newton´s law of cooling the Nusselt number can be achieved:

$$Nu = \frac{\alpha L}{\lambda_F} = \frac{\dot{q}_W L}{\lambda_F \Delta T} \tag{A.47}$$

Nu describes the ratio of convective heat transfer to conductive heat transfer and, hence, is a measure for the quality of heat transport from the wall into the fluid. For similar experiments with different geometry higher Nu can be obtained. Nu is a function of the geometry, the flow, the working fluid, the influence of natural convection to name only a few.
Characterizing the influence of buoyancy forces versus viscous forces and, hence, the the occurrence of natural convection flow is done with the help of the Grashof number Gr. It can be found in the component along the buoyancy direction (in this case subscribed with z) of the nondimensionalized momentum equation including gravitational forces $\vec{g} = g\vec{e}_z$ and substituting the pressure gradient with an additional buoyancy force $\rho g\vec{e}_z$:

$$\frac{\mathrm{D}u_z^+}{\mathrm{D}t^+} = \frac{Gr}{Re^2} T^+ + Re^{-1} \left[\frac{\partial^2 u_z^+}{\partial x_j^+ \partial x_j^+} \right] \tag{A.48}$$

Gr is defined as follows:

$$Gr = \frac{gL^3}{\nu_F^2}\beta(T_W - T) \tag{A.49}$$

Hereby, g is the gravitational force and β is the thermal expansion coefficient of the fluid and T_W - T the driving temperature difference. As the Reynolds number characterizes the convective flow, the Grashof number is a measure for the naturally occurring convection. For Gr$\rightarrow$ 0 no natural convection occurs. For Gr$>$ 1 natural convection flow arises and becomes stronger with increasing values of Gr. In terms of heat transfer Nu is strongly influences by the different convection forms. For $\mathrm{Gr/Re^2} \approx 1$, natural and forced convection are equal and Nu = f(Re,Pr,Gr). If $\mathrm{Gr/Re^2} \ll 1$ then forced convection is dominating and Nu = f(Re,Pr). The other way round natural convection dominates and Nu = f(Gr,Pr) when $\mathrm{Gr/Re^2} \gg 1$ (Herwig and Moschallski, 2009; Incropera et al., 2006). The ratio of Gr to the square of Re is termed Richardson number

$$Ri = \frac{gL_0}{U_0^2}\beta(T_W - T_0) \tag{A.50}$$

which is often used in literature.

In Tab. A.3 the most important dimensionless numbers are summarized. The numbers presented here are based on the works of Gersten and Herwig (1992), Herwig (2006), Herwig and Moschallski (2009), Incropera et al. (2006) and Baehr (2006).
For some cases it is more valuable to define a variable dimensionless number across the distance x, in order to evaluate the local behavior. Then the fixed length scale L is replaced by x, which is, for instance, the streamwise coordinate. As an example the Reynolds number Re_x is given:

$$Re = \frac{Ux}{\nu} \tag{A.51}$$

Considering a flat plate with streamwise coordinate x, Re_x increases with increasing x. For a certain value of Re_x the flow changes from laminar to turbulent. Denoted as critical Reynolds number a frequently given value is $\mathrm{Re}_x \equiv 5 \times 10^5$ (Incropera et al., 2006).

There are even more dimensionless quantities characterizing convection flows and in some cases more suitable to a special experiments. They can

Tab. A.3: Dimensionless numbers used to compare different fluid mechanical problems.

Name	**aka**	**Formula**	**Description**	**Characteristic for**
Reynolds number	Re	$\frac{\rho U L}{\eta}$	inertia force vs. viscous forces	differentiation of viscid and inviscid flow
Prandtl number	Pr	$\frac{\nu}{a}$	viscous diffusivity vs. thermal diffusivity or velocity boundary layer thickness vs. thermal boundary layer thickness	inviscid flows with consideration of boundary layer
Péclet number	Pe	Re·Pr= $\frac{LU}{a}$	convective heat transport vs. conductive heat transport	the capability of flows to transport heat or mass
Nusselt number	Nu	$\frac{\alpha L}{\lambda_f} = \frac{\dot{q}_W L}{\Delta T}$	convective heat transfer vs. conductive heat transfer	heat exchange processes with flowing fluid
Grashof number	Gr	$\frac{L^3 g}{\nu^2}\beta(T_W - T)$	buoyancy forces vs. viscous forces	inviscid flows with motion due to temperature differences
Eckert number	Ec	$\frac{U^2}{c_p \Delta T}$	kinetic energy vs. enthalpy	flows with large velocity gradients, where warming due to friction affects the temperature fields

be derived by combining the above presented dimensionless numbers.

Tab. A.4: Other dimensionless numbers important for heat transfer process and more suitable to certain experimental configurations. Some result from combinations of dimensionless numbers as given in Tab. A.3.

Name	**aka**	**Formula**	**Description**	**Characteristic for**
Biot number	Bi	$\frac{L1/\lambda_W}{1/\alpha} = \mathrm{Nu}\frac{\lambda_F}{\lambda_W}$	resistance to thermal conduction in solid vs. heat transfer resistance into fluid	unsteady heat transfer from solid bodies into fluid
Stanton number	St	$\frac{\mathrm{Nu}}{\mathrm{Re}\cdot\mathrm{Pr}} = \frac{\alpha}{\rho U c_p}$	conductive wall heat flux vs. convective heat flux due to flow	heat exchange processes with flowing fluid
Rayleigh number	Ra	$\mathrm{Gr}\cdot\mathrm{Pr} = \frac{g\beta(T_W - T)L^3}{\nu a}$	buoyancy force times momentum diffusivity vs. viscous force times thermal diffusivity	natural convection flows
Richardson number	Ri	$\frac{\mathrm{Gr}}{\mathrm{Re}^2} = \frac{g\beta(T_W - T)L}{U^2}$	natural convection vs. forced convection	flows around heated bluff bodies with lift and viscous forces

Appendix B

Double Pipe

B.1 Calculations of the Parameters for the Double Pipe

The following calculation rules were taken from VDI (2010). The material properties of water were used as given in VDI (2010) and Wagner and Kretzschmar (2008).

At first the transferred heat $\dot{Q}_s$ from the secondary flow was by

$$\dot{Q}_s = \rho(T_{s,m})\dot{V}_s c_p(T_{s,m})(T_{s,in} - T_{s,out}) \tag{B.1}$$

where $T_{s,m} = (T_{s,in} + T_{s,out})/2$. By assuming an adiabatic system boundary at the outer pipe wall the outlet bulk temperature could be estimated

$$T_{bulk,out} = \frac{\dot{Q}_s}{\rho(T_{bulk,in})\dot{V}_{bulk} c_p(T_{bulk,in})} + T_{bulk,in}. \tag{B.2}$$

After that it was possible to calculate

$$T_{bulk,m} = \frac{T_{bulk,in} + T_{bulk,out}}{2}, \tag{B.3}$$

$$\mathrm{Re}_{bulk} = \frac{U_{bulk} * D_h}{ny(T_{bulk,m})} \tag{B.4}$$

and the logarithmic temperature

$$\Delta T_{ln} = \frac{(T_w - T_{bulk,in}) - (T_w - T_{bulk,out})}{ln\frac{T_w - T_{bulk,in}}{T_w - T_{bulk,out}}}. \tag{B.5}$$

Hereby, T_w was estimated. For the Nusselt number the following equations were used for the thermally and hydrodynamically developed region

$$\mathrm{Nu}_1 = 3.66 + 1.2k^{-0.8}, \tag{B.6}$$

the hydrodynamically developed region with thermal entry

$$\mathrm{Nu}_2 = 1.615\left(1 + 0.14k^{-1.2}\right)\left(\frac{1}{L^+}\right)^{1/3} \tag{B.7}$$

and the thermal and hydrodynamical entry region

$$\mathrm{Nu}_3 = \left(\frac{2}{1 + 22\mathrm{Pr}}\right)^{1/6}\left(\frac{1}{L^+}\right)^{1/2}. \tag{B.8}$$

All Nu numbers are collected into a mean Nusselt number

$$\mathrm{Nu}_m = \left(\mathrm{Nu}_1^3 + \mathrm{Nu}_2^3 + \mathrm{Nu}_3^3\right)^{1/6}. \tag{B.9}$$

In order to consider the variability of the material properties the following correlation is applied:

$$\mathrm{Nu}_{est} = \mathrm{Nu}_m\left(\frac{\mathrm{Pr}}{\mathrm{Pr}_w}\right)^{0.11} \tag{B.10}$$

The estimated average Nusselt number is then used to derive the heat transfer coefficient

$$\alpha_{est} = \frac{\mathrm{Nu}_{est}\lambda(T_{bulk,m})}{D_h} \tag{B.11}$$

which then results in an estimate for the transferred heat

$$\dot{Q}_{est} = \alpha_{est}\pi D_h L \Delta T_{ln}. \tag{B.12}$$

B.2 Additional Plots

B.2.1 Heated Case

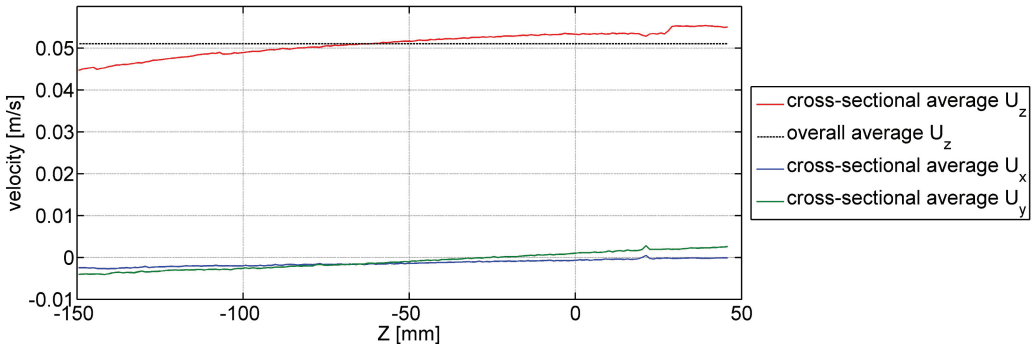

Fig. B.1: Cross-sectional average of the velocity components U in X- ,Y- and Z-direction for the heated case velocity data without 1st order correction.

B.2.2 Cooled Case

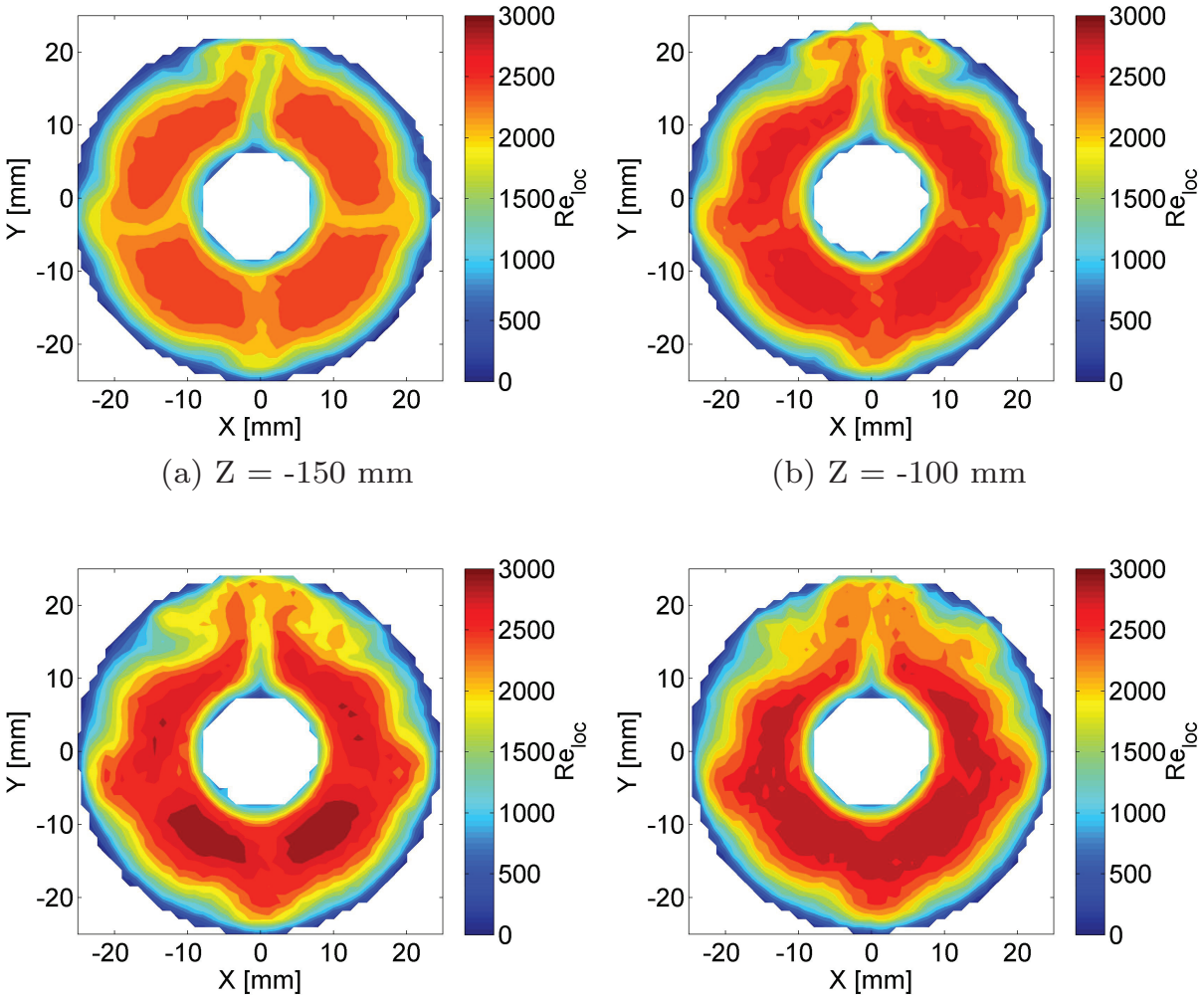

(a) Z = -150 mm

(b) Z = -100 mm

(c) Z = -50 mm

(d) Z = 0 mm

Fig. B.2: Contour plots showing the local Reynolds number Re(voxel) = $\frac{U_z(\text{voxel})D}{\nu(T_{bulk,in}+\Delta T(\text{voxel}))}$ for the heated case for different Z-positions. For the calculation the streamwise velocity value U_z(voxel) and the temperature-dependent kinematic viscosity of water $\nu(T_{bulk,in} + \Delta T(\text{voxel}))$ per voxel were used.

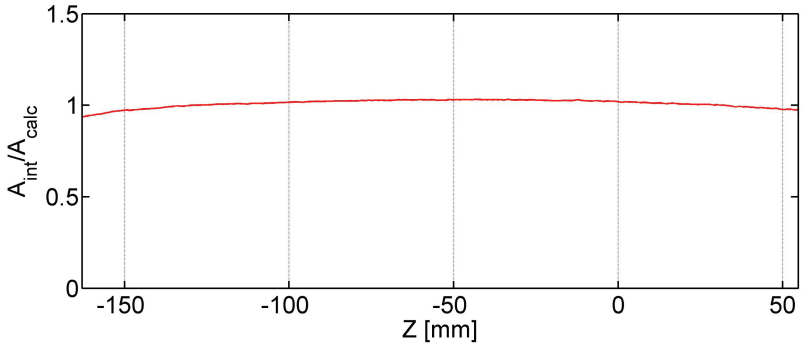

Fig. B.3: Average of the voxel-wise integrated cross-sectional area A_{int} referred to the calculated area A_{calc}.

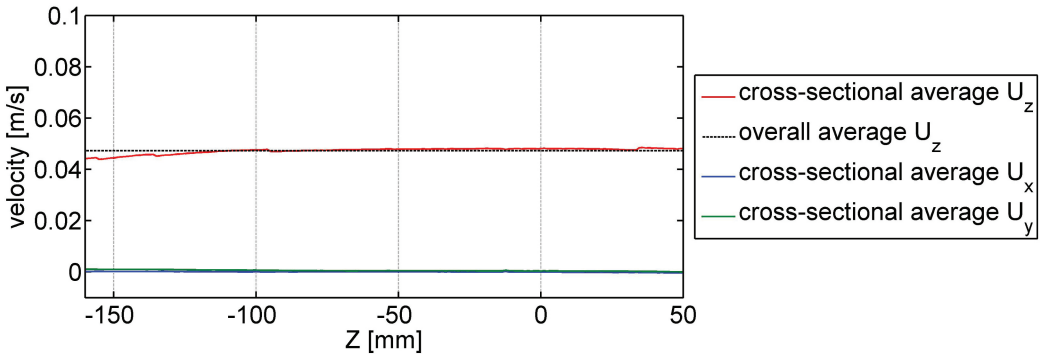

Fig. B.4: Cross-sectional average of the velocity components U in X- ,Y- and Z-direction.

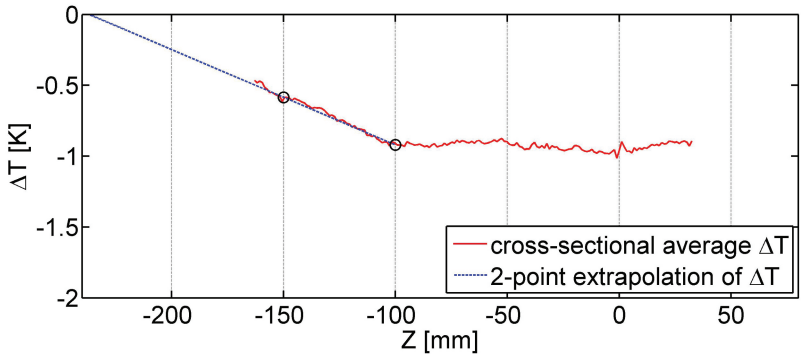

Fig. B.5: Cross-sectional average of the temperature difference field ΔT with two-point extrapolation..

Appendix C

Properties of Water

Tab. C.1: Fluid properties of water at a constant pressure of 1 bar taken from VDI (2010) and Wagner and Kretzschmar (2008).

T	v	ρ	h	s	c_p	w	κ	η	λ	β	a	Pr
								10^{-6}	10^{-3}	10^{-3}	10^{-6}	
[°C]	[m^3 kg^{-1}]	[kg m^{-3}]	[kJ kg^{-1}]	[kJ kg^{-1} K^{-1}]	[kJ kg^{-1} K^{-1}]	[m s^{-1}]	[-]	[kg m^{-1} s^{-1}]	[W m^{-1} K^{-1}]	[K^{-1}]	[$m^2 s^{-1}$]	[-]
0.0000	0.0010	999.8400	0.0597	-0.0001	4.2194	1402.4000	19665.0000	1791.8000	562.0000	-0.0677	0.1332	13.45252833
1.0000	0.0010	999.8900	4.2757	0.0152	4.2162	1407.3000	19804.0000	1732.6500	564.1000	-0.0497	0.1338	12.95003066
2.0000	0.0010	999.9400	8.4918	0.0306	4.2129	1412.2000	19943.0000	1673.5000	566.2000	-0.0324	0.1334	12.45193951
3.0000	0.0010	999.9550	12.7018	0.0459	4.2102	1416.9000	20076.5000	1620.4000	568.2500	-0.0156	0.135	12.00550297
4.0000	0.0010	999.9700	16.9119	0.0611	4.2074	1421.6000	20210.0000	1567.3000	570.3000	0.0006	0.1356	11.56278804
5.0000	0.0010	999.9550	21.1169	0.0762	4.2051	1426.1500	20338.5000	1519.4000	572.3000	0.0163	0.1361	11.16399261
6.0000	0.0010	999.9400	25.3219	0.0913	4.2027	1430.7000	20467.0000	1471.5000	574.3000	0.0315	0.1367	10.76836679
7.0000	0.0010	999.8950	29.5226	0.1063	4.2008	1435.0000	20590.0000	1428.1000	576.2500	0.0463	0.1372	10.4105702
8.0000	0.0010	999.8500	33.7233	0.1213	4.1988	1439.3000	20713.0000	1384.7000	578.2000	0.0606	0.1377	10.0554797
9.0000	0.0010	999.7751	37.9204	0.1362	4.1972	1443.4500	20830.5000	1345.3000	580.1000	0.0746	0.1382	9.733538864
10.0000	0.0010	999.7001	42.1174	0.1511	4.1955	1447.6000	20948.0000	1305.9000	582.0000	0.0881	0.1388	9.413923454
11.0000	0.0010	999.6002	46.3114	0.1658	4.1941	1451.5000	21060.0000	1269.9500	583.8500	0.1013	0.1393	9.122606487
12.0000	0.0010	999.5002	50.5054	0.1806	4.1926	1455.4000	21172.0000	1234.0000	585.7000	0.1142	0.1389	8.833307837
13.0000	0.0010	999.3704	54.6968	0.1952	4.1914	1459.2000	21279.0000	1201.1500	587.5000	0.1267	0.1403	8.569361889
14.0000	0.0010	999.2406	58.8881	0.2099	4.1902	1463.0000	21386.0000	1168.3000	589.3000	0.1389	0.1407	8.307162158
15.0000	0.0010	999.0908	63.0773	0.2244	4.1892	1466.5500	21488.0000	1138.2000	591.0500	0.1509	0.1412	8.067152576
16.0000	0.0010	998.9411	67.2664	0.2390	4.1881	1470.1000	21590.0000	1108.1000	592.8000	0.1620	0.1417	7.828666684
17.0000	0.0010	998.7666	71.4536	0.2534	4.1872	1473.5000	21686.5000	1080.4000	594.5000	0.1732	0.1421	7.609505265
18.0000	0.0010	998.5920	75.6407	0.2678	4.1863	1476.9000	21783.0000	1052.7000	596.2000	0.1843	0.1426	7.391677306
19.0000	0.0010	998.3976	79.8263	0.2822	4.1856	1480.1500	21874.5000	1027.1500	597.8500	0.1955	0.1430	7.191080844
20.0000	0.0010	998.2032	84.0118	0.2965	4.1848	1483.4000	21966.0000	1001.6000	599.5000	0.2066	0.1435	6.99165251
21.0000	0.0010	997.9723	88.1950	0.3106	4.1842	1486.3600	22048.6000	979.2800	601.1000	0.2167	0.1439	6.816707639
22.0000	0.0010	997.7414	92.3783	0.3248	4.1836	1489.3200	22131.2000	956.9600	602.7000	0.2267	0.1444	6.642734585
23.0000	0.0010	997.5105	96.5615	0.3389	4.1831	1492.2800	22213.8000	934.6400	604.3000	0.2368	0.1448	6.46972563
24.0000	0.0010	997.2796	100.7448	0.3531	4.1825	1495.2400	22296.4000	912.3200	605.9000	0.2468	0.1453	6.297673137
25.0000	0.0010	997.0487	104.9280	0.3672	4.1819	1498.2000	22379.0000	890.0000	607.5000	0.2569	0.1457	6.126569547
26.0000	0.0010	996.7688	109.1090	0.3811	4.1815	1500.7600	22449.4000	871.4400	609.0000	0.2661	0.1461	5.983487338
27.0000	0.0010	996.4888	113.2900	0.3950	4.1811	1503.3200	22519.8000	852.8800	610.5000	0.2753	0.1465	5.84113134
28.0000	0.0010	996.2089	117.4710	0.4089	4.1808	1505.8800	22590.2000	834.3200	612.0000	0.2845	0.1470	5.699496214
29.0000	0.0010	995.9290	121.6520	0.4229	4.1804	1508.4400	22660.6000	815.7600	613.5000	0.2937	0.1474	5.558576673
30.0000	0.0010	995.6490	125.8330	0.4368	4.1800	1511.0000	22731.0000	797.2000	615.0000	0.3029	0.1478	5.41836748
31.0000	0.0010	995.3264	130.0124	0.4504	4.1798	1513.2000	22790.0000	781.5800	616.4000	0.3114	0.1482	5.299883329
32.0000	0.0010	995.0037	134.1918	0.4641	4.1796	1515.4000	22849.0000	765.9600	617.8000	0.3199	0.1486	5.181946287
33.0000	0.0010	994.6811	138.3712	0.4778	4.1794	1517.6000	22908.0000	750.3400	619.2000	0.3283	0.1489	5.064552642
34.0000	0.0010	994.3584	142.5506	0.4915	4.1792	1519.8000	22967.0000	734.7200	620.6000	0.3368	0.1493	4.947698717
35.0000	0.0010	994.0358	146.7300	0.5051	4.1790	1522.0000	23026.0000	719.1000	622.0000	0.3453	0.1497	4.831380868
36.0000	0.0010	993.6728	150.9086	0.5186	4.1789	1523.8600	23074.0000	705.8200	623.3200	0.3532	0.1501	4.732024184
37.0000	0.0010	993.3099	155.0872	0.5320	4.1788	1525.7200	23122.0000	692.5400	624.6400	0.3611	0.1505	4.633090826
38.0000	0.0010	992.9469	159.2658	0.5455	4.1788	1527.5800	23170.0000	679.2600	625.9600	0.3691	0.1508	4.534578116
39.0000	0.0010	992.5839	163.4444	0.5589	4.1787	1529.4400	23218.0000	665.9800	627.2800	0.3770	0.1512	4.436483399
40.0000	0.0010	992.2210	167.6230	0.5724	4.1786	1531.3000	23266.0000	652.7000	628.6000	0.3849	0.1516	4.338804041
41.0000	0.0010	991.8221	171.8016	0.5856	4.1786	1532.8400	23303.8000	641.3200	629.8400	0.3924	0.1520	4.25480345
42.0000	0.0010	991.4232	175.9802	0.5989	4.1787	1534.3800	23341.6000	629.9400	631.0800	0.3998	0.1523	4.171131519
43.0000	0.0010	991.0243	180.1588	0.6121	4.1787	1535.9200	23379.4000	618.5600	632.3200	0.4073	0.1527	4.087786316

44.0000	0.0010	990.6254	184.3374	0.6254	4.1788	1537.4600	23417.2000	607.1800	633.5600	0.4147	0.1530	4.004765921
45.0000	0.0010	990.2265	188.5160	0.6386	4.1788	1539.0000	23455.0000	595.8000	634.8000	0.4222	0.1534	3.922068431
46.0000	0.0010	989.7901	192.6952	0.6516	4.1790	1540.2600	23483.0000	585.9400	635.9400	0.4292	0.1537	3.850394412
47.0000	0.0010	989.3537	196.8744	0.6647	4.1791	1541.5200	23511.0000	576.0800	637.0800	0.4363	0.1541	3.77897195
48.0000	0.0010	988.9174	201.0536	0.6777	4.1793	1542.7800	23539.0000	566.2200	638.2200	0.4433	0.1544	3.707799695
49.0000	0.0010	988.4810	205.2328	0.6907	4.1794	1544.0400	23567.0000	556.3600	639.3600	0.4504	0.1548	3.636876311
50.0000	0.0010	988.0447	209.4120	0.7038	4.1796	1545.3000	23595.0000	546.5000	640.5000	0.4574	0.1551	3.566200468
51.0000	0.0010	987.5772	213.5922	0.7166	4.1799	1546.2800	23613.8000	537.9200	641.5600	0.4641	0.1554	3.504629795
52.0000	0.0010	987.1097	217.7724	0.7294	4.1801	1547.2600	23632.6000	529.3400	642.6200	0.4708	0.1557	3.4432553
53.0000	0.0010	986.6422	221.9526	0.7423	4.1804	1548.2400	23651.4000	520.7600	643.6800	0.4776	0.1561	3.382076014
54.0000	0.0010	986.1747	226.1328	0.7551	4.1806	1549.2200	23670.2000	512.1800	644.7400	0.4843	0.1564	3.321090975
55.0000	0.0010	985.7072	230.3130	0.7679	4.1809	1550.2000	23689.0000	503.6000	645.8000	0.4910	0.1567	3.260299226
56.0000	0.0010	985.2072	234.4948	0.7806	4.1813	1550.9400	23699.0000	496.0800	646.8000	0.4974	0.1570	3.206940913
57.0000	0.0010	984.7071	238.6766	0.7932	4.1817	1551.6800	23709.0000	488.5600	647.8000	0.5038	0.1573	3.153738514
58.0000	0.0010	984.2070	242.8584	0.8059	4.1820	1552.4200	23719.0000	481.0400	648.8000	0.5103	0.1576	3.100691309
59.0000	0.0010	983.7069	247.0402	0.8185	4.1824	1553.1600	23729.0000	473.5200	649.8000	0.5167	0.1579	3.047798582
60.0000	0.0010	983.2068	251.2220	0.8312	4.1828	1553.9000	23739.0000	466.0000	650.8000	0.5231	0.1582	2.995059619
65.0000	0.0010	980.5652	272.1410	0.8935	4.1852	1556.3000	23749.0000	432.9000	655.4000	0.5541	0.1597	2.764377601
70.0000	0.0010	977.7752	293.0740	0.9550	4.1881	1557.6000	23722.0000	403.6000	659.6000	0.5841	0.1611	2.562639721
75.0000	0.0010	974.8584	314.0230	1.0156	4.1915	1557.8000	23658.0000	377.4000	663.5000	0.6132	0.1624	2.384132781
80.0000	0.0010	971.7984	334.9910	1.0754	4.1955	1557.1000	23561.0000	354.1000	667.0000	0.6417	0.1636	2.227326162
85.0000	0.0010	968.6262	355.9790	1.1344	4.2000	1555.4000	23432.0000	333.1000	670.2000	0.6695	0.1647	2.087466428
90.0000	0.0010	965.3162	376.9920	1.1926	4.2050	1552.8000	23275.0000	314.2000	673.0000	0.6970	0.1658	1.963166419
95.0000	0.0010	961.8899	398.0300	1.2502	4.2106	1549.3000	23090.0000	297.1000	675.5000	0.7241	0.1668	1.851916003

Nomenclature

Greek Letters

symbol	unit	descirption
α	$[^{\circ}]$	angle, flip angle
α	$[\frac{ppm}{C}]$	electronic screening rate
α	$[\frac{W}{m^2\ K}]$	heat transfer coefficient
β	$[\frac{10^{-3}}{K}]$	thermal expansion coefficient
β	[-]	open-area ratio
χ_V	[-]	volume magnetic susceptibility
γ	$[\frac{rad}{s\ T}]$	gyromagnetic constant
δ	[m]	boundary layer thickness
δ	$[^{\circ}]$	diffuser opening angle
η	$[\frac{kg}{m\ s}]$	dynamic viscosity
λ	$[\frac{W}{m\ K}]$	thermal conductivity
λ^*	$[\frac{N}{m^2}]$	first Lamé parameter
$\vec{\mu}$	$[\frac{N\ m}{T_2}]$	magnetic dipole moment vector
ν	$[[\frac{m^2}{s}]]$	kinematic viscosity
φ	$[^{\circ}]$	angular coordinate
Φ	$[^{\circ}]$	magnetic resonance signal phase angle
$\Delta\Phi$	$[^{\circ}]$	phase angle difference
ρ	$[\frac{kg}{m^3}]$	density
σ	[-]	electronic screening constant
σ_{vel}	$[\frac{m}{s}]$	phase noise velocity error

τ	[s]	duration
τ_{ji}	$[\frac{N}{m^2}]$	stress tensor
Θ	[°]	hydrogen bond angle
ω_L	$[s^{-1}]$	Larmor frequency

Latin Letters

symbol	unit	descirption
a	$[\frac{m^2}{s}]$	thermal diffusivity
A	$[m^2]$	area
A_{bulk}	$[m^2]$	bulk channel area
A_{calc}	$[m^2]$	calculated channel area
A_{int}	$[m^2]$	integrated channel area
B	$[\frac{V\ s}{m^2}]$	magnetic field strength
B_0	$[\frac{V\ s}{m^2}]$	main magnetic field
B_1	$[\frac{V\ s}{m^2}]$	radio-frequency field
B_{eff}	$[\frac{V\ s}{m^2}]$	effective magnetic field
B_{xy}	$[\frac{V\ s}{m^2}]$	transverse component of the radio-frequency field
$\vec{B}$	$[\frac{V\ s}{m^2}]$	magnetic field
c_p	$[\frac{kJ}{kg\ K}]$	isobaric specific heat capacity
c_v	$[\frac{kJ}{kg\ K}]$	isochoric specific heat capacity
C	$[\frac{1}{K}]$	Curie constant
d, D	[m]	diameter
d_h	[m]	hydraulic diameter
D	$[\frac{m^2}{s}]$	molecular diffusion coefficient
D_i	[m]	double pipe outer diameter of the inner pipe
D_o	[m]	double pipe inner diameter of the outer pipe
e_{ij}	$[\frac{1}{s}]$	deformation velocity tensor, strain tensor
$\vec{e}$	[-]	unit vector
e	$[\frac{J}{kg}]$	internal energy
E	[J]	energy
$\vec{E}$	$[\frac{V}{m}]$	electric field
$\vec{F}$	[N]	force
g	$\frac{m}{s^2}$	gravitational force
G_k	$[\frac{V\ s}{m^3}]$	magnetic gradient amplitude
$\vec{G}$	$[\frac{V\ s}{m^3}]$	magnetic gradient vector
h	$[\frac{J}{kg}]$	specific enthalpy
h	[m]	BFS inlet channel height
$\hbar$	[J s]	Planck constant
H	[J]	enthalpy
H	[m]	BFS outlet channel height
I	[-]	quantum mechanical spin number

$\vec{J}$	$[\frac{N\ m\ s}{rad}]$	spin angular momentum
k	$[\frac{J}{K}]$	Boltzmann constant
k	[-]	double pipe diameter ratio
k_i	$[\frac{m}{s^2}]$	specific body forces
$\vec{k}$	[-]	k-space position vector
L	[m]	length, BFS channel length, double pipe length
L_h	[m]	BFS heating length
L^+	[-]	double pipe dimensionless length
m	[kg]	mass
$\dot{m}$	$[\frac{kg}{s}]$	mass flow rate
M_0	[-]	magnetic resonance signal magnitude
M_0	$[\frac{A}{m}]$	equilibrium magnetization
M_{inh}	$[\frac{A}{m}]$	inherent magnetization
M_n	$[\frac{V\ s}{m^3}]$	gradient moment of n^{th} order
M_{xy}	$[\frac{A}{m}]$	transversal magnetization
M_z	$[\frac{A}{m}]$	longitudinal magnetization
$\vec{M}$	$[\frac{A}{m}]$	magnetization vector
N	[-]	number of spins
N_{acq}	[-]	number of acquisitions
$\vec{N}$	[Nm]	magnetic torque
p	[Pa]	static pressure
P_{ji}	$[\frac{N}{m^2}]$	friction stress tensor
q	[MeV]	elementary charge of a particle
Q	[J]	heat
$\dot{q}$	$[\frac{W}{m^2}]$	heat flux
$\dot{q}_W$	$[\frac{W}{m^2}]$	wall heat flux
$\dot{q}_i$	$[\frac{W}{m^2}]$	heat flux vector in index notation
$\dot{Q}$	[W]	heat transfer rate
r	[m]	radial coordinate
R	[m]	radius, radial coordinate
S	$[m^2]$	area, surface
S	[J]	magnetic resonance signal
S	[m]	BFS step height
t	$[s]$	time, time step
δt	$[s]$	duration
T	[°K]	temperature
ΔT	[K]	temperature difference
ΔT_{ln}	[-]	logarithmic temperature difference
T_{Res}	[ms]	temporal spacing between two phase steps

T_w	[°C]	wall temperature
T_1	[ms]	spin-lattice relaxation time
T_2	[ms]	spin-spin relaxation time
T_2'	[ms]	spin-spin relaxation time due to B_0-field imperfection
T_2^*	[ms]	apparent spin-spin relaxation time
T_{acq}	[min]	acquisition time
T_{ref}	[°C]	reference temperature
u_i	[$\frac{m}{s}$]	velocity vector in index notation
U	[$\frac{m}{s}$]	velocity component
U_{bulk}, U_0	[$\frac{m}{s}$]	bulk velocity
U_{HE}	[V]	heating elements voltage
U_x, U_y, U_z	[$\frac{m}{s}$]	velocity components in x-, y- and z-direction
U_R, U_Φ	[$\frac{m}{s}$]	velocity components in radial and angular direction
v	[$\frac{m^3}{kg}$]	specific volume
$\vec{v}$	[$\frac{m}{s}$]	velocity vector
V	[$\frac{m}{s}$]	velocity component
V	[m^3]	volume, integration region, control volume
V_{voxel}	[mm^3]	voxel volume
$\dot{V}$	[$\frac{m^3}{s}$]	volume flow rate
W	[$\frac{m}{s}$]	velocity component
W	[m]	channel width
W	[J]	work
x, y, z	[m]	coordinate
x´, y´	[m]	coordinate rotating frame of reference
x_r	[m]	BFS reattachment length
$\vec{x}$	[m]	position vector
x_i	[m]	position vector in index notation
X, Y, Z	[m]	coordinate
X_{voxel}	[mm]	voxel dimension

Dimensionless Numbers

symbol	descirption
Bi	Biot number
Ec	Eckert number
Gr	Grashof number
Nu	Nusselt number
Pe	Péclet number
Pr	Prandtl number
Ra	Rayleigh number
Re	Reynolds number
Ri	Richardson number
St	Stanton number

Mathematical Operators and Symbols

symbol	descirption
$\cdot$	scalar product
$\times$	vector product
$\frac{\partial}{\partial t}$	partial derivative
$\frac{\mathrm{d}}{\mathrm{d}t}$	total derivative
$\frac{\mathrm{D}}{\mathrm{D}t}$	material derivative
δ_{ji}	Kronecker delta
∇	gradient
$\nabla \times ()$	curl, rotation
$*+$	dimensionless parameter

Abbreviations

symbol	descirption
1D/2D/3D	One-/Two-/Three-Dimensions
4D	Phase-locked, Cine or Four-dimensional
1C/2C/3C	One-/Two-/Three-Components
AR	Aspect Ratio
BFS	Backward-Facing Step
BOS	Background-Oriented Schlieren
CAD	Computer-Aided Design
CANDU	Canadian Uranium Deuterium
CFD	Computational Fluid Dynamics
CLC	Cholesteric-based Liquid Crystal
CNL	Canada Nuclear Laboratories
CNLC	Chiral-Nematic-based Liquid Crystal
CNR	Contrast-to-Noise
CNSC	Canadian Nuclear Safety Commision
CSI	Center of Smart Interfaces
CTA	Constant Temperature Anemometry
DC	Duty Cycle [ms]
DFG	Deutsche Forschungsgemeinschaft
DP	Dephasing Parameter
ECG	Electrocardiogram
ER	Expansion Ratio
HVAC	Heating Ventilation and Air-conditioning
HWA	Hot Wire Anemometry
FE	Frequency Encoding
FID	Free Induction Decay
FLASH	Fast Low Angle Shot
FOP	Fiber Optical Probe
FOV	Field-Of-View
FFT	Fast Fourier Transformation
GE	Gradient Echo
GRAPPA	Generalized Auto-calibrated Partially Parallel Acquisition
HF	High Frequency
ID	Inner Diameter [m]
IEC	International Electronics Commission
iFT	inverse Fourier Transformation
LB-LOCA	Large Break Loss of Coolant Accident

LDA	Laser Doppler Anemometry
LDV	Laser Doppler Velocimetry
LSV	Laser Speckle Velocimetry
MC	Measurement Cycle [ms]
MHD	Magneto-Hydrodynamic effect
MR	Magnetic Resonance
MRC	Magnetic Resonance Concentration
MRI	Magnetic Resonance Imaging
MRS	Magnetic Resonance Spectroscopy
MRT	Magnetic Resonance Thermometry
MRV	Magnetic Resonance Velocimetry
NBR	Nitrile Rubber
NMR	Nuclear Magnetic Resonance
OD	Outer Diameter [m]
PA	Polyamide
PCI	Phase Contrast Imaging
PD	Proton Density
PE	Phase Encoding
PE	Polyethylene
PET	Polyethylenetherephtalate
PhD	Doctor of Philosophy
PIT	Particle Image Thermometry
PIV	Particle Image Velocimetry
PLIF	Planar Laser-Induced Fluorescence
PMMA	Poly(Methyl Methacrylate)
PRF	Proton Resonance Frequency
PS	Phase Steps
PSP	Pressure Sensitive Paint
PTV	Particle Tracking Velocimetry
PVC	Polyvinyl chloride
PHWR	Pressurized Heavy Water Reactor
RCCB	Residual Current-operated Circuit Brake
RF	Radio Frequency
RMS	Root Mean Square
RMSD	Root Mean Square Deviation
ROI	Region-Of-Interest
RTD	Platinum Resistance Thermometer
SD	Scan-cycle Duration [ms]
SE	Spin Echo

SENSE	Sensitivity Encoding
SMASH	Simultaneous Acquisition of Spatial Harmonics
SMP	Shape Memory Polymer
SNR	Signal-to-Noise Ratio
SNR_{mag}	Signal-to-Noise Ratio of the signal magnitude
SS	Slice Selection
SSFP	Steady-State Free Precession
STD	Standard Deviation
TAT	Total Acquisition Time [min]
TC	Thermocouple
TDH	Tetradecahedron, tetradecahedral
TE	Echo Time [ms]
TLC	Thermochromic Liquid Crystal
TR	Repetition Time [ms]
TSP	Temperature Sensitive Paint
TTL	Transistor-Transistor-Logic
VAC	Voltage in Alternating Current
Venc	Velocity Encoding Value [m/s]

List of Tables

List of Tables

List of Figures

References

Books

Albrecht, H.-E. et al. (2003). *Laser Doppler and Phase Doppler Measurement Techniques*. English. Berlin, Heidelberg: Springer Berlin Heidelberg.

Baehr, H. D. (2006). *Heat and mass-transfer*. 2nd rev. ed. Berlin; New York: Springer.

Bernstein, M. A. (2004). *Handbook of MRI pulse sequences*. Amsterdam; Boston: Academic Press.

Brown, M. A. et al. (2003). *MRI basic principles and applications*. English. Hoboken, N.J.: Wiley-Liss.

Bushberg, J. T. et al. (2002). *The essential physics of medical imaging*. 2nd ed. Philadelphia: Lippincott Williams & Wilkins.

Gennes, P. G. d. and J. Prost (2007). *The physics of liquid crystals*. eng. 2. ed., Reprint. The international series of monographs on physics 83. Oxford: Clarendon Press.

Gersten, K. and H. Herwig (1992). *Strömungsmechanik. Grundlagen der Impuls-, Wärme- und Stoffübertragung aus asymptotischer Sicht*. Ed. by B. Friedr. Vieweg & Sohn Verlagsgesellschaft mbH. 7.

Griffiths, D. J. (1999). *Introduction to electrodynamics*. 3rd ed. Upper Saddle River, N.J: Prentice Hall.

Haacke, M et al. (1999). *Magnetic resonance imaging: physical principles and sequence design*. New York: Wiley-Liss.

Books

Hendrix, A and J Krempe (2008). *Magnete, Spins und Resonanzen: Eine Einführung in die Grundlagen der Magnetresonanztomographie*.

Herwig, H. and A. Moschallski (2009). *Wärmeübertragung*. Vieweg+Teubner, Wiesbaden.

Herwig, H. (2006). *Strömungsmechanik eine Einführung in die Physik und die mathematische Modellierung von Strömungen*. German. Berlin; Heidelberg; New York: Springer.

Incropera, F. P. et al. (2006). *Fundamentals of Heat and Mass Transfer*. 6th ed. John Wiley & Sons.

Jeffrey, G. A. (1997). *An introduction to hydrogen bonding*. Topics in physical chemistry. New York: Oxford University Press.

Kalweit, A. (2006). *Handbuch für technisches Produktdesign: Material und Fertigung; Entscheidungsgrundlagen für Designer und Ingenieure*. German. Berlin: Springer.

Liboff, R. L. (2003). *Introductory quantum mechanics*. 4th ed. San Francisco: Addison-Wesley.

Lide, D. R., ed. (2014). *CRC handbook of chemistry and physics*. English. Oakville, US: Apple Academic Press Inc.

Liu, T. and J. P. Sullivan (2005). *Pressure and temperature sensitive paints*. Experimental fluid mechanics. Berlin ; New York: Springer.

McRobbie, D. et al. (2002). *MRI from Picture to Proton*. Cambridge University Press.

Nitsche, W. and A. Brunn (2006). *Strömungsmesstechnik*. de. VDI-Buch. Berlin/Heidelberg: Springer-Verlag.

Oswald, P. and P. Pieranski (2005). *Nematic and cholesteric liquid crystals: concepts and physical properties illustrated by experiments*. eng. The liquid crystals book series. Boca Raton: Taylor & Francis.

Raffel, M. (2007). *Particle image velocimetry a practical guide*. English. Heidelberg; New York: Springer.

Schlichting, H. (2000). *Boundary-layer theory*. 8th rev. and enl. ed. Berlin ; New York: Springer.

Spurk, J. and N. Aksel (2010). *Fluid Mechanics*. Springer Berlin / Heidelberg.

Stephan, P. (2013). *Thermodynamik Grundlagen und technische Anwendungen Band 1: Einstoffsysteme*. German. Berlin, Heidelberg: Imprint: Springer Vieweg.

Tropea, C. et al., eds. (2007). *Springer handbook of experimental fluid mechanics*. Berlin: Springer.

VDI (2010). *VDI heat atlas*. 2nd ed. VDI-Buch. Berlin; New York: Springer.

Wagner, W. and H.-J. Kretzschmar (2008). *International Steam Tables*. en. Berlin, Heidelberg: Springer Berlin Heidelberg.

Weishaupt, D. et al. (2009). *Wie funktioniert MRI?* Springer-Verlag Berlin Heidelberg.

Book Chapters

Camci, C. (2010). "Temperature and Heat Transfer Measurements". In: *Encyclopedia of Aerospace Engineering*. John Wiley & Sons, Ltd.

Fey, U. et al. (2013). "Investigation of Circular Cylinder Flow in Water Using Temperature-Sensitive Paint". English. In: *New Results in Numerical and Experimental Fluid Mechanics VIII*. Ed. by A. Dillmann et al. Vol. 121. Notes on Numerical Fluid Mechanics and Multidisciplinary Design. Springer Berlin Heidelberg, pp. 657–664.

PhD Thesis

Carlsson, A. (2009). "Susceptibility effects in MRI and ^{1}H MRS". PhD thesis. University of Gothenburg, Sweden.

Jung, B. (2005). "Neue kernspintomographische Techniken für funktionelle Untersuchungen des Herzmuskels". PhD thesis. Fakultät für Mathematik und Physik der Albert-Ludwigs-Universität Freiburg i. Brsg.

Noeske, R. (2000). "Anwendung der Hochfeld-(3-Tesla)- NMR-Tomographie: Abbildung des menschlichen Herzens und NMR-Thermographie an Phantomen fr eine Tiefenhyperthermie". PhD thesis. Freie Universität Berlin.

Peters, R. (2000). "Magnetic Resonance Thermometry for Image-Guided Thermal Therapy". PhD thesis. University of Toronto.

Journal Articles

Adrian, R. J. (1991). "Particle-Imaging Techniques for Experimental Fluid Mechanics". en. In: *Annual Review of Fluid Mechanics* 23.1, pp. 261–304.

Alkam, M. and M. Al-Nimr (1999). "Improving the performance of double-pipe heat exchangers by using porous substrates". In: *International Journal of Heat and Mass Transfer* 42.19, pp. 3609 –3618.

Armaly, B. et al. (1983). "Experimental and theoretical investigation of backward-facing step flow". In: *Journal of Fluid* 127.

Aung, W. (1983). "An experimental study of laminar heat transfer downstream of backsteps". In: *Journal of Heat Transfer* 1983.105, pp. 823–829.

Avancha, R. V. R. and R. H. Pletcher (2002). "Large eddy simulation of the turbulent flow past a backward-facing step with heat transfer and property variations". In: *Science* 23, pp. 601–614.

Benson, M. J. et al. (2010). "Three-dimensional concentration field measurements in a mixing layer using magnetic resonance imaging". In: *Experiments in Fluids* 49, pp. 43–55.

Bernstein, M. A. et al. (1998). "Concomitant gradient terms in phase contrast MR: analysis and correction". eng. In: *Magnetic Resonance in Medicine* 39.2, pp. 300–308.

Bloch, F. (1946). "Nuclear Induction". In: *Physical Review* 70.7-8, pp. 460–474.

Bowers, R. (1956). "Magnetic Susceptibility of Copper Metal at Low Temperatures". In: *Physical Review* 102 (6), pp. 1486–1488.

Bryant, D. J. et al. (1984). "Measurement of flow with NMR imaging using a gradient pulse and phase difference technique". In: *Journal of Computed Assisted Tomography* 8, pp. 588–593.

Buchenberg, W. B. et al. (2015). "Acquisition of 3D temperature distributions in fluid flow using proton resonance frequency thermometry". In: in press *Magnetic Resonance in Medicine*.

Buchenberg, W. B. et al. (2014). "Comparison of two fiber-optical temperature measurement systems in magnetic fields up to 9.4 Tesla". In: *Magnetic Resonance in Medicine* 73, pp. 2047–2051.

Budwig, R. (1994). "Refractive index matching methods for liquid flow investigations". English. In: *Experiments in Fluids* 17.5, pp. 350–355.

Childs, P. R. N. et al. (2000). "Review of temperature measurement". In: *Review of Scientific Instruments* 71.8, p. 2959.

Cohen, M (2001). "Real-Time Functional Magnetic Resonance Imaging". en. In: *Methods* 25.2, pp. 201–220.

Dabiri, D. (2009). "Digital particle image thermometry/velocimetry: a review". In: *Experiments in Fluids* 46, pp. 191–241.

De Poorter, J. (1995). "Noninvasive MRI thermometry with the proton resonance frequency method: study of susceptibility effects". eng. In: *Magnetic Resonance in Medicine* 34.3, pp. 359–367.

De Poorter, J. et al. (1994). "The Proton-Resonance-Frequency-Shift Method Compared with Molecular Diffusion for Quantitative Measurement of Two-Dimensional Time-Dependent Temperature Distribution in a Phantom". In: *Journal of Magnetic Resonance, Series B* 103.3, pp. 234 –241.

Duh, A. et al. (2003). "The elimination of magnetic susceptibility artifacts in the micro-image of liquid-solid interfaces: internal gradient modulation by the CPMG RF train". eng. In: *Journal of Magnetic Resonance (San Diego, Calif.: 1997)* 160.1, pp. 47–51.

Durmus, A. et al. (2002). "Investigation of heat transfer and pressure drop in a concentric heat exchanger with snail entrance". In: *Applied Thermal Engineering* 22.3, pp. 321 –332.

Eaton, J. K. and J. P. Johnston (1981). "A Review of Research on Subsonic Turbulent Flow Reattachment". en. In: *AIAA Journal* 19.9, pp. 1093–1100.

Eiamsa-ard, S. et al. (2008). "Turbulent flow heat transfer and pressure loss in a double pipe heat exchanger with louvered strip inserts". In: *International Communications in Heat and Mass Transfer* 35.2, pp. 120 –129.

Elkins, C. J. and M. T. Alley (2007). "Magnetic resonance velocimetry: applications of magnetic resonance imaging in the measurement of fluid motion". In: *Experiments in Fluids* 43.6, pp. 823–858.

Elkins, C. et al. (2003). "4D Magnetic resonance velocimetry for mean velocity measurements in complex turbulent flows". In: *Experiments in Fluids* 34, pp. 494–503.

Elkins, C. J. et al. (2004). "Full-field velocity and temperature measurements using magnetic resonance imaging in turbulent complex internal flows". In: *Journal of Heat and Fluid Flow* 25.5, pp. 702–710.

Ergin, Y. V. and L. I. Kostrova (1970). "Magnetic susceptibility of water as a function of temperature". en. In: *Journal of Structural Chemistry* 11.1, pp. 5–8.

Frenzel, T. et al. (1996). "Noninvasive temperature measurement in vivo using a temperature-sensitive lanthanide complex and 1H magnetic res-

onance spectroscopy". eng. In: *Magnetic Resonance in Medicine* 35.3, pp. 364–369.

Grimault, S. et al. (2004). "Quantitative measurement of temperature by proton resonance frequency shift at low field: a general method to correct non-linear spatial and temporal phase deformations". en. In: *Journal of Magnetic Resonance* 170.1, pp. 79–87.

Griswold, M. et al. (2002). "Generalized autocalibrating partially parallel acquisitions (GRAPPA)." In: *Magnetic Resonance in Medicine* 47.6, pp. 1202–10.

Grundmann, S. et al. (2012). "Experimental investigation of helical structures in swirling flows". In: *International Journal of Heat and Fluid Flow* 37, pp. 51–63.

Hattori, N. and S. Kotake (1978). "Combined free and forced-convection heat-transfer for fully-developed laminar flow in horizontal tubes - Experiments". In: *JSME International Journal Series B* 21, pp. 861–868.

Hindman, J. C. (1966). "Proton Resonance Shift of Water in the Gas and Liquid States". In: *The Journal of Chemical Physics* 44.12, p. 4582.

Hirota, M. et al. (2010). "Experimental study on turbulent mixing process in cross-flow type T-junction". In: *International Journal of Heat and Fluid Flow* 31.5, pp. 776–784.

Hirota, M. et al. (2006). "Three-Dimensional Structure of Turbulent Flow". In: *JSME International Journal* 49.4, pp. 1070–1077.

Iwai, H. and K. Nakabe (2000). "Flow and heat transfer characteristics of backward-facing step laminar flow in a rectangular duct". In: *Journal of Heat and Mass Transfer* 43, pp. 457–471.

Iwai, H. et al. (1999). "Numerical simulation of buoyancy-assisting, backward-facing step flow and heat transfer in a rectangular duct". In: *Heat Transfer Asian Research* 28.1, pp. 58–76.

Kamide, H. et al. (2009). "Study on mixing behavior in a tee piping and numerical analyses for evaluation of thermal striping". In: *Nuclear Engineering and Design* 239.1, pp. 58 –67.

Keating, a. et al. (2004). "Large-eddy simulation of heat transfer downstream of a backward-facing step". In: *Journal of Turbulence* 5.04, pp. 1–27.

Kimura, N. et al. (2010). "Experimental study on fluid mixing phenomena in T-pipe junction with upstream elbow". In: *Nuclear Engineering and Design* 240.10. 4th International Topical Meeting on High Temperature Reactor Technology (HTR 2008), with Regular Papers, pp. 3055 –3066.

Konstanczak, P. et al. (1997). "Thermometrie durch Messung der chemischen Verschiebung eines Lanthanidenkomplexes". German. In: *Strahlentherapie und Onkologie* 173.2, pp. 106–116.

Kuroda, K. (2005). "Non-invasive MR thermography using the water proton chemical shift". eng. In: *International Journal of Hyperthermia* 21.6, pp. 547–560.

Lingamneni, A. et al. (1995). "Validation of cine phase-contrast MR imaging for motion analysis". eng. In: *Journal of magnetic resonance imaging: JMRI* 5.3, pp. 331–338.

Liu, C. et al. (1990). "Flow in the coolant passages of an internal combustion engine cylinder head". English. In: *Experiments in Fluids* 10.1, pp. 50–54.

Lu, T. et al. (1998). "Heat transfer in open-cell metal foams". In: *Acta Materialia* 46.10, pp. 3619 –3635.

Macovski, A. (1996). "Noise in MRI". In: *Magnetic Resonance in Medicine* 36.3, pp. 494–497.

Marcon, P et al. (2011). "Magnetic susceptibility measurement using 2D magnetic resonance imaging". In: *Measurement Science and Technology* 22.10, p. 105702.

Markl, M. et al. (2003a). "Generalized reconstruction of phase contrast MRI: analysis and correction of the effect of gradient field distortions". eng. In: *Magnetic Resonance in Medicine* 50.4, pp. 791–801.

Markl, M. et al. (2003b). "Time-resolved three-dimensional phase-contrast MRI." In: *Journal of magnetic resonance imaging : JMRI* 17.4, pp. 499–506.

Mehta, R. D. (1977). "The Aerodynamic Design Of Blower Tunnels With Wide-Angle Diffusers". In: *Prog. Aerospace Sci.* 18, pp. 59–120.

Minn Khine, S. et al. (2013). "Heat-conduction error of temperature sensors in a fluid flow with nonuniform and unsteady temperature distribution". In: *Review of Scientific Instruments* 84.4, 044902.

Mohammed, H. et al. (2010). "Experimental study of forced and free convective heat transfer in the thermal entry region of horizontal concentric annuli". en. In: *International Communications in Heat and Mass Transfer* 37.7, pp. 739–747.

Morelli, J. N. et al. (2011). "An Image-based Approach to Understanding the Physics of MR Artifacts". en. In: *RadioGraphics* 31.3, pp. 849–866.

Nguyen, T. H. et al. (1983). "Combined Free and Forced Convection of Water Between Horizontal Concentric Cylinders". en. In: *Journal of Heat Transfer* 105.3, p. 498.

Nie, J. H. and B. F. Armaly (2003). "Reattachment of Three-Dimensional Flow Adjacent to Backward-Facing Step". In: *Journal of Heat Transfer* 125.3, p. 422.

Nie, J. (2002). "Three-dimensional convective flow adjacent to backward-facing step-effects of step height". In: *International Journal of Heat and Mass Transfer* 45, pp. 2431–2438.

Nieckele, A. O. and S. V. Patankar (1985). "Laminar Mixed Convection in a Concentric Annulus With Horizontal Axis". en. In: *Journal of Heat Transfer* 107.4, p. 902.

Onstad, A. J. et al. (2011). "Full-field measurements of flow through a scaled metal foam replica". In: *Experiments in Fluids* 50, pp. 1571–1585.

Pelc, N. J. et al. (1991). "Encoding strategies for three-direction phase-contrast MR imaging of flow". eng. In: *Journal of magnetic resonance imaging: JMRI* 1.4, pp. 405–413.

Peters, R. D. et al. (1998). "Ex vivo tissue-type independence in proton-resonance frequency shift MR thermometry". eng. In: *Magnetic Resonance in Medicine: Official Journal of the Society of Magnetic Resonance in Medicine / Society of Magnetic Resonance in Medicine* 40.3, pp. 454–459.

Piro, M. et al. (2015). "Progress in On-Going High Fidelity Experimental and Computational Fluid Dynamic Investigations within a CANDU Fuel Chanel". In: in press *Nuclear Engineering and Design*.

Poon, C. S. et al. (1989). "Fat/water quantitation and differential relaxation time measurement using chemical shift imaging technique". In: *Magnetic Resonance Imaging* 7.4, pp. 369 –382.

Ramaprabhu, P. and M. J. Andrews (2004). "Experimental investigation of RayleighTaylor mixing at small Atwood numbers". en. In: *Journal of Fluid Mechanics* 502, pp. 233–271.

Rieke, V. and K. Butts Pauly (2008). "MR thermometry." In: *Journal of Magnetic Resonance Imaging* 27.2, pp. 376–90.

Roméo, F. and D. I. Hoult (1984). "Magnet field profiling: analysis and correcting coil design". eng. In: *Magnetic Resonance in Medicine* 1.1, pp. 44–65.

Saldana, J. G. B. et al. (2005). "Numerical Simulation of Mixed Convective Flow Over a Three-Dimensional Horizontal Backward Facing Step". In: *Journal of Heat Transfer* 127.9, p. 1027.

Schenck, J. F. (1996). "The role of magnetic susceptibility in magnetic resonance imaging: MRI magnetic compatibility of the first and second kinds". In: *Medical Physics* 23.6, pp. 815–850.

Seltsam, M. M. (1995). "Experimental and Theoretical Study of Wide-Angle Diffuser Flow with Screens". In: *AIAA Journal* 33, No. 11, pp. 2092–2100.

Shmatukha, A. V. et al. (2007). "Correction of proton resonance frequency shift temperature maps for magnetic field disturbances using fat signal". eng. In: *Journal of Magnetic Resonance Imaging* 25.3, pp. 579–587.

Small, W. et al. (2009). "Magnetic resonance flow velocity and temperature mapping of a shape memory polymer foam device". eng. In: *Biomedical Engineering Online* 8.42, pp. 1–7.

Sodjavi, K. and J. Carlier (2013). "Experimental study of thermal mixing layer using variable temperature hot-wire anemometry". en. In: *Experiments in Fluids* 54.10.

Soher, B. J. et al. (2010). "Noninvasive temperature mapping with MRI using chemical shift water-fat separation". en. In: *Magnetic Resonance in Medicine* 63.5, pp. 1238–1246.

Song, Y. et al. (2014). "Characteristics of hydrogen bond revealed from water clusters". en. In: *The European Physical Journal D* 68.9.

Stephan, K. (1962). "Wärmeübergang bei turbulenter und bei laminarer Strömung in Ringspalten". de. In: *Chemie Ingenieur Technik - CIT* 34.3, pp. 207–212.

Sun, L. and L. Hall (2001). "An experimental solution of the graetz problem in heat exchangers". In: *International Communications in Heat and Mass Transfer* 28.4, pp. 461–466.

Tang, C et al. (1993). "Accuracy of phase-contrast flow measurements in the presence of partial-volume effects". eng. In: *Journal of Magnetic Resonance Imaging* 3.2, pp. 377–385.

Togun, H. et al. (2014). "A review of studies on forced, natural and mixed heat transfer to fluid and nanofluid flow in an annular passage". In: *Renewable and Sustainable Energy Reviews* 39.0, pp. 835 –856.

Tokgoz, S et al. (2012). "Temperature and velocity measurements in a fluid layer using background-oriented schlieren and PIV methods". In: *Measurement Science and Technology* 23.11, p. 115302.

Tsay, Y.-L. et al. (2004). "Heat transfer enhancement of backward-facing step flow in a channel by using baffle installation on the channel wall". In: *Acta Mechanica* 174.1-2, pp. 63–76.

Wassermann, F. et al. (2013). "Phase-locked 3D3C-MRV measurements in a bi-stable fluidic oscillator". In: *Experiments in Fluids* 54.3.

Wlodarczyk, W et al. (1998). "Three-dimensional monitoring of small temperature changes for therapeutic hyperthermia using MR". eng. In: *Journal of Magnetic Resonance Imaging* 8.1, pp. 165–174.

Xiong, J. et al. (2014). "Experimental investigation on anisotropic turbulent flow in a 6 × 6 rod bundle with LDV". In: *Nuclear Engineering and Design* 278.0, pp. 333–343.

Yapa, S. D. et al. (2014). "Comparison of magnetic resonance concentration measurements in water to temperature measurements in compressible air flows". en. In: *Experiments in Fluids* 55.11.

Zerari, K. et al. (2013). "Forced and mixed convection in the annulus between two horizontal confocal elliptical cylinders". en. In: *International Journal of Thermal Sciences* 74, pp. 126–144.

Proceedings of Conferences

Benson, M. et al. (2012). "Experimental-based Redesigns for Trailing Edge Film Cooling of Gas Turbine Blades". In: *Proceedings of ASME Turbo Expo 2012*.

Bruschewski, M. et al. (2014). "Measureing Turbulent Swirling Flow with Phase-Contrast MRI". In: *17th International Symposium on Applications of Laser Techniques to Fluid Mechanics Lisbon, Portugal, 07-10 July, 2014*.

Burton, L. S. et al. (2014). "MRI Based Diagnostics for Temperature Measurements in Turbulent Flows". In: *67th Annual Meeting of the APS Division of Fluid Dynamics*.

Michaelis, D. et al. (2006). "A 3D Time-resolved CCylinder Wake Survey by Tomographic PIV". In: *12th International Symposium on Flow Visualization September 10-14, 2006, German Aerospace Center (DLR), Göttingen, Germany*.

Piro, M. et al. (2014). "Progress in on-going Fluid Dynamic Investigations of a Deformed CANDU Fuel Bundle". In: *CFD4NRS-5 Workshop, 9-11 September, Zurich*.

Rezaey, R. et al. (2013). "Experimental Investigation of Heat Transfer and Fluid Flow in Laser Sintered Heat Exchangers". In: *8th World Conference on Experimental Heat Transfer, Fluid Mechanics, and Thermodynamics June 16-20, 2013, Lisbon, Portugal*.

Scholz, P. et al. (2012). "PIV measurements of the flow through an intake port using refractive index matching". In: *16th Int Symp on Applications*

of Laser Techniques to Fluid Mechanics Lisbon, Portugal, 09-12 July, 2012.

Testud, F. and M. Zaitsev (2009). "B0 Field Monitoring by Air-Matched Phantoms". In: *Proceedings of the 17th Annual Meeting of Intl. Soc. Magn. Reson. Med., Honolulu, Hawai'i, USA*, p. 2791.

Vogel, J. and J. Eaton (1985). "The transport of heat in a turbulent reattaching flow". In: *5th Symposium on Turbulent Shear Flows*.

Wassermann, F. et al. (2014a). "Applying Magnetic Resonance Thermometry to Engineering Flows". In: *17th International Symposium on Applications of Laser Techniques to Fluid Mechanics Lisbon, Portugal*.

Wassermann, F. et al. (2014b). "Flow through Tetradecahedrons". In: *17th International Symposium on Applications of Laser Techniques to Fluid Mechanics Lisbon, Portugal, 07-10 July, 2014*.

Wassermann, F. et al. (2014c). "Magnetic Resonance Velocimetry Measurements of the Flow through a Fuel Bundle". In: *CFD4NRS-5 Workshop, 9-11 September, Zurich*.

Westin, J. et al. (2008). "High-Cycle Thermal Fatigue in Mixing Tees: Large-Eddy Simulations Compared to a New Validation Experiment". In: *Proceedings of the 16th International Conference on Nuclear Engineering*. Asme, pp. 515–525.

Student research projects realized at Technische Universität Darmstadt within the scope of this PhD thesis

Basbug, S. et al. (2012). "Conception of a Flow Supply System for Flow Measurements using Magnetic Resonance Imaging". Advanced Design Project.

Bauer, A. (2013). "Conception and Construction of a wide-angle Diffuser for Future MRV-setups". Bachelor Thesis.

Freudenhammer, D. (2012). "Development of an Experimental Setup for in-situ Temperature Gradient Generation inside a MR scanner". Master Thesis.

Kiekebusch, N. P. von et al. (2015). "Conception of an MR-suitable experimental setup for the mixing of two fluid flows with different temperatures".
Siebner, J. (2013). "Conception and implementation of a transportable flow supply system for water flows". Bachelor Thesis.
Tsoukas, T. (2014). "Temperaturmessungen mittels MR-Thermometrie". Forschungsseminar.

Manuals

LDA and PDA Reference Manual (2011). Dantec Dynamics.